Linear and Nonlinear Damping Identification in Vibrations of Thin-Walled Structures

by
Prabakaran Balasubramanian

Department of Mechanical Engineering
McGill University
Montreal, Quebec, Canada

April 2019

A thesis submitted to McGill University
in partial fulfilment of the requirement of the degree of Doctor of Philosophy

SUMMARY

Dissipation of mechanical energy is one of the most important aspects of designing any structure. Understanding the amount of dissipation or, in other words, damping present in the structure is of critical importance while designing mission-critical components. The dissipation defines the maximum vibration amplitude reached by the system at its resonance for a given excitation. Higher vibration amplitude results in lower fatigue life or other vibration related damage.

Damping in a structure is typically characterized by experimental modal analysis and linear models. However, this assumption is not valid for structures experiencing large amplitude vibrations (larger than the characteristic dimension, for example, the thickness). Thin-walled structures such as rocket fuselage, nano/micro resonators, circular saws and nuclear fuel rods are modeled as plates, panels, and shells exhibit large amplitude vibrations. Experiments show that the damping value that is determined through conventional experimental modal analysis corresponds to a large overestimation of the maximum vibration amplitude reached by these thin-walled structures during large amplitude vibrations. Studies have in fact shown that the damping-amplitude relationship is nonlinear for large amplitude vibrations, hence requiring nonlinear models to characterize damping for these structures.

A small number of studies have focused on measuring damping variations and developing nonlinear damping models for large amplitude vibrations of elastic structures. However, limited research was found on the applicability of viscoelastic plates and slender beams. Many bio-mechanical and engineering structures like ear drum diaphragm (cochlea) and nuclear fuel rods are essentially viscoelastic plates and slender beams. Understanding the damping variation in large amplitude vibrations of these structures can help develop efficient and safe structures.

The objective of this thesis is to add to the existing body of knowledge to this domain of characterization of damping for viscoelastic plates and slender beams by means of experimental studies and development of validated nonlinear damping models.

In this thesis, an extensive series of experiments were conducted on plates made of different viscoelastic materials and slender elastic beams to study their large amplitude vibrations around the fundamental mode. Forced vibration measurements were carried out using laser Doppler vibrometers (LDV) and the nonlinear response was recorded using a stepped sine procedure. Accurate numerical models were also developed for each structure under test. In particular, reduced-order models were applied. A single-degree-of-freedom system identification tool was also developed.

Structural damping was estimated during large amplitude vibrations by comparing the experimental response to the response of two numerical models: (a) a validated reduced order model (b) a SDOF model based identification tool. The results obtained confirmed earlier studies finding that the damping of thin-walled structures increases nonlinearly as they undergo large amplitude vibrations. The equivalent viscous damping value increases as much as twice with respect to the value observed for small amplitude (linear) vibrations. The traditional linear viscous damping model is not capable to capture this variation and hence a change of the damping ratio with respect to vibration amplitude is required. Three nonlinear damping models (loss factor based on dissipated and stored energies, linear viscoelasticity based on the Kelvin-Voigt (KV) material model and Standard Linear Solid (SLS) material model) were developed to capture the damping variation. Among the three models, the SLS model proved to be more accurate in capturing the damping variation than the other two models. The SLS model essentially introduces an additional nonlinear damping term $x^2\dot{x}$ along with the linear viscous damping term $\dot{x}$. The SLS model also confirms the phenomenological nonlinear damping term sometimes arbitrarily introduced by other researchers to capture the nonlinear damping variation in MEMS and NEMS.

RÉSUMÉ

La dissipation de l'énergie mécanique est l'un des aspects les plus importants de la conception d'une structure. Comprendre la quantité de dissipation ou, en d'autres termes, l'amortissement présent dans la structure est d'une importance cruciale lors de la conception de composants critiques. La dissipation définit l'amplitude maximale de vibration atteinte par le système à sa résonance pour une excitation donnée. Une amplitude de vibration plus élevée réduit la durée de vie en fatigue ou engendre d'autres dommages liés aux vibrations.

L'amortissement dans une structure est généralement caractérisé par une analyse modale expérimentale et des modèles linéaires. Cependant, cette hypothèse n'est pas valable pour les structures soumises à des vibrations de grande amplitude (supérieures à la dimension caractéristique, par exemple l'épaisseur). Les structures à paroi mince telles que le fuselage d'une fusée, les nano- et micro-résonateurs, les scies circulaires et les barres de combustible nucléaire sont modélisées sous la forme de plaques, de panneaux et de coques présentant des vibrations de grande amplitude. Les expériences montrent que l'amortissement estimé par l'analyse modale expérimentale conventionnelle correspond à une surestimation importante de l'amplitude maximale de vibration atteinte par ces structures à paroi mince lors de vibrations de grande amplitude. Des études ont en effet montré que la relation amortissement-amplitude est non linéaire pour les vibrations de grande amplitude, d'où la nécessité de modèles non linéaires pour caractériser l'amortissement de ces structures.

Peu d'études ont été consacrées à la mesure des variations de l'amortissement et au développement de modèles d'amortissement non linéaires pour les vibrations d'amplitude importante de structures élastiques. Cependant, ont été trouvées peu de recherches conduites sur leur applicabilité sur des plaques viscoélastiques et des poutres élancées. De nombreuses structures mécaniques et biomécaniques telles que le diaphragme du tympan (cochlée) et les barres de combustible nucléaire sont essentiellement des plaques viscoélastiques et des poutres élancées. Comprendre la variation de l'amortissement des vibrations de grande amplitude de ces structures peut aider à développer des structures efficaces et sûres. L'objectif de cette thèse est de contribuer à la connaissance dans ce domaine de la caractérisation de l'amortissement des

plaques viscoélastiques et des poutres élancées à l'aide d'études expérimentales et du développement de modèles d'amortissement non linéaires validés.

Dans cette thèse, une vaste série d'expériences a été menée sur des plaques en différents matériaux viscoélastiques et sur des poutres élastiques élancées afin d'étudier leurs vibrations de grande amplitude autour du mode fondamental. Des mesures de vibrations forcées ont été effectuées à l'aide de vibromètres laser à effet Doppler (VLD) et la réponse non linéaire a été enregistrée à l'aide d'une procédure sinusoïdale progressive. Des modèles numériques précis ont également été développés pour chaque structure testée. Des modèles d'ordre réduit ont notamment été appliqués. Un outil d'identification de modèles à un degré de liberté a également été mis au point.

L'amortissement structural a été estimé lors de vibrations de grande amplitude en comparant la réponse expérimentale à la réponse de deux modèles numériques: (a) un modèle d'ordre réduit validé et, grâce à un outil d'identification, (b) un modèle à un seul degré de liberté. Les résultats obtenus confirment des études antérieures montrant que l'amortissement des structures à paroi mince augmente de façon non linéaire à mesure qu'elles subissent des vibrations de plus grande amplitude. La valeur d'amortissement visqueux équivalente augmente jusqu'à deux fois par rapport à la valeur observée pour les vibrations (linéaires) de faible amplitude. Le modèle d'amortissement visqueux linéaire traditionnellement utilisé n'est pas capable de capturer cette variation et il convient donc de modifier le taux d'amortissement en fonction de l'amplitude de vibration. Trois modèles (facteur de perte basé sur les énergies dissipée et stockée, viscoélasticité linéaire basée sur les matériaux de Kelvin-Voigt (KV) et solide linéaire standard (SLS)) ont été développés pour prendre en compte l'évolution non linéaire de l'amortissement. Parmi les trois modèles, le modèle SLS s'est avéré le plus précis pour reproduire la variation d'amortissement que les deux autres modèles. Le modèle SLS introduit essentiellement un terme d'amortissement non linéaire supplémentaire $x^2\dot{x}$ ainsi que le terme d'amortissement visqueux linéaire $\dot{x}$. Le modèle SLS valide le modèle phénoménologique d'amortissement non linéaire introduit par d'autres chercheurs pour reproduire la variation d'amortissement non linéaire dans les nanosystèmes et microsystèmes électromécaniques.

Linear and Nonlinear Damping Identification in Vibrations of Thin-Walled Structures

ACKNOWLEDGEMENT

Last but not least, I am grateful to my parents Malarkodi and Balasubramanian, who have provided me with their unending love and support, without which all this would have been impossible. I am also grateful to my siblings and friends who have supported me along the way. Finally, to my lovely wife Asha for being the hope of my life.

யாதும் ஊரே யாவரும் கேளிர்
-கணியன் பூங்குன்றனார்

To us all towns are our own, everyone our kin
-Kaniyan Poongunranar

Linear and Nonlinear Damping Identification in Vibrations of Thin-Walled Structures

TABLE OF CONTENTS

LIST OF FIGURES

LIST OF TABLES

CONTRIBUTION TO ORIGINAL KNOWLEDGE

The objective of this thesis is to add to the existing body of knowledge to this domain of characterization of damping for viscoelastic plates and slender beams by means of experimental studies and development of validated nonlinear damping models. Limited research was found on its applicability to viscoelastic plates and slender beams. Many bio-mechanical and engineering structures such as ear drum diaphragm (cochlea) and nuclear fuel rods are essentially viscoelastic plates and slender beams. Understanding the damping variation in large amplitude vibrations of these structures can help develop efficient and safe structures. The most original and innovative contributions of the thesis are (a) conducting large amplitude vibration measurements on viscoelastic rubber plates of different materials (b) estimating the damping variation of the rubber plates using a novel nonlinear damping model (c) conducting large amplitude vibration measurements on slender beams in various configurations with and without fluid structure interaction and (d) estimating the damping variation of slender beams using a simplified single degree of freedom model.

Large amplitude vibrations were experimentally measured around the fundamental mode of rubber plates and slender beams. These experiments captured nonlinearity and hysteresis characteristics providing insight into the nonlinear response. To the best knowledge of the authors this is the first time the nonlinear response of such structures has been characterized. These experiments were based on fixtures which were designed such that: (a) they ensured the application of the required boundary conditions (fixed-fixed) (b) their natural frequencies were farther away from the structure's fundamental natural frequency to ensure that there was no fixture-structure interaction.

For the experiments on rubber plates, large amplitude vibration measurements were obtained on three plates manufactured from three different materials (silicone, hard silicone and, neoprene). The nonlinear force – displacement plots of the plates were obtained at every excitation frequency.

For the experiments on slender beams, large amplitude vibration measurements were obtained on three zirconium alloy beams (modeling nuclear fuel rods found in pressurized water reactors) with three different configurations: empty tube, tube with freely moving pellets (modeling nuclear fuel pellets) and tube with fixed pellets. These three tubes were tested both in air and in water. In total, six different configurations of the slender beams were tested. These six configurations were chosen to understand and study the impact of characteristics such as: stiffness, damping, one-to-one internal resonance, and fluid-structure interaction. These experiments provide designers with wealth of information to understand the impact of their design choice using these structures.

Structural damping was estimated during large amplitude vibrations by comparing the experimental response to the numerical models. First, the numerical models were validated by comparing the nonlinear stiffness between the model and experiments. The linear viscous damping of the structures was identified using validated models during large amplitude vibrations. Subsequently, the following three nonlinear damping models were developed to evaluate its suitability to capture the observed behavior.

   a) Kelvin-Voigt (KV) based nonlinear damping model
   b) Standard Linear Solid (SLS) based nonlinear damping model
   c) Loss factor based on dissipated and stored energies model

Among the three models –first two models were based on the theory of linear viscoelasticity applied to geometric nonlinear vibration, while the third one was based on energies. The SLS model proved to be more accurate in capturing the damping variation than the other two models. The SLS model essentially introduces an additional nonlinear damping term $x^2\dot{x}$ along with the linear viscous damping term $\dot{x}$. The SLS model also confirms the phenomenological nonlinear damping term introduced by other scholars to capture the nonlinear damping variation in MEMS and NEMS.

Finally, a simple parameter identification tool based on the Single Degree of Freedom (SDOF) model approximation and on the Harmonic Balance method was also developed to extract the nonlinear stiffness and damping parameters from the experimental responses.

As per the authors best knowledge this is the probably first time any such effort has been undertaken to estimate damping in large amplitude vibration for viscoelastic plates and slender beams.

CONTRIBUTION OF THE AUTHORS

This is a manuscript-based thesis comprising of four journal papers [1-4]. Among the four papers, three are published [1, 2, 4] and one has been submitted [3] in peer-reviewed international journals.

The author is the primary author for the first two journal papers [1, 2]. These two journal papers deal with nonlinear vibration measurement and numerical modelling of viscoelastic elastic plates. The author conducted all the experiments, developed the validated numerical models and wrote the manuscript. The co-authors including the author's supervisor provided guidance and support including review of results and manuscripts.

The third journal paper [3] also concerns with the nonlinear vibration measurement and numerical modelling of viscoelastic plates. This paper has been submitted for review. The author's supervisor, Professor Marco Amabili developed the numerical model, contributed to the manuscript and provided guidance. The author conducted the experiments, validated the numerical model using the experimental data and estimated the nonlinear damping characteristics. The author also partly contributed to the manuscript related to this publication. The co-author, Dr. Giovani Ferrari offered valuable suggestions during experiments and reviewed the results.

The fourth journal paper [4] deals with the nonlinear vibration measurement and numerical modelling of slender beams. The author of this thesis designed and manufactured the fixture required for testing the slender tubes both in air and in water. Together with Dr. Giovanni Ferrari and Mr. Lorenzo Piccagli, he performed the linear and nonlinear vibration measurements. He contributed to the manuscript of the paper along with Mr. Giovanni Ferrari. Mr. Stanislas Le Guisquet developed the procedure to extract nonlinear parameters and damping using the

harmonic balance method in the frequency domain. Prof. Marco Amabili, Mr. Brian Painter and Dr. Kostas Karazis supervised the work.

OUTLINE OF THE THESIS

This thesis primarily concerns with modelling the nonlinear damping characteristics of viscoelastic plates and slender beams under large amplitude vibrations. The thesis is divided into six chapters.

Chapter 1 introduces some concepts and methods used throughout the thesis for modeling both large amplitude vibration and damping. A detailed literature review on nonlinear vibrations of viscoelastic plates and elastic slender tubes is presented in the same chapter. The motivation and the objectives of the present work are also presented in the same chapter.

Chapter 2, 3 and 4 deal with the large amplitude vibration measurement and damping identification of rubber plates. The following papers are presented in the corresponding chapters.

a) Chapter 2 - "Experimental and theoretical study on large amplitude vibrations of clamped rubber plates" published in the International Journal of Nonlinear Mechanics [1].

b) Chapter 3 – "Identification of the viscoelastic response and nonlinear damping of a rubber plate in nonlinear vibration regime" published in the journal Mechanical Systems and Signal Processing[2].

c) Chapter 4 – "Nonlinear Fractional Damping and Frequency-Depending Storage Modulus in Nonlinear Vibrations of Viscoelastic Rectangular Plates" submitted to an international journal [3].

Chapter 5 concerns with the large amplitude vibration measurement and damping identification of slender beams in various configurations. The paper "Non-linear vibrations of nuclear fuel rods" published in the journal of Nuclear Engineering and Design [4] is presented in this chapter.

The final chapter provides the conclusion of the study and suggested future areas of research.

1   INTRODUCTION AND LITERATURE REVIEW

1.1   THEORETICAL BACKGROUND

It is common to use linear theories to understand the dynamics of any structure and subsequently modify them for its intended purpose. Real life structures, however, are inherently nonlinear; thus, a linear theory is just a first-order approximation of their actual behavior. Linearized approximations, typically performed around the operating region, adequately capture the behavior of many engineering structures and are sufficient in many practical scenarios. Their advantages are that they can be solved readily, because the superposition principle is valid. These advantages combined with the availability of well-established tools and computational ease made linear theory the *de facto* standard for dynamic problems. It should be noted that linear models can predict the onset of many nonlinear behaviors such as buckling or dynamic divergence. But nonlinear models are necessary to predict the behavior of the structure after such incidents.

With the advent of lightweight, micro, and nanomechanical structures, and the usage of soft materials combined with an ever-increasing demand for efficiency, mechanical systems are becoming thinner and lighter. Thin-walled structures present complex nonlinear dynamics when compared to its thicker counterparts. Understanding the dynamics exhibited by thin-walled structures has become a necessity to ensure safety, long life and efficiency. Computational capabilities over the past few decades have grown exponentially to cater to the sophisticated calculations required for the solution of nonlinear models.

The nonlinear response of structures can be attributed to many sources. They are broadly classified into, but not limited to, material or physical, geometrical, inertial and boundary conditions related nonlinearities. The stress-strain relationship of all materials is essentially nonlinear, and the type of nonlinearity due to this is called material or physical nonlinearity. If the strain experienced by the material is sufficiently small, it can be approximated by Hooke's law (linear stress-strain law). However, for large strains, nonlinear stress-strain relationships, such as neo-Hookean, Mooney-Rivlin, Ogden, etc., are required. Most metals and soft materials around a small strain range can be modeled as Hookean materials. In this thesis, all the materials

are modeled as Hookean materials. The relationship between the strain and displacement of any structure experiencing a large amount of vibration or deflection is also nonlinear. The nonlinearity introduced by this type of phenomenon is called geometrical nonlinearity. Further explanation about this is given in the following section, as this thesis mainly revolves around it. Inertial nonlinearity arises from the presence of concentrated or distributed masses. Nonlinearities introduced by body forces such as magnetic and electric forces, are also possible. Nonlinearities can be given by boundary conditions as well; such as nonlinear springs, contact and slip at the boundaries. In this thesis, geometrical nonlinearities are considered while the other types of nonlinearities are ignored, as they are negligible in the structures under study.

1.1.1 GEOMETRICALLY NONLINEAR VIBRATIONS

When a structure vibrates at amplitudes close to or larger than its characteristic dimension (e.g. its thickness), it is said to be vibrating at large amplitude. Practical examples of structures experiencing large amplitude or geometrically nonlinear vibrations are aircraft fuselage, wings, fins, nano-resonators, large human arteries, turbine blades, nuclear fuel rods, [5] etc. Here, the relationship between strain and displacement cannot be approximated as linear anymore, as it is instead done for small amplitude vibrations. This specific nonlinearity is called geometrical nonlinearity. For example, a thin rectangular plate with thickness h (as shown in Fig. 1-1), which is much smaller than its width and length, vibrating with an amplitude of around h would exhibit geometrical nonlinearity.
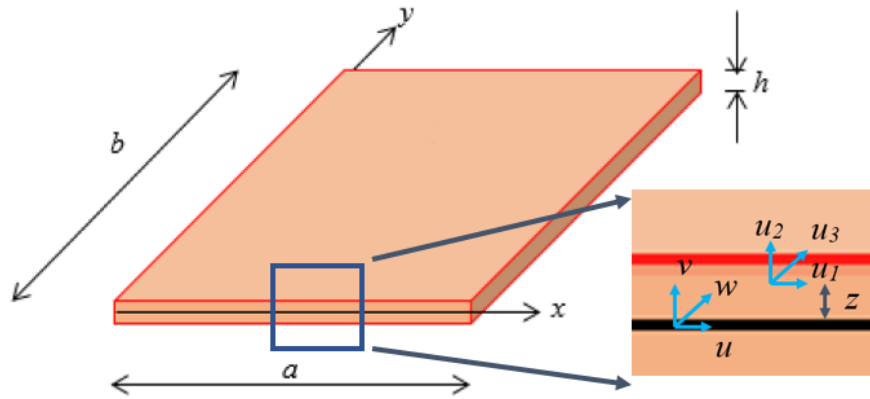
Fig. 1-1: A thin rectangular plate

This is because beyond a certain amplitude of vibration, the stretching energy of the plate must be taken in to account in the numerical model along with the bending energy. The stretching of the plate involves nonlinear terms with respect to the normal displacement of the plate, while bending includes only linear terms with respect to normal displacement. The Green-Lagrange strain-displacement relationship would be required to model such behavior and is given below.

$$
\begin{aligned}
\varepsilon_{xx} &= \frac{\partial u_1}{\partial x} + \frac{1}{2}\left[\left(\frac{\partial u_1}{\partial x}\right)^2 + \left(\frac{\partial u_2}{\partial x}\right)^2 + \left(\frac{\partial u_3}{\partial x}\right)^2\right], \\
\varepsilon_{yy} &= \frac{\partial u_2}{\partial y} + \frac{1}{2}\left[\left(\frac{\partial u_1}{\partial y}\right)^2 + \left(\frac{\partial u_2}{\partial y}\right)^2 + \left(\frac{\partial u_3}{\partial y}\right)^2\right], \\
\gamma_{xy} &= \frac{1}{2}\left[\frac{\partial u_1}{\partial y} + \frac{\partial u_2}{\partial x} + \left(\frac{\partial u_1}{\partial x}\frac{\partial u_1}{\partial y} + \frac{\partial u_2}{\partial x}\frac{\partial u_2}{\partial y} + \frac{\partial u_3}{\partial x}\frac{\partial u_3}{\partial y}\right)\right],
\end{aligned}
\tag{1.1}
$$

where, ε_{xx}, ε_{yy} and γ_{xy} are the strain in the xx, yy and xy direction respectively, u_1, u_2 and u_3 are the displacements of a generic point of the plate at a distance z from the middle surface in the x, y and z directions respectively. u_1, u_2 and u_3 are defined as below,

$$
\begin{aligned}
u_1 &= u(x, y) - z\frac{\partial w}{\partial x}, \\
u_2 &= v(x, y) - z\frac{\partial w}{\partial x}, \\
u_3 &= w(x, y),
\end{aligned}
\tag{1.2}
$$

where, u, v, and w are middle surface deflections of the plate in the x, y and z directions respectively. It can be clearly seen that the strain-displacement relationship is nonlinear, containing stretching part and bending part. Ignoring the stretching part (which is an acceptable assumption for structures experiencing small amplitude vibrations), the classical linear strain-displacement relationship is obtained as below (eq. (1.3)). In some cases, in-plane displacements (u and v) can also be ignored as they can be extremely small for small amplitude vibrations.

$$\varepsilon_{xx} = \frac{\partial u_1}{\partial x} = \frac{\partial u}{\partial x} - z\frac{\partial^2 w}{\partial x^2},$$

$$\varepsilon_{yy} = \frac{\partial u_2}{\partial y} = \frac{\partial v}{\partial y} - z\frac{\partial^2 w}{\partial y^2}, \tag{1.3}$$

$$\gamma_{xy} = \frac{1}{2}\left[\frac{\partial u_1}{\partial y} + \frac{\partial u_2}{\partial x}\right] = \frac{1}{2}\left[\frac{\partial u}{\partial x} + \frac{\partial v}{\partial y} - 2z\frac{\partial w}{\partial x \partial y}\right].$$

1.1.2 MODELLING OF A STRUCTURE

All structures are essentially three dimensional in nature, with a finite length, width, and thickness. However, it is often possible to model them with fewer dimensions without compromising the accuracy of the model to reduce the computational effort and time. For example, a beam has its length much larger than its width and thickness and can be modeled as a one-dimensional structure. A plate has its length and width much larger than its thickness and can be modeled as a two-dimensional structure. Similarly, a shell can also be modeled as a two-dimensional structure with length and radius. Based on the fewer dimensions description model of the structure, other points of the structure can be identified using an appropriate approximation.

There are various ways a continuous system can be modeled including geometric nonlinearity. Real-life structures would require infinite degrees of freedom to be modeled, as each atom of the structure represents a degree of freedom. The assumption that the displacement of the structure is a continuous function and no sudden change is possible allows us to use continuum mechanics to model structures with a finite number of degrees of freedom. Partial Differential Equations (PDE) are required to represent a continuous structure with boundary conditions, whereas, Ordinary Differential Equations (ODE) with initial conditions represent a discrete system. Hence it is common to discretize a continuous structure using one of the many discretization methods available, to a finite degree of freedom system. The Galerkin (or Ritz-Galerkin), direct Lagrangian, Finite Element, and Collocation methods are some of the widely used approaches for the discretization of continuous structures [6].

Direct Lagrangian discretization has gained popularity in the past few decades due to its versatility and is used throughout this thesis for modeling the structures of interest with a sufficient number of degrees of freedoms. In this method, the unknown displacements of the structure (*u*, *v*, and *w*) are expanded using truncated series of admissible functions that satisfy the geometric and natural boundary conditions. Subsequently, the potential, kinetic, dissipative, and virtual work energies of the structure are calculated. For example, the potential energy of a thin plate can be calculated under Kirchhoff's hypothesis using the equation,

$$U = \frac{1}{2} \int_{-\frac{h}{2}}^{\frac{h}{2}} \int_{0}^{a} \int_{0}^{b} \left(\sigma_{xx}\, \varepsilon_{xx} + \sigma_{yy}\, \varepsilon_{yy} + \tau_{xy}\, \gamma_{xy} \right) dx\, dy\, dz \qquad (1.4)$$

where σ_{xx}, σ_{yy} and τ_{xy} are Kirchhoff stresses and; *a*, *b* and *h* are the length, width and thickness of the plate respectively.

The calculated energies are directly inserted into the Lagrangian equation of motion (1.5) to get a set of Ordinary Differential Equations. The number of ODEs is the same as the number of generalized coordinates used to expand the unknown displacement of the structure. The Lagrangian equation of motion is,

$$\frac{d}{dt}\left(\frac{\partial T}{\partial q_j} \right) - \frac{\partial T}{\partial q_j} + \frac{\partial U}{\partial q_j} = -\frac{\partial F}{\partial q_j} + \frac{\partial W}{\partial q_j}, \qquad for \;\; j = 1, \dots (N_u + N_v + N_w), \qquad (1.5)$$

where, *T* is the kinetic energy, *U* is the potential energy, *F* is the dissipative energy, *W* is the virtual work from external forces, q_j are the generalized coordinates and N_u, N_v, and N_w are the number of generalized coordinates used to expand the *u*, *v*, and *w* displacement functions respectively.

This method is quite powerful because the unknown displacement functions need to satisfy only the geometric boundary conditions while the natural boundary conditions are automatically satisfied by the energy minimization of the Lagrangian equation. However, fewer degrees of freedom are required for the solutions to converge if displacement functions satisfying both geometric and natural boundary conditions are used. Essentially, the geometrically nonlinear model of a continuous structure can be written as a set of nonlinear Ordinary Differential

Equations. Fluid-structure interactions can be modeled readily by adding fluid-related energies to kinetic, potential and dissipative energies [5].

1.1.3 NONLINEAR DYNAMICS

A set of Nonlinear Ordinary Differential Equations (ODE) can be solved using any of the many available techniques to get the response of the structure for a given loading and initial conditions. Compared to linear systems, nonlinear systems can present complicated responses. The steady-state response of nonlinear systems depends on the initial conditions and is not unique, contrary to their linear counterpart. The characteristics of nonlinear systems include, but are not limited to, amplitude-dependent resonant frequency, super, and sub-harmonic, quasi-periodic, and chaotic responses as well as internal resonances. The procedure chosen to solve the nonlinear ODEs should be able to capture the nonlinear behaviors of the system, since not all available techniques have the capability to reproduce the entirety of possible nonlinear behaviors. For example, time integration methods such as Runge-Kutta cannot identify unstable solutions and give erroneous results when stiff and not stiff equations are coupled together. Similarly, quasi-periodic and chaotic responses cannot be captured by the pseudo-arclength continuation methods such as those implemented in the software AUTO [7]. In this thesis, for solving nonlinear ODEs, the pseudo-arclength continuation method via AUTO software was used widely, as the systems under study are not expected to present quasi-periodic or chaotic responses.

Even though many degrees of freedom are required to represent a continuous structure, the single degree of freedom approximation of the whole structure might be helpful in many situations. In particular, around the fundamental vibration mode, the response of the structure can be approximated using a single degree of freedom (SDOF) model. It is important to note that the fundamental mode's contribution to the total response of the structure is the most significant. For example, a flat thin plate under harmonic excitation exhibiting geometrically nonlinear vibrations can be approximated using a SDOF model with nonlinear springs. It is often useful for engineers to approximate the nonlinear behavior of their structures using a SDOF approximation rather than a full-fledged complex numerical model. Based on SDOF approximation, any easy tool to

extract the nonlinear parameters such as quadratic & cubic stiffness and damping from the experimental data will be extremely helpful for the engineering community. The equation of motion of such SDOF is none other than the famous modified Duffing equation as shown (1.6):

$$m\ddot{x} + c\dot{x} + k_1 x + k_2 x^2 + k_1 x^3 = 0, \tag{1.6}$$

where m is the mass, c is the damping, k_1 is the linear stiffness, k_2 is the quadradic stiffness, k_3 is the cubic stiffness, x is the displacement and over dot means differentiation with respect to time.

(a)   (b)
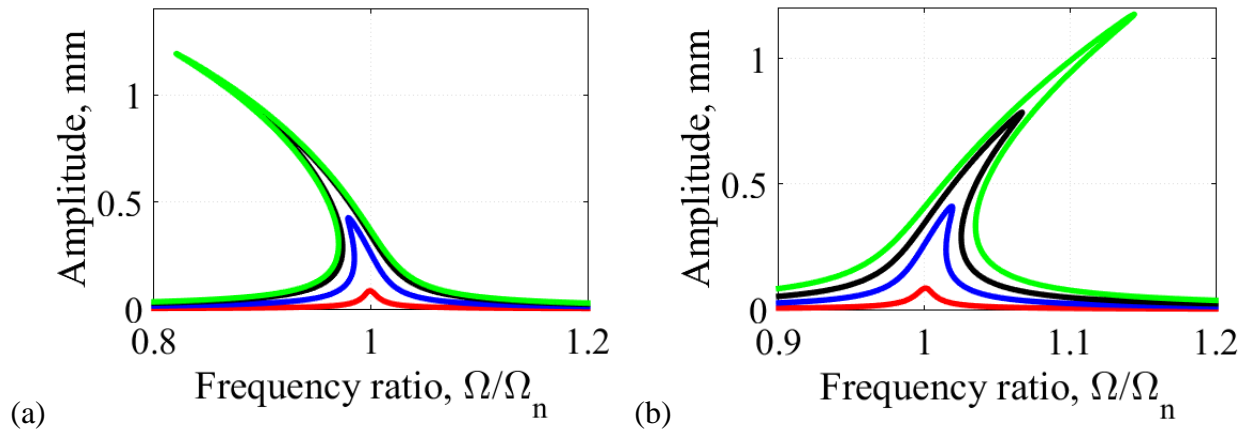
Fig. 1-2: Softening and hardening response of a modified Duffing oscillator

The amplitude dependence of the resonance frequency is one of the characteristics of nonlinear systems. At very low vibration amplitudes, the resonance frequency of the nonlinear system will coincide with its linear approximation. But as the vibration amplitude increases, the resonance frequency will either increase or decrease due to the nonlinear stiffness component in the eq. (1.6). If the resonance frequency decreases, the system is said to be of the softening type (as shown in Fig. 1-2(a)), whereas, if the resonance frequency increases, the system is said to be of the hardening type (as shown in Fig. 1-2(b)). Flat plates typically exhibit a hardening type of response, whereas, panels and shells exhibit a softening type of response. However, it is also possible for structures to present an initially softening and eventually hardening type of response. Plates with initial imperfections are one example of this kind of system.

Besides the hardening or softening behavior, nonlinear systems can exhibit other complex responses with sub and super-harmonics, internal resonances, quasi-static and chaotic responses. Internal resonance is a phenomenon in which the energy applied to one mode gets transferred to other modes, the natural frequencies of which are an integer multiple of the natural frequency of the mode the energy is applied to. This transfer of energy helps to reduce the maximum amplitude of vibration reached by the structure, thereby reducing fatigue. If the natural frequencies of the modes which are under study are equal or similar, then the transfer of energy between these modes is called one-to-one internal resonance. This is of critical importance in the case of shell-like, square plate-like or beam-like structures that are typically symmetric in nature and feature couples of vibration modes which are identical in frequency and orthogonal to each other.

1.1.4 DAMPING

The dissipation of energy in any structure is important to ensure that the structure does not vibrate at an amplitude which is detrimental to itself and the overall system. Dissipation is present in all structures whether it is desired or not, however, the amount of dissipation varies wildly. The amount of dissipation present in a structure is an important factor known as, damping. Damping controls the peak amplitude of vibration experienced at resonance for a given input, and, thereby it can affect the life of the structure. The dissipation of energy during vibration can be due to the internal sliding of molecules, the friction in joints or at boundaries, the movement of the structure through its surrounding media such as air or water or a combination of these mechanisms. As many sources are the cause of dissipation in one vibrating system, it is cumbersome to model them individually. Hence, it is globally accepted for many practical purposes to use an equivalent dissipation description to model all the dissipation energy present in a structure.

1.1.4.1 LINEAR DAMPING

There are various equivalent dissipation models used by the scientific community. The most common of them are the viscous, hysteretic and Coulomb damping models. Viscous damping is by far the most common because of the simplicity of its introduction in numerical models. For a single degree of freedom system, viscous damping can be introduced in the equation of motion

as below:

$$m\ddot{x} + c\dot{x} + kx = 0, \tag{1.7}$$

where m is the mass, c is the damping, k is the stiffness. For multi-degree of freedom systems, the viscous damping model can be extended by means of proportional damping as per the Raleigh damping expression:

$$\mathbf{M}\ddot{\mathbf{x}} + \mathbf{C}\dot{\mathbf{x}} + \mathbf{K}\mathbf{x} = 0, \tag{1.8}$$

where $\mathbf{M}$, $\mathbf{C}$ and $\mathbf{K}$ are the mass, damping and stiffness matrices. By coordinate transformation, the eq. (1.8) can be written in modal coordinates as,

$$\mathbf{I}\ddot{\mathbf{x}} + \begin{bmatrix} 2\omega_1\zeta_1 & \cdots & 0 \\ \vdots & \ddots & \vdots \\ 0 & \cdots & 2\omega_n\zeta_n \end{bmatrix}\dot{\mathbf{x}} + \begin{bmatrix} \omega_1^2 & \cdots & 0 \\ \vdots & \ddots & \vdots \\ 0 & \cdots & \omega_n^2 \end{bmatrix}\mathbf{x} = 0, \tag{1.9}$$

where ζ_1 is the viscous damping associated with mode 1, also known as modal damping, ω_1 is the natural frequency of mode 1, $\mathbf{I}$ is the identity matrix. The assumption that damping is a linear combination of the mass and stiffness matrices does not correspond in general to the damping of any real structure; however, it is implied widely because of its simple implementation, which allows a straightforward estimation of modal damping from experimental data.

Hysteresis damping, instead, represents the dissipation due to the internal friction between the internal planes that slip or slide as the material deforms. Hysteresis damping is proportional to stiffness and is independent on frequency. It is found that the material damping of many materials has in fact a low dependence on the frequency of excitation. Hence, hysteresis damping is used in many areas where damping is independent on frequency. Viscous damping instead is proportional to the frequency of excitation and for many practical systems would imply excessive damping at higher frequencies. However, damping has much less effect before and after resonance and the viscous damping value is measured based on its effect at resonance. Coulomb friction damping is used for modeling dry friction. More information about these damping models can be found in many basic vibrations textbooks [8].

1.1.4.2 NONLINEAR DAMPING

The damping models explained before are linear, meaning that the damping force depends linearly on the displacement or velocity of the vibration. However, it is clear from the experimental evidence that damping during large amplitude vibrations is nonlinear, even when the strain experienced by the material is sufficiently small to justify the use of linear stress-strain approximations. Several nonlinear damping models do also exist in the literature, among them nonlinear damping models based on large strain can be ignored, as it is not relevant for the present study. The loss factor based on dissipated and stored energies and linear viscoelasticity models with geometric nonlinear springs are interesting.

Loss factor based on dissipated and stored energies can be calculated from the hysteresis loop. For harmonic oscillations, the stress (force) can be plotted against the strain (displacement) to form the hysteresis loop. For linear vibrations this loop takes the form of an ellipse (as shown in Fig. 1.3 (a)); for nonlinear vibrations the shape of the loop can instead be different (as shown in Fig. 1.3 (b)), since non-sinusoidal responses can correspond to sinusoidal inputs. The area inside this loop represents the energy lost during the cycle of harmonic oscillation. The elastic or stored energy is the area below the storage modulus line.

(a)   (b)
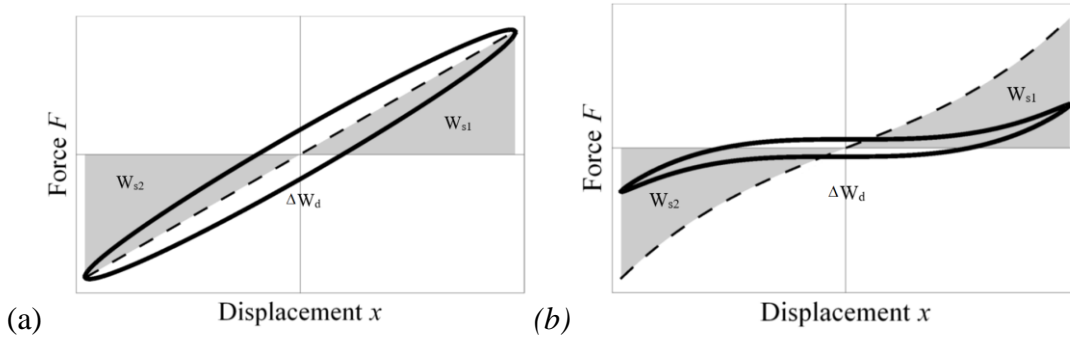
Fig. 1-3: Force-displacement loop: (a) linear system, (b) nonlinear system. The storage modulus is represented by the dashed line and the grey area is the stored energy. The area inside the loop is the dissipated energy.

From the ratio of dissipated and stored energies, the damping of the system can be calculated in the form of a loss factor using eq. (1.10),

$$\eta = \frac{\Delta W_d}{2\pi W_s} \qquad\qquad (1.10)$$

where, ΔW_d is the dissipated energy, W_s is the stored energy of the system, and η is the loss factor. Since this description is true both for linear and for nonlinear systems, this can be applied immediately to nonlinear vibrations.

From the linear viscoelastic material models, such as Maxwell, Kelvin-Voigt and Standard Linear Solid, nonlinear damping models can be derived by introducing geometric nonlinear springs. Even though the Kelvin-Voigt model does not capture all the behaviors of real viscoelastic material well, e.g. creep, it is being used widely due to its simplicity. The Standard Linear Solid or Zener model captures all the behavior of viscoelastic materials instead. While, these two models are ideal candidates for the description of damping in the nonlinear field, neither was applied to experimental data to evaluate their effectiveness in capturing the nonlinear damping variation observed in the large amplitude vibrations of plates, panels or shells.

1.2 LITERATURE REVIEW

In this section, the literature review for three main topics the thesis is based on will be presented: Viscoelastic plates, slender tubes with and without fluid interaction and nonlinear damping.

1.2.1 VISCOELASTIC PLATES

Plates are flat structures with a relatively small thickness compared to the in-plane dimensions. Plates are used in many engineering applications with various boundary conditions, in various materials and shapes. Composite and Functionally Graded Materials (FGM) are gaining popularity lately due to their customization capabilities. The dynamic response of plates has been studied for many decades. Linear dynamics studies are summarized by the works of Leissa [9] and others.

The geometrical nonlinear vibration of plates has also been studied for many years and the nonlinearity has been exploited in various applications to the engineer's advantage. The classical theory used for understanding the geometrically nonlinear vibrations of plates is by Von Kármán

[10]. He extended Kirchhoff's method including nonlinear terms to study large amplitude vibrations. For thicker laminated plates the Reissenr-Mindlin theory of plates is used. Reviews of the nonlinear studies of plates can be found in the literature [5, 9, 11, 12]. The first study of the nonlinear vibrations of elastic plates is attributed to Chu and Herrmann [13]. They studied the simply supported rectangular plate and obtained the backbone curves, which are found to be in good agreement with later studies by Ganapathi et al. [14] and Rao et al. [15]. Amabili [16, 17] studied the large amplitude vibration of plates methodically for different boundary conditions and compared it with supporting experimental results. The large amplitude vibration responses of laminated composite plates were studied in detail by Noor et al. [18] and Harras et al. [19]. Alijani and Amabili [20] studied the response of free-free rectangular composite plate using versatile energy based approach and compared it with experimental results [21]. Alijani and Amabili [22], through series of studies on plates showed that damping increases nonlinearly with respect the amplitude of vibration. The effect of geometric imperfection on the response of the plate was initially studied by Hui [23] and later by Amabili [17]. It is shown that an imperfect plate will have both softening and hardening type of nonlinearity depending upon the amplitude of vibration experienced.

Viscoelastic plates received the attention of the scholars as many biological structures can be modelled through them. For example, the ear drum or the audio speakers can be modelled as viscoelastic plates. Viscoelastic materials have unique properties when compared to their elastic counterparts. Relaxation, creep and frequency dependent modulus and loss factor are among them. For the harmonic response of the plates, the relaxation and creep phenomena can be ignored, as they are not related to dynamic response. The frequency dependent stiffness and loss factors cannot instead be ignored.

The study on viscoelastic structures is found to be very limited because of the complexities in modeling the time dependent stress-strain responses. The response of viscoelastic structures can be modeled using many different models; among them Maxwell, Kelvin-Voigt, Standard Linear Solid (SLS) and Boltzmann models are commonly used [24, 25]. Stress relaxation and creep are unique properties of these materials and are captured well in Standard Linear Solid and

Boltzmann models. Even though the Kelvin-Voigt model has limitations in describing the relaxation of stress, it accurately captures creep phenomenon and is widely used for modelling vibrations of viscoelastic materials.

Mahmoodi et al. [26] and Ghayesh et al. [27] investigated theoretically and experimentally the nonlinear vibration response of viscoelastic beams by using the Kelvin-Voigt model for the cantilever and the simply supported and axially travelling conditions, respectively. Viscoelastic plates have also been studied by using different models. Notably, Esmailzadeh and Jalali [28] and Sun and Zhang [29] used the Kelvin-Voigt model to study the nonlinear vibrations of plates, while the experimental investigation of sandwich composite plates with viscoelastic layers was carried out by Balkan and Mecitoglu [30]. Amabili [31] modeled the viscoelastic plate using both the Kelvin-Voigt model and linear viscous damping model to understand the effects of nonlinear damping terms in the forced vibration response. The nonlinear vibration analysis of viscoelastic panels, described by the Kelvin-Voigt model and by a very simple model with only two degrees of freedom, was conducted by Han and Hu [32]. The standard linear solid type model was used to represent the viscoelastic characteristics in the nonlinear vibrations and the dynamic stability of plates by Eshmatov [33] and Salehi and Safi-Djahanshahi [34]. Kim and Kim [35] used the Boltzmann model to study the nonlinear vibration of viscoelastic laminated composite plates, and concluded that geometric nonlinearities do not affect the dissipative characteristics. The literature on the nonlinear vibration of viscoelastic shells is also quite scarce. The linear vibrations of viscoelastic shells were studied by Ramesh [36]. The geometrically nonlinear vibrations of viscoelastic shells were first investigated by Badalov et al. [37]. In his paper nonlinear integro-differential equations arising in the case of shell are solved through the averaging method. Eshmatov used the Galerkin method to understand the response of the viscoelastic shell using a relaxation function [38].

Though analytical studies on the vibration (linear and nonlinear) of viscoelastic plates and shells using different models are available, experimental results are quite scarce in the literature. Thus, this research is aimed at filling this gap by experimentally and numerically studying the geometrically nonlinear vibrations of plates using various appropriate models.

1.2.2 SLENDER TUBES

The study of slender tubes (or cylinders) in axial flow has gained attention because of its importance in the field of nuclear fuel rods and heat exchangers. Even though the vibration induced by the axial flow on the cylinders is small in amplitude, it has to be given importance as it causes fretting, fatigue and stress-corrosion cracking [39].

The dynamics of a single cylinder in axial flow was first studied both analytically and experimentally by Paidoussis [39]. He showed that the axial flow increased the damping of the cylinder and also the effective mass. Even though it was shown that at sufficiently high flow velocities it could lead to fluid elastic instabilities and buckling, it was practically of small concern as this happens outside the range of normal engineering applications. During the study the following is assumed (i) the fluid is incompressible, (ii) the mean flow velocity is constant, (iii) the cylinder is slender, so that the Euler–Bernoulli beam theory is applicable, and (iv) the deflections of the cylinder may be large, but strains remain small. The different forces acting on the cylinder in axial flow are considered using different theories and the equation of motion can be obtained by equating forces and moments. The inviscid forces acting on the cylinder can be calculated using the slender body potential flow theory (Lighthill [40]), containing the added virtual mass due to the surrounding fluid. Moreover for cylinders in confined flow, the added virtual mass need to be scaled by a factor [41, 42]. The viscous forces and pressure change in an unconfined flow are calculated and experimentally validated by Taylor and Mateescu *et al.,* [43, 44]. The linear dynamics of the system, ignoring the nonlinear terms was studied by many scholars for static divergence and coupled-mode flutter using commercial Finite Element packages (ANSYS-Fluent) [45, 46] , the differential quadrature method [47] and by the Finite Difference Method [48]. Even though linear studies give us information about divergence, nonlinear studies are important to understand post-divergence bifurcations and non-standard dynamics. The nonlinear equation of motion for cantilever cylinders in axial flow was derived by Lopes *et al.,* [49] and the dynamics are studied by Paidoussis *et al.,* and Semler *et al.,* [39, 49]. The results predict the subsequent buckling of the first and second mode due to subcritical pitchfork bifurcation as the flow velocity increases, followed by a second mode flutter due to subcritical Hopf bifurcation. The results are close with the experimental results. The solution

methods used for these studies are the Finite Difference Method and AUTO (continuation problem solver) [50]. Similarly, simply supported and clamped-clamped cylindrical shells were studied by Modarres-Sadeghi *et al.,* [51-53] with good correlation with experimental results in his following papers.

Clusters of cylinders present two additional effects, inviscid and viscous coupling. The works by Moretti & Lowery [54] and by Chen and Jendrzejczyk [55] were the starting point of the consideration of the coupling between cylinders in a cluster. Different number of cylinders were considered in a confinement by various authors and the resulting effects were studied: Two [50, 56], Three [50], Four or more [57] . The virtual mass and viscous terms due to the fluid become a virtual mass matrix and viscous coupling matrix in the case of clusters of cylinders. Though there are many theoretical and experimental studies, the literature on the damping variation considering various boundary conditions and large amplitude vibrations for a single beam or cluster of beams in quiescent or axial flow conditions is limited, thus reinforcing the need for this study.

1.2.3   NONLINEAR DAMPING

It appears experimentally that the equivalent viscous damping increases nonlinearly during the large amplitude vibrations of thin-walled structures [22, 58-60]. The evidence to support this claim is scarce but gaining momentum. Structural damping in aircrafts was found to be increasing nonlinearly with vibration amplitude by Fearnow [61] and Fellowes et al., [62]. Micro-speakers present in mobile phones and laptops has been found to have nonlinear damping characteristics by Klippel [63]. Zaitsev et al., [59] studied experimentally the nonlinear damping of a micromechanical oscillator. The nonlinear damping model used by them is phenomenological and contains the term $x^2\dot{x}$ along with the typical linear viscous damping term. The same model was used for a spherical pendulum to model its nonlinear damping behavior by Eichler et. al [60]. One nonlinear damping model is of the x^3 type, and it was proposed in [64]. In conclusion, there is no consensus on the type of nonlinear damping present in thin-walled structures. Proper derivation is still elusive, mainly because of the lack of a sufficient amount of experimental results. Current industrial practice is to select a damping value for the structure

under study based on experimental modal analysis (during small amplitude vibrations) and keep it constant for higher vibration amplitudes. This clearly leads to over-design and inefficiency in structures experiencing large amplitude vibrations. Thus, making any study to properly model the damping behavior of structures will advance the way engineers design them across many disciplines in the future.

1.3   MOTIVATION

This thesis primarily concerns with modeling the nonlinear damping characteristics of thin walled structures. Thin-walled structures such as rocket fuselage, nano/micro resonators, human arteries, circular saws and nuclear fuel rods are modeled as plates, panels, and shells. These structures typically experience large amplitude vibrations (more than its thickness) under their operating conditions. It is of critical importance to model damping of these structures accurately because damping influences the degree of nonlinearity and the peak amplitude observed at resonance.

Typically, the damping of thin walled structures experiencing large amplitude vibration are characterized using linear models based on experimental modal analysis. Recent studies [17, 22, 58, 65, 66] have indicated that this may not be the right approach. Studies conducted at the McGill vibrations and hydrodynamic laboratory [20, 21, 67, 68] have indicated that linear models could grossly underestimate the damping in large amplitude vibrations by as much as 60% up to 300% depending upon the structure and the level of vibration. The same behavior was also observed in other types of thin walled structures like MEMS and NEMS (graphene plates, carbon nanotubes, and microcantilevers) as well [59, 60, 69].

Very limited studies have been carried out to model the nonlinear damping characteristics of thin walled structures. Some of these studies [59, 60] use phenomenologically introduced nonlinear damping terms to capture the nonlinear damping variation. Characterizing the damping behavior for thin walled structures is complex and time consuming. There are several underlying mechanisms behind damping. It is complex and difficult to account for each one of these mechanisms individually and accurately. Experimental data is required to model the nonlinear

damping behavior characteristics. Further, there is no consensus on a correct approach to model this nonlinear damping in large amplitude vibrations of thin-walled structures yet.

In summary, thin walled structures are important engineering structures. It is important to recognize that linear models cannot capture the nonlinear behavior observed during large amplitude vibrations. There is a need to develop models which can capture the nonlinear characteristics and to add to existing limited body of knowledge on this subject. As we strive towards light-weight efficient thin-structures, accurate estimation of damping will lead to better designs and safe structures.

Even if there is experimental data, there is no simple tool available to engineers to extract the nonlinear parameters and damping. The available methods involve creating complex MDOF models and validating against experimental data to estimate damping.

1.4 OBJECTIVES

As noted in the previous section, thin walled structures undergoing large amplitude vibrations exhibit nonlinear damping variation [20, 21]. These studies were performed on plates, panels and shells made of elastic materials like steel, aluminum, graphene and, composites. No such studies were found on viscoelastic plates and elastic slender beams. Many bio-mechanical and engineering structures like ear drum diaphragm (cochlea) and nuclear fuel rods are modelled as viscoelastic plates and slender beams. The objective of this thesis is to add to the existing body of knowledge to this domain of characterization of damping by:

(a) Conducting large amplitude experimental studies on
   a. viscoelastic plates made of different materials,
   b. slender tubes with and without fluid-structure interaction in various configurations (an empty tube, with moving pellets inside and blocked pellets inside) to understand their effect.

(b) Estimating the linear viscous damping of the above-mentioned structures using appropriate numerical models.

(c) Developing reduced order models which can capture the observed nonlinear damping behavior.

(d) Developing a simplified SDOF model-based parameter identification tool to quickly estimate the damping of the structures.

2   KELVIN-VOIGT MODEL OF RUBBER PLATES

As the first step of this thesis work, large amplitude vibrations of two rubber plates made of silicone and neoprene were measured after establishing a proper measurement setup and manufacturing the required fixtures. Corresponding numerical models were developed with classical linear viscous and Kelvin-Voigt model damping. The experimental responses were compared with numerical responses and found to be in good agreement. It was concluded that the equivalent linear viscous damping increases nonlinearly as rubber plates undergo large amplitude vibrations, supporting the hypothesis already proven for metallic and composite plates. Moreover, the nonlinear damping introduced by the Kelvin-Voigt model is unable to capture the nonlinear damping variation observed in experimental measurements. The result of this study is presented in the International Journal of Nonlinear Mechanics and is given below.

Experimental and Theoretical Study on Large Amplitude Vibrations of Clamped Rubber Plates

Prabakaran Balasubramanian[a], Giovanni Ferrari[a],
Marco Amabili[a], Zenon J. Guzman N. del Prado[b]

[a] Department of Mechanical Engineering, McGill University,
[b] School of Civil Engineering, Federal University of Goias - UFG

2.1   ABSTRACT

In this paper, the large amplitude forced vibrations of thin rectangular plates made of different types of rubbers are investigated both experimentally and theoretically. The excitation is provided by a concentrated transversal harmonic load. Clamped boundary conditions at the edges are considered, while rotary inertia, geometric imperfections and shear deformation are neglected since they are negligible for the studied cases. The von Kármán nonlinear strain-displacement relationships are used in the theoretical study; the viscoelastic behaviour of the material is modelled using the Kelvin-Voigt model, which introduces nonlinear damping. An equivalent

viscous damping model has also been created for comparison. In-plane pre-loads applied during the assembly of the plate to the frame are taken into account. In the experimental study, two rubber plates with different material and thicknesses have been considered; a silicone plate and a neoprene plate. The plates have been fixed to a heavy rectangular metal frame with an initial stretching. The large amplitude vibrations of the plates in the spectral neighbourhood of the first resonance have been measured at various harmonic force levels. A laser Doppler vibrometer has been used to measure the plate response. Maximum vibration amplitude larger than three times the thickness of the plate has been achieved, corresponding to a hardening type nonlinear response. Experimental frequency-response curves have been very satisfactorily compared to numerical results. Results show that the identified retardation time increases when the excitation level is increased, similar to the equivalent viscous damping but to a lesser extent due to its nonlinear nature. The nonlinearity introduced by the Kelvin-Voigt viscoelasticity model is found to be not sufficient to capture the dissipation present in the rubber plates during large amplitude vibrations.

2.2 INTRODUCTION

Plates are widely used structural elements, which are flat and with a relatively small thickness compared to the in-plane dimensions. They exhibit geometrically nonlinear vibrations under certain loading conditions that have been studied over the past few decades by many scholars. Detailed review of these studies can be found in the literature [5, 11, 12]. Many scholars have studied such problems generating a vast literature in terms of both theoretical and experimental front in the elastic plate domain. The study on viscoelastic materials is found to be very limited due to the complexities in modeling the time dependent stress-strain responses. Metals under high temperature, elastomer and many biological materials show viscoelastic characteristics. Nowadays, elastomers are being used increasingly in many automobile and aerospace applications for their excellent damping characteristics. Moreover, they are also used in combination with composite or metal layers to produce effective structural members. Thus, modeling their dynamic response is crucial for effective design in such application areas. Viscoelastic material responses can be modeled using many different models; among them Maxwell, Kelvin-Voigt, standard linear solid and Boltzmann models are commonly used [24,

25]. Stress relaxation and creep are unique properties of these materials and are captured well in standard linear solid and Boltzmann models. Even though Kelvin-Voigt model has limitations in describing relaxation of stress, it accurately captures creep phenomenon and is widely used for modelling vibrations of viscoelastic materials. Mahmoodi et al. [26] and Ghayesh et al. [27] investigated theoretically and experimentally the nonlinear vibration response of viscoelastic beams by using the Kelvin-Voigt model for the cantilever and the simply supported and axially travelling conditions, respectively. Viscoelastic plates have also been studied by using different models. Notably, Esmailzadeh and Jalali [28] and Sun and Zhang [29] used the Kelvin-Voigt model to study the nonlinear vibrations of plates, while the experimental investigation of sandwich composite plates with viscoelastic layers was carried out by Balkan and Mecitoglu [30]. Amabili [31] compared the viscoelastic plates to its equivalent viscous model in order to understand the effects of nonlinear damping terms in the forced vibration response. Nonlinear vibration analysis of viscoelastic panels, described by Kelvin-Voigt model and using a very simple model with only two degrees of freedom, was conducted by Han and Hu [32]. Standard linear solid type model was used to represent the viscoelastic characteristics in nonlinear vibrations and dynamic stability of plates by Eshmatov [33] and Salehi and Safi-Djahanshahi [34]. Kim and Kim [35] used the Boltzmann model to study the nonlinear vibration of viscoelastic laminated composite plates, and concluded that geometric nonlinearities do not affect the dissipative characteristics. Though analytical studies on vibration (linear and nonlinear) of viscoelastic plates using different models are available, experimental results are quite scarce in the literature. In this paper, the geometrically nonlinear response of clamped rubber plates is experimentally studied, and the results are compared to those obtained by theoretical nonlinear models by using (i) the Kelvin-Voigt viscoelasticity and (ii) a viscous damping model.

2.3 EXPERIMENTAL SET-UP

The experimental setup is composed of two subsystems: (i) the vibrating rubber plate with its supporting frame, and (ii) the transducers and data acquisition system used to perform forced vibration testing. In the following subsections these two subsystems will be described briefly.

2.3.1   THE RUBBER PLATES

Two viscoelastic plates are considered here; a silicone plate with 1.5 mm thickness and a neoprene plate with 3 mm thickness. The dimensions of both plates are 0.26×0.26 *m* and their nonlinear vibrations were investigated. In reality, bigger square plates were cut from commercially available rolls, as part of the area had to be used to realize the desired boundary conditions. The silicone plate has the hardness of 50 A and density of 1430 *kg/m³* as per commercial catalogue, whereas neoprene plate has 70 A hardness and 1230 *kg/m³* density. While part of this study is intended to obtain the material characterization of these plates, it has to be noted that the Poisson's ratio was considered to be 0.5 (incompressibility condition).
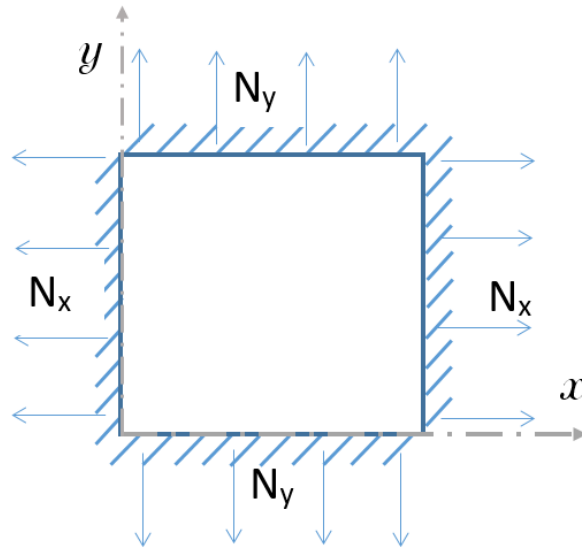
Fig. 2-1 Clamped viscoelastic plate with in-plane loads.

As both materials are relatively soft and yielding, an in-plane stretching (load in both directions) was adopted to guarantee the flatness of the plates. In-plane tension was obtained by cutting 28 holes in the plate and mounting it onto 28 perpendicular M12 fasteners, installed on a metal frame. The holes in the plate were uniformly distributed on a square perimeter, the side of which was 0.31 *m*. The M12 rods, again equally-spaced, were cantered onto a square perimeter, the side of which was 0.315 *m*. The plates were therefore manually stretched to be mounted onto the threaded rods. The diameter of the holes is slightly bigger than the diameter of the bolts. The resulting in-plane tension can be described as an initial perpendicular displacement of 0.0025 *m*

imposed to each side of the 0.31×0.31 *m* square. As the distance between the holes is modest, the stretch can be considered uniform along the length of the square. A representation of the pre-stretching procedure is shown in Fig. 2-1. This initial in-plane stretch should be perfectly symmetric; however, dynamic tests, described later in this paper, reveal that the tension state is not perfectly symmetric. This can be due to the localized deformation of the plates at the anchor points. Moreover, few tenths of a millimeter of stretch correspond to a large variation in the stress state. The square shape introduces even higher incertitude about the strain distribution, as its corners constitute stress concentration factors. As mentioned above, the vibrating portion of the plates considered here is a square area, 0.26 *m* of side, concentric with respect to the previously described offsets of holes and threaded rods.

(a)   (b)
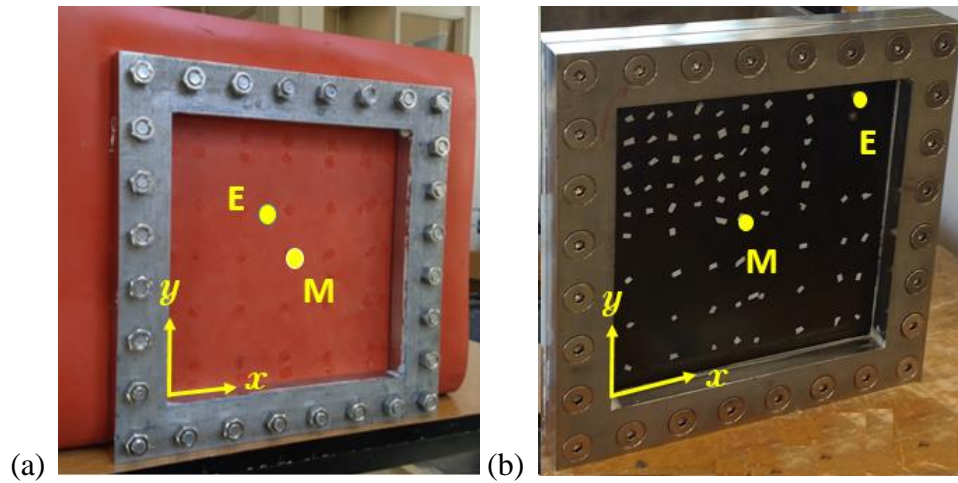
Fig. 2-2: Viscoelastic plates with their respective co-ordinate system; (a) Silicone plate

(a) Neoprene Plate; *E* - Excitation Point; *M*- Measurement Point.

The 0.26 *m* side of the vibrating square area is defined in the stretched side, and therefore corresponds to a smaller area in the relaxed state. Fixed boundary conditions were realized pressing the rubber plates between two heavy-weight metal frames matching square openings leaving the vibrating area free. The thickness, width and rigidity of the frames guarantee a clamped condition. The resulting system is then connected rigidly to the ground. The two metal frames exert a pressure on the rubber plates by means of the same threaded elements used to

keep the rubber into a pre-stretched state. The resulting friction force between metal and viscoelastic plate is important in constituting the boundary condition; however, the two materials have a low friction coefficient and would require very a high torque on the threaded bolts. As rubber is nearly incompressible, higher torques would squeeze it between the two rigid frames, forcing it eventually to move into the free area. This complex transfer of material would buckle the originally free flat area and would appear as a pre-stretch reduction. In order to avoid this, sandpaper was glued onto a portion of the metal-silicone/neoprene contact area to increase the friction coefficient. Fig. 2-2 shows the plates clamped using the metal frames.

The planar square vibrating area was maintained vertical during the experiments, with two sides parallel to the horizontal, since the effect of gravity was considered negligible with respect to the pre-stretch. A right-hand coordinate system was considered as having the x direction parallel to the horizontal and the z direction perpendicular to the plate. The positive direction being the face pointing towards the laser from the observer's point of view. With this convention, the y axis will be vertical and pointing upwards. Bottom left corner was taken as the origin for the described coordinate system. Fig. 2-2 represents the coordinate system adopted, the position of the excitation (E) and measurement (M). A transversal excitation (perpendicular to the plate) was positioned at $x = 0.22$ m and $y = 0.24$ m for the neoprene plate and at $x = 0.11$ m and $y = 0.19$ m for the silicone plate. This location was chosen since modes with both odd and even symmetry had to be excited. The distance from the edges of the domain under study (0.26 ✕ 0.26 m square perimeter) was chosen as a trade-off. A reduced distance would correspond to a low energy transfer to the structure, being the edges subjected to a fixed boundary condition. A larger distance would instead give a wider unwanted interaction between the vibration of the structure and the excitation system, typical of nonlinear vibrations. A punctual excitation was a rigid aluminium base, 5 mm in diameter and negligible in weight, was centered on the chosen excitation point and glued by means of cyanoacrylic glue. The bond of aluminium and silicone through cyanoacrylic glue is weak, however it was deemed acceptable, the force amplitude involved in these experiments being low.
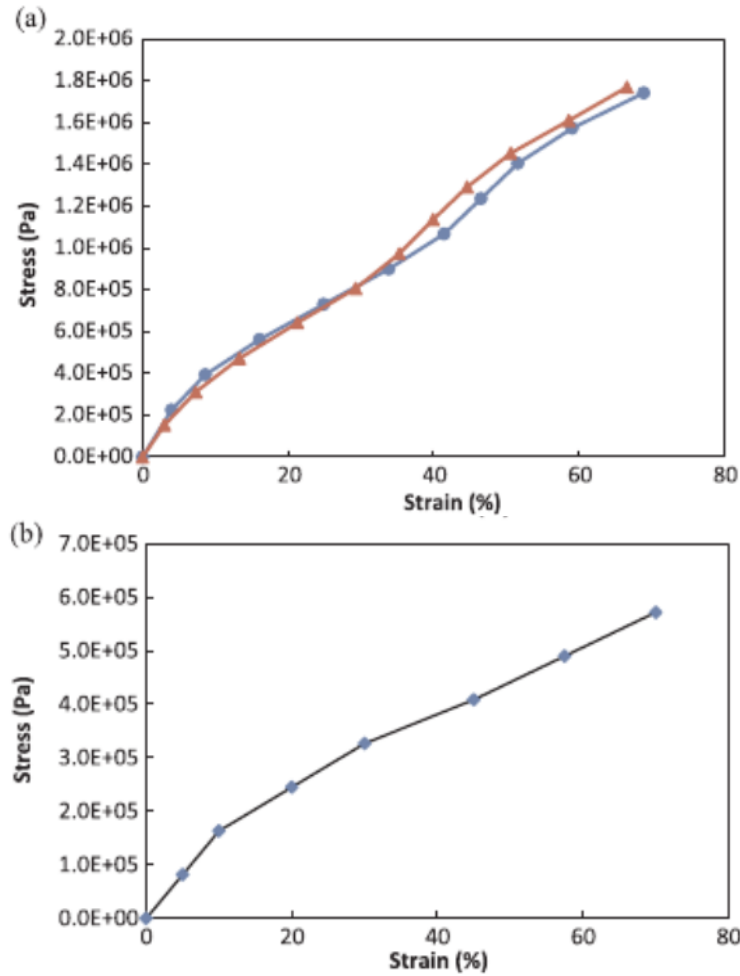
Fig. 2-3: Uni-axial traction tests on rubbers. (a) Silicone rubber; (b) neoprene rubber.

Fig. 2-3(a) and Fig. 2-3(b) show the stress-strain behaviour of the silicone and neoprene rubbers, respectively, as obtained by uniaxial traction tests with weights on rubber strips. The results show that, even if the tests confirm the hyperelastic rubber behaviour, the stress-strain relationship is practically linear for strains up to the order of 2 %, as those achieved during our vibration tests. For this reason, linear visco-elasticity is assumed for the rubbers in the present study, with Young's modulus of 5.62 MPa for the silicone plate and 2.45 MPa for the neoprene plate. The storage modulus of both silicone and neoprene rubbers were measured around the fundamental frequency of respective plates and found to be 4.28 and 2.62 times the static Young's modulus. This has been taken in to account in the model.

2.3.2 MEASUREMENT SET-UP

During dynamic testing, a Brüel Kjær 8203 miniaturized force transducer was used to measure the value of the excitation force. The transducer is connected by a stinger to the Brüel Kjær 4810 electrodynamic exciter (shaker), powered by a Brüel Kjær 2718 power amplifier. Fig. 2-4 shows an overall image of the excitation system applied to the silicone/neoprene plate.
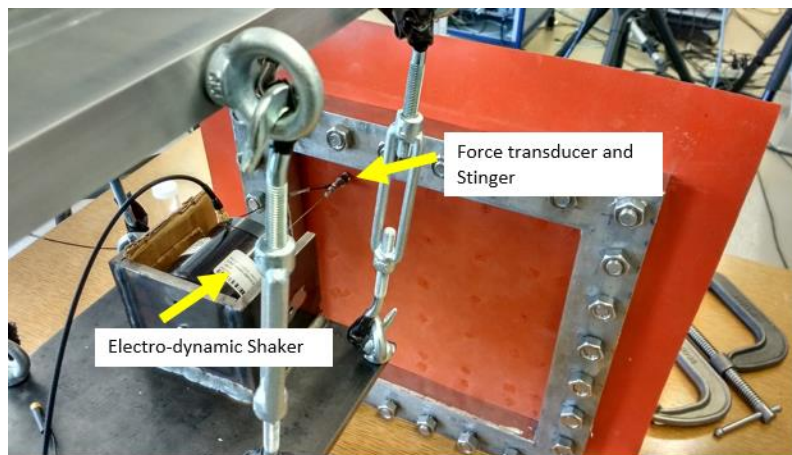
Fig. 2-4: Excitation setup with electrodynamic shaker.

The shape of normal vibration modes was obtained by means of scanning laser Doppler vibrometer (Polytec PSV-400). This technique allows the non-contact measurement of a multitude of points on the surface of the silicone plate, disposed on a fine grid. A Polytec OFV-505 single point laser Doppler vibrometer was instead used in case of nonlinear vibrations. As the relevant stepped-sine procedure studies nonlinear vibrations around one underlying natural frequency and one vibration mode only, the measurement of one point is sufficient. Non-contact measurement systems were favoured also because they do not introduce unwanted added masses. Fig. 2-5 shows the measurement set-up with the sensors described above. Modal analysis was performed using a dedicated Polytec OFV-5000 data acquisition system. Subsequently, the data were transferred and processed by the LMS Test.Lab modal analysis module software. The nonlinear tests required the connection of the laser Doppler vibrometer and of the force transducer to a LMS SCADAS III data acquisition system and the use of the software LMS Test.Lab stepped sine module. Stepped-sine tests were performed at various fixed levels of force

amplitude, applying a sinusoidal excitation sweeping monotonously (forwards and then backwards) by small steps the frequency neighbourhood of one chosen natural frequency. The apparatus is capable of maintaining constant amplitude of the sinusoidal excitation by means of a feedback loop control; it must be observed that the control of the input signal to the power amplifier is not an acceptable technique, since the impedance of the structure near resonance changes significantly. The LMS Test.Lab system records the signals from vibration and force sensors both in time and frequency domain.
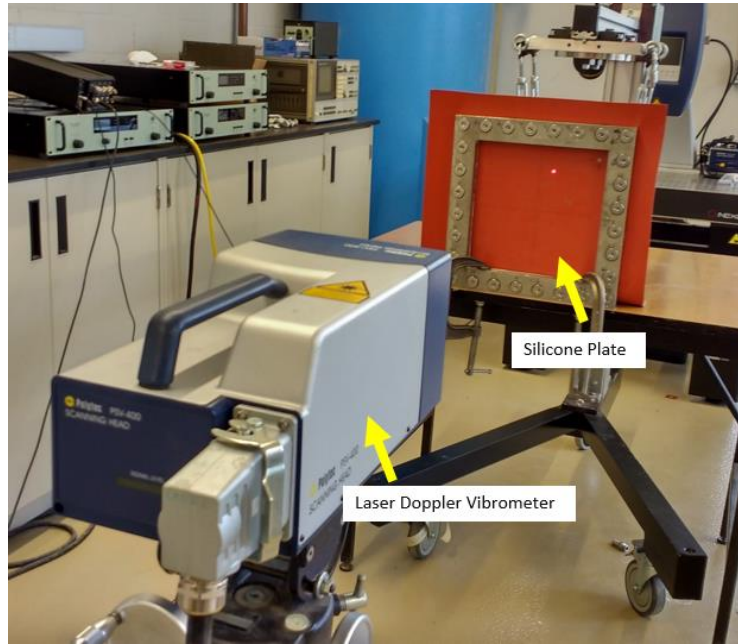
Fig. 2-5: Measurement setup with Laser Doppler Vibrometer.

2.4 THEORETICAL MODEL

A viscoelastic rectangular plate with coordinate system (*O; x; y; z*) having the origin (*O*) at one corner is considered, as shown in Fig. 2-6. The plate dimensions in *x* and *y* directions are *a* and *b*, respectively, and the thickness is *h*. The displacements of an arbitrary point of coordinates (*x, y*) on the middle surface of the plate are denoted by *u, v* and *w* in the *x, y* and *z* directions, respectively.
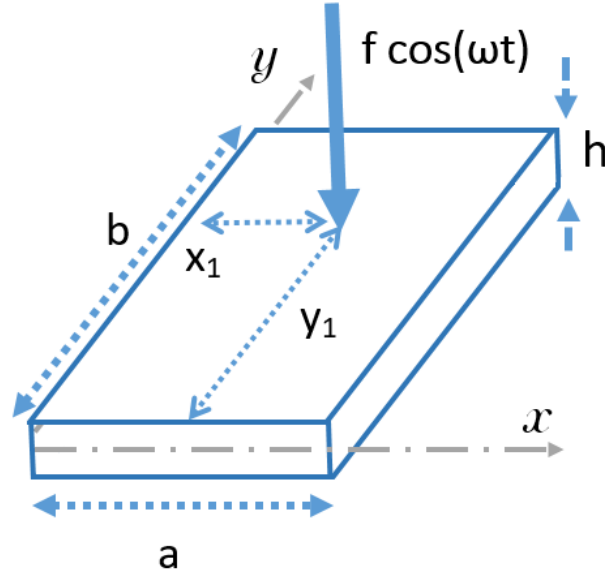
Fig. 2-6: The viscoelastic plate.

Rotary inertia, shear deformation and geometric imperfections are neglected since the plates tested in the experiments are very thin and are assembled with initial stretching, which ensures an initial flatness of the plate. Clamped boundary condition on all four edges and the von Kármán strain-displacement relationships are considered. According to the von Kármán strain-displacement relationship, the strain components $\varepsilon_x, \varepsilon_y, \gamma_{xy}$ at an arbitrary point of the plate are related to the middle surface strains $\varepsilon_{x,0}$, $\varepsilon_{y,0}$, $\gamma_{xy,0}$ and to the changes of curvature and torsion of the middle surface k_x, k_y, k_{xy} by

$$\varepsilon_x = \varepsilon_{x,0} + z\,k_x; \quad \varepsilon_y = \varepsilon_{y,0} + z\,k_y; \qquad \gamma_{xy} = \gamma_{xy,0} + z\,k_{xy}; \tag{2.1}$$

$$\varepsilon_{x,0} = \frac{\partial u}{\partial x} + \frac{1}{2}\left(\frac{\partial w}{\partial x}\right)^2, \qquad \varepsilon_{y,0} = \frac{\partial v}{\partial y} + \frac{1}{2}\left(\frac{\partial w}{\partial y}\right)^2, \qquad \gamma_{xy,0} = \frac{\partial u}{\partial x} + \frac{\partial v}{\partial y} + \frac{\partial w}{\partial x}\frac{\partial w}{\partial y}, \tag{2.2}$$

$$k_x = -\frac{\partial^2 w}{\partial x^2}, \qquad k_y = -\frac{\partial^2 w}{\partial y^2}, \qquad k_{xy} = -2\frac{\partial^2 w}{\partial x\,\partial y}. \tag{2.3}$$

The kinetic energy of the plate is given by

32

$$T = \frac{1}{2} \rho \, h \int_0^a \int_0^b (\dot{u}^2 + \dot{v}^2 + \dot{w}^2) \, dx \, dy, \tag{2.4}$$

where ρ is the density in kg/m^3 and the over-dot indicates the time derivative. The viscoelastic behaviour of the material is modelled by using the Kelvin-Voigt model. Hence, the stress-strain relationship is defined by

$$\boldsymbol{\sigma} = \mathbf{E} \, (\boldsymbol{\varepsilon} + \eta \, \dot{\boldsymbol{\varepsilon}} \,), \tag{2.5}$$

that written in extended form is

$$
\begin{bmatrix} \sigma_x \\ \sigma_y \\ \tau_{xy} \end{bmatrix} =
\begin{bmatrix} \dfrac{E}{1-v^2} & \dfrac{vE}{1-v^2} & 0 \\ \dfrac{vE}{1-v^2} & \dfrac{E}{1-v^2} & 0 \\ 0 & 0 & \dfrac{E}{2(1+v)} \end{bmatrix}
\begin{bmatrix} \varepsilon_x \\ \varepsilon_y \\ \gamma_{xy} \end{bmatrix} + \eta
\begin{bmatrix} \dfrac{E}{1-v^2} & \dfrac{vE}{1-v^2} & 0 \\ \dfrac{vE}{1-v^2} & \dfrac{E}{1-v^2} & 0 \\ 0 & 0 & \dfrac{E}{2(1+v)} \end{bmatrix}
\begin{bmatrix} \dot{\varepsilon}_x \\ \dot{\varepsilon}_y \\ \dot{\gamma}_{xy} \end{bmatrix}, \tag{2.6}
$$

where E is Young's Modulus and η is retardation time in seconds; here the stresses are due to the plate vibration and the contribution of initial pre-load of the plate is not included. In eq. (2.6) a linear viscoelastic material is assumed, i.e. linear elasticity is assumed for static loads; the reason for this choice is justified in Section 2.3.1 where the hyperelastic behaviour of rubber is characterized and the range of strains during experimental tests is discussed. Since it is assumed that the transverse stresses are negligible, the potential energy of the plate is given by

$$U_P = \frac{1}{2} \int_{-\frac{h}{2}}^{\frac{h}{2}} \int_0^a \int_0^b \left(\sigma_x \varepsilon_x + \sigma_y \varepsilon_y + \tau_{xy} \gamma_{xy} \right) dx \, dy \, dz \,. \tag{2.7}$$

Using constitutive eq. (2.6) and strain-displacements relationships eq. (2.1), the potential energy of the plate can be written as a sum of the elastic (U_E) and the viscoelastic terms (U_V)

$$U_P = U_E + U_V \tag{2.8}$$

where,

$$U_E = \frac{E\,h}{2(1-v^2)} \int_0^a \int_0^b \left(\varepsilon_{x,0}^2 + \varepsilon_{y,0}^2 + 2v\,\varepsilon_{x,0}\varepsilon_{y,0} + \frac{1-v}{2}\gamma_{xy,0}^2 \right) dx\,dy +$$

$$\frac{E\,h^3}{2(12(1-v^2))} \int_0^a \int_0^b \left(k_x^2 + k_y^2 + 2v\,k_x k_y + \frac{1-v}{2}k_{xy}^2 \right) dx\,dy + O(h^4),$$

(2.9)

$$U_V = \eta \frac{E\,h}{(1-v^2)} \int_0^a \int_0^b \left(\varepsilon_{x,0}\frac{\partial \varepsilon_{x,0}}{\partial t} + \varepsilon_{y,0}\frac{\partial \varepsilon_{y,0}}{\partial t} + v\,\varepsilon_{x,0}\frac{\partial \varepsilon_{y,0}}{\partial t} + v\,\varepsilon_{y,0}\frac{\partial \varepsilon_{x,0}}{\partial t} + \frac{1-v}{2}\gamma_{xy,0}\frac{\partial \gamma_{xy,0}}{\partial t} \right) dx\,dy +$$

$$\frac{E\,h^3}{12(1-v^2)} \int_0^a \int_0^b \left(k_x \frac{\partial k_x}{\partial t} + k_y \frac{\partial k_y}{\partial t} + v\,k_x \frac{\partial k_y}{\partial t} + vk_y \frac{\partial k_x}{\partial t} + \frac{1-v}{2}k_{xy}\frac{\partial k_{xy}}{\partial t} \right) dx\,dy + O(h^4).$$

(2.10)

In-plane loads have been applied to the plate as shown in Fig. 2-1. The energy from the in-plane loads applied to the plate is given by (see Appendix A – Section 2.8)

$$U_M = N_x^s \int_0^a \int_0^b \left(\frac{\partial u}{\partial x} + \left(\frac{\partial w}{\partial y} \right)^2 \right) dx\,dy + N_y^s \int_0^a \int_0^b \left(\frac{\partial v}{\partial x} + \left(\frac{\partial w}{\partial y} \right)^2 \right) dx\,dy +$$

$$\eta \left(N_x^s \int_0^a \int_0^b \frac{\partial}{\partial t}\left(\frac{\partial u}{\partial x} + \left(\frac{\partial w}{\partial y} \right)^2 \right) dx\,dy + N_y^s \int_0^a \int_0^b \frac{\partial}{\partial t}\left(\frac{\partial v}{\partial x} + \left(\frac{\partial w}{\partial y} \right)^2 \right) dx\,dy \right)$$

(2.11)

where N_x^s and N_y^s are in-plane loads per unit length in x and y directions, respectively, measured in N/m. Tensile and compressive loads are positive and negative, respectively.

The virtual work done by external transversal punctual harmonic load is given by

$$W = \int_0^a \int_0^b f \cos(\omega t)\delta(x - x_1)\,\delta(y - y_1)\,w\,dx\,dy,$$

$$= f \cos(\omega t)(w)_{x=x_1, y=y_1},$$

(2.12)

where f is the harmonic point load (N), applied at the point ($x = x_1, y = y_1$), and δ is Dirac delta function.

The boundary conditions of the considered plate are given as below,

$$u = v = w = 0,\ M_x = \pm k \frac{\partial w}{\partial x},\ at\ x = 0, a;$$

(2.13)

$$u = v = w = 0,\ M_y = \pm k \frac{\partial w}{\partial y},\ at\ y = 0, b;$$

(2.14)

the minus sign in eq. (2.13) and eq. (2.14) applies at the boundaries $x = 0$ and $y = 0$. They give

any rotational constraint from zero bending moment ($M_x = 0$ and $M_y = 0$, unconstrained rotation, obtained for $k = 0$) to perfectly clamped plate ($\partial w / \partial x, = 0$ and $\partial w / \partial y, = 0$, obtained as limit for $k = \infty$), according to the value of k, where k is the stiffness per unit length of the elastic, distributed rotational springs placed at the four edges. In the present study, a very large value of k is assumed in order to approximate clamped boundary conditions.

In order to reduce the system to finite dimensions, the mid surface displacements u, v and w are expanded by using approximate functions, which satisfy the geometric boundary conditions (eq. (2.13) and eq. (2.14))

$$u(x, y, t) = \sum_{m=1}^{M} \sum_{n=1}^{N} u_{m,n}(t) \sin\left(\frac{m \pi x}{a}\right) \sin\left(\frac{n \pi y}{b}\right);$$

$$v(x, y, t) = \sum_{m=1}^{M} \sum_{n=1}^{N} v_{m,n}(t) \sin\left(\frac{m \pi x}{a}\right) \sin\left(\frac{n \pi y}{b}\right); \qquad (2.15)$$

$$w(x, y, t) = \sum_{m=1}^{M} \sum_{n=1}^{N} w_{m,n}(t) \sin\left(\frac{m \pi x}{a}\right) \sin\left(\frac{n \pi y}{b}\right);$$

where, m and n are the number of half-waves in x and y directions respectively and t is the time. M and N the number of terms used to expand the corresponding displacements. The energy due to the rotational springs is given by

$$U_R = \frac{1}{2} \int_0^b k \left[\left(\left(\frac{\partial w}{\partial x} \right)_{x=0} \right)^2 + \left(\left(\frac{\partial w}{\partial x} \right)_{x=a} \right)^2 \right] dy + \frac{1}{2} \int_0^a k \left[\left(\left(\frac{\partial w}{\partial y} \right)_{y=0} \right)^2 + \left(\left(\frac{\partial w}{\partial y} \right)_{y=b} \right)^2 \right] dx. \quad (2.16)$$

The following notation is introduced for brevity

$$\mathbf{q} = \left\{ \mathbf{u}_{m,n}, \mathbf{v}_{m,n}, \mathbf{w}_{m,n} \right\}^T. \qquad (2.17)$$

The generic element of the time-dependent vector of the generalized coordinates q is referred to as q_j; the dimension of q is equal to the degrees of freedom used in the mode expansion, N_q. The generalized forces Q_j are obtained by differentiating the virtual work done by external forces

$$Q_j = \frac{\partial W}{\partial q_j}, \qquad for \;\; j = 1, \ldots N_q. \qquad (2.18)$$

The Lagrangian equations of motion are given by

$$\frac{d}{dt}\left(\frac{\partial T}{\partial \dot{q}_j}\right) - \frac{\partial T}{\partial q_j} + \frac{\partial U}{\partial q_j} = Q_j, \qquad for \;\; j = 1, \ldots N_q, \tag{2.19}$$

where, $U = U_P + U_K + U_M$. Eq. (2.19) can be written in the following matrix form,

$$\mathbf{M\ddot{q}} + \left[\mathbf{G} + \mathbf{G_2}(\mathbf{q}) + \mathbf{G_3}(\mathbf{q},\mathbf{q})\right]\dot{\mathbf{q}} + \left[\mathbf{K} + \mathbf{K_2}(\mathbf{q}) + \mathbf{K_3}(\mathbf{q},\mathbf{q})\right]\mathbf{q} = \mathbf{f_0}\cos(\omega t) \tag{2.20}$$

where $\mathbf{M}$ is the diagonal mass matrix of dimension $N_q \times N_q$; $\mathbf{G}$ is the linear viscoelasticity matrix, $\mathbf{G_2}$ gives the quadratic nonlinear viscoelasticity terms, $\mathbf{G_3}$ denotes the cubic nonlinear viscoelasticity terms; $\mathbf{K}$ is the linear stiffness matrix, $\mathbf{K_2}$ gives the quadratic nonlinear stiffness terms, $\mathbf{K_3}$ denotes the cubic nonlinear stiffness terms and $\mathbf{f_0}$ is the vector representing the projection of the concentrated harmonic force on the generalized coordinates. In order to obtain the equations of motion in a suitable form for numerical implementation, the system is multiplied by the inverse of the mass matrix and then is written in the state-space form as follows,

$$\dot{\mathbf{q}} = \mathbf{y};$$

$$\dot{\mathbf{y}} = -\left[\mathbf{M^{-1}G} + \mathbf{M^{-1}G_2}(\mathbf{q}) + \mathbf{M^{-1}G_3}(\mathbf{q},\mathbf{q})\right]\dot{\mathbf{q}} + \left[\mathbf{M^{-1}K} + \mathbf{M^{-1}K_2}(\mathbf{q}) + \mathbf{M^{-1}K_3}(\mathbf{q},\mathbf{q})\right]\mathbf{q} \tag{2.21}$$
$$+ \mathbf{M^{-1}f_0}\cos(\omega t);$$

Eq. (2.20) can be modified by removing the viscoelasticity terms $(\mathbf{G}, \mathbf{G_2}, \mathbf{G_3})$ and adding the $\mathbf{C}$ viscous damping matrix to generate an equivalent viscous damping model.

$$\mathbf{M\ddot{q}} + \mathbf{C\dot{q}} + \left[\mathbf{K} + \mathbf{K_2}(\mathbf{q}) + \mathbf{K_3}(\mathbf{q},\mathbf{q})\right]\mathbf{q} = \mathbf{f_0}\cos(\omega t) \tag{2.22}$$

The state space form of the eq. (2.22) is as given below,

$$\dot{\mathbf{q}} = \mathbf{y};$$
$$\dot{\mathbf{y}} = -\mathbf{M^{-1}C\dot{q}} + \left[\mathbf{M^{-1}K} + \mathbf{M^{-1}K_2}(\mathbf{q}) + \mathbf{M^{-1}K_3}(\mathbf{q},\mathbf{q})\right]\mathbf{q} + \mathbf{M^{-1}f_0}\cos(\omega t); \tag{2.23}$$

The viscous damping matrix is assumed to be given by

$$\mathbf{M^{-1}C} = \begin{bmatrix} 2\omega_{1,1}\zeta_{1,1} & \cdots & 0 \\ \vdots & \ddots & \vdots \\ 0 & \cdots & 2\omega_{1,1}\zeta_{1,1} \end{bmatrix}, \tag{2.24}$$

where, $\omega_{1,1}$ is the natural frequency of the mode (m=1, n=1), being m and n the number of axial half-waves in the x and y direction respectively, and $\zeta_{1,1}$ is the corresponding assumed modal damping ratio.

2.5   NUMERICAL SIMULATION

The software Mathematica [70] has been used to perform the surface integrals and to obtain the $2 \times$ Nq first-order ordinary differential equations (ODEs) written in state space form, as shown in eq. (2.21) and eq. (2.23). They are very long expressions containing nonlinear stiffness and damping terms and are not given in this paper for sake of brevity. Nondimensionalization of variables has been carried out for computational convenience; the vibration amplitude has been divided by the plate thickness and time has been multiplied with the resonance frequency in rad/s. These $2 \times$ Nq first-order ODEs are solved by using a bifurcation analysis software AUTO and also integrated in time. The AUTO software uses pseudo arc-length continuation and collocation methods to follow the solution path. It is important to note that, along with stable solutions, unstable solutions are also obtained [71]. In particular, the analysis has been started by considering the excitation force as the bifurcation parameter, having fixed the excitation frequency far away from the resonance. The solution starts at zero magnitude of excitation and is increased slowly to reach the desired magnitude. Then, the solution is continued by varying the previously fixed excitation frequency, spanning the frequency range around the resonance in order to obtain the frequency-response curves. The equations are also directly integrated in time by using the Adams-Gear scheme to get the time-response of the structure.

2.6   COMPARISON AND DISCUSSION

2.6.1   LINEAR ANALYSIS

Initially, a linear modal analysis of both the plates has been carried out by exciting them with pseudo-random signals using the measurement apparatus and setup explained earlier. Many Frequency Response Functions (FRF) have been measured on a predefined grid of points to capture the first (lower frequency) few modes of interest. A summation of all the FRFs measured for each plate is shown in Fig. 2-7. The peaks of the FRFs' sum are marked with their corresponding mode shapes in the format of number of half waves in (x, y) direction.

Subsequently, a linear analysis has been performed on the respective nonlinear numerical model by eliminating the nonlinear terms from eq. (2.20). The rotational spring constant (k) value has been calculated by using convergence analysis and a value of $k = 1000$ *N/rad* has been found to give good results. Any further increase in the rotational spring constant does not affect significantly the natural frequency of the viscoelastic plate.
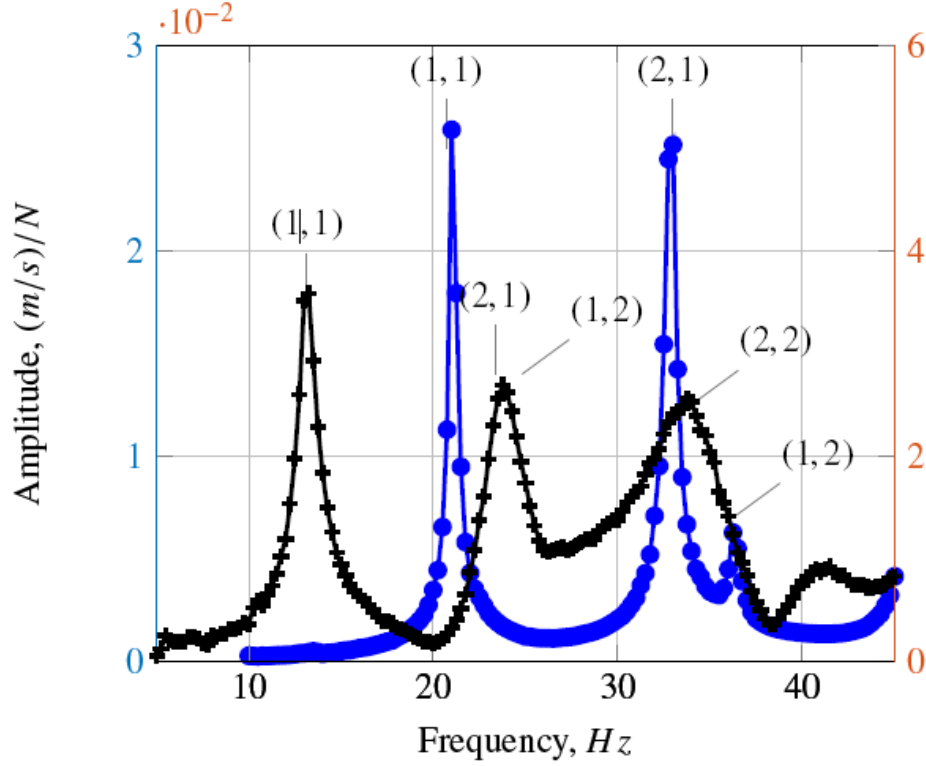
Fig. 2-7: Sum of Frequency Response Functions; +, neoprene plate (vertical axis scale on the left); ●, silicone plate (vertical axis scale on the right).

Further, unknown in-plane loads (N_x^s and N_y^s) applied on the plates during experimental setup have been obtained by an optimization algorithm. The experimentally identified natural frequencies of both plates are matched using a commercial finite element model while adjusting in-plane loads. The optimization criterion is to minimize the error function E_f in the following form:

$$E_f = \sum_{k=1}^{4} p_k \left(f_k^{EXP} - f_k^{COM} \right)^2 \qquad (2.25)$$

In eq. (2.25), f_k^{EXP} are the natural frequencies determined experimentally and f_k^{COM} are the frequencies computed from the finite element model used; p_k is a weight coefficient assigned to each of four modes considered. The error function (2.25) is minimized and the optimum in-plane loads are identified for both plates. These in-plane loads are also obtained by using a linear model with 507 degrees of freedom (DOFs), which is obtained by the expansion (2.15) taken with $M = N = 13$, and by the Abaqus commercial Finite Element code.
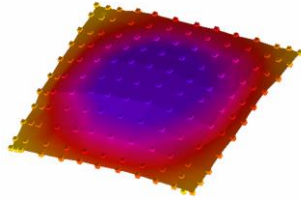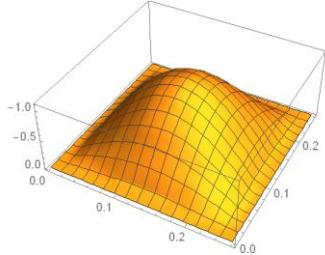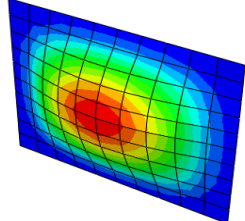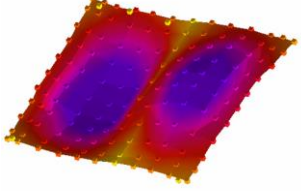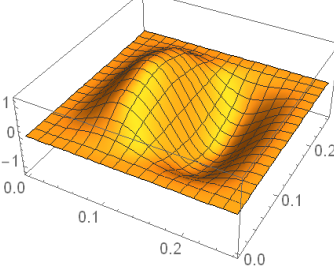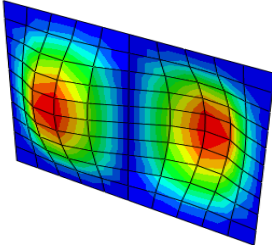
In the nonlinear analysis, reduced-order numerical models with 39 and 54 DOFs, which are the number of terms inserted in the expansion of u, v and w given in eq. (2.15), are used. A 39 DOF model with the following generalized coordinates $w_{1,1}, w_{3,1}, w_{5,1}, w_{7,1}, w_{1,3}, w_{3,3}, w_{5,3}, w_{7,3},$ $w_{1,5}, w_{3,5}, w_{5,5}, w_{1,7}, w_{3,7}, u_{2,1}, u_{4,1}, u_{6,1}, u_{8,1}, u_{2,3}, u_{4,3}, u_{6,3}, u_{8,3}, u_{2,5}, u_{4,5}, u_{6,5}, u_{2,7}, u_{4,7}, v_{1,2}, v_{3,2}, v_{5,2},$ $v_{7,2}, v_{1,4}, v_{3,4}, v_{5,4}, v_{7,4}, v_{1,6}, v_{3,6}, v_{5,6}, v_{1,8}, v_{3,8}$ has been built to study the silicone plate. Since, for the neoprene plate the mode (2,1) gives a relevant contribution, a larger 54 DOF model has been developed with the following generalized coordinates $w_{1,1}, w_{1,3}, w_{1,5}, w_{3,1}, w_{3,3}, w_{3,5}, w_{5,1}, w_{5,3},$ $w_{5,5}, w_{2,1}, w_{2,3}, w_{2,5}, w_{2,7}, w_{4,1}, w_{4,3}, w_{4,5}, w_{4,7}, w_{6,1}, u_{2,1}, u_{2,3}, u_{2,5}, u_{4,1}, u_{4,3}, u_{4,5}, u_{6,1}, u_{6,3}, u_{6,5}, u_{3,1},$ $u_{3,3}, u_{3,5}, u_{3,7}, u_{5,1}, u_{5,3}, u_{5,5}, u_{5,7}, u_{7,1}, v_{1,2}, v_{3,2}, v_{5,2}, v_{1,4}, v_{3,4}, v_{5,4}, v_{1,6}, v_{3,6}, v_{5,6}, v_{1,3}, v_{3,3}, v_{5,3}, v_{7,3}, v_{1,5},$ $v_{3,5}, v_{5,5}, v_{7,5}, v_{1,7}$.

It must be observed here that in the nonlinear models (with 39 or 54 DOFs), the in-plane load found to have the best match with the experimental natural frequencies are about 60 % smaller than the actual in-plane loads determined by the Finite Element Method (FEM) or by the 507 DOFs linear model. In fact, the reduced number of in-plane modes in the nonlinear model makes it stiffer to in-plane loads. So, in order to keep a small size of the nonlinear model, it is necessary to use different in-plane load values. Tab. 2-1 shows the linear natural frequencies along with the in-plane loads used in the nonlinear and linear models.

The first two mode shapes obtained experimentally, by the 507 DOFs linear model and by the commercial FEM code are shown in Tab. 2-2 for the neoprene plate and they are very close each other.

Sample	Mode shape	Exp. Freq.	Nonlinear Model				Linear Model: DOFs- 507			FEM	
				Natural Freq	N_x^s, N_y^s	k	Natural Freq	N_x^s, N_y^s	k	Natural Freq	N_x^s, N_y^s
	m, n	Hz	$DOFs$	Hz	N/m	N/rad	Hz	N/m	N/rad	Hz	N/m
Silicone	1, 1	21.00	39	20.90	105, 75	1000	21.29	115, 85	1000	21.08	115, 84
Neoprene	1, 1	13.16	54	13.14	40, 30	1000	13.43	50, 38	1000	13.07	50, 40
	2, 1	23.34		22.30			22.46			22.41	

Tab. 2-1: Characteristics of the different models.

Mode (*m, n)*	Experiments	Linear Model	FEM
1, 1			
2, 1			

Tab. 2-2: Mode shapes determined by experiments, linear model and FEM for the neoprene plate.

2.6.2   NONLINEAR ANALYSIS

2.6.2.1   COMPARISON WITH THE KELVIN-VOIGT MODEL

The nonlinear response of both plates has been measured at various force levels. For the silicone plate, the response has been measured at the centre of the plate (0.13 m, 0.13 m) with the excitation located at (0.11 m, 0.19 m), for four different force levels: 0.01N, 0.04N, 0.07N and 0.1N. The frequency of excitation has been varied from 17 to 25 Hz for sweep-up curves and from 25 to 17 Hz for the sweep-down curves. Sweeping up and down curves are necessary to capture the jump-up and jump-down phenomenon (hysteresis) present in the nonlinear responses. Since, the measurement has been taken at the plate's centre, the influence of the first mode is predominant while the contribution of the subsequent modes is negligible.
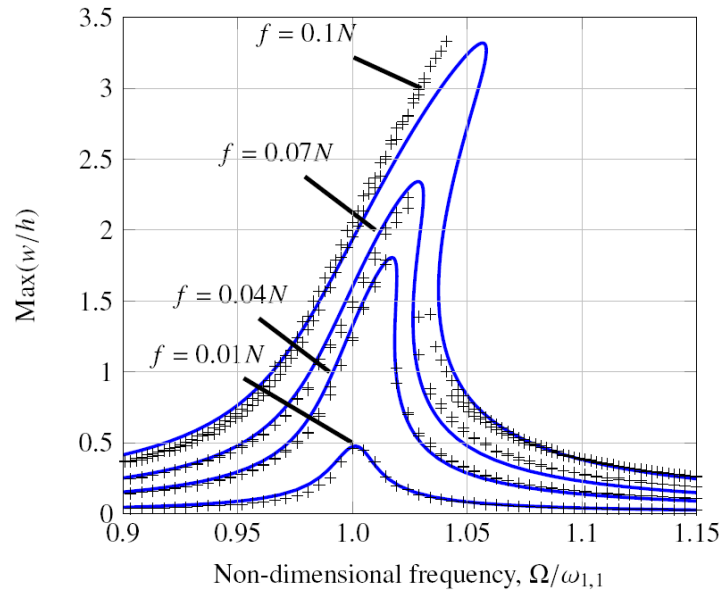
Fig. 2-8: Comparison between experimental and simulation (Kelvin Voigt model) results for the silicone plate; +, experimental results; ——, numerical results.
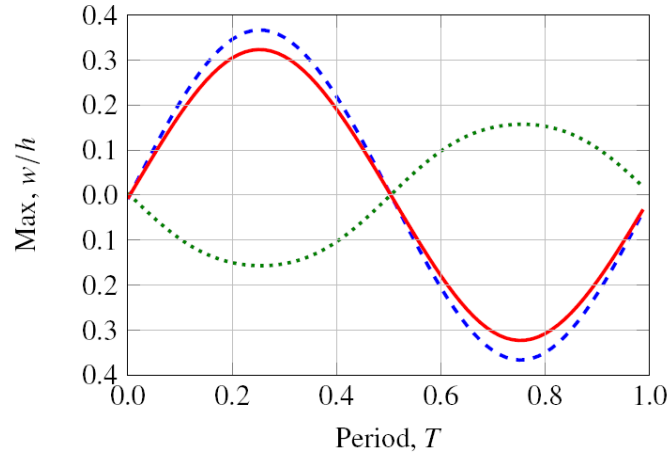
Fig. 2-9: Time response at (0.12 m, 0.14 m) for the neoprene plate for $\Omega/\omega_{1,1}$=0.6;
- -, $w_{1,1}(t)$ only; $\cdots$, $w_{2,1}(t)$ only; ——, total response with contribution of both modes.
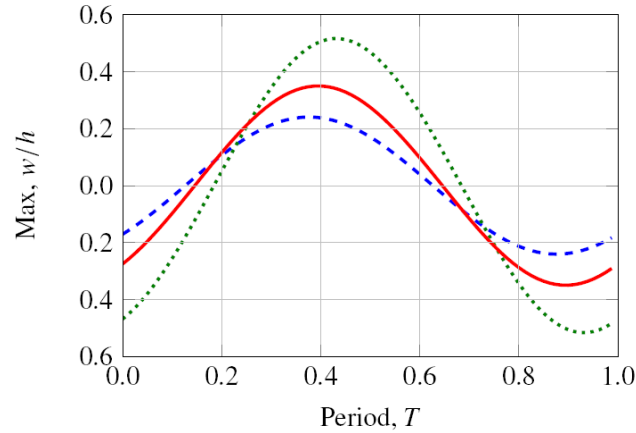
Fig. 2-10: Time response at (0.12 m, 0.14 m) for the neoprene plate for $\Omega/\omega_{1,1}$=1.6;
- -, $w_{1,1}(t)$ only; $\cdots$, $w_{2,1}(t)$ only; ——, total response with contribution of both modes.

The comparison between the experimental results and numerical simulation is shown in Fig. 2-8. The numerical response obtained by using the software AUTO is shown here and it has been calculated for all the four force levels by using the 39 DOF model. The response of the plate is practically linear for the force level 0.01 N. Numerical results are matching very well with the experimental responses. A retardation time η of 0.000121 seconds has been used in the

numerical model to match the experimental results at the first force level. The response from the plate becomes nonlinear in the consecutive force levels and maximum vibration amplitude of more than 3 times the thickness of the plate has been reached for the largest force level. At the force levels of 0.04 and 0.07 N, the numerical model is accurately capturing the hardening behaviour of the plate. Whereas, at the highest force level, the numerical model slightly over-predicts the nonlinear behaviour of the plate. This could be due to the reduced number of DOFs used in the model. The retardation time of the plate, joined to the viscoelastic dissipation, increases when the vibration amplitudes become larger. In particular, the retardation time η used for matching the experimental results of the second, third and fourth excitation level are 0.000121, 0.000162 and 0.000145 seconds, respectively.
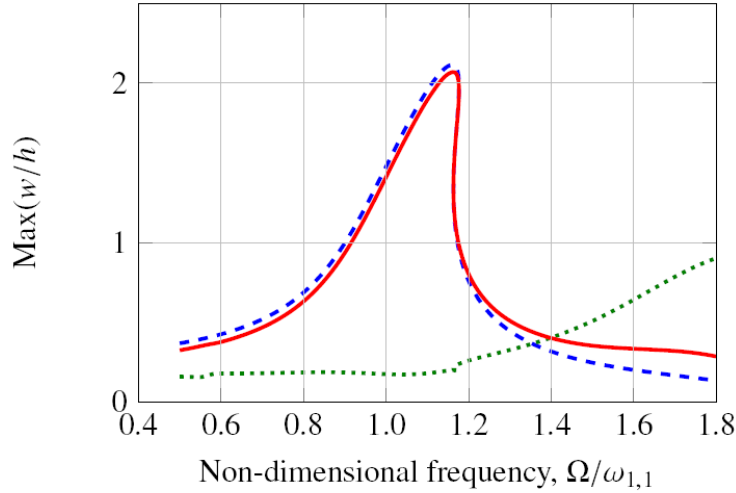
Fig. 2-11: Frequency response at (0.12 m, 0.14 m) for the neoprene plate; - -, $w_{1,1}(t)$ only; ···, $w_{2,1}(t)$ only; ——, total response with contribution of both modes.

For the neoprene plate, the nonlinear response has been measured at five different force levels: 0.1N, 0.5N, 1.5N, 2.5N and 3.5N. The response has been measured at (0.12 m, 0.14 m), which is close to the centre, with the excitation located at (0.22 m, 0.24 m), which is close to a corner; this is the reason for the higher forces necessary with respect to the silicone plate. As the measurement has not been carried out at the centre of the plate, the response of the plate around the resonance of the fundamental mode (1,1) presents a contribution of the second mode (2,1). So, a larger model with 54 DOFs (sufficient to capture the first two resonances) has been used to

get the nonlinear response during the numerical simulation. The time response of the two predominant modes, $w_{1,1}(t)$ and $w_{2,1}(t)$, at $\frac{\Omega}{\omega_{1,1}} = 0.6$ and at $\frac{\Omega}{\omega_{1,1}} = 1.6$ are shown in Fig. 2-9 and Fig. 2-10, respectively, for one excitation period. From the time response, it is clear that the displacements of both modes, at the point of measure, are out of phase (180 ° degree phase difference) before and in-phase (0° degree phase difference) after the first natural frequency. So, the total response has been calculated at each frequency while taking into account the phase difference between them. The frequency response calculated for the 2.5N force level is shown in Fig. 2-11.
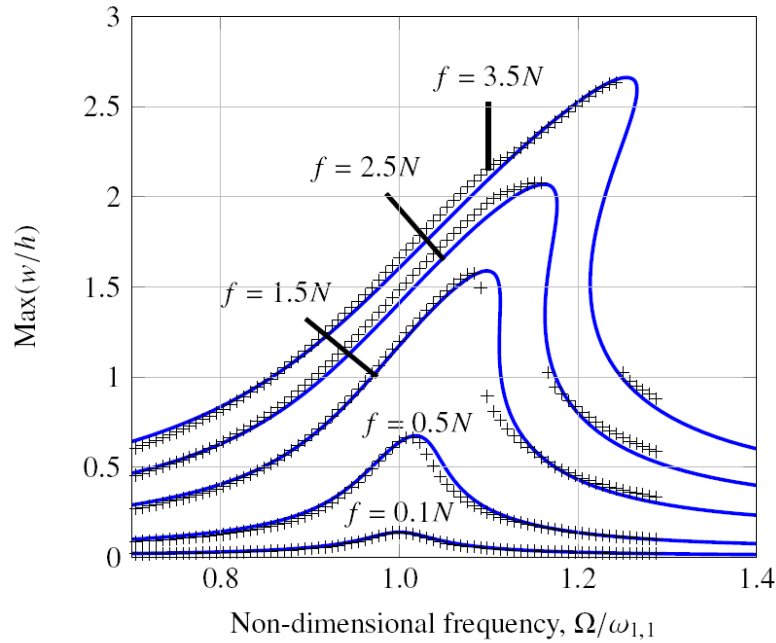
Fig. 2-12: Comparison between experimental and simulation (Kelvin Voigt model) results for the neoprene plate; +, experimental results; ——, numerical results.

The comparison between the experimental and numerical results obtained from the 54 DOF model for the neoprene plate is shown in Fig. 2-12. The plate responses at the force levels of 0.1 and 0.5 N are practically linear and, as expected, they match very well with the experimental results. The retardation time η at these force levels is 0.000924 and 0.00924 seconds, respectively. As the force level is increased, the plate response becomes nonlinear with hardening behaviour. At the force levels of 1.5 N, 2.5 N and 3.5 N, the experimental results

compare well with the numerical results. Moreover, the influence of second mode is also captured very well by the numerical model, as it can be seen by the good agreement of experimental and numerical results after the vibration peak, where the influence of the second mode is more relevant. The small differences observed between experimental and numerical results could be due to the reduced number of DOFs used in the numerical model. Increasing the excitation levels, similar to silicone plate, it is observed that the retardation time η increases. The values corresponding to the five force levels in increasing order are 0.000924, 0.00924, 0.001016, 0.00115 and 0.00122 seconds.
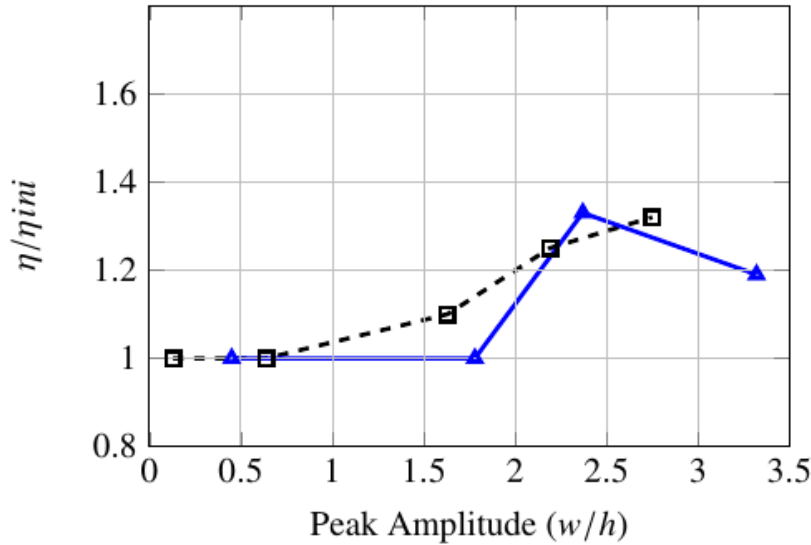
Fig. 2-13: Variation of retardation time with the peak vibration amplitude; —▲—, silicone plate; - -□- -, neoprene plate.

The retardation times η used in the numerical simulations to match the experimental data are non-dimensionalized, by divided by the initial retardation time η_{ini} obtained for the lowest force excitation (linear), and then plotted in Fig. 2-13 against the non-dimensionalized peak vibration amplitude. The graph shows the variation of the retardation time versus the vibration amplitude. This is quite interesting since a nonlinear damping model is introduced by the Kelvin-Voigt viscoelasticity. Even the nonlinearity introduced by this model is unable to predict the variation of damping during large amplitude vibrations of both rubber plates. Hence retardation time has to be increased to match the experimental response at higher vibration amplitudes for both cases.

Very interesting is that, for two plates of different rubber material and thickness, the same behaviour is obtained in Fig. 2-13, with an increase of the retardation time of about 20% and 30% for the silicone and neoprene plates respectively.

2.6.2.2 COMPARISON WITH THE VISCOUS DAMPING MODEL

The equivalent viscous damping model was also used to study the response of both the plates as per eq. (2.23). The modal damping ratio $\zeta_{1,1}$ was varied at each force level for both plates to match the experimental results. The comparison between the viscous damping model and experimental results for silicone and neoprene plates is shown in Fig. 2-14 and Fig. 2-15, respectively. The agreement is good also for this model, even if a little less good than for the viscoelastic dissipation. The modal damping ratio used in the simulation increases with the excitation level and vibration amplitude for both the plates. The damping ratios of the silicone plate are 0.008, 0.0081, 0.011 and 0.0105 for the force levels in increasing order. Similarly, the damping ratios of neoprene plate are 0.0382, 0.0389, 0.0465, 0.0558 and 0.0573 for the force levels in an increasing order.
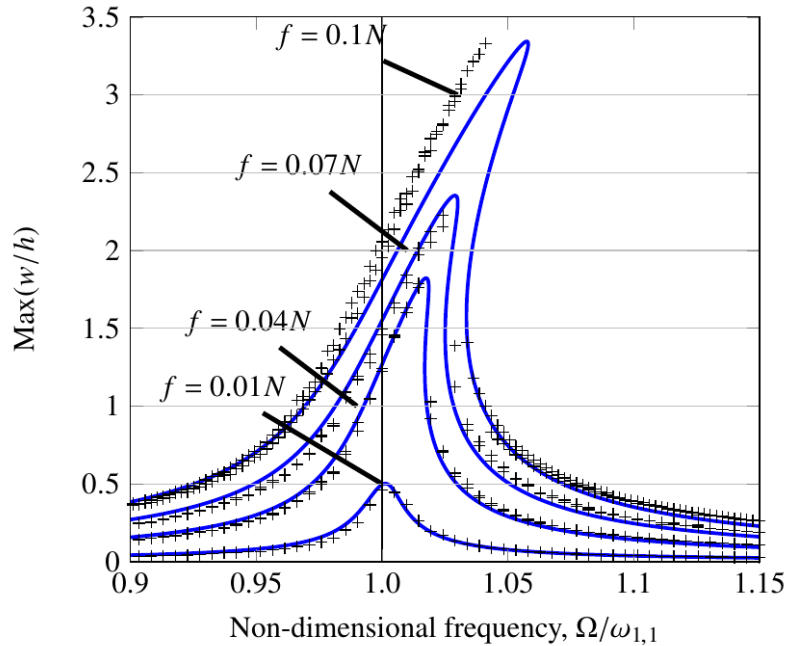
Fig. 2-14: Comparison between experimental and simulation (viscous damping model) results for the silicone plate; +, experimental results; ——, numerical results.
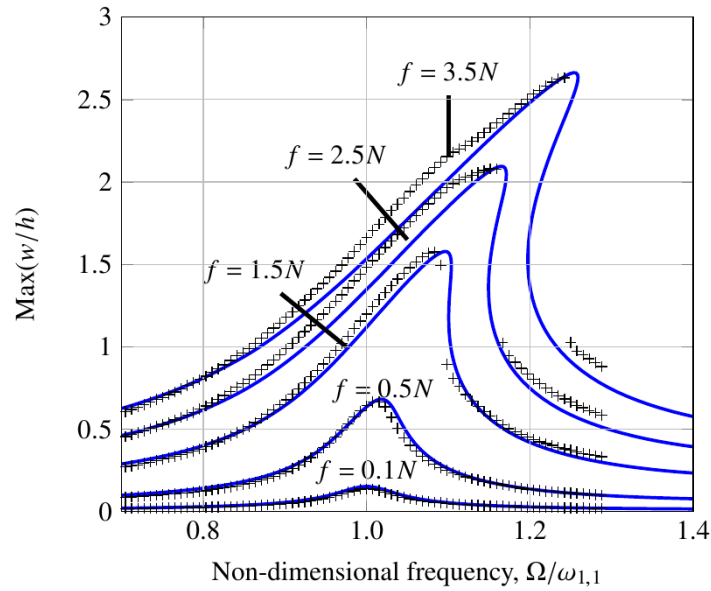
Fig. 2-15: Comparison between experimental and simulation (viscous damping model) results for the neoprene plate; +, experimental results; ——, numerical results.

The damping ratio $\zeta_{1,1}$, non-dimensionalized with respect to the damping value for linear vibrations $\zeta_{1,1}(ini)$, is plotted in Fig. 2-16 against the non-dimensionalized maximum vibration amplitude. Fig. 2-16 shows that in case of viscous damping, which is a linear dissipation model, an increase of damping ratio is identified by the nonlinear results, however the increase is more than the increase of retardation time (nonlinear damping model) as it is a linear damping model. The damping increase in this case with viscous damping model is different for the two plates of different rubber material. For the silicone plate, the damping ratio is basically constant up to peak vibration amplitudes about 1.8 times the thickness, and then it increases of about 30 %. Instead the neoprene plate shows a regular increase of the damping ratio with the peak vibration amplitude, up to almost 60 %.
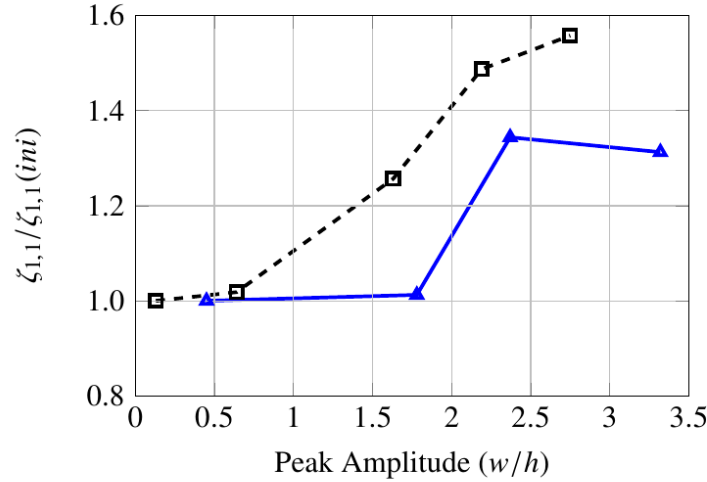
Fig. 2-16: Variation of the viscous damping with the peak vibration amplitude;
—▲—, silicone plate; - -□- -, neoprene plate.

2.7 CONCLUSIONS

Geometrically nonlinear vibrations of clamped rubber plates have been studied experimentally and theoretically. Two thin rectangular plates made of different materials and thicknesses have been considered; a silicone rubber plate with 0.0015 m of thickness and a neoprene rubber plate with 0.003 m of thickness. The viscoelastic characteristics of the material have been modeled using the Kelvin-Voigt model and the geometrically nonlinear strain-displacement relationships using the von Kármán nonlinear plate theory. Numerical results are matching very well the experimental responses and allow to identify the damping parameters. The increasing trend of retardation time with increasing vibration amplitude has been found in both the plates. This behaviour is similar to the one observed for the equivalent viscous damping model but the increase in retardation time is lesser. The difference in the behaviour is surely due to the nonlinear damping terms introduced by the Kelvin-Voigt viscoelastic dissipation model, since the liner part of the two dissipation models can be made equivalent. It must be pointed out here that the plates investigated are hardening type systems, for which the nonlinear damping terms are introducing an increase in the dissipation. However, this increase is not sufficient to follow the experimental behaviour, so that the retardation time must be increased with the vibration

amplitude, i.e. just as a global increase of damping ratios found with the viscous damping model. At this point, it would be interesting to investigate a softening type system with rubber shells, since in that case the nonlinear damping terms should reduce the dissipation with the increase of the vibration amplitude. This is left for a future study. However, what seems clear from this study is that traditional damping models, namely viscous damping and Kevin-Voight viscoelasticity, present a poor description of the dissipation in rubber plates. In fact, dissipation parameter must be varied with the force excitation (or the peak vibration amplitude) in order to reproduce correctly the vibration response experimentally measured.

2.8 APPENDIX A

The elastic potential energy of the vibrating plate, subjected to in-plane static pre-load in x and y direction uniform along each edge, is given by

$$U = \frac{1}{2} \int_{-h/2}^{h/2} \int_0^a \int_0^b \left(\sigma_x^t \varepsilon_x + \sigma_y^t \varepsilon_y + \tau_{xy}^t \gamma_{xy} \right) \mathrm{d}z \, \mathrm{d}x \, \mathrm{d}y \tag{2.26}$$

where the total stresses (indicated with superscript *t*) are given by the contribution of static pre-load (indicated with superscript *s*) and the dynamic component due to vibration

$$\sigma_x^t = \sigma_x^s + \sigma_x, \quad \sigma_y^t = \sigma_y^s + \sigma_y, \quad \tau_{xy}^t = \tau_{xy}^s + \tau_{xy}, \tag{2.27}$$

where it assumed that the static pre-load gives $\tau_{xy}^s = 0$. In eq. (2.26), the strains are only due to the vibration since it is assumed that the initial configuration of the plate, which is the reference configuration in the present study, is pre-loaded. Eq. (2.27) are then substituted in eq. (2.26)

$$
\begin{aligned}
U &= \frac{1}{2} \int_{-h/2}^{h/2} \int_0^a \int_0^b \left[\left(\sigma_x^s \varepsilon_x + \sigma_y^s \varepsilon_y \right) + \left(\sigma_x \varepsilon_x + \sigma_y \varepsilon_y + \tau_{xy} \gamma_{xy} \right) \right] \mathrm{d}z \, \mathrm{d}x \, \mathrm{d}y \\
&= U_E + \frac{1}{2} \int_{-h/2}^{h/2} \int_0^a \int_0^b \left(\sigma_x^s \varepsilon_x + \sigma_y^s \varepsilon_y \right) \mathrm{d}z \, \mathrm{d}x \, \mathrm{d}y,
\end{aligned}
\tag{2.28}
$$

where U_E is given in eq. (2.7). Substituting eq. (2.1) into eq. (2.28), the following expression is obtained for the elastic potential energy of the plate

$$
\begin{aligned}
U &= U_E + \frac{1}{2} \int\limits_{-h/2}^{h/2} \int\limits_{0}^{a} \int\limits_{0}^{b} \left(\sigma_x^s \varepsilon_{x,0} + \sigma_y^s \varepsilon_{y,0} + \sigma_x^s z\, k_x + \sigma_y^s z\, k_y \right) \mathrm{d}z\, \mathrm{d}x\, \mathrm{d}y \\
&= U_E + \frac{1}{2} \int\limits_{0}^{a} \int\limits_{0}^{b} \left(N_x^s \varepsilon_{x,0} + N_y^s \varepsilon_{y,0} \right) \mathrm{d}x\, \mathrm{d}y,
\end{aligned}
\tag{2.29}
$$

where the assumption of uniform σ_x^s and σ_y^s through the thickness is used. The integral on the right inside of eq. (2.29) gives the plate potential energy due to initial in-plane static pre-load.

3   COMPARISON OF VARIOUS MODELS TO UNDERSTAND NONLINEAR DAMPING

After it was clear that the Kelvin-Voigt model is not suitable to capture the damping variation, various other damping models were considered to understand the variation of damping during the large amplitude vibration of a hard silicone rubber plate. Linear viscous damping, loss factor based on dissipated and storage energies, nonlinear damping based on the SLS model are among them. It became clear that the SDOF model based on SLS material model captures the variation very well. With this model, one single value of the damping parameter is sufficient to model the dissipation during forced vibrations from the linear to the nonlinear domain. During this study, a SDOF model parameter identification routine based on the Harmonic Balance method was also developed and the time response measured from experimental data was used to estimate the nonlinear parameters of the system along with damping. The results of this part of the study are published in the journal Mechanical Systems and Signal Processing and the manuscript is given below.

Identification of the Viscoelastic Response and Nonlinear Damping of a Rubber Plate in Nonlinear Vibration Regime

Prabakaran Balasubramanian, Giovanni Ferrari, Marco Amabili

Department of Mechanical Engineering, McGill University,
817 Sherbrooke Street West, Montreal, H3A 0C3, Canada

3.1   ABSTRACT

Three different dissipation models have been used to identify the increase of damping with the vibration amplitude for a rubber rectangular plate. For this purpose, a square rubber plate made of silicone with fixed edges has been tested and its linear and nonlinear responses have been measured by laser Doppler vibrometers. First, a reduced-order model, using energy based approach and global discretization, has been constructed, taking into account geometric imperfections; the linear viscous damping at each excitation level in the nonlinear regime has been identified from the experimental data. This numerical model with linear viscous damping has been widely validated and constitutes the basis for comparison with subsequent damping identifications. Then, three different single degree of freedom models have been fitted to the

same experimental data; each model has a different damping description. Specifically, the models are based on a modified Duffing oscillators with linear, quadratic and cubic stiffness and: (i) a linear viscous damping; (ii) a nonlinear viscoelastic dissipation described by the loss factor; (iii) a standard linear solid viscoelastic model with nonlinear springs. The dissipation identified by the different models is discussed and confirms the major nonlinear nature of damping as a function of the vibration amplitude.

3.2   INTRODUCTION

Understanding the structural damping is of critical importance for effective design. The importance increases manifolds when the structure experiences large amplitude vibrations, as its nonlinear dynamics is even more influenced on the amount of damping than in the linear (i.e. small amplitude) vibration regime [64]. Experimental data is mandatory to identify the damping present in a structure, both in linear and nonlinear regime. However, damping cannot be directly measured, so a dissipation model must be introduced in order to identify its value. Dissipation depends, among others, on the geometry, material, surrounding fluid, boundary conditions and vibration mode shape.

   There are well established tools available to extract the viscous damping ratio in the linear vibration regime. Experimental modal analysis is one among them and has become the industrial standard decades ago. However, thin walled structures such as plates, panels and shells experience large amplitude vibrations, i.e. vibration amplitude of the order of the thickness giving rise to geometrical nonlinearity, during their normal operating conditions and experimental modal analysis or any other tools based on the linear vibration assumption cannot be used to extract the damping of them. Hence there is a clear need for developing tools to extract damping in the nonlinear vibration regime for thin walled structures.

   Recent experimental studies show that the damping present in a structure increases nonlinearly as the vibration amplitude increases. This phenomenon is well documented in cantilever beams [72], plates [22, 69], panels [22] and shells [67] considering viscous damping model for representing the dissipation energy.

   In order to predict the nonlinear dynamics of a structure using a reasonable amount of degrees

of freedom, with intrinsic numerical advantages in reliability and computational cost, it is necessary to build a Reduced Order Model (ROM) [5, 73]. Often the damping in the ROM is introduced as linear viscous damping, e.g. by using Rayleigh's dissipation function [5]. Developing an accurate ROM for a structure involves numerous complexities. A simple tool to extract the damping of a structure from its experimentally measured nonlinear response, without the need of developing a ROM, would give engineers/scientists clear advantage. To address this need, a tool based on harmonic balance method was developed considering viscous damping model in a modified Duffing nonlinear resonator with quadratic and cubic stiffness terms [58]. This tool successfully extracts the damping ratio present in a structure from its amplitude-response curves at different excitation levels and the results match very well with the damping identified from the sophisticated ROM of the structure. Experimental results show that the increase in damping with the peak vibration amplitude (and the level of harmonic force excitation) is substantially large [58]. Not taking it into account would lead to inefficient design of such structures and very large overprediction of the vibration amplitude. In fact, most of the studies in nonlinear vibration show complicated nonlinear dynamics which is fully destroyed by the increase of the actual damping due to the large amplitude of vibrations.

Structures made of rubber-like or biological materials exhibit substantial viscoelastic behaviour [74]. For these structures, the viscous damping model does not capture accurately the dissipated energy. Viscoelastic damping models such as the Kelvin-Voigt, hysteretic, standard linear solid or Boltzmann models have been used for that purpose [75-78]. A previous study by our research group shows the variation of relaxation time (dissipation parameter of Kelvin-Voigt model viscoelastic model) versus the vibration amplitude of rubber plates [1]. The nonlinear damping introduced by the Kelvin-Voigt model is not sufficient to capture the damping exhibited by the structure during large amplitude vibrations. So, the relaxation time has to be increased as the vibration amplitude increases to match the numerical response with experimental measurements, implying that Kelvin-Voigt model is not sufficient for modelling the nonlinear damping.

Hysteretic damping (where stiffness and damping are represented together by a complex spring) has been used extensively to describe the dissipation present in viscoelastic systems using the loss tangent. For example, the loss tangent of an aluminium plate having viscoelastic

core with various fiber orientation was identified experimentally by Berthelot et al. [79]. A novel method to identify the loss tangent in the linear regime was developed by Liu and Ewing [80]. The loss and storage energies were experimentally calculated by dividing the mobility at the driving point by the mobility of the measurement point. The loss tangent was also identified by frequency response functions measured on different points of the geometry for a composite plate [81]. However, the variation of hysteretic damping during large-amplitude vibrations of a structure has not been completely addressed yet, as per authors' knowledge.

It is evident that a nonlinear dissipation model is necessary to predict structural dynamics at large-amplitude vibration [22]. Few researchers have attempted to use phenomenological nonlinear damping for various structures. Zaitsev et.al. [59] used the Kelvin-Voigt model for describing the nonlinear damping of micromechanical oscillator and concluded that the model is better than linear viscous damping but not sufficient and further work is required. Gottlieb and Habib [82] used a phenomenological nonlinear damping model to understand the large amplitude, quasi-periodic and chaotic vibrations of a spherical pendulum. Eichler et. al. [60] used a damping model containing a nonlinear term proportional to the square of the vibration amplitude multiplied by the velocity, similar to the one previously introduced in [18], without any derivation; it was applied to estimate the damping in carbon nanotubes and graphene devices. Recently Amabili [83] derived a model of nonlinear damping based on a fractional standard linear solid material after introducing geometric nonlinearity in it. The model was successfully compared to experimental results for vibrations of a plate, a beam and a curved panel in geometrically nonlinear regime.

In the present study, three different dissipation models have been used to identify the increase of damping with the vibration amplitude for a rubber rectangular plate. An overview of the organization of the study with the different models developed is shown in Fig. 3-1. For this purpose, a square rubber plate made of silicone with fixed edges has been tested and its linear and nonlinear responses have been measured by laser Doppler vibrometers. First, a ROM, using energy based approach and global discretization, has been constructed, taking into account geometric imperfections; the linear viscous damping at each excitation level in the nonlinear regime has been identified from the experimental data. This numerical model with linear viscous damping has been widely validated and constitutes the basis for comparison with subsequent

damping identifications. Then, three different single degree of freedom (SDOF) models have been fitted to the same experimental data; each model has a different damping description. Specifically, the models are based on a modified Duffing oscillators with linear, quadratic and cubic stiffness and: (i) a linear viscous damping; (ii) a nonlinear viscoelastic dissipation described by the loss factor; (iii) a standard linear solid viscoelastic model with nonlinear springs. The dissipation identified by the different models is discussed and confirms the major nonlinear nature of damping as a function of the vibration amplitude.
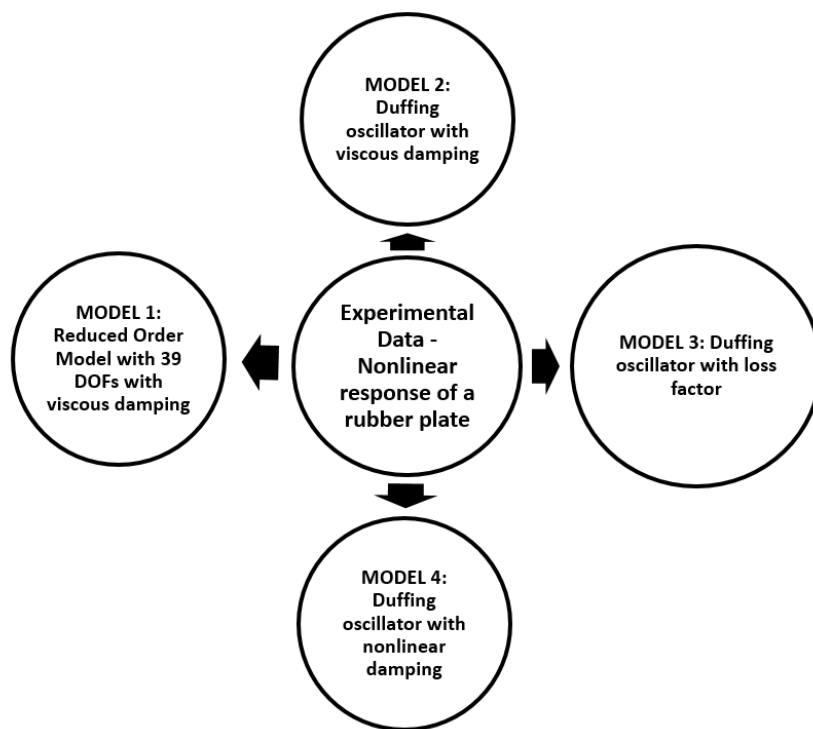
Fig. 3-1: Different models used to identify the damping from the experimental data

3.3   EXPERIMENTAL STUDY ON A RUBBER PLATE

A thin walled rubber plate made of silicone was chosen for this study. The sheet of rubber was purchased from commercial market with the description of "high-temperature silicone sheet". The shore hardness is 90A, the density is approximately 1430 kg/m^3 and the thickness is 3.35 mm. Viscoelastic structures such as the plate under study here exhibit frequency dependent complex modulus. To measure the same, a strip of the rubber sheet was cut with the width of 11

mm and length of 94 mm and assembled as fixed-fixed beam without initial pre-tension. The beam was excited laterally (in the direction of the smaller dimension) at middle-length by using an electrodynamic shaker equipped with piezoelectric load cell and stinger. From the beam deflection at various frequencies, the frequency dependent complex modulus is calculated and shown in Fig. 3-2. The real part of the complex modulus is called the storage modulus (solid line in Fig. 3-2) and the imaginary part is named the loss modulus (dotted line in Fig. 3-2). The storage modulus is increasing nonlinearly as the frequency increases. Whereas, loss modulus is increasing linearly with respect to frequency within the frequency range studied. The loss factor of the material, which is given by the ratio between the loss and storage moduli, is shown in Fig. 3-3. The loss factor increases from about 0.01 at 5 Hz to 0.13 at 100 Hz.
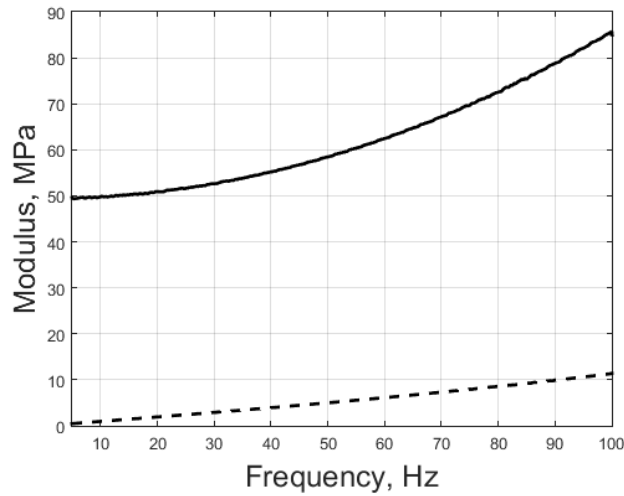
Fig. 3-2: Identified complex modulus of the silicone rubber. ——, Storage modulus;

− −, loss modulus.
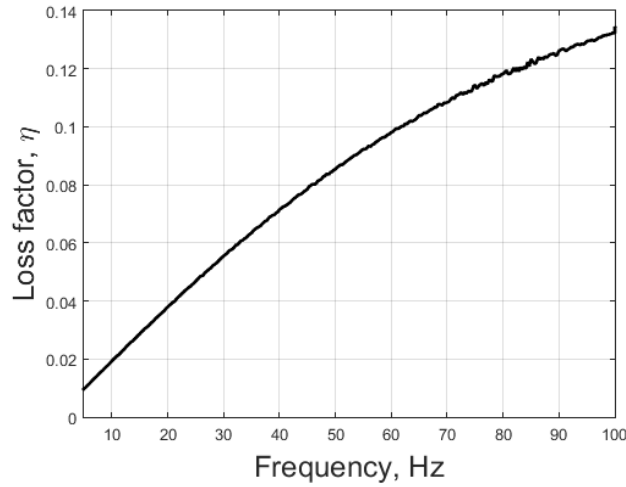
Fig. 3-3: Identified loss factor of the silicone rubber.

3.3.1   RUBBER PLATE

A square plate was glued to a heavy metal frame for experiments in large-amplitude vibration regime. The dimensions of the free part of the plate inside the frame were 260×260 mm. The glue ensures fixed boundary conditions in the out-of-plane direction since it is stiffer than the plate in bending. However, the in-plane stiffness of the plate is larger than that of the glue, which ends in approximately obtain free-edge boundary conditions in both the in-plane directions. The glued rubber plate is shown in Fig. 3-4. Since no in-plane stretch was applied to the rubber plate during gluing, the plate is not perfectly flat and geometric imperfections are present. The geometric imperfections are very important for correctly simulating the nonlinear vibration response of plates and shells. To measure the geometric imperfections of the plate, the FAROARM® scanning system was used. The glued rubber plate was kept on the scanning table and the profile of the rubber plate was scanned. The scanned points were imported and the 3D image of the surface of the plate was constructed as shown in Fig. 3-5.

3.3.2   MEASUREMENT SETUP

For dynamic tests, the structure was excited by means of transversal punctual excitation using a thin stinger connected to an electrodynamic exciter (Brüel & Kjær model 4824). The excitation was positioned close to the top left corner, at a distance of 50 mm from the left vertical edge and 60 mm from the top horizontal edge (point E in Fig. 3-4). This excitation position is chosen in

such a way that all the low-frequency fundamental modes are excited and there is little interaction between the shaker and the plate during large amplitude vibrations. A very small force transducer (Brüel & Kjær model 8203) glued to the plate was used to measure the force applied and it was connected to the electrodynamic exciter through a stinger, as shown in Fig. 3-5.
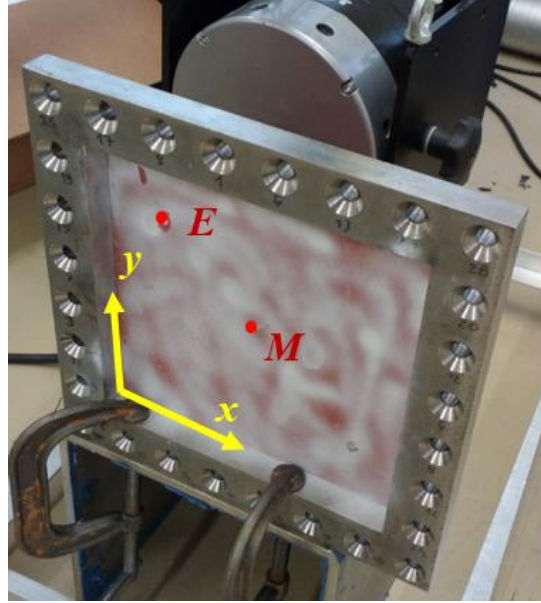
Fig. 3-4: Silicone rubber plate glued to a metal frame; **E**, Excitation point, **M**, Measurement point. The spray paint is applied to increase reflectivity for the laser measurement.
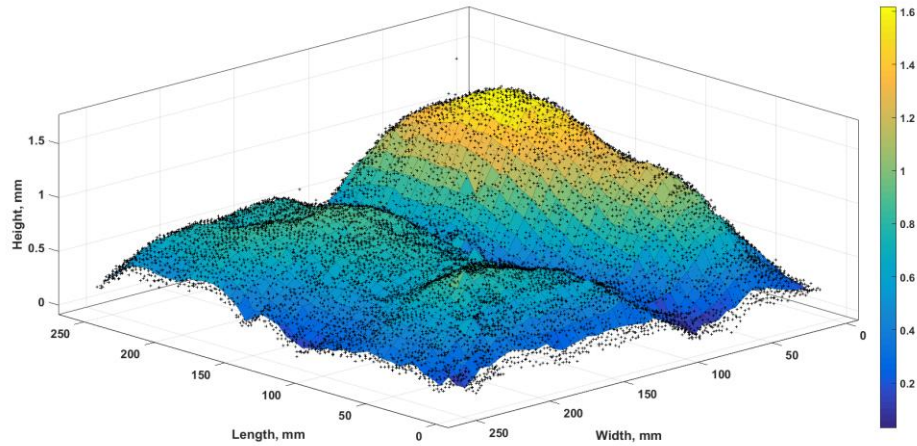
Fig. 3-5: Measured surface of the glued rubber plate, which gives the geometric imperfections.

In the linear experiments, an automatic scanning laser Doppler vibrometer (Polytec PSV 400)

was used to measure the vibration. The scanning laser system was employed to measure the Frequency Response Functions (FRFs) at a large number of predefined points covering the whole plate. The plate was excited with pseudo-random signal in the linear study as it eliminates the leakage effect. The measured FRFs were exported to LMS Test.Lab software for modal parameter extraction using the PolyMAX algorithm [84].

(a)

(b)
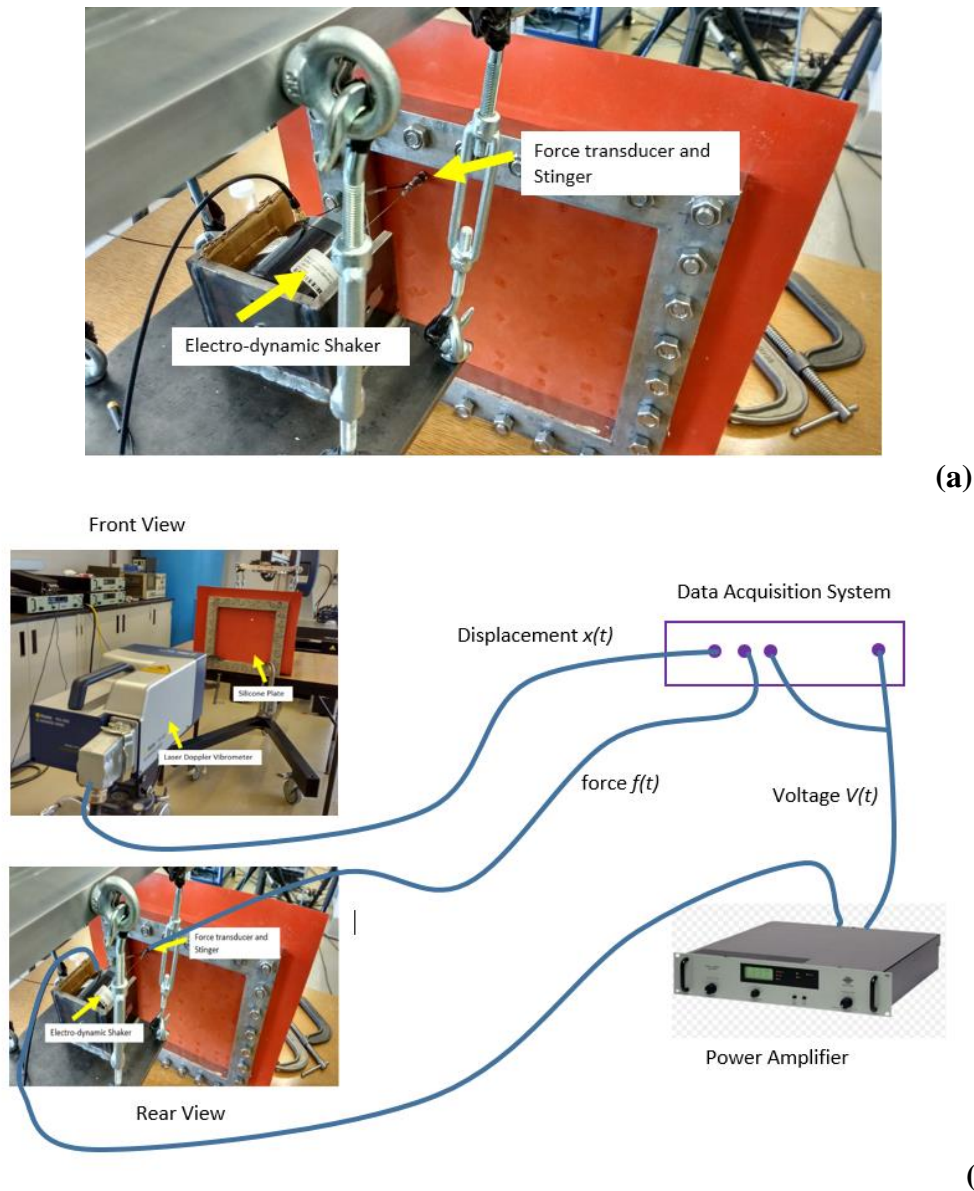
Fig. 3-6: Measurement setup for the vibration experiments on the rubber plate. (a) Electro-dynamic exciter, piezoelectric load transducer and stinger; (b) overview of the experimental set-up.

During large-amplitude vibration experiments, a single-point laser vibrometer (Polytec OFV 505) was used. The laser was pointed at the centre of the plate, since the fundamental mode has its antinode in that position. The plate was excited with harmonic force at a predefined level with a frequency lower than the fundamental natural frequency. The excitation frequency was then increased in steps (0.05 Hz) while keeping the predefined force within the tolerance specified ($\pm$ 0.5%) using feedback controller. After this test was completed, the excitation frequency was decreased from a frequency higher than the fundamental natural frequency in a similar way. At the end of the experimental test, every force level has two curves: one obtained increasing and the other one decreasing the excitation frequency. These two curves should be superimposed in case of linear response of the system, but present jumps and hysteresis in case of nonlinear response. Every time that the excitation frequency is changed during the measurement, 40 periods of the signal are discharged in order to remove the transient response of the system. The next 40 periods are recorded and used to calculate the vibration amplitude and phase at that excitation frequency. The time domain signals are measured at the sampling frequency of 6400 Hz. The typical measurement setup is explained in Fig. 3-6.

3.3.3   LINEAR RESULTS

The set of FRFs measured from the plate was used to extract the modal parameters. The first four mode shapes are shown in Fig. 3-7. In the figure caption, the number n and m of half-waves in x and y direction, respectively, of the mode shape is given. The natural frequencies and damping ratios are reported in Tab. 3-1. The fundamental mode of the plate is at 17.1 Hz and its damping ratio is 2.98 %. A Finite Element Model (FEM) of the plate was also created using shell elements in ANSYS®. The storage modulus of the material at 17.1 Hz is used as the Young's modulus (51 MPa) in the FE model. The results from the FEM are in good agreement with the experimental results, as shown Tab. 3-1.
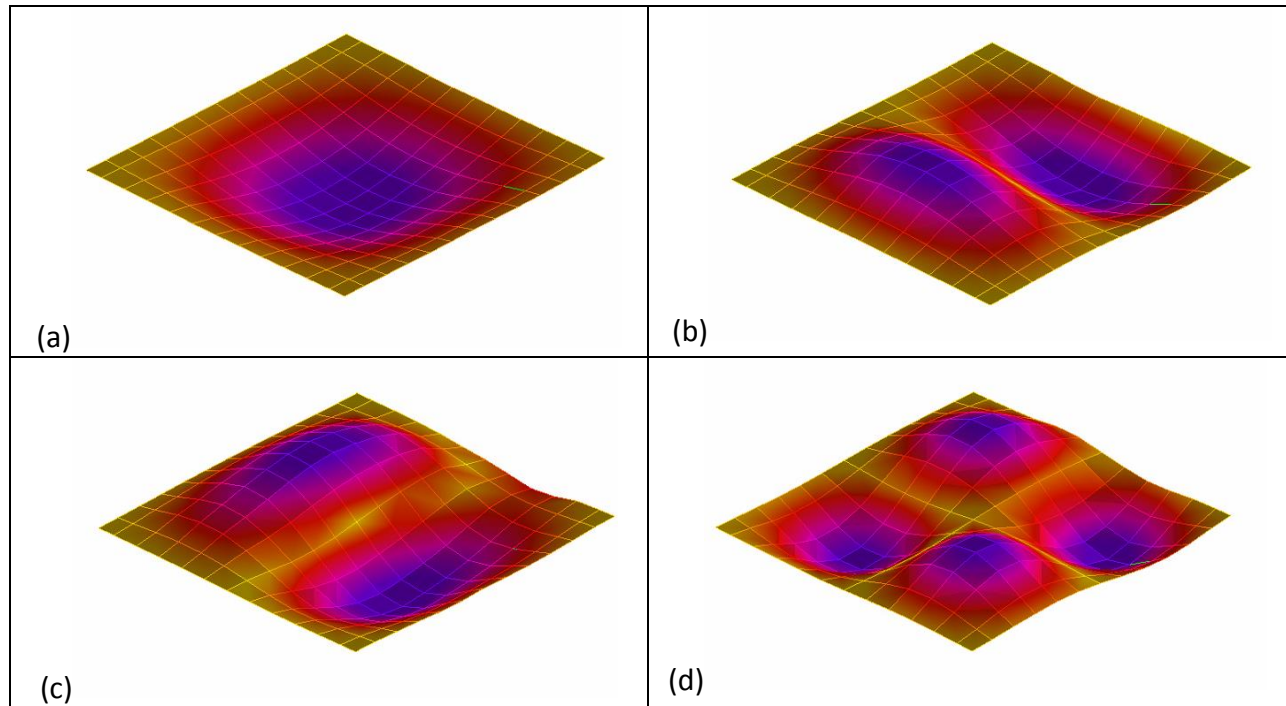
Fig. 3-7: Mode shapes of the glued rubber plate. (a) 1st mode (n = 1, m = 1); (b) 2nd mode (n = 2, m = 1); (c) 3rd mode (n = 1, m = 2); (d) 4th mode (n = 2, m = 2).

	Experimental Data		ANSYS	ROM (linear)
Mode	Frequency, Hz	Damping Ratio, %	Frequency, Hz	Frequency, Hz
1	17.10	2.98	17.85	17.34
2	35.67	3.17	36.48	37.14
3	37.45	3.25	36.48	37.14
4	54.78	3.11	53.69	55.63

Tab. 3-1: Experimental modal analysis results for the rubber plate compared with numerical results.

3.3.4   NONLINEAR RESULTS

The fundamental mode was chosen for the large-amplitude vibration study. Six force levels (0.1, 0.25, 0.5, 0.75, 1.5 and 2.5 N) were selected and the nonlinear frequency-response curves of the plate were obtained. The amplitudes of the experimental responses are plotted in the Fig. 3-8 and the corresponding phases are shown in Fig. 3-9. The excitation frequency ω is non-

dimensionalized by the natural frequency of the fundamental mode Ω in both figures. Similarly, the vibration amplitude is non-dimensionlized by the plate thickness. The two lowest force levels (0.1 and 0.25 N) show a linear behaviour and the frequency of the peak is practically the same as the linear natural frequency. However, from the third force level onwards, the resonance frequency increases, which is typical of hardening-type nonlinear systems. The largest two force levels (1.5 and 2.5 N) display significant hysteresis and jumps in both the amplitude and phase curves. A maximum vibration amplitude of 1.6 times the thickness was achieved for the highest force level (2.5 N). The increase in the resonance frequency is almost 20 % from the natural frequency.
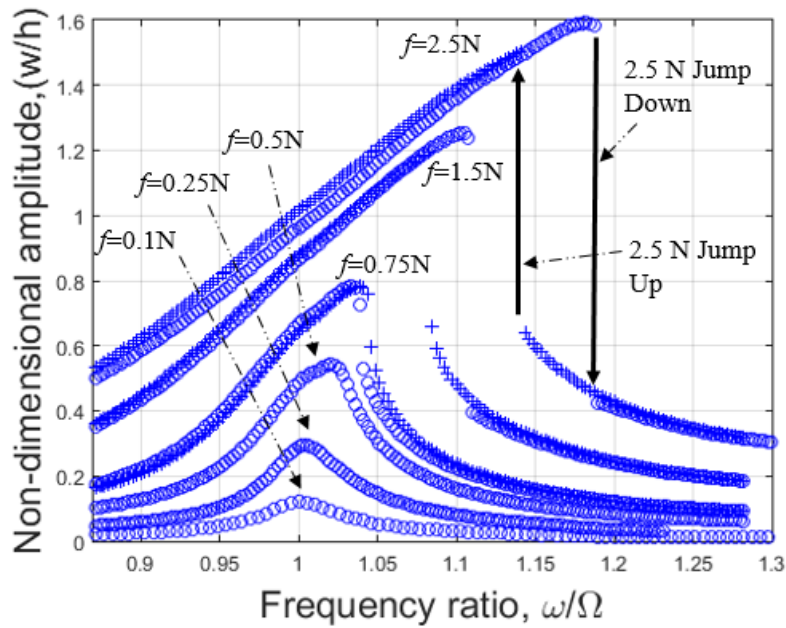
Fig. 3-8: Amplitude of the nonlinear response of the rubber plate. O, up curves (increasing excitation frequency); +, down curves (decreasing excitation frequency).
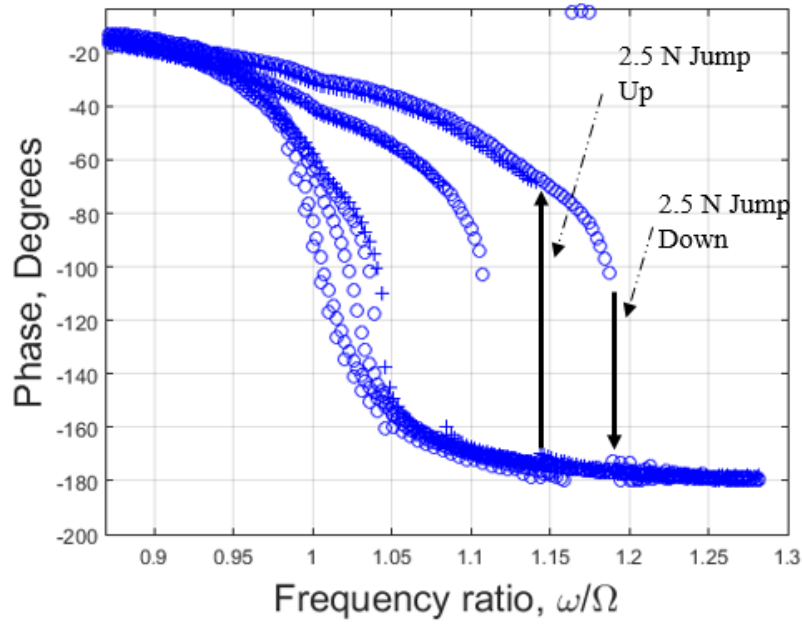
Fig. 3-9: Phase of the nonlinear response of the rubber plate. O, up curves (increasing excitation frequency); +, down curves (decreasing excitation frequency).

3.4   REDUCED ORDER MODEL (MODEL 1)

3.4.1   THEORY
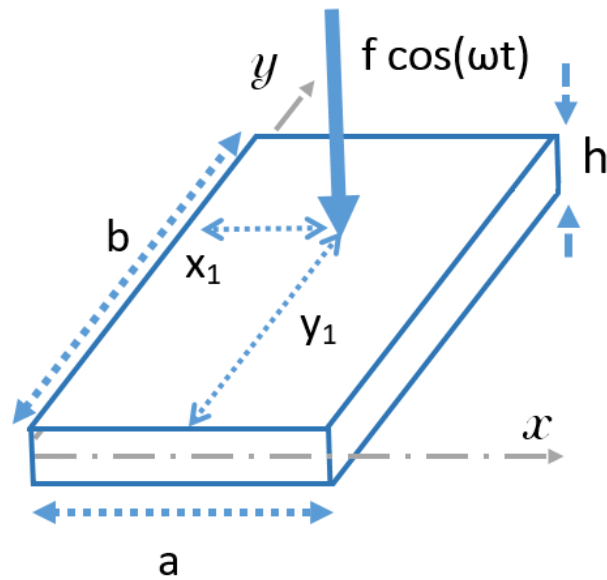
Fig. 3-10: Scheme of the rubber plate under study.

A viscoelastic rectangular plate with coordinate system ($O; x; y; z$) having the origin (O) at one corner is considered, as presented in Fig. 3-10. The plate dimensions in x and y directions are a and b, respectively, and the thickness is h. The displacements of an arbitrary point of coordinates (x,y) on the middle surface of the plate are denoted by u, v and w in the x, y and z directions, respectively. Initial geometric imperfections in z direction of the plate are denoted by w_0. Shear deformation and rotary inertia are neglected since the plate tested here is very thin ($h \ll a$, b) and their effects on the dynamics is negligible. According to the von Kármán strain-displacement relationship, the strain components ε_x, ε_y, γ_{xy} at an arbitrary point of the plate are related to the middle surface strains $\varepsilon_{x,0}$, $\varepsilon_{y,0}$, $\gamma_{xy,0}$ and to the changes of curvature and torsion of the middle surface k_x, k_y, k_{xy} by

$$\varepsilon_x = \varepsilon_{x,0} + z\,k_x, \quad \varepsilon_y = \varepsilon_{y,0} + z\,k_y, \qquad \gamma_{xy} = \gamma_{xy,0} + z\,k_{xy}, \tag{3.1}$$

$$\varepsilon_{x,0} = \frac{\partial u}{\partial x} + \frac{1}{2}\left(\frac{\partial w}{\partial x}\right)^2, \qquad \varepsilon_{y,0} = \frac{\partial v}{\partial y} + \frac{1}{2}\left(\frac{\partial w}{\partial y}\right)^2, \qquad \gamma_{xy,0} = \frac{\partial u}{\partial x} + \frac{\partial v}{\partial y} + \frac{\partial w}{\partial x}\frac{\partial w}{\partial y}, \tag{3.2}$$

$$\varepsilon_{x,0} = \frac{\partial u}{\partial x} + \frac{1}{2}\left(\frac{\partial w}{\partial x}\right)^2 + \frac{\partial w}{\partial x}\frac{\partial w_0}{\partial x}, \qquad \varepsilon_{y,0} = \frac{\partial v}{\partial y} + \frac{1}{2}\left(\frac{\partial w}{\partial y}\right)^2 + \frac{\partial w}{\partial y}\frac{\partial w_0}{\partial y},$$

$$\gamma_{xy,0} = \frac{\partial u}{\partial x} + \frac{\partial v}{\partial y} + \frac{\partial w}{\partial x}\frac{\partial w}{\partial y} + \frac{\partial w}{\partial x}\frac{\partial w_0}{\partial y} + \frac{\partial w_0}{\partial x}\frac{\partial w}{\partial y}, \tag{3.3}$$

$$k_x = -\frac{\partial^2 w}{\partial x^2}, k_y = -\frac{\partial^2 w}{\partial y^2}, k_{xy} = -2\frac{\partial^2 w}{\partial x \partial y} \tag{3.4}$$

The kinetic energy of the plate is given by

$$T = \frac{1}{2}\rho h \int_0^a \int_0^b \left(\dot{u}^2 + \dot{v}^2 + \dot{w}^2\right) \mathrm{d}x\,\mathrm{d}y \tag{3.5}$$

where ρ is the density of the plate material (kg/m^3) and the over-dot indicates the time derivative. The stress-strain relationship is assumed to be following the linear elasticity constitutive equation for plane stress

$$\begin{bmatrix} \sigma_x \\ \sigma_y \\ \tau_{xy} \end{bmatrix} = \begin{bmatrix} \dfrac{E}{1-v^2} & \dfrac{vE}{1-v^2} & 0 \\ \dfrac{vE}{1-v^2} & \dfrac{E}{1-v^2} & 0 \\ 0 & 0 & \dfrac{E}{2(1+v)} \end{bmatrix} \begin{bmatrix} \varepsilon_x \\ \varepsilon_y \\ \gamma_{xy} \end{bmatrix}, \tag{3.6}$$

where E is Young's Modulus and v is Poisson ratio. Since it is assumed that the transverse stresses are negligible, the elastic potential energy of the plate is given by

$$U_P = \frac{1}{2}\int_{-\frac{h}{2}}^{\frac{h}{2}}\int_0^a\int_0^b \left(\sigma_x \varepsilon_x + \sigma_y \varepsilon_y + \tau_{xy}\gamma_{xy}\right)\mathrm{d}x\,\mathrm{d}y\,\mathrm{d}z\ . \tag{3.7}$$

Using the constitutive eq. (3.6) and relationships eq. (3.1), the potential energy of the plate can be rewritten as

$$
\begin{aligned}
U_P &= \frac{Eh}{2(1-v^2)}\int_0^a\int_0^b\left(\varepsilon_{x,0}{}^2 + \varepsilon_{y,0}{}^2 + 2v\,\varepsilon_{x,0}\varepsilon_{y,0} + \frac{1-v}{2}\gamma_{xy,0}{}^2\right)\mathrm{d}x\,\mathrm{d}y + \\
&\quad \frac{Eh^3}{2(12(1-v^2))}\int_0^a\int_0^b\left(k_x^2 + k_y^2 + 2v\,k_x k_y + \frac{1-v}{2}k_{xy}{}^2\right)\mathrm{d}x\,\mathrm{d}y + O\left(h^4\right).
\end{aligned} \tag{3.8}
$$

The virtual work done by the external transversal harmonic force is given by

$$
\begin{aligned}
W &= \int_0^a\int_0^b f\cos\left(\omega t\right)\delta\left(x - x_1\right)\delta\left(y - y_1\right)w\,\mathrm{d}x\,\mathrm{d}y, \\
&= f\cos\left(\omega t\right)\left(w\right)_{x=x_1, y=y_1},
\end{aligned} \tag{3.9}
$$

where f is the amplitude of the harmonic point load, applied at the point ($x = x_1, y = y_1$), and δ is Dirac delta function. The non-conservative damping forces are assumed of viscous type and are taken into account by using the Rayleigh's dissipation function given

$$F = \frac{1}{2}c\int_0^a\int_0^b \left(\dot{u}^2 + \dot{v}^2 + \dot{w}^2\right)\mathrm{d}x\,\mathrm{d}y, \tag{3.10}$$

where the viscous damping coefficient c is assumed to be function of the mode shape, i.e. on the

integer numbers n and m. In particular, $c_{m,n} = 2m_{m,n}\omega_{m,n}\zeta_{m,n}$, where $m_{m,n}$, $\omega_{m,n}$ and $\zeta_{m,n}$ are the mass, the natural frequency and the damping ratio of the corresponding mode (m, n).

The boundary conditions of the considered plate are given by

$$w = N_x = N_{xy} = 0, \quad M_x = \pm k \frac{\partial w}{\partial x}, \quad \text{at } x = 0, a, \tag{3.11}$$

$$w = N_y = N_{xy} = 0, \quad M_y = \pm k \frac{\partial w}{\partial y}, \quad \text{at } y = 0, b. \tag{3.12}$$

The minus sign in eq. (3.11) and eq. (3.12) applies at the boundaries $x = a$ and $y = b$. Eq. (3.11) and eq. (3.12) give any rotational constraint from zero bending moment ($M_x = 0$ and $M_y = 0$, unconstrained rotation, obtained for $k = 0$) to zero rotation ($\partial w / \partial x = 0$ and $\partial w / \partial y = 0$, obtained as limit for $k \to \infty$), according to the value of k, where k is the stiffness per unit length of the elastic, distributed rotational springs placed at the four edges. In the present study, a very large value of k is assumed in order to approximate clamped boundary conditions for the out-of-plane displacement w, while the in-plane displacements u and v are assumed to be free at the edges.

In order to discretize the system, the mid surface displacements u, v and w are expanded by using trial functions, which satisfy the geometric boundary conditions (3.11),

$$u(x, y, t) = \sum_{m=1}^{M}\sum_{n=1}^{N} u_{m,n}(t)\cos\left(\frac{m\pi x}{a}\right)\cos\left(\frac{n\pi y}{b}\right),$$

$$v(x, y, t) = \sum_{m=1}^{M}\sum_{n=1}^{N} v_{m,n}(t)\cos\left(\frac{m\pi x}{a}\right)\cos\left(\frac{n\pi y}{b}\right), \tag{3.13}$$

$$w(x, y, t) = \sum_{m=1}^{M}\sum_{n=1}^{N} w_{m,n}(t)\sin\left(\frac{m\pi x}{a}\right)\sin\left(\frac{n\pi y}{b}\right),$$

where $u_{m,n}(t)$, $v_{m,n}(t)$ and $w_{m,n}(t)$ are the generalized coordinates and t is the time. M and N the number of terms used to expand the corresponding displacements in the two directions. The initial geometric imperfections of the plate in z direction are assumed to be given by

$$w_0(x, y) = \sum_{m=1}^{\tilde{M}}\sum_{n=1}^{\tilde{N}} A_{m,n} \sin\left(\frac{m\pi x}{a}\right)\sin\left(\frac{n\pi y}{b}\right) \tag{3.14}$$

The elastic energy accumulated by the distributed rotational springs, which ensure the rotational

constraint, can be written as

$$U_R = \frac{1}{2}\int_0^b k\left[\left(\left(\frac{\partial w}{\partial x}\right)_{x=0}\right)^2 + \left(\left(\frac{\partial w}{\partial x}\right)_{x=a}\right)^2\right]\mathrm{d}\,y + \frac{1}{2}\int_0^a k\left[\left(\left(\frac{\partial w}{\partial y}\right)_{y=0}\right)^2 + \left(\left(\frac{\partial w}{\partial y}\right)_{y=b}\right)^2\right]\mathrm{d}\,x. \quad (3.15)$$

The following notation is introduced for brevity,

$$\mathbf{q} = \left\{u_{1,1},\ldots v_{1,1},\ldots w_{1,1},\ldots w_{m,n}\right\}^{\mathrm{T}}. \quad (3.16)$$

The generic element of the time-dependent vector of the generalized coordinates $\mathbf{q}$ is referred as q_j; the dimension of $\mathbf{q}$ is equal to the number N_q of degrees of freedom used in the mode expansion. The generalized forces Q_j are obtained by differentiating the virtual work done by external forces and the Rayleigh dissipation function

$$Q_j = \frac{\partial W}{\partial q_j} - \frac{\partial F}{\partial \dot{q}_j}, \qquad \text{for } j = 1,\ldots N_q. \quad (3.17)$$

The Lagrange equations of motion are given by

$$\frac{d}{dt}\left(\frac{\partial T}{\partial \dot{q}_j}\right) - \frac{\partial T}{\partial q_j} + \frac{\partial U}{\partial q_j} = Q_j, \qquad \text{for } j = 1,\ldots N_q, \quad (3.18)$$

where, $U = U_P + U_R$. Eq. (3.18) can be rewritten in the following matrix form,

$$\mathbf{M}\ddot{\mathbf{q}} + \mathbf{C}\dot{\mathbf{q}} + \left[\mathbf{K} + \mathbf{K_2}(\mathbf{q}) + \mathbf{K_3}(\mathbf{q},\mathbf{q})\right]q = \mathbf{f}_0\cos(\omega t) \quad (3.19)$$

where $\mathbf{M}$ is the diagonal mass matrix of dimension $N_q \times N_q$; $\mathbf{C}$ is the linear viscous damping matrix, $\mathbf{K}$ is the linear stiffness matrix, $\mathbf{K_2}$ is the quadratic nonlinear stiffness terms, $\mathbf{K_3}$ denotes the cubic nonlinear stiffness terms and $\mathbf{f_0}$ is the vector representing the projection of the concentrated harmonic force on the generalized coordinates.

3.4.2 NUMERICAL IMPLEMENTATION

In order to obtain the equations of motion in a suitable form for numerical implementation, the system is multiplied by the inverse of the mass matrix and then is rewritten in the state-space form as follows,

$$\dot{\mathbf{q}} = \mathbf{y},$$
$$\dot{\mathbf{y}} = -\mathbf{M}^{-1}\mathbf{C}\mathbf{y} - \mathbf{M}^{-1}\left[\mathbf{K} + \mathbf{K}_2(\mathbf{q}) + \mathbf{K}_3(\mathbf{q},\mathbf{q})\right]\mathbf{q} + \mathbf{M}^{-1}\mathbf{f}_0\cos(\omega t). \tag{3.20}$$

The viscous damping matrix is assumed to be given by

$$\mathbf{M}^{-1}\mathbf{C} = \begin{bmatrix} 2\omega_{1,1}\zeta_{1,1} & \cdots & 0 \\ \vdots & \ddots & \vdots \\ 0 & \cdots & 2\omega_{m,n}\zeta_{m,n} \end{bmatrix}, \tag{3.21}$$

where $\omega_{m,n}$ is the natural frequency of the mode (m, n) and $\zeta_{m,n}$ is the corresponding modal damping ratio. The software *Mathematica* [85] has been used to perform the surface integrals and to obtain the $2 \times N_q$ first-order ordinary differential equations (ODEs) written in state space form, as shown in eq. (3.20). They are very long expressions containing nonlinear stiffness. Nondimensionalization of variables has been carried out for computational convenience; the vibration amplitude has been divided by the plate thickness and time has been multiplied by natural frequency. These $2 \times N_q$ first-order ODEs are solved by using the bifurcation and continuation software AUTO [7]. The AUTO software uses pseudo arc-length continuation and collocation methods to follow the solution path. It is important to note that, along with stable solutions, unstable solutions are also obtained. In particular, the analysis has been started by considering the excitation force as the bifurcation parameter, having fixed the excitation frequency far away from the resonance. The solution starts at zero amplitude of excitation and is increased slowly to reach the desired harmonic force level. Then, the solution is continued by varying the previously fixed excitation frequency, spanning the frequency range around the resonance in order to obtain the frequency-response curves.

3.4.3 RESULTS AND DISCUSSION

Initially, a linear analytical model with 507 degrees of freedom (DOFs) was developed. The storage modulus of the rubber is a function of frequency (typical of viscoelastic materials), as shown in Fig. 3-2. The storage modulus at the first natural frequency of the plate (17.1 Hz) was used as Young's modulus (51 MPa) in the model. The stiffness of the distributed rotational springs was fixed at 2000 N/rad, which was found, by convergence, analysis to accurately simulated a fixed rotation. The natural frequencies of the linear analytical model are matching

closely with the experimentally identified ones, as shown in Tab. 3-1.

In the nonlinear analysis, a reduced-order model with 39 DOFs, which are the number of terms inserted in the expansion of u, v and w given in eq. (3.13), is used. In particular, the generalized coordinates are

$$w_{1,1}, w_{3,1}, w_{5,1}, w_{7,1}, w_{1,3}, w_{3,3}, w_{5,3}, w_{7,3}, w_{1,5}, w_{3,5}, w_{5,5}, w_{1,7}, w_{3,7}, u_{2,1}, u_{4,1}, u_{6,1}, u_{8,1}, u_{2,3}, u_{4,3},$$

$$u_{6,3},\ u_{8,3}, u_{2,5}, u_{4,5}, u_{6,5}, u_{2,7}, u_{4,7}, v_{1,2}, v_{3,2}, v_{5,2}, v_{7,2}, v_{1,4}, v_{3,4}, v_{5,4}, v_{7,4}, v_{1,6}, v_{3,6}, v_{5,6}, v_{1,8}, v_{3,8}.$$

Mode $_{(\tilde{M}, \tilde{N})}$	(1,1)	(1,2)	(2,1)	(2,2)	(1,3)	(3,1)	(3,3)
$\dfrac{A_{\tilde{M},\tilde{N}}}{h}$	0.45	0.07	-0.03	-0.02	0.18	0.07	0.03

Tab. 3-2: Detailed modal expansion of the measured surface of the rubber plate.

The measured surface of rubber plate (see Fig. 3-5) was approximated using 7 fundamental modes of the plate and its respective coefficients are given in Tab. 3-2. The coefficient of the fundamental mode is $A_{1,1} = 0.45\ h$, which is much higher when compared to other modes' coefficients. Hence, the geometric imperfection of the plate was introduced in the model with the fundamental mode only in eq. (3.14) ($\tilde{M} = 1; \tilde{N} = 1$)[16]. The nonlinear vibration response was obtained by the computer program AUTO for all the six force levels (0.1, 0.25, 0.5, 0.75, 1.5 and 2.5N). Lowest two force levels show typical linear response; the damping ratio used for these two levels matches with the experimental modal analysis results ($\zeta = 0.031$). After these two force levels, the response presents nonlinearities. At the third and fourth force levels ($f=0.5$ and 0.75N), the resonance frequency (i.e. the frequency of the peak of the response) is higher than the linear natural frequency confirming the typical hardening nonlinear behaviour of plates. The linear viscous damping value was adjusted to fit each experimental response. At the last two force levels ($f=1.5$ and 2.5 N), the responses present significant hysteresis and jumps. The comparison between the model and experiments is shown in Fig. 3-11. They match well and the model captures the nonlinear response of the system accurately. It is interesting to point out that the geometric imperfection reduces the hardening behaviour of the plate [17]. The variation of

the damping ratios used to matching the response at each force level is plotted against the maximum amplitude (obtained at the peak) of vibration reached at that specific excitation in Fig. 3-12. Specifically, the damping ratios are 0.031, 0.031, 0.033, 0.036, 0.042 and 0.048 for the six force levels in the respective order. The increase of the damping ratio with the vibration amplitude confirms earlier results [1, 22, 60]. The dissipation of the system is nonlinear and needs to be taken in to account for better estimation of the nonlinear response. The increase of damping from its linear value is 60 % when the vibration amplitude is 1.6 times the thickness of the plate.
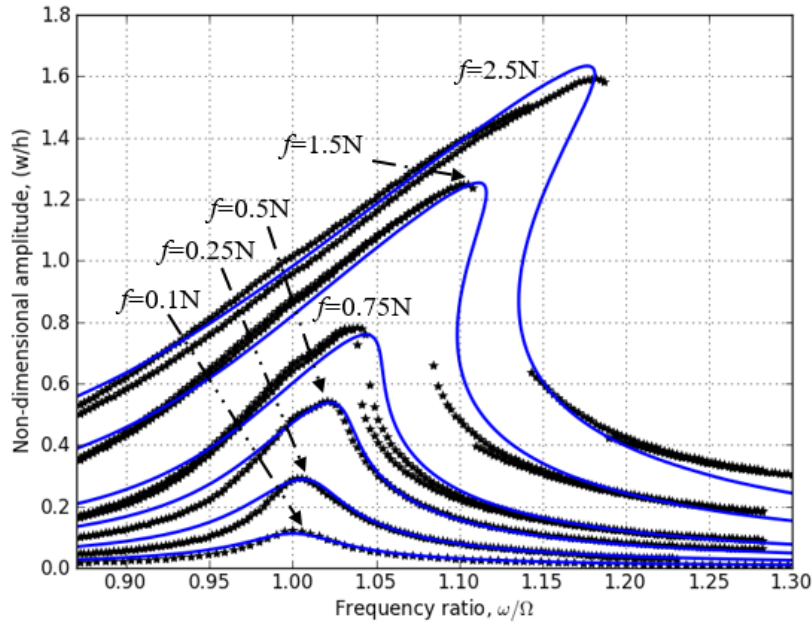
Fig. 3-11: Comparison between ROM (MODEL 1) and experimental results for the non-dimensional vibration amplitude versus the non-dimensional excitation frequency. ——, ROM; ∗, experimental data.
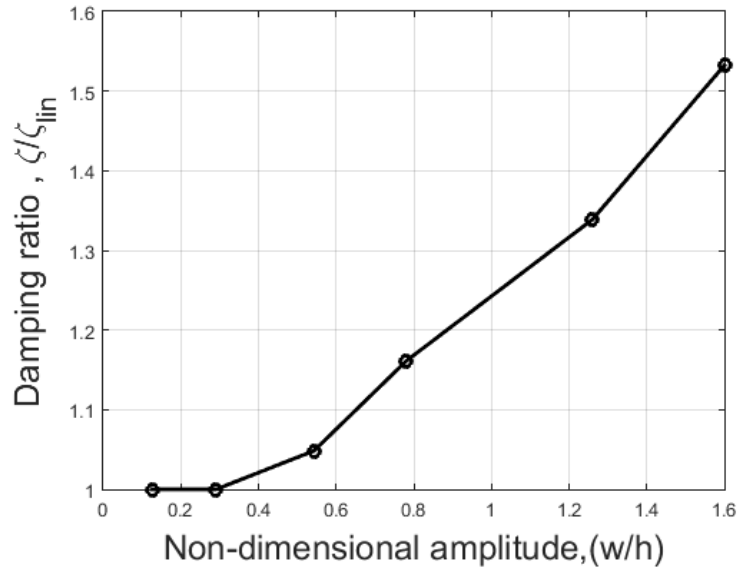
Fig. 3-12: Variation of the normalized viscous damping ratio (using MODEL 1) *versus* the vibration amplitude.

3.5 SINGLE DEGREE OF FREEDOM APPROXIMATION (MODEL 2&3)

3.5.1 PARAMETER IDENTIFICATION

The geometrically nonlinear response of a structure around its fundamental mode can be approximated as single-degree-of-freedom (SDOF) system with nonlinear stiffness, i.e. a modified Duffing oscillator [86]. This assumption is valid for many cases, including plates and panels, when no internal resonances appear. Here, two SDOF models will be considered. Model 1: SDOF with classical linear viscous damping, shown in Fig. 3-13. Model 2: SDOF with nonlinear damping represented by the loss factor, shown in Fig. 3-14. Model 1 is reduced to Model 2 when the plate is approximated with a SDOF, as both uses linear viscous damping description.
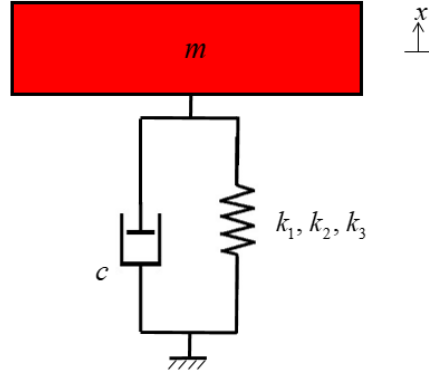
Fig. 3-13: Single degree of freedom model with linear viscous damping and geometrically nonlinear spring (MODEL 2).
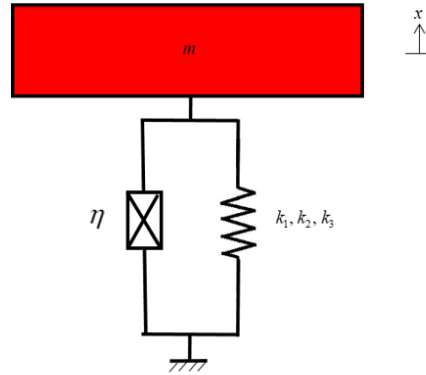
Fig. 3-14: Single degree of freedom model with dissipation represented by the loss factor (MODEL 3).

3.5.2 SDOF WITH LINEAR VISCOUS DAMPING (MODEL 2)

The equation of motion for the MODEL 2 is given by [8]

$$m\ddot{x}(t) + c\,\dot{x}(t) + k_1 x(t) + k_2 x(t)^2 + k_3 x(t)^3 = p\,f(t) \tag{3.22}$$

where, m is the modal mass, c is the viscous damping coefficient of the dashpot, k_1, k_2, k_3 are linear, quadric and cubic stiffness, respectively, $x(t)$ is displacement response, the over dot indicates differentiation with respect to time, $f(t)$ is the harmonic force and p is the modal projection coefficient (projection of the force on the mode). Various methods are available to fit experimental data to a dynamic model, and a comprehensive list can be found in [87]. Here the Temporal Method is chosen due to the availability of time domain data from experiments. As per

the method, the response and applied force is expanded using truncated Fourier series with one harmonic component as below,

$$x(t) = a_0 + a_1 \cos(\omega t) + a_2 \sin(\omega t),$$
$$f(t) = b_0 + b_1 \cos(\omega t) + b_2 \sin(\omega t),$$

(3.23)

where, a_0 is the constant part of the displacement, a_1 and a_2 are cosine and sine coefficients of the expansion, b_0 is the constant part of the force, b_1 and b_2 are cosine and sine coefficients of the expansion of the excitation force. Additional harmonic terms can be considered to improve the accuracy of the model, but they do not give any improvement in the problem studied. In fact, the feedback controller used in the experiments acts only on the first harmonic, so that higher harmonics of the excitation can appear around the resonance. This means that, any higher harmonic detected in the response could be due to nonlinearity or generated by the distorted harmonic excitation. Therefore, the higher harmonics are discharged in the present identification since affected by measurement error.

Eq. (3.23) is non-dimensionalized using the following expressions

$$\tau = \omega t, \quad \tilde{x}(t) = x(t)/h,$$

(3.24)

which give

$$\tilde{x}(\tau) = \tilde{a}_0 + \tilde{a}_1 \cos(\tau) + \tilde{a}_2 \sin(\tau),$$
$$f(\tau) = b_0 + b_1 \cos(\tau) + b_2 \sin(\tau),$$

(3.25)

where ω is the natural frequency in rad/s, t is the time in s, τ is the non-dimensional time, and the superimposed tilde indicates coefficients divided by the thickness h of the plate. Eq. (3.22) can be rewritten making use of eq. (3.24) and eq. (3.25) as,

$$m\omega^2 h\, \ddot{\tilde{x}}(\tau) + c\,\omega h\, \dot{\tilde{x}}(\tau) + k_1 h\, \tilde{x}(\tau) + k_2 h^2 \tilde{x}(\tau)^2 + k_3 h^3 \tilde{x}(\tau)^3 = p\, f(\tau).$$

(3.26)

Dividing by $k_1 h$, the above equation can be rearranged as

$$\Omega^2 \ddot{\tilde{x}}(\tau) + 2\zeta\,\Omega\,\dot{\tilde{x}}(\tau) + \tilde{x}(\tau) + \beta_2 \tilde{x}(\tau)^2 + \beta_3 \tilde{x}(\tau)^3 = \lambda f(\tau)$$

(3.27)

Where,

$$\Omega = \frac{\omega}{\omega_n}, \quad \lambda = \frac{p}{m\omega_n^2 h}, \quad \omega_n = \sqrt{\frac{k_1}{m}}, \quad c = 2\zeta m\omega_n, \quad \beta_2 = \frac{k_2}{k_1}h, \quad \beta_3 = \frac{k_3}{k_1}h^2, \qquad (3.28)$$

ω_n is the natural frequency in rad/s, ζ is the viscous damping ratio, Ω is the ratio between the excitation frequency and the natural frequency. To estimate the parameters λ and ζ, the non-dimensional nonlinear stiffness terms β_2 and β_3 are initially removed from eq. (3.27), giving

$$2\zeta \Omega \dot{\tilde{x}}(\tau) - \lambda f(\tau) = -\Omega^2 \ddot{\tilde{x}}(\tau) - \tilde{x}(\tau) \qquad (3.29)$$

Eq. (3.29) is valid for every time point. Hence, there are two unknowns and as many equations as the number n of data points for the linear experimental curves. The least square error minimization method can be employed to solve the following over constrained system and obtain ζ and λ that give the best fitting of all the linear time responses

$$\begin{bmatrix} 2\zeta \Omega \dot{\tilde{x}}(\tau_1) & -f(\tau_1) \\ 2\zeta \Omega \dot{\tilde{x}}(\tau_2) & -f(\tau_2) \\ \vdots & \vdots \\ 2\zeta \Omega \dot{\tilde{x}}(\tau_n) & -f(\tau_n) \end{bmatrix} \begin{bmatrix} \zeta \\ \lambda \end{bmatrix} = \begin{bmatrix} -\Omega^2 \ddot{\tilde{x}}(\tau_1) - \tilde{x}(\tau_1) \\ -\Omega^2 \ddot{\tilde{x}}(\tau_2) - \tilde{x}(\tau_2) \\ \vdots \\ -\Omega^2 \ddot{\tilde{x}}(\tau_n) - \tilde{x}(\tau_n) \end{bmatrix} \qquad (3.30)$$

Representing the above problem with the matrix A and two vectors X and B, the error function can be created and minimized

$$err = \| A.X - B \|^2 . \qquad (3.31)$$

Since there are two force levels that can be considered linear in the experimental data set, the average λ from these two sets of data is used for further calculations. In the analysis of the nonlinear experimental curves, the nonlinear stiffness terms are retained and ζ, β_2 and β_3 are identified using the same procedure as above, while λ has been already identified. In particular,

$$2\zeta \Omega \dot{\tilde{x}}(\tau) + \beta_2 \tilde{x}(\tau)^2 + \beta_3 \tilde{x}(\tau)^3 = \lambda f(\tau) - \Omega^2 \ddot{\tilde{x}}(\tau) - \tilde{x}(\tau) \qquad (3.32)$$

which gives

$$\begin{bmatrix} 2\zeta\Omega\,\dot{\tilde{x}}(\tau_1) & \tilde{x}(\tau_1)^2 & \tilde{x}(\tau_1)^3 \\ 2\zeta\Omega\,\dot{\tilde{x}}(\tau_2) & \tilde{x}(\tau_2)^2 & \tilde{x}(\tau_2)^3 \\ \vdots & \vdots & \vdots \\ 2\zeta\Omega\,\dot{\tilde{x}}(\tau_n) & \tilde{x}(\tau_n)^2 & \tilde{x}(\tau_n)^3 \end{bmatrix} \begin{bmatrix} \zeta \\ \beta_2 \\ \beta_3 \end{bmatrix} = \begin{bmatrix} \lambda f(\tau_1) - \Omega^2\ddot{\tilde{x}}(\tau_1) - \tilde{x}(\tau_1) \\ \lambda f(\tau_2) - \Omega^2\ddot{\tilde{x}}(\tau_2) - \tilde{x}(\tau_2) \\ \vdots \\ \lambda f(\tau_n) - \Omega^2\ddot{\tilde{x}}(\tau_n) - \tilde{x}(\tau_n) \end{bmatrix} \tag{3.33}$$

The parameter λ and the set of β_2, β_3 and ζ, identified at each force level, fully characterize the plate nonlinear response in the frequency neighbourhood of the fundamental mode.

3.5.3   LOSS FACTOR WITH A SDOF (MODEL 3)

A nonlinear SDOF with nonlinear viscoelastic dissipation described by the loss factor (MODEL 3) is represented in Fig. 3-14. The viscoelastic (or hysteretic) damping is most commonly measured by the loss tangent and applied to linear systems, for which the loss tangent coincides with the loss factor. While the loss tangent is defined in linear regime, the loss factor is defined based on the ratio of dissipated and storage energies. This makes it valid for nonlinear systems such as biological and rubber structures, because the energies can still be calculated from the force-displacement loops [75, 88]. The loss factor η, which is equal to the loss tangent $\tan\delta$ only for a linear system, is defined as

$$\eta = \frac{\Delta W_d}{2\pi W_s} \tag{3.34}$$

where ΔW_d is the energy dissipated per cycle and W_s is the storage energy, also per cycle. It is useful to recall that the specific damping capacity is instead defined as $\Psi = \Delta W_d / W_s$.
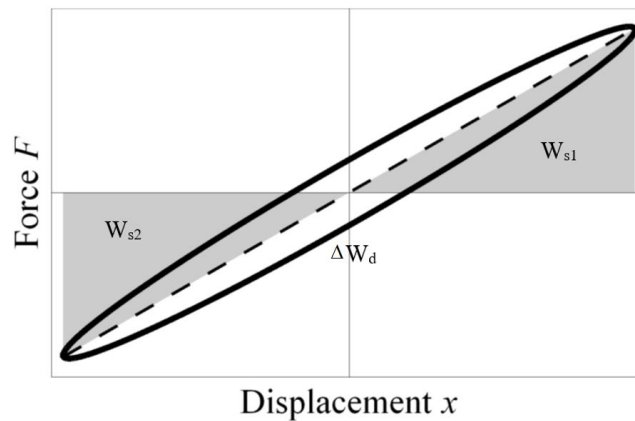
Fig. 3-15: Force-displacement loop for a linear system. The storage modulus is represented by the dashed line.
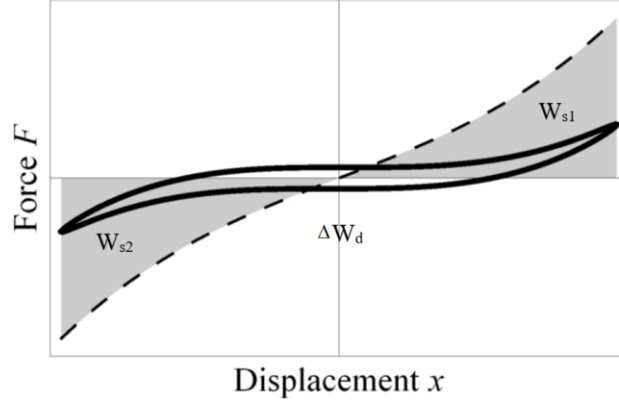
Fig. 3-16: Force-displacement loop for an hardening nonlinear system. The storage modulus is represented by the dashed curve.

The calculation of dissipated and storage energies is simple for linear systems. As shown in Fig. 3-15, both energies can be evaluated from the force and displacement data measured for a vibration cycle at any excitation frequency. The dissipated energy is represented by the area inside the force-displacement loop (thick line in Fig. 3-15). The shape of the loop is always an ellipse for linear systems. The storage energy is half of the area below the storage modulus line (shaded areas in Fig. 3-15, where the area for negative displacements is changed of sign to be positive). For linear systems, the areas W_{s1} and W_{s2} for traction and compression are the same. The storage energy is obtained as

$$W_s = \frac{W_{s1} + W_{s2}}{2} \tag{3.35}$$

$$W_s = W_{s1} = W_{s2} = \frac{1}{2}k_1 X^2 \tag{3.36}$$

where k_1 is the stiffness (or storage modulus) of the system, represented by the slope of the dashed line in Fig. 3-15, and X is the maximum displacement.

For nonlinear systems, the same procedure can be extended. The dissipated energy for nonlinear system is still represented by the area inside the force-displacement loop (thick line in Fig. 3-16).

But, because of the nonlinearities in the response, this loop may not be an ellipse anymore and can exhibit complex shapes. The force-displacement loop for a hardening nonlinear system (like a plate) is shown in Fig. 3-16 at resonance. It is important to note that, as the frequency of excitation increases, the loop rotates clockwise in the force-displacement plane, for both linear and nonlinear systems. This is due to the phase change between force and displacement as the frequency of excitation changes. Nevertheless, the area can be calculated from the experimentally measured force and displacement if enough resolution in time is used.

The storage energy of the structure can also be estimated as shown in Fig. 3-16, by extending the definition for linear systems. For nonlinear systems, the areas for negative and positive displacements can be different, especially for softening type systems. Eq. (3.35) is still valid and the storage energy can be defined as half of the area below storage modulus curve (dashed curve in Fig. 3-16). Here, for MODEL 3, the system parameters identified by MODEL 2, except the damping ratio, are used as the elastic part is common for both models. In particular, the non-dimensional nonlinear stiffness β_2 and β_3 are utilized to evaluate the non-dimensional storage energy (for convenience both storage and dissipated energy are evaluated using the non-dimensionalization introduced in eq. (3.25))

$$
\begin{aligned}
W_{s1} &= \frac{X_{max}^2}{2} + \frac{\beta_2 X_{max}^3}{3} + \frac{\beta_3 X_{max}^4}{4}, \\
W_{s2} &= \frac{X_{min}^2}{2} + \frac{\beta_2 X_{min}^3}{3} + \frac{\beta_3 X_{min}^4}{4},
\end{aligned}
\tag{3.37}
$$

where, X_{min} (negative in Fig. 3-16) and X_{max} are the non-dimensional maximum and minimum vibration amplitudes in a cycle, respectively. From the two energies, the loss factor of the system can be calculated using eq. (3.34), eq. (3.35) and eq. (3.37), which gives a measure of the nonlinear viscoelastic damping of the plate vibrating at the fundamental mode.

3.5.4   PARAMETER IDENTIFICATION PROCEDURE

An identification tool was constructed using the programming language MATLAB based on the Temporal Method. This tool makes use of the time domain data measured during the nonlinear response measurement by stepped sine tests. Typical time domain data (voltage, force,

displacement and frequency) measured from a stepped sine test at constant force excitation are shown in Fig. 3-17. It is interesting to observe that the voltage necessary to drive the electrodynamic exciter during a test varies significantly, even if the force is kept constant within ± 5 %, by the feedback controller. Therefore, keeping the voltage constant during stepped sine tests is not a good practice since it introduces different excitation levels in the same experiment. The duration of one test could be anywhere from a few minutes to a few hours, depending upon the frequency range, frequency resolution and difficulty in ensuring the force level within the tolerance specified.

During the stepped sine test, the initial frequency of excitation is chosen away from the resonance and slowly increased (UP curve) /decreased (DOWN curve) in steps while ensuring constant force via closed loop feedback. This is necessary to capture the multiple stable solutions appearing around the resonance, which is a characteristics of nonlinear systems. The force and displacement time series are chopped into time segments pertaining to one particular frequency of excitation. The number of cycles at every frequency step may vary because of the feedback control, but there are at least 80 cycles (40 cycles for eliminating the transient vibration and 40 cycles to capture the steady state vibration). Hence the tool uses the last 40 cycles for estimating the energies of the plate.
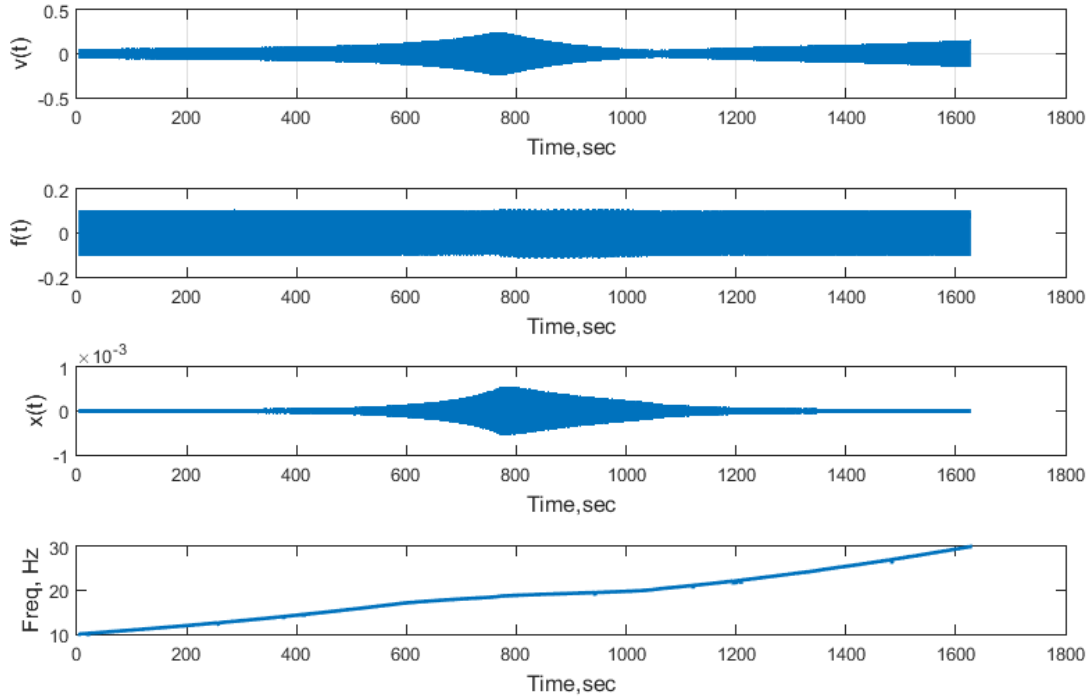
Fig. 3-17: Typical time domain data measured from a stepped sine vibration test. V(t), voltage used to drive the shaker; f(t), measured force excitation; x(t), dynamic displacement at the center of the plate; Freq., excitation frequency.

3.5.5 RESULTS AND DISCUSSION

3.5.5.1 SDOF WITH LINEAR VISCOUS DAMPING (MODEL 2)

From the measured data, the parameters defining the system are obtained using the Temporal Method. The identified parameters are given in Tab. 3-3. These parameters are inserted in eq. (3.27) and the response of the plate is calculated using integration methods and plotted against the respective experimental response in Fig. 3-18. A reasonably good agreement between the SDOF model's response and experimental data is found. The damping ratio ζ, identified using this model, is plotted against the maximum vibration amplitude and shown in Fig. 3-19. The trend and values are similar to those obtained by MODEL 1, thus reinforcing the validity of the SDOF identification tool. It is advantageous to have such a simple tool to extract the damping from experimental nonlinear response without building a complex and computationally expensive ROM as MODEL 1. However, the simple tool provided by MODEL 2 does not have such limitation and can be used to identify the damping in a nonlinear structure, as long as the

nonlinear response involves one predominant mode.

	ζ	β_2	β_3	$\tilde{\beta}_2$	$\tilde{\beta}_3$	Force, N
Model 2	0.0232					0.1
	0.0232					0.25
	0.0254					0.5
	0.0271	0	0.215	-	-	0.75
	0.032					1.5
	0.038					2.5
Model 4	0.0232	0	0.21	0	0.39	-

Tab. 3-3: Identified system parameters by Model 2 and Model 4.
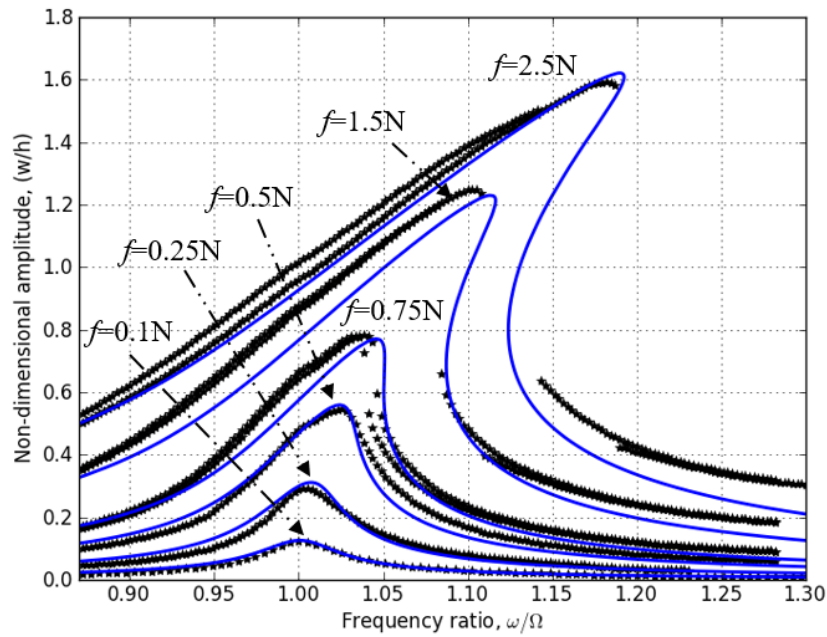
Fig. 3-18: Comparison between MODEL 2 and experimental results for the non-dimensional vibration amplitude versus the non-dimensional excitation frequency. ——, MODEL 2; *, experimental data.
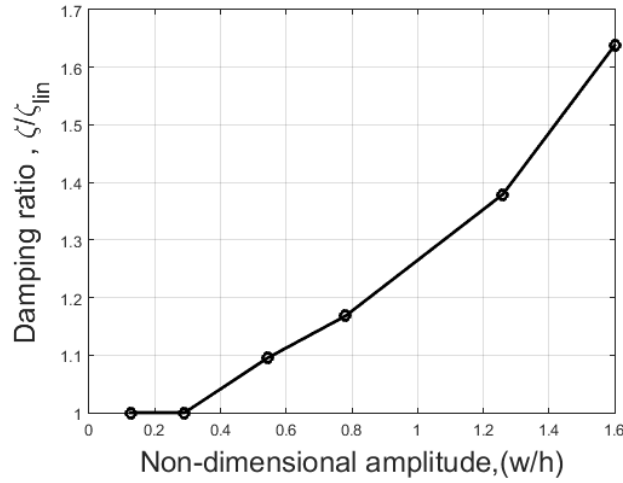
Fig. 3-19: Variation of the normalized viscous damping ratio (using MODEL 2) versus the vibration amplitude.

3.5.5.2 LOSS FACTOR IN A SDOF (MODEL 3)

The dissipated energy for the plate is shown in Fig. 3-20. The storage energy was calculated by using eq. (3.37) and plotted in Fig. 3-21. The dissipated and storage energies increase as the structure undergoes large amplitude vibrations. The loss factor calculated as the ratio of the two energies is plotted in Fig. 3-22. The loss factor of the plate for the two lowest excitation levels is not constant and decreases with the excitation frequency. It gradually drops with a constant slope and equals to twice the value of the previously identified damping ratio at the linear resonance, confirming the theory. As the plate undergoes nonlinear vibrations (from 0.5 N onwards), the loss factor coincides with the linear curves away from resonance and significantly increases as it approaches the resonance. This confirms that the dissipation energy increases more than the storage energy in large amplitude vibrations. The identified loss factor at the resonance, for each force level, is 0.048, 0.048, 0.053, 0.055, 0.061 and 0.072, from the lowest to the highest force. The loss factor increases around 50 % from its linear value.
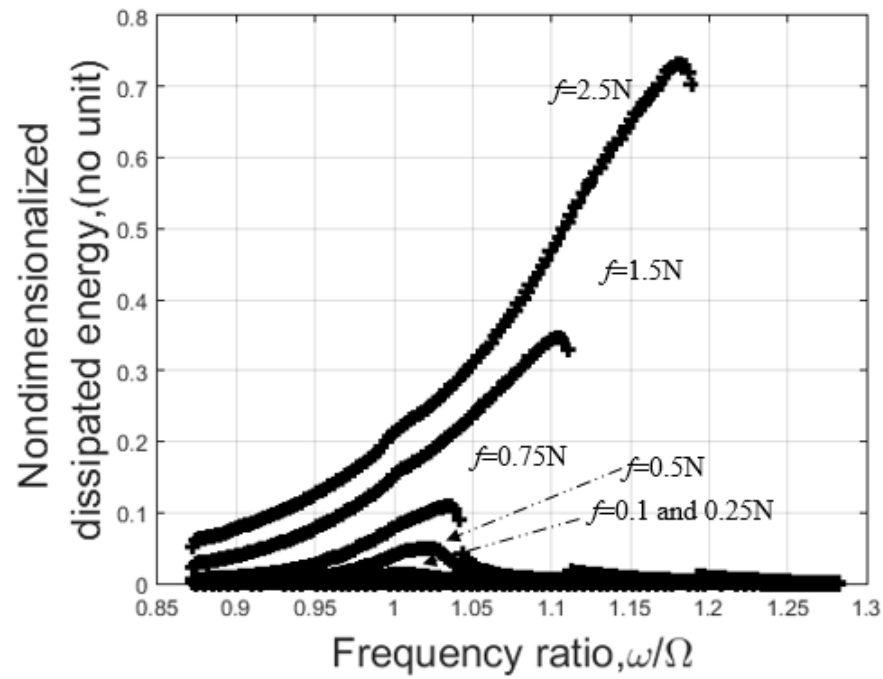
Fig. 3-20: Dissipated energy at the different harmonic force levels *versus* excitation frequency.
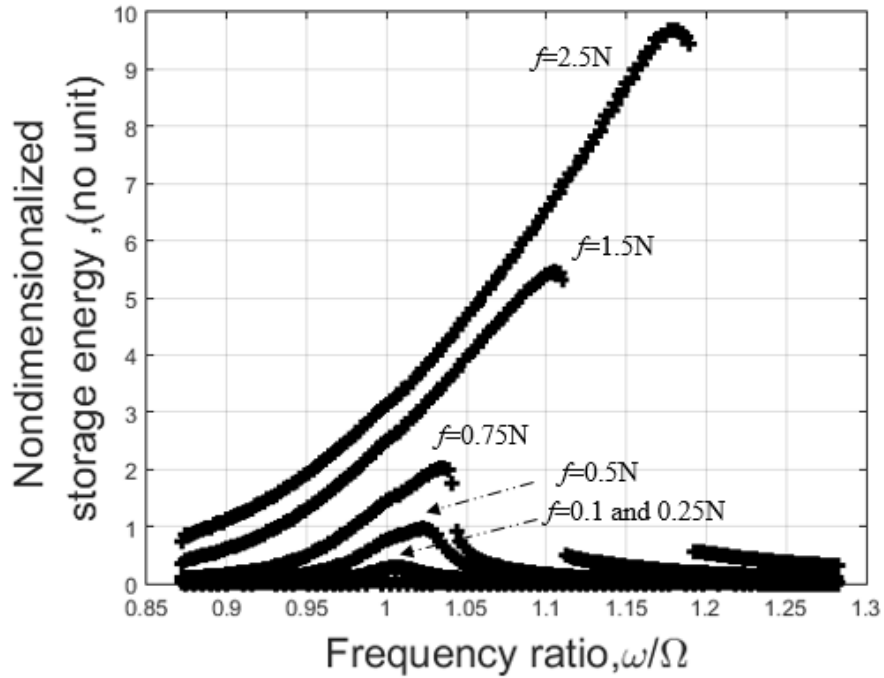
Fig. 3-21: Storage energy at the different harmonic force levels versus excitation frequency.
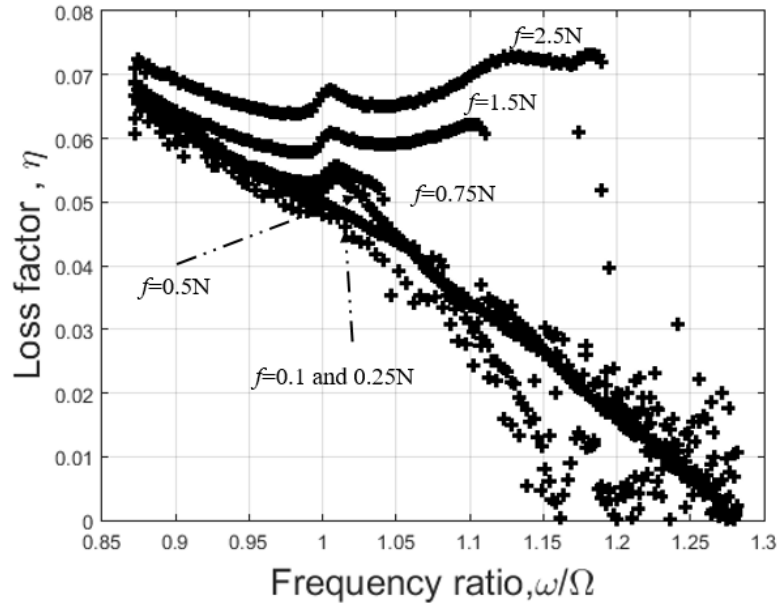
Fig. 3-22: Loss factor at the different harmonic force levels versus excitation frequency.

MODEL 3 identifies the damping at every frequency and it is based on the energy ratio of the system; so, it can be used for systems which cannot be described by simple damping models. This has the potential to be used also in highly damped, biological and rubber structures where the material is also physically nonlinear (hyperelastic and viscoelastic). The loss factor cannot be directly used as a nonlinear damping model since it is not associated to an expression to be inserted in the equation of motion, differently from the complex modulus which is its linear counterpart.

3.6 STANDARD LINEAR SOLID MODEL (MODEL 4)

The last model used to identify nonlinear damping is derived from the standard solid model of linear viscoelasticity where geometric nonlinearity is introduced in both the springs. The model is shown in Fig. 3-23.
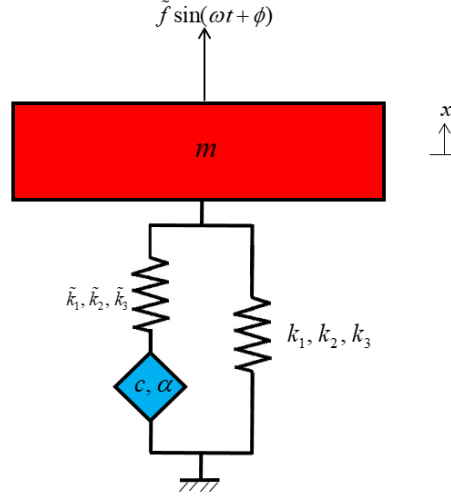
Fig. 3-23: SDOF fractional standard linear solid model with nonlinear springs (MODEL 4). The details of the formulation are given in [83]. The stress-strain relationship for the standard linear solid model is

$$\sigma + \tau_r \frac{\mathrm{d}\sigma}{\mathrm{d}t} = E_2\left(\varepsilon + \tau_r \frac{\mathrm{d}\varepsilon}{\mathrm{d}t}\right) + E_1\,\tau_r\,\frac{\mathrm{d}\varepsilon}{\mathrm{d}t} \tag{3.38}$$

where σ is the stress, ε the strain, E_1 and E_2 the Young moduli of the two springs of the mechanically equivalent model in Fig. 3-23, $\tau_r = \eta / E_1$ is the viscoelastic relaxation time constant, and η is the viscosity parameter of the dashpot. The nonlinear damping introduced by this model is proportional to $x^2\dot{x}$, which is coherent with the expression introduced in reference [60]. Detailed explanation about the identification method used can be found in [83]. The SDOF model takes the form [30]

$$\ddot{x}(t) + \frac{2\zeta\,\omega_n}{1 + \left(2\zeta\,\omega/\omega_n\right)^2}\left[\dot{x}(t) + 2\frac{\tilde{\beta}_2}{h}\,x(t)\,\dot{x}(t) + 3\frac{\tilde{\beta}_3}{h^2}\,x^2(t)\,\dot{x}(t)\right] +$$

$$\omega_n^2\left[x(t) + \frac{\beta_2}{h}\,x^2(t) + \frac{\beta_3}{h^2}\,x^3(t)\right] + \frac{\left(2\zeta\,\omega\right)^2}{1 + \left(2\zeta\,\omega/\omega_n\right)^2}$$

$$\left[\left[x(t) - \text{avg}\left(x(t)\right)\right] + \frac{\tilde{\beta}_2}{h}\left[x^2(t) - \text{avg}\left(x^2(t)\right)\right] + \frac{\tilde{\beta}_3}{h^2}\left[x^3(t) - \text{avg}\left(x^3(t)\right)\right]\right] \tag{3.39}$$

$$= \frac{p}{m}\,f\sin(\omega t),$$

where avg indicates the average value of the function in the vibration period and

$$\frac{k_1}{m} = \omega_n^2, \beta_2 = \frac{k_2\,h}{k_1}, \beta_3 = \frac{k_3\,h^2}{k_1}, \tau_r = \frac{2\zeta}{\omega_n}, \tag{3.40}$$

$$\tilde{k}_1 = k_1, \tilde{\beta}_2 = \frac{\tilde{k}_2\,h}{k_1}, \tilde{\beta}_3 = \frac{\tilde{k}_3\,h^2}{k_1} \tag{3.41}$$

β_2, β_3, $\tilde{\beta}_2$, $\tilde{\beta}_3$ are the non-dimensional nonlinear stiffness coefficients of the two geometrically nonlinear springs. It can be observed that the stiffness in eq. (3.39) is a function of the vibration frequency ω, which also matches with the experimental results in Fig. 3-2 and Fig. 3-3 for the silicone material.

3.6.1 RESULTS AND DISCUSSION

The response from the model and experimental data are shown in Fig. 3-24. The close agreement between them confirms the accurate identification of nonlinear damping variation present in the experimental measurements. The identified parameters are given in Tab. 3-3. The quadratic and cubic stiffness terms are extremely between MODEL 2 and 4. The linear viscous damping of the MODEL 4 is identical to the experimental damping ratio. The single value description of damping covering the linear and nonlinear regime is particularly significant as it eliminates the necessity to adjust the damping depending upon the vibration amplitude.
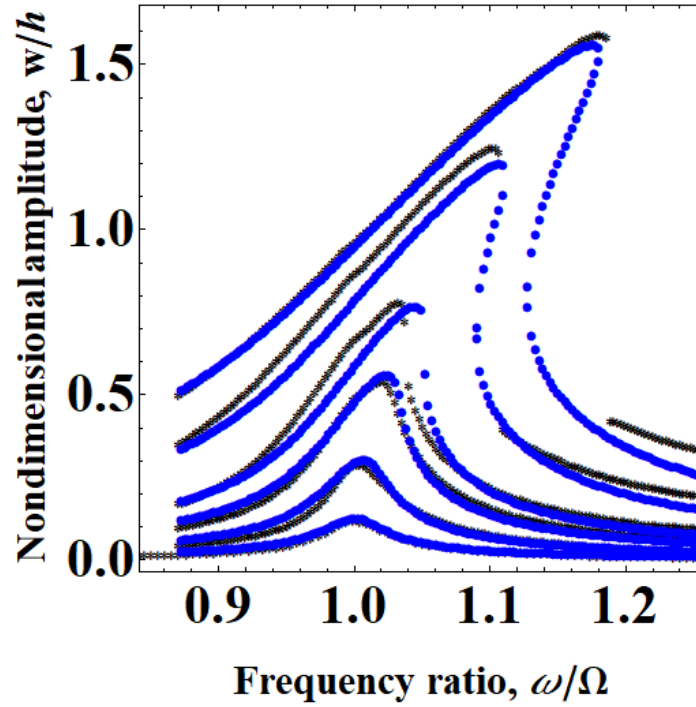
Fig. 3-24: Comparison between MODEL 4 and experimental results for the non-dimensional vibration amplitude versus the non-dimensional excitation frequency. •, MODEL 4; ∗, experimental data.

3.7 COMPARISON OF ALL MODELS

Comparison of all the three models' response with the experimental response is shown in Fig. 3-25 for the highest force level (2.5 N). It can be seen that all three models identify the nonlinear stiffness of the rubber plate during large amplitude vibrations very well. All three models are appropriate to model nonlinear stiffness exhibited by plates and shells during large amplitude vibrations. However, for MODEL 1 and MODEL 2, the damping value needs to be adjusted during large amplitude vibrations to correctly estimate the maximum vibration amplitude experienced by the structure. This is not the case for the MODEL 4, as the damping model is inherently nonlinear and captures the nonlinear damping variation shown by the plate with good accuracy.
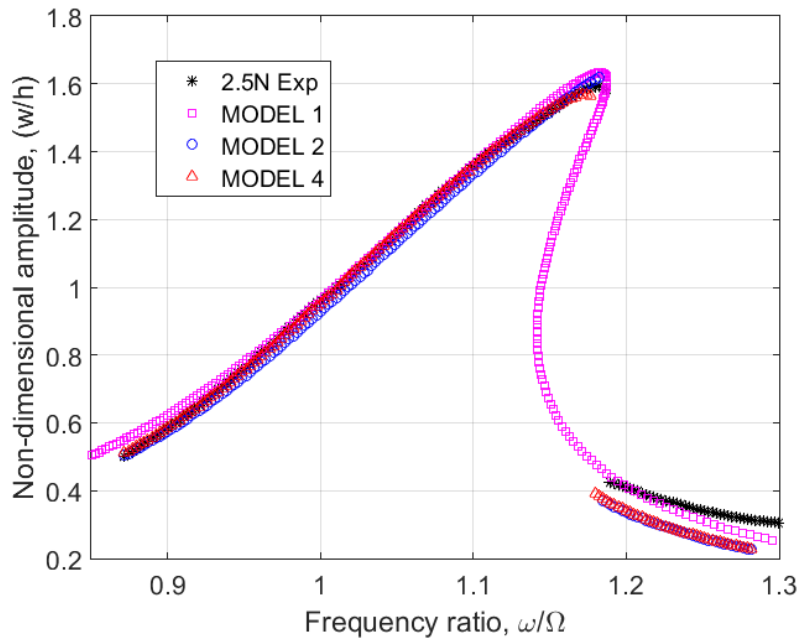
Fig. 3-25: Comparison between experimental and all three numerical models' responses at 2.5N. ∗, experimental data; □ − MODEL 1; o - MODEL 2; Δ - MODEL 4.
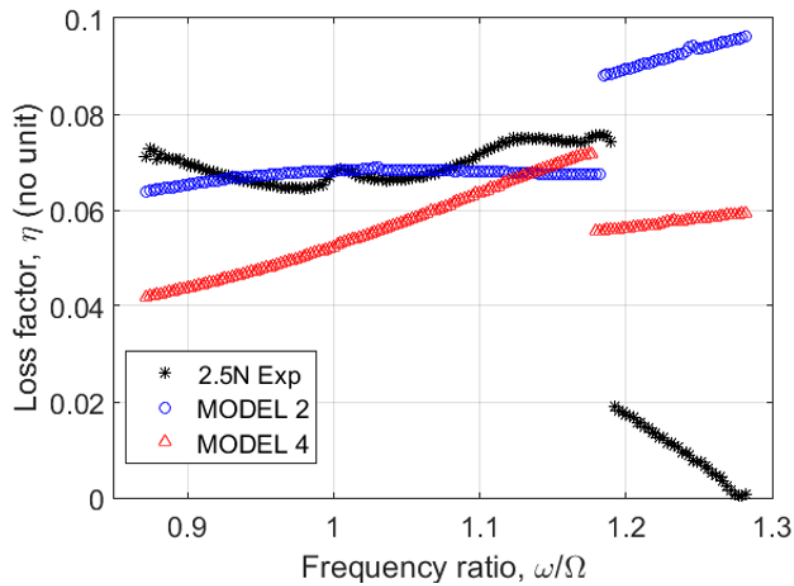
Fig. 3-26: Comparison between loss factors calculated using different models at 2.5N. ∗, experimental data; o - MODEL 2; Δ - MODEL 4.

Experimentally identified loss factors are compared with loss factors calculated from the numerical time response of Model 2 and Model 4 and shown in Fig. 3-26 (for 2.5N force only).

The area inside the force-displacement loop was calculated from the time response of both models from the eq. (3.27) and eq. (3.39). It can be noticed that the loss factors are similar between all three models only around the resonance of the plate. The trend of loss factors away from resonance is completely different from the numerical and experimentally obtained values. This could be acceptable as the influence of damping on the structure's response is only around the resonance. Away from resonance, mass and stiffness of the structure play dominant role. However, the structure's damping can be modelled using a generalized Maxwell model to match the experimental values at all frequencies. This is left a future study.

3.8   CONCLUSIONS

As the practical importance of understanding damping in large amplitude vibrations grows, several applicable damping descriptions were compared to the reference case of the damping identification based on a reduced order model with linear viscous damping. Experiments were performed on a square rubber plate made of silicone to measure its nonlinear response and consequently capture its nonlinear damping, which increases with the excitation level. State-of-the-art experimental techniques were used with success to record the nonlinear response of the structure, which features a hardening behaviour. A non-contact measurement of the plate profile was also performed to take into account geometric imperfections in the model. The reduced order model captures the nonlinear dynamics of the rubber plate very well. The damping values estimated by matching the peak amplitude of the experimental response at each force level show nonlinear variation, confirming earlier studies. The increase of damping is found to be around 60% when the vibration amplitude is 1.6 times the plate thickness. Three SDOF models were fit to the experimental data, each one with a different damping description. All the three procedures are capable to identify the linear and nonlinear response and damping of the plate. If viscous damping is considered, the damping value has to be increased with the forcing amplitude since the damping description cannot take into account the nonlinear variation. The loss factor does not provide a damping model per se, but the identified results clearly show and larger increase of the dissipated energy, with respect to the storage energy, in case of large amplitude vibrations. The standard linear solid model with geometrically nonlinear springs, originally introduced by Amabili [21, 30], introduces a nonlinear damping model which is capable to reproduce

numerical results in agreement with experiments for the full range of harmonic force excitation investigated without any need to adjust the dissipation parameters. It can be concluded that the MODEL 4 is preferred to model the nonlinear stiffness and nonlinear damping of any panel structure during large amplitude vibrations.

3.9 ACKNOWLEDGEMENTS

4   NONLINEAR DAMPING USING STANDARD LINEAR SOLID MODEL

From the previous studies, it was apparent that the SLS material model captures the nonlinear damping variation very well during large amplitude vibrations based on a SDOF model approximation. So, a complete MDOF model based on the Lagrange method was developed based on the SLS material model. The damping of the hard silicone plate was estimated accordingly. The experimental results agree well with the numerical response ensuring that the model captures nonlinear stiffness and nonlinear damping very well. In addition to the comparison of numerical and experimental frequency-amplitude responses, for the first time, experimental and numerical dissipated and stored energies were compared and found to be in good agreement. It can be concluded that the SLS model is best suited for modeling damping and stiffness variation of viscoelastic structures. The results of this study are submitted to an international journal and the manuscript is given below.

Nonlinear Fractional Damping and Frequency-Depending Storage Modulus in Nonlinear Vibrations of Viscoelastic Rectangular Plates

Marco Amabili, **Prabakaran Balasubramanian**, Giovanni Ferrari

Department of Mechanical Engineering, McGill University
817 Sherbrooke Street West, Montreal, Canada H3A 0C3

4.1   ABSTRACT

Damping is largely increasing with the vibration amplitude during nonlinear vibrations of rectangular plates. At the same time, soft materials present an increase of their stiffness with the vibration frequency. These two phenomena appear together and are both explained in the framework of the viscoelasticity. While the literature on nonlinear vibrations of plates is very large, these aspects are rarely touched. The present study uses the fractional solid model to describe the viscoelastic material behaviour. This allows to capture at the same time (i) the increase in the storage modulus with the vibration frequency and (ii) the frequency-dependent nonlinear damping in nonlinear vibrations of rectangular plates. The solution of the nonlinear vibration problems is obtained through Lagrange equations by deriving the potential energy of

the plate and the dissipated energy, both geometrically nonlinear and frequency-dependent. The model is then applied to a silicone rubber rectangular plate tested experimentally. The plate was glued to a metal frame and harmonically excited by stepped sine testing at different force levels and the vibration response was measured by a laser Doppler vibrometer. The comparison of numerical and experimental results very was satisfactorily carried out for: (i) nonlinear vibration responses in the frequency and time domain at different excitation levels, (ii) dissipated energy versus excitation frequency and excitation force, (iii) storage energy and (iv) loss factor, which is particularly interesting to evaluate the plate dissipation versus frequency at different excitation levels. Finally, the linear and nonlinear damping terms are compared.

4.2 INTRODUCTION

Nonlinear vibrations of rectangular plates received significant attention in the literature [5, 12, 14, 16, 17, 89-93]. A rectangular plate is a strongly hardening system, which can be transformed to an initially softening system, turning to hardening for larger vibration amplitudes, in case of geometric imperfections of amplitude confrontable with the plate thickness. The geometric nonlinearity gives quadratic and cubic nonlinear stiffness terms in the equations of motion; the cubic terms are largely prevalent on the quadratic ones for perfectly flat plates and plates with small imperfections. Boundary conditions have a strong effect on the nonlinear vibration response of plates [16, 93].

The literature on nonlinear vibrations of viscoelastic plates is small but very interesting [29-31, 94-104]. These studies utilize viscoelastic material models of different complexity (Kelvin-Voigt; standard linear solid, which is also named Zener model; fractional Zener model) to address dynamic problems of plates retaining geometric nonlinearity. Even if some of these investigations derived nonlinear damping (e.g., [31]), this is or proportional to the stiffness or not proved to be capable to reproduce the nonlinear damping experimentally observed in nonlinear vibrations of plates.

The problem of nonlinear damping during nonlinear vibrations of different systems was very scarcely approached in the literature [59, 60, 82, 105-107]. Gottlieb and his co-workers [59, 82] introduced phenomenological nonlinear damping of the type $x^2\dot{x}$, where x is the displacement of a characteristic point of the system. The same nonlinear damping term was successfully applied

to simulate nonlinear damping in nano-systems (Eichler et al., [60]). A similar nonlinear damping was obtained as effect of two combined dashpots inclined respect to each other (Jeong et al., [106]). However, a different nonlinear damping of the type $\dot{x}^3$ was also proposed (Elliot, Ghandchi Tehrani & Langley [64]). In order to clarify these discrepancies and to find a justification to the phenomenological damping previously introduced, Amabili [108] derived the nonlinear damping for a single-degree-of-freedom system undergoing nonlinear vibrations by using a fractional solid viscoelastic model. Numerical and experimental results for three difference systems matched very well. This study was extended (Amabili, [109]) to obtain a differential expression of the nonlinear damping for easy numerical implementation; experiments for free-edge boundary conditions were added to verify the formulation with a system without energy escape at the boundaries. Nonlinear damping for rectangular plates was derived from linear viscoelasticity by Amabili [108] in case of small damping and frequency-independent stiffness and validated for a supported stainless-steel plate.

Experiments are fundamental to identify linear and nonlinear damping coefficients since, differently from stiffness, they cannot be modelled with accuracy at the present level of knowledge. Some studies present forced nonlinear vibration experiments at different excitation levels that allow to identify the equivalent viscous linear damping ratios [1, 2, 22, 58, 59, 64, 69]. They show that an increasing damping is necessary to match the system response at larger excitation.

Damping is largely increasing with the vibration amplitude during nonlinear vibrations of continuous systems. At the same time, soft materials present an increase of their stiffness with the vibration frequency. These two phenomena appear together and are both explained in the framework of the viscoelasticity.

The present study starts from the approach developed by Amabili [108] to introduce geometrically nonlinear damping in rectangular plates but uses the more refined fractional solid model to describe the viscoelastic material behaviour. This allows to capture at the same time (i) the increase in the storage modulus with the vibration frequency and (ii) the frequency-dependent nonlinear damping in nonlinear vibrations of rectangular plates. The solution of the nonlinear vibration problems is obtained through Lagrange equations by deriving the potential energy of the plate and the dissipated energy, both geometrically nonlinear and frequency-

dependent. The model is then applied to a silicone rubber rectangular plate. The plate was glued to a metal frame and harmonically excited by stepped sine testing at different force levels and the vibration response was measured by a laser Doppler vibrometer. The comparison of numerical and experimental results was very satisfactorily carried out for: (i) nonlinear vibration responses in the frequency and time domain at different excitation levels, (ii) dissipated energy versus excitation frequency and excitation force, (iii) storage energy and (iv) loss factor, which is particularly interesting to evaluate the plate dissipation versus frequency at different excitation levels. Finally, the linear and nonlinear damping terms are compared.

4.3 VISCOELASTIC MATERIAL AND CONSTITUTIVE EQUATION

The fractional linear solid material is described by the mechanical model shown in Fig. 4-1, where the E and E_1 stiffness moduli appear as springs, as well as a spring-pot [110], which is something in-between a spring and a dashpot, with coefficient of viscosity η measured in (N s m^{-2}). The ordinary differential constitutive equation describing the viscoelastic standard linear solid material is [93, 111, 112]

$$\sigma + \tau_r^\alpha \frac{\mathrm{d}^\alpha \sigma}{\mathrm{d}t^\alpha} = E\left(\varepsilon + \tau_r^\alpha \frac{\mathrm{d}^\alpha \varepsilon}{\mathrm{d}t^\alpha}\right) + E_1 \tau_r^\alpha \frac{\mathrm{d}^\alpha \varepsilon}{\mathrm{d}t^\alpha} \tag{4.1}$$

in which σ is the stress, $\tau_r = \eta / E_1$ is the retardation time, t is time and ε is the strain.
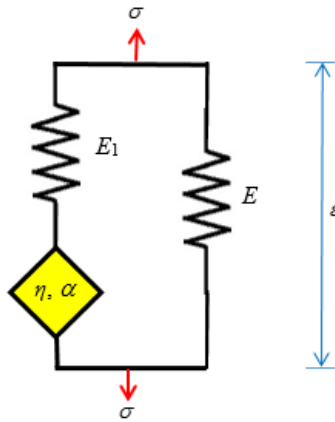
Fig. 4-1: Fractional linear solid model.

In particular, E is the Young's modulus of the material and E_1 is the additional dynamic modulus in the sense that, for extremely fast strain and for $\alpha = 1$ in the spring-pot (i.e. in case of pure dashpot), the material storage modulus is given by $E + E_1$. On the other hand, after an infinite relaxation time, the residual stiffness is simply the Young's modulus E. In eq. (4.1), $D_t^\alpha = \mathrm{d}^\alpha / \mathrm{d}t^\alpha$ is the fractional derivative operator of order α, where $0 < \alpha \leq 1$. It is assumed that the system dynamic response $x(t)$ is a periodic forced vibration, that can be represented by (i) a constant component, (ii) a fundamental harmonic component of frequency ω identical to the excitation frequency and (iii) its super-harmonics. In nonlinear vibrations, it means that quasi-periodic and chaotic dynamics cannot be represented by this description. Under this hypothesis, the Weyl fractional derivative (West, Bologna & Grigolini, [113]), see Appendix A, is conveniently used since it is developed for periodic functions, i.e. for steady-state vibrations, and does not involve a hereditary integral.

The harmonic balance is initially used to find the solution of eq. (4.1). Then, a more general differential formulation is introduced. For this reason, just zero-order (constant) and first-order terms are retained in the harmonic balance formulation since the solution is then reformulated in a more general way. Also, being eq. (4.1) a linear differential equation, the introduction of higher-order terms in the harmonic balance method do not alter the zero-order and first-order terms. The stress and strain linked by eq. (4.1) for a fractional viscoelastic material can be transformed into

$$\varepsilon(t) = \varepsilon_0 + \varepsilon_1 \sin(\omega t) + ... \tag{4.2}$$

$$\sigma(t) = \sigma_0 + \sigma_{1s} \sin(\omega t) + \sigma_{1c} \cos(\omega t) + ... \tag{4.3}$$

in which ω is the oscillation frequency and ε_0, ε_1, σ_0, σ_{1s}, σ_{1c} are unknown coefficients to be obtained. The Weyl fractional derivative of order α gives (see Appendix A – Section 4.12)

$$D_t^\alpha \sin(\omega t) = \omega^\alpha \left[\cos\left(\alpha \frac{\pi}{2} \right) \sin(\omega t) + \sin\left(\alpha \frac{\pi}{2} \right) \cos(\omega t) \right] \tag{4.4}$$

that shows a component in-phase with $\sin(\omega t)$ and an orthogonal component at 90° phase. In

eq. (4.4), the in-phase component disappears in case of $\alpha = 1$, i.e. for the classical first derivative. Eq. (4.2) and eq. (4.3) are substituted into eq. (4.1), making use of eq. (4.4); this gives

$$
\begin{aligned}
&\sigma_0 + \sigma_{1s}\sin(\omega t) + \sigma_{1c}\cos(\omega t) + \tau_r^\alpha \omega^\alpha \left\{ \sigma_{1s}\left[\cos(\alpha\pi/2)\sin(\omega t) + \sin(\alpha\pi/2)\cos(\omega t)\right] \right. \\
&\left. + \sigma_{1c}\left[\cos(\alpha\pi/2)\cos(\omega t) - \sin(\alpha\pi/2)\sin(\omega t)\right] \right\} = E\varepsilon_0 + E\varepsilon_1\sin(\omega t) \\
&+ (E+E_1)\tau_r^\alpha \omega^\alpha \varepsilon_1 \left[\cos(\alpha\pi/2)\sin(\omega t) + \sin(\alpha\pi/2)\cos(\omega t)\right].
\end{aligned}
\tag{4.5}
$$

The zero-order terms give

$$
\sigma_0 = E\varepsilon_0
\tag{4.6}
$$

and the first-order terms produce the following equations:

$$
\sigma_{1s} + \tau_r^\alpha \omega^\alpha \left[\sigma_{1s}\cos(\alpha\pi/2) - \sigma_{1c}\sin(\alpha\pi/2)\right] = E\varepsilon_1 + (E+E_1)\tau_r^\alpha \omega^\alpha \varepsilon_1 \cos(\alpha\pi/2);
\tag{4.7}
$$

$$
\sigma_{1c} + \tau_r^\alpha \omega^\alpha \left[\sigma_{1s}\sin(\alpha\pi/2) + \sigma_{1c}\cos(\alpha\pi/2)\right] = (E+E_1)\tau_r^\alpha \omega^\alpha \varepsilon_1 \sin(\alpha\pi/2);
\tag{4.8}
$$

The solution of the system of eq. (4.7) and eq. (4.8) is

$$
\sigma_{1s} = E\varepsilon_1 + \frac{\tau_r^{2\alpha}\omega^{2\alpha} + \tau_r^\alpha \omega^\alpha \cos(\alpha\pi/2)}{1 + \tau_r^{2\alpha}\omega^{2\alpha} + 2\tau_r^\alpha \omega^\alpha \cos(\alpha\pi/2)} E_1\varepsilon_1;
\tag{4.9}
$$

$$
\sigma_{1c} = \frac{\tau_r^\alpha \omega^\alpha \sin(\alpha\pi/2)}{1 + \tau_r^{2\alpha}\omega^{2\alpha} + 2\tau_r^\alpha \omega^\alpha \cos(\alpha\pi/2)} E_1\varepsilon_1;
\tag{4.10}
$$

Eq. (4.6) and eq. (4.9) can be combined into

$$
\sigma = \sigma_0 + \sigma_{1s}\sin(\omega t) + \sigma_{1c}\cos(\omega t) = E\varepsilon + \frac{\tau_r^{2\alpha}\omega^{2\alpha}(\varepsilon - \varepsilon_0) + \tau_r^\alpha D_t^\alpha \varepsilon}{1 + \tau_r^{2\alpha}\omega^{2\alpha} + 2\tau_r^\alpha \omega^\alpha \cos(\alpha\pi/2)} E_1
\tag{4.11}
$$

Without making use of the harmonic balance truncation, it is possible to verify that eq. (4.11) represents the particular solution of the differential eq. (4.1). It is convenient to identify two contributions in the stress σ: the elastic contribution

$$
\sigma_E = E\varepsilon
\tag{4.12}
$$

and the viscoelastic contribution σ_V, which is possible to divide in three terms

$$
\sigma_{E_1} = \frac{\tau_r^{2\alpha}\omega^{2\alpha}(\varepsilon - \varepsilon_0)}{1 + \tau_r^{2\alpha}\omega^{2\alpha} + 2\tau_r^\alpha \omega^\alpha \cos(\alpha\pi/2)} E_1
\tag{4.13}
$$

$$\sigma_{V_I} + \sigma_{V_O} = \frac{\tau_r^{\alpha} D_t^{\alpha} \varepsilon}{1 + \tau_r^{2\alpha} \omega^{2\alpha} + 2\tau_r^{\alpha} \omega^{\alpha} \cos(\alpha \pi / 2)} E_1 \tag{4.14}$$

The contribution in eq. (4.13) presents a stress in phase with the strain. On the other hand, eq. (4.14) is linked to the fractional derivative and, as shown by eq. (4.4), can be subdivided into a component in phase with ε, σ_{V_I}, and a component orthogonal to it, named σ_{V_O}. It is clear that

$$\sigma = \sigma_E + \sigma_V = \sigma_E + \sigma_{E_1} + \sigma_{V_I} + \sigma_{V_O} \tag{4.15}$$

The retardation time constant is linked to the damping ratio ζ traditionally used in vibration analysis by

$$\tau_{r_i} = \frac{1}{\omega_i} \left[\frac{2\zeta_i}{\sin(\alpha \pi/2)} \right]^{1/\alpha} \tag{4.16}$$

in which ζ_i is the damping ratio of the corresponding i-th natural mode and ω_i represents the associated natural frequency of the system. This is particularly significant since the retardation time coefficients $\tau_{r,i}$ take different values for each mode shape considered; this is the same of what observed for the damping ratios. As an extension of this, the retardation time is a function of the vibration shape of the system.

4.4 POTENTIAL AND DISSIPATED ENERGY OF A PLATE
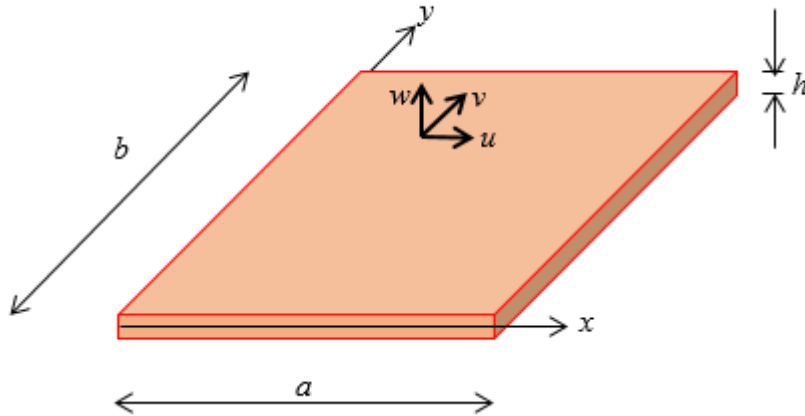
Fig. 4-2: Rectangular plate: coordinate system, dimensions and displacements of a point.

A rectangular coordinate system (O; *x, y, z*) with origin O placed at one corner of a rectangular viscoelastic plate is shown in Fig. 4-2. The material of the plate respects the fractional viscoelastic law introduced by eq. (4.1) and is homogeneous and isotropic. A thin plate is considered: rotary inertia and shear deformation are neglected. The displacements of a middle-surface point of the plate are denoted as *u, v* and *w* in the *x, y* and *z* directions, respectively. The plate is assumed to have initial geometric imperfections in the transverse direction *z* described by the function w_0; these are considered associated to an initial zero stress state. A thin plate approximation makes use of the assumption $\sigma_z = \sigma_{xz} = \sigma_{yz} = 0$. The link between elastic stresses and strains is given by [93],

$$\sigma_{x,E} = \frac{E}{1-v^2}\left(\varepsilon_x + v\,\varepsilon_y\right); \tag{4.17}$$

$$\sigma_{y,E} = \frac{E}{1-v^2}\left(\varepsilon_y + v\,\varepsilon_x\right); \tag{4.18}$$

$$\tau_{xy,E} = \frac{E}{2(1+v)}\gamma_{xy}; \tag{4.19}$$

in which v is the Poisson ratio and E is the Young's modulus, which is the frequency-independent part of storage modulus (see Fig. 4-1). Making use of eq. (4.15), the viscoelastic stresses $\sigma_{x,V}$, $\sigma_{y,V}$ and $\tau_{xy,V}$ are linked to the strains by

$$\sigma_{x,V} = \frac{E_1}{1-v^2}\frac{\tau_r^{2\alpha}\omega^{2\alpha}\left(\varepsilon_x + v\varepsilon_y - \bar{\varepsilon}_x - v\bar{\varepsilon}_y\right) + \tau_r^{\alpha}D_t^{\alpha}\left(\varepsilon_x + v\varepsilon_y\right)}{1+\tau_r^{2\alpha}\omega^{2\alpha} + 2\tau_r^{\alpha}\omega^{\alpha}\cos(\alpha\pi/2)}; \tag{4.20}$$

$$\sigma_{y,V} = \frac{E_1}{1-v^2}\frac{\tau_r^{2\alpha}\omega^{2\alpha}\left(\varepsilon_y + v\varepsilon_x - \bar{\varepsilon}_y - v\bar{\varepsilon}_x\right) + \tau_r^{\alpha}D_t^{\alpha}\left(\varepsilon_y + v\varepsilon_x\right)}{1+\tau_r^{2\alpha}\omega^{2\alpha} + 2\tau_r^{\alpha}\omega^{\alpha}\cos(\alpha\pi/2)}; \tag{4.21}$$

$$\tau_{xy,V} = \frac{E_1}{2(1+v)}\frac{\tau_r^{2\alpha}\omega^{2\alpha}\left(\gamma_{xy} - \bar{\gamma}_{xy}\right) + \tau_r^{\alpha}D_t^{\alpha}\gamma_{xy}}{1+\tau_r^{2\alpha}\omega^{2\alpha} + 2\tau_r^{\alpha}\omega^{\alpha}\cos(\alpha\pi/2)}; \tag{4.22}$$

where E_1 is the additional dynamic modulus and $\bar{\varepsilon}_x$, $\bar{\varepsilon}_y$ and $\bar{\gamma}_{xy}$ are the zero-order (average value) strains. Eq. (4.20), (4.21) and (4.22) have been generalized to the plate from the single-

dimensional standard linear solid model. According to eq. (4.16), the retardation time coefficient varies with the mode shape. A base of low-frequency natural vibration mode shapes is used to discretize the plate displacements. Since the strains are related to the displacements, they are also discretized with the same base. Strains are quadratic functions of the generalized modal coordinates $q_i(t)$, which are time functions, and have the following expression

$$\varepsilon = \sum_{i=1}^{N} a_i\, q_i(t) f_i(x) g_i(y) + \sum_{i=1}^{N} \sum_{j=1}^{N} a_{i,j}\, q_i(t) q_j(t) f_i(x) f_j(x) g_i(y) g_j(y) \tag{4.23}$$

where a_i and $a_{i,j}$ are the coefficients of the linear and quadratic terms, respectively, $f_i(x) g_i(y)$ is the vibration shape of the i-th mode and the integer N represents the number of degrees of freedom utilized to discretize the plate. Quadratic terms appear in eq. (4.23) due to geometric nonlinearity. The time derivative of eq. (4.23) takes the form

$$D_t^\alpha \varepsilon = \sum_{i=1}^{N} a_i\, D_t^\alpha \left[q_i(t) \right] f_i(x) g_i(y) + \sum_{i=1}^{N} \sum_{j=1}^{N} 2a_{i,j}\, D_t^\alpha \left[q_i(t) \right] q_j(t) f_i(x) f_j(x) g_i(y) g_j(y) \tag{4.24}$$

where the symmetry of the coefficients a_{ij} was used to simplify eq. (4.24). A generic viscoelastic stress σ_V, which is added to the elastic stresses σ_E in eq. (4.15), can be expressed by three contributions

$$
\begin{aligned}
\sigma_{E_l} =\ & \frac{E_1}{1-v^2} \left\{ \sum_{i=1}^{N} \frac{\tau_{r_i}^{2\alpha} \omega^{2\alpha}}{1 + \tau_{r_i}^{2\alpha} \omega^{2\alpha} + 2\tau_{r_i}^{\alpha} \omega^{\alpha} \cos(\alpha\,\pi/2)} b_i \left[q_i(t) - \overline{q_i(t)} \right] f_i(x) g_i(y) \right. \\
& \left. + \sum_{i=1}^{N} \sum_{j=1}^{N} b_{i,j} \frac{\tau_{r_{i,j}}^{2\alpha} \omega^{2\alpha}}{1 + \tau_{r_{i,j}}^{2\alpha} \omega^{2\alpha} + 2\tau_{r_{i,j}}^{\alpha} \omega^{\alpha} \cos(\alpha\,\pi/2)} \left[q_i(t) q_j(t) - \overline{q_i(t) q_j(t)} \right] f_i(x) f_j(x) g_i(y) g_j(y) \right\},
\end{aligned}
\tag{4.25}
$$

$$
\begin{aligned}
\sigma_{V_l} + \sigma_{V_o} =\ & \frac{E_1}{1-v^2} \left\{ \sum_{i=1}^{N} \frac{\tau_{r_i}^{\alpha}}{1 + \tau_{r_i}^{2\alpha} \omega^{2\alpha} + 2\tau_{r_i}^{\alpha} \omega^{\alpha} \cos(\alpha\,\pi/2)} c_i\, D_t^\alpha \left[q_i(t) \right] f_i(x) g_i(y) \right. \\
& \left. + \sum_{i=1}^{N} \sum_{j=1}^{N} \frac{\tau_{r_{i,j}}^{\alpha}}{1 + \tau_{r_{i,j}}^{2\alpha} \omega^{2\alpha} + 2\tau_{r_{i,j}}^{\alpha} \omega^{\alpha} \cos(\alpha\,\pi/2)} 2c_{i,j}\, D_t^\alpha \left[q_i(t) \right] q_j(t) f_i(x) f_j(x) g_i(y) g_j(y) \right\},
\end{aligned}
\tag{4.26}
$$

where b_i, c_i are coefficients of the linear terms, $b_{i,j}$ and $c_{i,j}$ are coefficients of the quadratic terms and $\overline{q_i(t)}$ are the average values of the generalized coordinates in the time period; $\tau_{r,i}$ and $\tau_{r,ij}$ are the retardation time coefficients, functions of the integers i and i,j, respectively, which

indicate the corresponding mode shape. The coefficient $\tau_{r,i}$ is linked to the linear mode shape $f_i(x)g_i(y)$, while $\tau_{r,ij}$ is linked to the quadratic mode shape $f_i(x)f_j(x)g_i(y)g_j(y)$, which represents a surface very different in shape from $f_i(x)g_i(y)$.

No linear coupling between the transverse bending and in-plane stretching is observed whiting the hypothesis of thin isotropic plates. The variation of the potential energy U_P of a rectangular plate, considering σ_z negligible under Kirchhoff's hypotheses, is given by the following three contributions:

$$\delta U_E = \int_0^a \int_0^b \int_{-h/2}^{h/2} \left(\sigma_{xE}\, \delta\varepsilon_x + \sigma_{yE}\, \delta\varepsilon_y + \tau_{xyE}\, \delta\gamma_{xy} \right) dx\, dy\, dz \tag{4.27}$$

$$\delta U_{E_1} = \int_0^a \int_0^b \int_{-h/2}^{h/2} \left(\sigma_{xE_1}\, \delta\varepsilon_x + \sigma_{yE_1}\, \delta\varepsilon_y + \tau_{xyE_1}\, \delta\gamma_{xy} \right) dx\, dy\, dz \tag{4.28}$$

$$\delta U_{V_I} = \int_0^a \int_0^b \int_{-h/2}^{h/2} \left(\sigma_{xV_I}\, \delta\varepsilon_x + \sigma_{yV_I}\, \delta\varepsilon_y + \tau_{xyV_I}\, \delta\gamma_{xy} \right) dx\, dy\, dz \tag{4.29}$$

in which a and b indicate the in-plane dimensions in the x and y directions, respectively, h represents the plate thickness, and the symbol δ is used here for the functional derivative. The potential energy of the plate is

$$U_P = U_E + U_{E_1} + U_{V_I} \tag{4.30}$$

The virtual work developed by the non-conservative viscous stresses is given by the following expression:

$$\delta W_{V_O} = \int_0^a \int_0^b \int_{-h/2}^{h/2} \left(\sigma_{xV_O}\, \delta\varepsilon_x + \sigma_{yV_O}\, \delta\varepsilon_y + \tau_{xyV_O}\, \delta\gamma_{xy} \right) dx\, dy\, dz \tag{4.31}$$

By using eq. (4.23), eq. (4.25) and eq. (4.28) gives

$$U_{E_1} = \frac{1}{2}\frac{E_1}{1-v^2}\int_0^a\int_0^b\int_{-h/2}^{h/2}\left\{\left[\sum_{i=1}^N\frac{\tau_{r_i}^{2\alpha}\omega^{2\alpha}}{1+\tau_{r_i}^{2\alpha}\omega^{2\alpha}+2\tau_{r_i}^{\alpha}\omega^{\alpha}\cos(\alpha\pi/2)}\tilde{b}_i\left[q_i(t)-\overline{q_i(t)}\right]f_i(x)g_i(y)\right.\right.$$

$$+\sum_{i=1}^N\sum_{j=1}^N\frac{\tau_{r_{i,j}}^{2\alpha}\omega^{2\alpha}}{1+\tau_{r_{i,j}}^{2\alpha}\omega^{2\alpha}+2\tau_{r_{i,j}}^{\alpha}\omega^{\alpha}\cos(\alpha\pi/2)}\tilde{b}_{i,j}\left[q_i(t)q_j(t)-\overline{q_i(t)q_j(t)}\right]f_i(x)f_j(x)g_i(y)g_j(y)\right] \quad (4.32)$$

$$\times\left[\sum_{i=1}^N\tilde{a}_i\,q_i(t)f_i(x)g_i(y)+\sum_{i=1}^N\sum_{j=1}^N\tilde{a}_{i,j}\,q_i(t)q_j(t)f_i(x)f_j(x)g_i(y)g_j(y)\right]dx\,dy\,dz,$$

which gives

$$U_{E_1} = \frac{1}{2}\frac{E_1}{1-v^2}\int_0^a\int_0^b\int_{-h/2}^{h/2}\left\{\sum_{i=1}^N\sum_{k=1}^N\frac{\tau_{r_i}^{2\alpha}\omega^{2\alpha}}{1+\tau_{r_i}^{2\alpha}\omega^{2\alpha}+2\tau_{r_i}^{\alpha}\omega^{\alpha}\cos(\alpha\pi/2)}\left[d_{i,k}\left[q_i(t)-\overline{q_i(t)}\right]q_k(t)\,f_i(x)f_k(x)g_i(y)g_k(y)\right.\right.$$

$$+\sum_{l=1}^N d_{i,k,l}\left[q_i(t)-\overline{q_i(t)}\right]q_k(t)q_l(t)f_i(x)f_k(x)f_l(x)g_i(y)g_k(y)g_l(y)\right]$$

$$+\sum_{i=1}^N\sum_{j=1}^N\sum_{k=1}^N\frac{\tau_{r_{i,j}}^{2\alpha}\omega^{2\alpha}}{1+\tau_{r_{i,j}}^{2\alpha}\omega^{2\alpha}+2\tau_{r_{i,j}}^{\alpha}\omega^{\alpha}\cos(\alpha\pi/2)} \quad (4.33)$$

$$\left[e_{i,j,k}\left[q_i(t)q_j(t)-\overline{q_i(t)q_j(t)}\right]q_k(t)f_i(x)f_j(x)f_k(x)g_i(y)g_j(y)g_k(y)\right.$$

$$+\sum_{l=1}^N e_{i,j,k,l}\left[q_i(t)q_j(t)-\overline{q_i(t)q_j(t)}\right]q_k(t)q_l(t)f_i(x)f_j(x)f_k(x)f_l(x)g_i(y)g_j(y)g_k(y)g_l(y)\right]\right\}dx\,dy\,dz,$$

where $d_{i,k}$, $d_{i,k,l}$, $e_{i,j,k}$ and $e_{i,j,k,l}$ are coefficients. The quadratic coefficients $d_{i,k}$ are associated to τ_{r_i}, the cubic coefficients $d_{i,k,l}$ and $e_{i,j,k}$ are linked to τ_{r_i} and $\tau_{r_{i,j}}$, and the quartic coefficients $e_{i,j,k,l}$ are associated to $\tau_{r_{i,j}}$. The tilde superimposed to the coefficients is used in eq. (4.32) since eq. (4.28) is more general than the integral of the multiplication of eq. (4.23) and eq. (4.25). Eq. (4.32) and eq. (4.33) show the structure of eq. (4.28).

Similarly,

$$U_{V_I}+W_{V_O} = \frac{E_1}{1-v^2}\int_0^a\int_0^b\int_{-h/2}^{h/2}\left\{\left[\sum_{i=1}^N\frac{\tau_{r_i}^{\alpha}}{1+\tau_{r_i}^{2\alpha}\omega^{2\alpha}+2\tau_{r_i}^{\alpha}\omega^{\alpha}\cos(\alpha\pi/2)}\tilde{c}_i\,D_t^{\alpha}\left[q_i(t)\right]f_i(x)g_i(y)\right.\right.$$

$$+\sum_{i=1}^N\sum_{j=1}^N\frac{\tau_{r_{i,j}}^{\alpha}}{1+\tau_{r_{i,j}}^{2\alpha}\omega^{2\alpha}+2\tau_{r_{i,j}}^{\alpha}\omega^{\alpha}\cos(\alpha\pi/2)}2\tilde{c}_{i,j}\,D_t^{\alpha}\left[q_i(t)\right]q_j(t)f_i(x)f_j(x)g_i(y)g_j(y)\right] \quad (4.34)$$

$$\times\left[\sum_{i=1}^N\tilde{a}_i\,q_i(t)f_i(x)g_i(y)+\sum_{i=1}^N\sum_{j=1}^N\tilde{a}_{i,j}\,q_i(t)q_j(t)f_i(x)f_j(x)g_i(y)g_j(y)\right]dx\,dy\,dz,$$

Which gives

$$
\begin{aligned}
U_{V_I} + W_{V_O} = \frac{E_1}{1-v^2} \int_0^a \int_0^b \int_{-h/2}^{h/2} \Bigg\{ & \sum_{i=1}^N \sum_{k=1}^N \frac{\tau_{r_i}^\alpha}{1+\tau_{r_i}^{2\alpha}\omega^{2\alpha}+2\tau_{r_i}^\alpha\omega^\alpha \cos(\alpha\pi/2)} \Bigg[f_{i,k} D_t^\alpha [q_i(t)] q_k(t) f_i(x) f_k(x) g_i(y) g_k(y) \\
& + \sum_{l=1}^N f_{i,k,l} D_t^\alpha [q_i(t)] q_k(t) q_l(t) f_i(x) f_k(x) f_l(x) g_i(y) g_k(y) g_l(y) \Bigg] \\
& + \sum_{i=1}^N \sum_{j=1}^N \sum_{k=1}^N \frac{\tau_{r_{i,j}}^\alpha}{1+\tau_{r_{i,j}}^{2\alpha}\omega^{2\alpha}+2\tau_{r_{i,j}}^\alpha\omega^\alpha \cos(\alpha\pi/2)} \Bigg[2g_{i,j,k} D_t^\alpha [q_i(t)] q_j(t) q_k(t) f_i(x) f_j(x) f_k(x) g_i(y) g_j(y) g_k(y) \\
& + \sum_{l=1}^N 2g_{i,j,k,l} D_t^\alpha [q_i(t)] q_j(t) q_k(t) q_l(t) f_i(x) f_j(x) f_k(x) f_l(x) g_i(y) g_j(y) g_k(y) g_l(y) \Bigg] \Bigg\} dx\,dy\,dz,
\end{aligned}
$$

(4.35)

where $f_{i,k}$, $f_{i,k,l}$, $g_{i,j,k}$ and $g_{i,j,k,l}$ are coefficients.

The strain-displacement relationships from the von Kármán nonlinear plate theory are applied. The components ε_x, ε_y and γ_{xy} of the strain at a generic point of the plate are linked to the middle-surface strains $\varepsilon_{x,0}$, $\varepsilon_{y,0}$, $\gamma_{xy,0}$ and to the curvature and torsion of the middle plane k_x, k_y and k_{xy} by

$$
\varepsilon_x = \varepsilon_{x,0} + z\,k_x; \qquad \varepsilon_y = \varepsilon_{y,0} + z\,k_y; \qquad \gamma_{xy} = \gamma_{xy,0} + z\,k_{xy};
$$

(4.36)

in which z represents the distance of the point from the plate middle plane.

Making use of eq. (4.19-4.21) and (4.36), eq. (4.28) can be written as

$$
\begin{aligned}
U_{E_1} = & \frac{1}{2}\frac{E_1 h}{1-v^2} \int_0^a \int_0^b \frac{\tau_r^{2\alpha}\omega^{2\alpha}}{1+\tau_r^{2\alpha}\omega^{2\alpha}+2\tau_r^\alpha\omega^\alpha \cos(\alpha\pi/2)} \Bigg(\varepsilon_{x,0}^2 + \varepsilon_{y,0}^2 + 2v\,\varepsilon_{x,0}\varepsilon_{y,0} + \frac{1-v}{2}\gamma_{xy,0}^2 - \varepsilon_{x,0}\bar{\varepsilon}_{x,0} - \varepsilon_{y,0}\bar{\varepsilon}_{y,0} \\
& - v\,\varepsilon_{x,0}\bar{\varepsilon}_{y,0} - v\,\varepsilon_{y,0}\bar{\varepsilon}_{x,0} - \frac{1-v}{2}\gamma_{xy,0}\bar{\gamma}_{xy,0} \Bigg) dx\,dy + \frac{1}{2}\frac{E_1 h^3}{12(1-v^2)} \int_0^a \int_0^b \frac{\tau_r^{2\alpha}\omega^{2\alpha}}{1+\tau_r^{2\alpha}\omega^{2\alpha}+2\tau_r^\alpha\omega^\alpha \cos(\alpha\pi/2)} \\
& \times \Bigg(k_x^2 + k_y^2 + 2v\,k_x k_y + \frac{1-v}{2}k_{xy}^2 - k_x \bar{k}_x - k_y \bar{k}_y - v\,k_x \bar{k}_y - v\,k_y \bar{k}_x - \frac{1-v}{2}k_{xy}\bar{k}_{xy} \Bigg) dx\,dy.
\end{aligned}
$$

(4.37)

Different values of the retardation time coefficients must be used in eq. (4.37) for different shape functions.

Similarly,

$$U_{V_I} + W_{V_O} = \frac{E_1 h}{1-v^2} \int_0^a \int_0^b \frac{\tau_r^\alpha}{1+\tau_r^{2\alpha}\omega^{2\alpha}+2\tau_r^\alpha\omega^\alpha\cos(\alpha\pi/2)} \Big(\varepsilon_{x,0} D_t^\alpha(\varepsilon_{x,0}) + \varepsilon_{y,0} D_t^\alpha(\varepsilon_{y,0}) + v\varepsilon_{x,0} D_t^\alpha(\varepsilon_{y,0})$$

$$+v D_t^\alpha(\varepsilon_{x,0})\varepsilon_{y,0} + \frac{1-v}{2}\gamma_{xy,0} D_t^\alpha(\gamma_{xy,0}) \Big) dx\,dy + \frac{E_1 h^3}{12(1-v^2)} \int_0^a \int_0^b \frac{\tau_r^\alpha}{1+\tau_r^{2\alpha}\omega^{2\alpha}+2\tau_r^\alpha\omega^\alpha\cos(\alpha\pi/2)} \quad (4.38)$$

$$\times \Big(k_x D_t^\alpha(k_x) + k_y D_t^\alpha(k_y) + v k_x D_t^\alpha(k_y) + v D_t^\alpha(k_x)k_y + \frac{1-v}{2}k_{xy} D_t^\alpha(k_{xy}) \Big) dx\,dy + O(h^4).$$

The elastic energy of the plate is written as

$$U_E = \frac{1}{2}\frac{E h}{1-v^2} \int_0^a \int_0^b \Big(\varepsilon_{x,0}^2 + \varepsilon_{y,0}^2 + 2v\varepsilon_{x,0}\varepsilon_{y,0} + \frac{1-v}{2}\gamma_{xy,0}^2 \Big) dx\,dy$$

$$+ \frac{1}{2}\frac{E h^3}{12(1-v^2)} \int_0^a \int_0^b \Big(k_x^2 + k_y^2 + 2v k_x k_y + \frac{1-v}{2}k_{xy}^2 \Big) dx\,dy + O(h^4). \qquad (4.39)$$

The first term in eq. (4.39) is the membrane energy, followed by the bending energy. Eq. (4.37) can be obtained from eq. (4.39) as

$$U_{E_1} = \frac{\tau_r^{2\alpha}\omega^{2\alpha}}{1+\tau_r^{2\alpha}\omega^{2\alpha}+2\tau_r^\alpha\omega^\alpha\cos(\alpha\pi/2)}\frac{E_1}{E}(U_E - \bar{U}_E) \qquad (4.40)$$

where $\bar{U}_E$ is defined as

$$\bar{U}_E = \frac{1}{2}\frac{E h}{1-v^2} \int_0^a \int_0^b \Big(\varepsilon_{x,0}\bar{\varepsilon}_x + \varepsilon_{y,0}\bar{\varepsilon}_y + v\varepsilon_{x,0}\bar{\varepsilon}_y + v\varepsilon_{y,0}\bar{\varepsilon}_x + \frac{1-v}{2}\gamma_{xy,0}\bar{\gamma}_{xy} \Big) dx\,dy$$

$$+ \frac{1}{2}\frac{E h^3}{12(1-v^2)} \int_0^a \int_0^b \Big(k_x\bar{k}_x + k_y\bar{k}_y + v k_x\bar{k}_y + v k_y\bar{k}_x + \frac{1-v}{2}k_{xy}\bar{k}_{xy} \Big) dx\,dy. \qquad (4.41)$$

Eq. (4.38) can be obtained from eq. (4.39) as

$$U_{V_I} + W_{V_O} = \frac{\tau_r^\alpha}{1+\tau_r^{2\alpha}\omega^{2\alpha}+2\tau_r^\alpha\omega^\alpha\cos(\alpha\pi/2)}\frac{E_1}{E}D_t^\alpha(U_E) \qquad (4.42)$$

It must be considered that, in eq. (4.40) and eq. (4.42), τ_r must be inserted inside the double integrals and then it takes a different value according to the associated shape function.

4.5   SYSTEM DISCRETIZATION

The displacements of an arbitrary point on the middle plane of the plate in x, y and z directions are denoted u, v and w, respectively. The boundary conditions for simply supported rectangular plates with movable edges and additional rotational distributed springs at the four edges are (Amabili [93])

$$w = v = N_x = 0, \quad M_x = k_t \, \partial w / \partial x \quad \text{at } x = 0, a, \tag{4.43}$$

$$w = u = N_y = 0, \quad M_y = k_t \, \partial w / \partial y \quad \text{at } y = 0, b, \tag{4.44}$$

where N_x and N_y are the in-plane force resultants per unit length, and M_x and M_y are the moment resultants; they are given by (Amabili [93])

$$\left\{ \begin{matrix} N_x \\ M_x \end{matrix} \right\} = \int_0^h \sigma_x \left\{ \begin{matrix} 1 \\ z \end{matrix} \right\} \mathrm{d}z \tag{4.45}$$

$$\left\{ \begin{matrix} N_y \\ M_y \end{matrix} \right\} = \int_0^h \sigma_y \left\{ \begin{matrix} 1 \\ z \end{matrix} \right\} \mathrm{d}z \tag{4.46}$$

In eq. (4.43) and (4.44), k_t is the stiffness of the elastic distributed rotational springs (N/rad) at the panel edges; a zero rotational stiffness is obtained for k_t=0 (simply supported movable edges), while completely rotational constrained boundaries are obtained for $k_t \rightarrow \infty$, which corresponds to $\partial w / \partial x = \partial w / \partial y = 0$.

The middle plane displacements u, v and w are expanded in series of trigonometric trial functions to discretize the system. They identically satisfy the geometric boundary conditions (4.43) and (4.44) (Amabili [93])

$$u(x, y, t) = \sum_{m=1}^{\tilde{M}} \sum_{n=1}^{\tilde{N}} u_{m,n}(t) \cos(m \pi x / a) \, \sin(n \pi y / b);$$

$$v(x, y, t) = \sum_{m=0}^{\tilde{M}} \sum_{n=0}^{\tilde{N}} v_{m,n}(t) \sin(m \pi x / a) \, \cos(n \pi y / b); \tag{4.47}$$

$$w(x, y, t) = \sum_{m=0}^{\hat{M}} \sum_{n=0}^{\hat{N}} w_{m,n}(t) \, \sin(m \pi x / a) \sin(n \pi y / b),$$

where m and n indicate the integer numbers of half-waves in x and y directions, respectively, and

t is time; $u_{m,n}(t)$, $v_{m,n}(t)$ and $w_{m,n}(t)$ are functions of time representing the generalized coordinates. $\tilde{M}$ and $\tilde{N}$ indicate the number of terms necessary in the series expansion of the in-plane displacements u and v; they are larger than $\hat{M}$ and $\hat{N}$ that indicate the number of terms in the series of w.

Geometric imperfections of the plate are assumed to be present only in the z direction since the plate is thin. Zero initial stress is considered associated to the initial imperfections. It is also assumed $w_0 = 0$ at the four edges (perfectly flat edges), i.e. the imperfection in normal direction w_0 is represented by a double sine Fourier series

$$w_0(x, y) = \sum_{m=1}^{\bar{M}} \sum_{n=1}^{\bar{N}} A_{m,n} \sin(m\pi x / a) \sin(n\pi y / b), \tag{4.48}$$

where $A_{m,n}$ are the coefficients of the Fourier series; the integers $\bar{N}$ and $\bar{M}$ indicate the number of terms. Natural boundary conditions (4.43) and (4.44) are not satisfied by eq. (4.47). They do not need to be satisfied in an energy approach. However, if they are satisfied, the convergence of the solution is obtained with a smaller number of terms in the expansions (4.47). Eliminating null terms at the panel edges, eq. (4.43) and (4.44) can be rewritten as

$$
\begin{aligned}
\hat{u}(t) = &-\sum_{n=1}^{\hat{N}} \sum_{m=1}^{\hat{M}} (m\pi / a) \left\{ \frac{1}{2} w_{m,n}(t) \sin(n\pi y / b) \sum_{k=1}^{\hat{N}} \sum_{s=1}^{\hat{M}} \frac{s}{m+s} w_{s,k}(t) \sin(k\pi y / b) \right. \\
&\times \sin\left[(m+s)\pi x / a\right] + w_{m,n}(t) \sin(n\pi y / b) \sum_{j=1}^{\tilde{N}} \sum_{i=1}^{\tilde{M}} \frac{i}{m+i} \\
&\left. \times A_{i,j} \sin(j\pi y / b) \sin\left[(m+i)\pi x / a\right] \right\}, ; \\
\hat{v}(t) = &-\sum_{n=1}^{\hat{N}} \sum_{m=1}^{\hat{M}} (n\pi / b) \left\{ \frac{1}{2} w_{m,n}(t) \sin(m\pi x / a) \sum_{k=1}^{\hat{N}} \sum_{s=1}^{\hat{M}} \frac{k}{n+k} w_{s,k}(t) \sin(s\pi x / a) \right. \\
&\times \sin\left[(n+k)\pi y / b\right] + w_{m,n}(t) \sin(m\pi x / a) \sum_{j=1}^{\tilde{N}} \sum_{i=1}^{\tilde{M}} \frac{j}{n+j} \\
&\left. \times A_{i,j} \sin(i\pi x / a) \sin\left[(n+j)\pi y / b\right] \right\},
\end{aligned}
\tag{4.49}
$$

where $\hat{u}$ and $\hat{v}$ are terms added to the expansion of u and v, given in eq. (4.47), in order to satisfy the boundary conditions (4.43) and (4.44); $\hat{u}$ and $\hat{v}$ are second-order terms in the panel displacements.

According to the von Kármán's nonlinear plate theory, the middle plane strain-displacement relationships and the changes in curvature and torsion are expressed as (Amabili [93])

$$
\begin{aligned}
\varepsilon_{x,m} &= \frac{\partial u}{\partial x} + \frac{1}{2}\left(\frac{\partial w}{\partial x}\right)^2 + \frac{\partial w}{\partial x}\frac{\partial w_0}{\partial x}, \\[4pt]
\varepsilon_{y,m} &= \frac{\partial v}{\partial y} + \frac{1}{2}\left(\frac{\partial w}{\partial y}\right)^2 + \frac{\partial w}{\partial y}\frac{\partial w_0}{\partial y}, \\[4pt]
\gamma_{xy,m} &= \frac{\partial u}{\partial y} + \frac{\partial v}{\partial x} + \frac{\partial w}{\partial x}\frac{\partial w}{\partial y} + \frac{\partial w}{\partial x}\frac{\partial w_0}{\partial y} + \frac{\partial w_0}{\partial x}\frac{\partial w}{\partial y}, \\[4pt]
k_x &= -\frac{\partial^2 w}{\partial x^2}, \\[4pt]
k_y &= -\frac{\partial^2 w}{\partial y^2}, \\[4pt]
k_{xy} &= -2\frac{\partial^2 w}{\partial x \partial y},
\end{aligned}
\tag{4.50}
$$

The kinetic energy T_P of a thin rectangular plate is given by (Amabili [93])

$$
T_P = \frac{1}{2}\rho_P\, h \int_0^a\!\!\int_0^b (\dot{u}^2 + \dot{v}^2 + \dot{w}^2)\,\mathrm{d}x\,\mathrm{d}y
\tag{4.51}
$$

where ρ_P indicates the plate mass density. In eq. (4.51), the superimposed dot indicates the time derivative.

The additional potential energy stored by the viscoelastic rotational constraint at the plate edges (here it is considered that the rotational springs and spring-pot at the edges are also governed by the fractional solid model) must be added to the previously obtained (Amabili [108]). This potential energy and the work done by the dissipative force are given by

$$
U_{k_E} = \frac{1}{2}\int_0^b k_t \left\{ \left[\left(\frac{\partial w}{\partial x}\right)_{x=0}\right]^2 + \left[\left(\frac{\partial w}{\partial x}\right)_{x=a}\right]^2 \right\}\mathrm{d}y + \frac{1}{2}\int_0^a k_t \left\{ \left[\left(\frac{\partial w}{\partial y}\right)_{y=0}\right]^2 + \left[\left(\frac{\partial w}{\partial y}\right)_{y=b}\right]^2 \right\}\mathrm{d}x,
\tag{4.52}
$$

$$U_{k_{E_1}} = \frac{1}{2}\frac{E_1}{E}\int_0^b \frac{\tau_r^{2\alpha}\omega^{2\alpha}}{1+\tau_r^{2\alpha}\omega^{2\alpha}+2\tau_r^\alpha\omega^\alpha\cos(\alpha\pi/2)}k_t\left\{\left[\left(\frac{\partial w}{\partial x}\right)_{x=0}\right]^2+\left[\left(\frac{\partial w}{\partial x}\right)_{x=a}\right]^2\right.$$

$$\left.-\left(\frac{\partial w}{\partial x}\right)_{x=0}\left(\frac{\partial \overline{w}}{\partial x}\right)_{x=0}-\left(\frac{\partial w}{\partial x}\right)_{x=a}\left(\frac{\partial \overline{w}}{\partial x}\right)_{x=a}\right\}\mathrm{d}\,y+\frac{1}{2}\frac{E_1}{E}\int_0^a \frac{\tau_r^{2\alpha}\omega^{2\alpha}}{1+\tau_r^{2\alpha}\omega^{2\alpha}+2\tau_r^\alpha\omega^\alpha\cos(\alpha\pi/2)} \quad (4.53)$$

$$\times k_t\left\{\left[\left(\frac{\partial w}{\partial y}\right)_{y=0}\right]^2+\left[\left(\frac{\partial w}{\partial y}\right)_{y=b}\right]^2-\left(\frac{\partial w}{\partial y}\right)_{y=0}\left(\frac{\partial \overline{w}}{\partial y}\right)_{y=0}-\left(\frac{\partial w}{\partial y}\right)_{y=b}\left(\frac{\partial \overline{w}}{\partial y}\right)_{y=b}\right\}\mathrm{d}\,x,$$

$$U_{k_{V_I}}+W_{k_{V_O}} = \frac{1}{2}\int_0^b \frac{\tau_r^\alpha}{1+\tau_r^{2\alpha}\omega^{2\alpha}+2\tau_r^\alpha\omega^\alpha\cos(\alpha\pi/2)}\frac{E_1 k_t}{E}D_t^\alpha\left\{\left[\left(\frac{\partial w}{\partial x}\right)_{x=0}\right]^2+\left[\left(\frac{\partial w}{\partial x}\right)_{x=a}\right]^2\right\}\mathrm{d}\,y$$

$$+\frac{1}{2}\int_0^a \frac{\tau_r^\alpha}{1+\tau_r^{2\alpha}\omega^{2\alpha}+2\tau_r^\alpha\omega^\alpha\cos(\alpha\pi/2)}\frac{E_1 k_t}{E}D_t^\alpha\left\{\left[\left(\frac{\partial w}{\partial y}\right)_{y=0}\right]^2+\left[\left(\frac{\partial w}{\partial y}\right)_{y=b}\right]^2\right\}\mathrm{d}\,x, \quad (4.54)$$

where k_t is the stiffness of the rotational distributed springs and $\overline{w}$ is the average value of w in a vibration period. Eq. (4.53) and eq. (4.54) have been obtained from eq. (4.52) by using eq. (4.40) and eq. (4.42). In eq. (4.53) and eq. (4.54), the retardation time constant takes different values according to the shape functions; only quadratic terms in the plate displacements appear in eq. (4.53) and eq. (4.54).

4.6   LAGRANGE EQUATIONS

The virtual work W produced by a harmonic point force $\tilde{f}$, which keeps the same z direction during the plate vibration, is

$$W = \int_0^a\int_0^b \tilde{f}\,\delta(y-\tilde{y})\,\delta(x-\tilde{x})\cos(\omega t)w\,\mathrm{d}x\,\mathrm{d}y = \tilde{f}\cos(\omega t)\left(w\right)_{x=\tilde{x},\,y=\tilde{y}} \quad (4.55)$$

In eq. (4.55) ω represents the excitation frequency, t indicates time, δ is the Dirac delta function, $\tilde{x}$ and $\tilde{y}$ indicate the position where the force is applied.

The vector of the generalized coordinates $\mathbf{q}$ is introduced as

$$\mathbf{q} = \left\{u_{m,n}, v_{m,n}, w_{m,n}\right\}^{\mathrm{T}}, \quad m=1,\dots\tilde{M}\text{ or }\hat{M} \quad\text{and}\quad n=1,\dots\tilde{N}\text{ or }\hat{N} \quad (4.56)$$

The generic element of **q** is q_j, which is a function of time. The dimension of **q** coincides with the number N of degrees of freedom (dofs) utilized in the discretization.

The differentiation of the virtual work produced by external forces and the virtual work dissipated by the non-conservative viscoelastic forces, taken with negative sign, gives the generalized forces Q_j

$$Q_j = \frac{\partial W}{\partial q_j} - \frac{\partial}{\partial q_j}\left(W_{V_O} + W_{k_{V_O}}\right),$$

in which $\quad\quad\quad\quad\quad\quad\quad\quad\quad\quad\quad\quad\quad\quad\quad\quad$ (4.57)

$$\frac{\partial W}{\partial q_j} = \begin{cases} 0 & \text{if } q_j = u_{m,n}, v_{m,n}; \text{ or } w_{m,n} \text{ with } m,n \text{ even,} \\ \tilde{f}\cos(\omega t) & \text{if } q_j = w_{m,n} \text{ with } m,n \text{ odd,} \end{cases}$$

and $W_{V_O} + W_{k_{V_O}}$ indicates the work dissipated by the non-conservative forces. The right-hand term in eq. (4.57) is the dissipative generalized force.

The discretized equations of motion are derived by the Lagrange equations (Amabili [93])

$$\frac{\mathrm{d}}{\mathrm{d}t}\left(\frac{\partial T_P}{\partial \dot{q}_j}\right) + \frac{\partial}{\partial q_j}\left(U_E + U_{E_1} + U_{V_I} + U_{k_E} + U_{k_{E_1}} + U_{k_{V_I}}\right) = Q_j \quad j = 1,\dots N \quad\quad (4.58)$$

The first element in eq. (4.58) is given by

$$\frac{\mathrm{d}}{\mathrm{d}t}\left(\frac{\partial T_P}{\partial \dot{q}_j}\right) = \rho_P \, h \, (ab/4)\, \ddot{q}_j \quad\quad\quad\quad (4.59)$$

Eq. (4.59) shows that there is no inertial coupling among the equations of motion for the discretized plate.

The differentiation of the stiffness and viscoelastic potential energies of the plate with respect to the generalized coordinates give linear, quadratic and cubic nonlinear terms in the stiffness and damping

$$\frac{\partial}{\partial q_j}\left(U_E+U_{E_1}+U_{V_I}+U_{k_E}+U_{k_{E_1}}+U_{k_{V_I}}\right)+\frac{\partial}{\partial q_j}\left(W_{V_O}+W_{k_{V_O}}\right)=\sum_{i=1}^{N}\left(k_{j,i}+k_{j,i}^{(E_1)}(\omega)\right)q_i$$

$$+\sum_{i,k=1}^{N}\left(k_{j,i,k}+k_{j,i,k}^{(E_1)}(\omega)\right)q_i\,q_k+\sum_{i,k,l=1}^{N}\left(k_{j,i,k,l}+k_{j,i,k,l}^{(E_1)}(\omega)\right)q_i\,q_k\,q_l+\sum_{i=1}^{N}g_{j,i}(\omega)\,D_t^\alpha(q_i) \qquad (4.60)$$

$$+\sum_{i,k=1}^{N}g_{j,i,k}(\omega)\,D_t^\alpha(q_i)\,q_k+\sum_{i,k,l=1}^{N}g_{j,i,k,l}(\omega)\,D_t^\alpha(q_i)\,q_k\,q_l,$$

where the coefficients k have particularly long expressions that are derived by a computer program for algebraic manipulation. It can be observed that $k^{(E_1)}$ and g are functions of the excitation frequency ω. Differently from the coefficients k, the functions $k^{(E_1)}$ and g must be identified from experiments since the retardation time constants τ_r vary with the vibration mode shape.

Eq. (4.58) can be rewritten in the following matrix form

$$\mathbf{M}\ddot{\mathbf{q}}+\left[\mathbf{G}(\omega)+\mathbf{G_2}(\omega,\mathbf{q})+\mathbf{G_3}(\omega,\mathbf{q},\mathbf{q})\right]D_t^\alpha(\mathbf{q})+\left[\mathbf{K}+\mathbf{K}^{(E_1)}(\omega)+\mathbf{K_2}(\mathbf{q})+\mathbf{K_2}^{(E_1)}(\omega,\mathbf{q})\right.$$
$$\left.+\mathbf{K_3}(\mathbf{q},\mathbf{q})+\mathbf{K}_3^{(E_1)}(\omega,\mathbf{q},\mathbf{q})\right]\mathbf{q}=\mathbf{f_0}\cos(\omega t), \qquad (4.61)$$

in which $\mathbf{M}$ represents the $N\times N$ diagonal mass matrix, $\mathbf{G}$ represents the frequency-dependent linear damping matrix with elements $g_{j,i}$, $\mathbf{G_2}$ is associated to the quadratic nonlinear damping, $\mathbf{G_3}$ gives the cubic nonlinear damping; $\mathbf{K}$ represents the $N\times N$ linear stiffness matrix with elements $k_{j,i}$, $\mathbf{K_2}$ is associated to the quadratic nonlinear stiffness, $\mathbf{K_3}$ represents the cubic nonlinear stiffness and $\mathbf{f_0}$ is the vector giving the projection of the harmonic force excitation on the generalized coordinates. The elements $k_{2_{j,i}}$, $k_{2_{j,i}}^{(E_1)}$, $k_{3_{j,i}}$, $k_{3_{j,i}}^{(E_1)}$, $g_{2_{j,i}}$ and $g_{3_{j,i}}$ of the matrices $\mathbf{K_2}$, $\mathbf{K_2}^{(E_1)}$, $\mathbf{K_3}$, $\mathbf{K}_3^{(E_1)}$, $\mathbf{G_2}$ and $\mathbf{G_3}$ are given by

$$k_{2_{j,i}}(\mathbf{q})=\sum_{k=1}^{N}k_{j,i,k}\,q_k, \qquad k_{3_{j,i}}(\mathbf{q},\mathbf{q})=\sum_{k,l=1}^{N}k_{j,i,k,l}\,q_k\,q_l,$$

$$k_{2_{j,i}}^{(E_1)}(\omega,\mathbf{q})=\sum_{k=1}^{N}k_{j,i,k}^{(E_1)}(\omega)\,q_k, \qquad k_{3_{j,i}}^{(E_1)}(\omega,\mathbf{q},\mathbf{q})=\sum_{k,l=1}^{N}k_{j,i,k,l}^{(E_1)}(\omega)\,q_k\,q_l, \qquad (4.62)$$

$$g_{2_{j,i}}(\omega,\mathbf{q})=\sum_{k=1}^{N}g_{j,i,k}(\omega)\,q_k, \qquad g_{3_{j,i}}(\omega,\mathbf{q},\mathbf{q})=\sum_{k,l=1}^{N}g_{j,i,k,l}(\omega)\,q_k\,q_l$$

It is interesting to observe that, making use of eq. (4.4), the fractional derivative of the vector $\mathbf{q}$

of the generalized coordinates in eq. (4.61) gives two main terms: one proportional to $\mathbf{q}$, which contributes to the stiffness of the system, and a second one proportional to the first derivative $\dot{\mathbf{q}}$, which generates damping. Therefore, in case of harmonic vibration with the same frequency of the excitation, eq. (4.61) can transformed into

$$
\begin{aligned}
&\mathbf{M\ddot{q}} + \left[\mathbf{\hat{G}}(\omega,\alpha) + \mathbf{\hat{G}_2}(\omega,\alpha,\mathbf{q}) + \mathbf{\hat{G}_3}(\omega,\alpha,\mathbf{q},\mathbf{q}) \right]\dot{\mathbf{q}} + \left[\mathbf{K} + \mathbf{\tilde{G}}(\omega,\alpha) + \mathbf{K_2}(\mathbf{q}) \right. \\
&\left. + \mathbf{\tilde{G}_2}(\omega,\alpha,\mathbf{q}) + \mathbf{K_3}(\mathbf{q},\mathbf{q}) + \mathbf{\tilde{G}_3}(\omega,\alpha,\mathbf{q},\mathbf{q}) \right]\mathbf{q} + \mathbf{K}^{(E_1)}(\omega,\alpha)\left(\mathbf{q} - \overline{\mathbf{q}}/2 \right) \qquad (4.63) \\
&+ \mathbf{K_2}^{(E_1)}(\omega,\alpha,\mathbf{q})\mathbf{q} + \mathbf{K_3}^{(E_1)}(\omega,\alpha,\mathbf{q},\mathbf{q})\mathbf{q} = \mathbf{f_0}\cos(\omega t),
\end{aligned}
$$

where the matrices $\mathbf{\hat{G}}$ and $\mathbf{\tilde{G}}$ are both originated from the corresponding $\mathbf{G}$ and the dependence from the fractional derivative order α has been explicitly indicated. Eq. (4.63) is useful to understand the structure of the problem, even if it must be modified if superharmonics (or subharmonics) contributions to the response are considered. In particular, all the frequency-dependent matrices also depend on the superharmonic integer order n.

It is convenient to introduce the modal matrix $\mathbf{U}$, which is the matrix of the normalized eigenvectors and respects the condition $\mathbf{U}^T\mathbf{M}\mathbf{U} = \mathbf{I}$, where $\mathbf{I}$ is the identical matrix. Pre-multiplying eq. (4.63) by $\mathbf{U}^T$ and introducing the coordinate transformation $\mathbf{q} = \mathbf{U}\boldsymbol{\eta}$ from the generalized coordinate vector $\mathbf{q}$ to the normal coordinate vector $\boldsymbol{\eta}$, the following expression is obtained

$$
\begin{aligned}
&\mathbf{I}\ddot{\boldsymbol{\eta}} + \mathbf{U}^T\left[\mathbf{\hat{G}}(\omega,\alpha) + \mathbf{\hat{G}_2}(\omega,\alpha,\boldsymbol{\eta}) + \mathbf{\hat{G}_3}(\omega,\alpha,\boldsymbol{\eta},\boldsymbol{\eta}) \right]\mathbf{U}\dot{\boldsymbol{\eta}} + \mathbf{U}^T\left[\mathbf{K} + \mathbf{\tilde{G}}(\omega,\alpha) + \mathbf{K_2}(\boldsymbol{\eta}) \right. \\
&\left. + \mathbf{\tilde{G}_2}(\omega,\alpha,\boldsymbol{\eta}) + \mathbf{K_3}(\boldsymbol{\eta},\boldsymbol{\eta}) + \mathbf{\tilde{G}_3}(\omega,\alpha,\boldsymbol{\eta},\boldsymbol{\eta}) \right]\mathbf{U}\boldsymbol{\eta} + \mathbf{U}^T\mathbf{K}^{(E_1)}(\omega,\alpha)\mathbf{U}\left(\boldsymbol{\eta} - \overline{\boldsymbol{\eta}}/2 \right) \qquad (4.64) \\
&+ \mathbf{U}^T\mathbf{K_2}^{(E_1)}(\omega,\alpha,\boldsymbol{\eta})\mathbf{U}\boldsymbol{\eta} + \mathbf{U}^T\mathbf{K_3}^{(E_1)}(\omega,\alpha,\boldsymbol{\eta},\boldsymbol{\eta})\mathbf{U}\boldsymbol{\eta} = \mathbf{U}^T\mathbf{f_0}\cos(\omega t),
\end{aligned}
$$

where $\mathbf{U}^T\mathbf{K}\mathbf{U} = \left[\begin{smallmatrix} \diagdown & \omega_i^2 & \diagdown \end{smallmatrix} \right]$ is the diagonal matrix with the square of the natural frequencies ω_i^2, ordered with i, as elements of the main diagonal for $i=1,\ldots,N$.

4.7 NONLINEAR DAMPING AND DYNAMIC STIFFNESS

The linear and nonlinear damping coefficients in eq. (4.64) must be identified from experiments. In eq. (4.64) the linear damping is represented by the matrix $\mathbf{U}^T\mathbf{\hat{G}}(\omega,\alpha)\mathbf{U}$, which is assumed to

have the following diagonal expression

$$\mathbf{U}^\mathrm{T}\hat{\mathbf{G}}(\omega,\alpha)\mathbf{U} =$$

$$\begin{bmatrix} \dfrac{2\zeta_{1,1}\omega_{1,1}^{2-\alpha}\omega^{\alpha-1}}{1+\left(\dfrac{2\zeta_{1,1}}{\sin(\alpha\pi/2)}\right)^2\left(\dfrac{\omega}{\omega_{1,1}}\right)^{2\alpha}+4\zeta_{1,1}\cot\left(\dfrac{\alpha\pi}{2}\right)\left(\dfrac{\omega}{\omega_{1,1}}\right)^{\alpha}} & \cdots & 0 \\ \vdots & \ddots & \vdots \\ 0 & \cdots & \dfrac{2\zeta_{m,n}\omega_{m,n}^{2-\alpha}\omega^{\alpha-1}}{1+\left(\dfrac{2\zeta_{m,n}}{\sin(\alpha\pi/2)}\right)^2\left(\dfrac{\omega}{\omega_{m,n}}\right)^{2\alpha}+4\zeta_{m,n}\cot\left(\dfrac{\alpha\pi}{2}\right)\left(\dfrac{\omega}{\omega_{m,n}}\right)^{\alpha}} \end{bmatrix} \quad (4.65)$$

where $\omega_{m,n}$ is the natural frequency of the mode (m, n), m and n are the numbers of axial half-waves of the vibration mode shape in x and y direction, respectively, and $\zeta_{m,n}$ represents the corresponding modal damping ratio. These notations are used for natural frequencies and damping ratios in the following part of this study. Eq. (4.16) has been used to obtain eq. (4.65). Eq. (4.65) gives a diagonal modal damping matrix, which is surely obtained in case of proportional damping. This requires a number N of damping ratios and an identical number of natural frequencies as input parameters in eq. (4.65), in addition to the fraction derivative order α. While the natural frequencies can be numerically calculated, the damping ratios require identification from experimental data.

The quadratic nonlinear damping matrix $\mathbf{U}^\mathrm{T}\hat{\mathbf{G}}_2(\omega,\alpha,\boldsymbol{\eta})\mathbf{U}$ and the cubic nonlinear damping matrix $\mathbf{U}^\mathrm{T}\hat{\mathbf{G}}_3(\omega,\alpha,\boldsymbol{\eta},\boldsymbol{\eta})\mathbf{U}$ also need to be written in a simple form in order to allow an experimental identification of a small number of nonlinear damping coefficients. For this reason, it is convenient to introduce the following simplifying hypothesis: the nonlinear damping produced by generalized coordinates that have small vibration amplitude with respect to the plate thickness h can be neglected. This hypothesis brings the consequence that only normal coordinates associated to transverse displacement w must be retained in nonlinear damping. For vibrations with excitation frequency close to the natural frequency of the fundamental mode ($m=1$, $n=1$), the fundamental coordinate $w_{1,1}(t)$ presents the largest amplitude and nonlinear damping terms not containing this coordinate may become negligible; in fact, nonlinear damping depends on the vibration amplitude.

If the nonlinear dynamics does not present internal resonances or chaos, but instead is

dominated by a single nonlinear mode, experiments clearly show that the quadratic damping is negligible Amabili [109, 111, 114]. Therefore, it is possible to write

$$\mathbf{U}^{\mathrm{T}}\hat{\mathbf{G}}_2(\omega,\alpha,\boldsymbol{\eta})\,\mathbf{U} = \mathbf{0} \tag{4.66}$$

Eq. (4.66) is not a surprise for hardening systems (e.g. flat rectangular plates), which present dominating cubic stiffness nonlinearity. However, this may be unexpected for softening systems (e.g. curved panels and plates with very large initial imperfections).

In case of absence of internal resonances and chaos, the cubic damping matric can be written as

$$\mathbf{U}^{\mathrm{T}}\hat{\mathbf{G}}_3(\omega,\alpha,\boldsymbol{\eta},\boldsymbol{\eta})\,\mathbf{U} = \begin{bmatrix} 0 & \cdots & & 0 & & \cdots & 0 \\ \vdots & \ddots & & \vdots & & \iddots & \vdots \\ 0 & \cdots & \dfrac{4\zeta_{m,n}\beta_{m,n}\,\omega_{m,n}^{2-\alpha}\omega^{\alpha-1}\eta_i^2(t)}{1+\left(\dfrac{2\zeta_{m,n}}{\sin(\alpha\,\pi/2)}\right)^2\left(\dfrac{\omega}{\omega_{m,n}}\right)^{2\alpha}+4\zeta_{m,n}\cot\!\left(\dfrac{\alpha\,\pi}{2}\right)\!\left(\dfrac{\omega}{\omega_{m,n}}\right)^{\alpha}} & \cdots & 0 \\ \vdots & \iddots & & \vdots & & \ddots & \vdots \\ 0 & \cdots & & 0 & & \cdots & 0 \end{bmatrix} \tag{4.67}$$

with great simplification for experimental identification of damping parameters; $\beta_{m,n}$ is a cubic viscoelastic parameter. This formulation is justified since only the vibration mode (m,n) with natural frequency $\omega_{m,n}$ close to the excitation frequency has large-amplitude vibration with respect to the plate thickness, while all the remaining generalized coordinates, associated to other modes, have smaller vibration amplitude that generate only linear damping (for small amplitude vibrations nonlinear damping is negligible). Therefore, only one term on the diagonal of the matrix on the right-hand side of eq. (4.67) is different from zero; $\eta_i(t)$ is the normal coordinate associated to the normal mode (m,n). for the fundamental mode of the plate, the normal coordinate is $\eta_1(t)$ and the normal mode is $(1,1)$. Eq. (4.67) gives a major reduction of the number of viscoelastic parameters to identify experimentally and describes the plate dissipation with accuracy, as experimentally verified. The nondimensional coefficient $\tilde{\beta}_{m,n}$ is defined as

$$\tilde{\beta}_{m,n} = \beta_{m,n}h^2\mu^2, \tag{4.68}$$

where h is the plate thickness and μ is a normalization coefficient that transform the normal coordinate $\eta_i(t)$ into $w(\tilde{x}, \tilde{y}, t)$, which is the measurement of the transverse displacement of the plate at the point of coordinates $(x = \tilde{x}, y = \tilde{y})$ on the middle plane of the plate $(z = 0)$.

The viscoelastic contribution to the dynamic stiffness matrices can be divided in two components: one is related to the second spring element in the material model and appears with dynamic modulus E_1 in eq. (4.1), while the second one is due to the fractional derivative in the material constitutive eq. (4.1). The linear dynamic stiffness matrix associated to the fractional derivative, which vanishes for $\alpha = 1$, is given by

$$\mathbf{U}^{\mathrm{T}}\tilde{\mathbf{G}}(\omega, \alpha)\mathbf{U} =$$

$$
\begin{bmatrix}
\dfrac{2\zeta_{1,1}\omega_{1,1}^{2-\alpha}\omega^{\alpha}\cot\left(\dfrac{\alpha\pi}{2}\right)}{1+\left(\dfrac{2\zeta_{1,1}}{\sin(\alpha\pi/2)}\right)^{2}\left(\dfrac{\omega}{\omega_{1,1}}\right)^{2\alpha}+4\zeta_{1,1}\cot\left(\dfrac{\alpha\pi}{2}\right)\left(\dfrac{\omega}{\omega_{1,1}}\right)^{\alpha}} & \cdots & 0 \\
\vdots & \ddots & \vdots \\
0 & \cdots & \dfrac{2\zeta_{m,n}\omega_{m,n}^{2-\alpha}\omega^{\alpha}\cot\left(\dfrac{\alpha\pi}{2}\right)}{1+\left(\dfrac{2\zeta_{m,n}}{\sin(\alpha\pi/2)}\right)^{2}\left(\dfrac{\omega}{\omega_{m,n}}\right)^{2\alpha}+4\zeta_{m,n}\cot\left(\dfrac{\alpha\pi}{2}\right)\left(\dfrac{\omega}{\omega_{m,n}}\right)^{\alpha}}
\end{bmatrix}
\tag{4.69}
$$

Eq. (4.69) is diagonal since this is directly related to eq. (4.65). As a consequence of eq. (4.66), the quadratic dynamic stiffness matrix associated to the fractional derivative is also zero

$$\mathbf{U}^{\mathrm{T}}\tilde{\mathbf{G}}_{2}(\omega, \alpha, \boldsymbol{\eta})\mathbf{U} = \mathbf{0} \tag{4.70}$$

The cubic dynamic stiffness matrix associated to the fractional derivative is related to eq. (4.67) and is given by

$$
\mathbf{U}^{\mathrm{T}}\tilde{\mathbf{G}}_{3}(\omega, \alpha, \boldsymbol{\eta}, \boldsymbol{\eta})\,\mathbf{U} =
\begin{bmatrix}
0 & \cdots & & 0 & & \cdots & 0 \\
\vdots & \ddots & & \vdots & & \iddots & \vdots \\
0 & \cdots & \dfrac{4\zeta_{m,n}\beta_{m,n}\,\omega_{m,n}^{2-\alpha}\omega^{\alpha}\cot\left(\dfrac{\alpha\pi}{2}\right)\eta_i^{2}(t)}{1+\left(\dfrac{2\zeta_{m,n}}{\sin(\alpha\pi/2)}\right)^{2}\left(\dfrac{\omega}{\omega_{m,n}}\right)^{2\alpha}+4\zeta_{m,n}\cot\left(\dfrac{\alpha\pi}{2}\right)\left(\dfrac{\omega}{\omega_{m,n}}\right)^{\alpha}} & & \cdots & 0 \\
\vdots & \iddots & & \vdots & & \ddots & \vdots \\
0 & \cdots & & 0 & & \cdots & 0
\end{bmatrix}
\tag{4.71}
$$

The linear dynamic stiffness matrix associated to the dynamic modulus E_1 is expressed as

$$\mathbf{U}^{\mathrm{T}}\mathbf{K}^{(E_1)}(\omega,\alpha)\mathbf{U} =$$

$$\begin{bmatrix} \dfrac{4\zeta_{1,1}^2\omega^{2\alpha}\omega_{1,1}^{2-2\alpha}/\sin^2(\alpha\pi/2)}{1+\left(\dfrac{2\zeta_{1,1}}{\sin(\alpha\pi/2)}\right)^2\left(\dfrac{\omega}{\omega_{1,1}}\right)^{2\alpha}+4\zeta_{1,1}\cot\left(\dfrac{\alpha\pi}{2}\right)\left(\dfrac{\omega}{\omega_{1,1}}\right)^{\alpha}} & \cdots & 0 \\ \vdots & \ddots & \vdots \\ 0 & \cdots & \dfrac{4\zeta_{m,n}^2\omega^{2\alpha}\omega_{m,n}^{2-2\alpha}/\sin^2(\alpha\pi/2)}{1+\left(\dfrac{2\zeta_{m,n}}{\sin(\alpha\pi/2)}\right)^2\left(\dfrac{\omega}{\omega_{m,n}}\right)^{2\alpha}+4\zeta_{m,n}\cot\left(\dfrac{\alpha\pi}{2}\right)\left(\dfrac{\omega}{\omega_{m,n}}\right)^{\alpha}} \end{bmatrix} \quad (4.72)$$

Again, the quadratic dynamic stiffness matrix associated to the dynamic modulus E_1 is assumed to be zero

$$\mathbf{U}^{\mathrm{T}}\mathbf{K}_2^{(E_1)}(\omega,\alpha,\boldsymbol{\eta})\mathbf{U} = \mathbf{0} \tag{4.73}$$

Finally, the cubic dynamic stiffness matrix associated to the dynamic modulus E_1 is written as

$$\mathbf{U}^{\mathrm{T}}\mathbf{K}_3^{(E_1)}(\omega,\alpha,\boldsymbol{\eta},\boldsymbol{\eta})\mathbf{U} = \begin{bmatrix} 0 & \cdots & 0 & \cdots & 0 \\ \vdots & \ddots & \vdots & & \vdots \\ 0 & \cdots & \dfrac{4\zeta_{m,n}^2\beta_{m,n}\omega^{2\alpha}\omega_{m,n}^{2-2\alpha}\left(\eta_i^2(t)-\overline{\eta_i^2(t)}/2\right)/\sin^2(\alpha\pi/2)}{1+\left(\dfrac{2\zeta_{m,n}}{\sin(\alpha\pi/2)}\right)^2\left(\dfrac{\omega}{\omega_{m,n}}\right)^{2\alpha}+4\zeta_{m,n}\cot\left(\dfrac{\alpha\pi}{2}\right)\left(\dfrac{\omega}{\omega_{m,n}}\right)^{\alpha}} & \cdots & 0 \\ \vdots & \ddots & \vdots & & \vdots \\ 0 & \cdots & 0 & \cdots & 0 \end{bmatrix} \quad (4.74)$$

In eq. (4.74), the overline indicates the average value of the function in a vibration period.

4.8 VIBRATION EXPERIMENTS ON A SILICONE RUBBER PLATE

A silicone rubber plate with shore hardness 90A, density 1430 kg/m³ and thickness 3.35 mm ($h = 0.00335$ m) was glued to a metal frame leaving an unglued rectangular portion of dimensions 260×260 mm ($a = b = 0.26$ m), as shown in Fig. 4-3. The storage and loss modulus of the silicon rubber material are given in (Balasubramanian, Ferrari & Amabili, [2]); both increase with frequency. The boundary conditions given by the glue and the metal frame are zero displacement at the edges in transverse direction, elastic rotational constraint at the four plate edges with rotational stiffness per unit length $k_t = 2000$ N/m (large value for the studied plate,

giving a very stiff rotational constraint), while in the in-plane direction no significant constraint is given by the glue in the direction orthogonal to the edge (simply supported movable edges). This is justified since the plate is glued to the frame on one side, with the consequence that in-plane displacements at the edges in direction orthogonal to them are allowed due to the shear of silicone for half the thickness of the plate (distance between the glued surface and the middle-plane of the plate) and the shear of the glue. However, no in-plane displacement is allowed by the glue at the edge in direction parallel to it.

The plate presents geometric imperfections and no significant in-plane stretch is applied to the plate during the gluing process. The geometric imperfections were measured by a FaroArm 3D scanning system. The contour plot showing the geometric deviation from the flat surface is shown in Fig. 4-4.

Mode Shape	Frequency, Hz	Damping Ratio, %
(1, 1)	17.10	2.20
(1, 2)	35.67	3.17
(2, 1)	37.45	3.25
(2, 2)	54.78	3.11

Tab. 4-1: Experimental modal analysis of the silicone rubber plate.
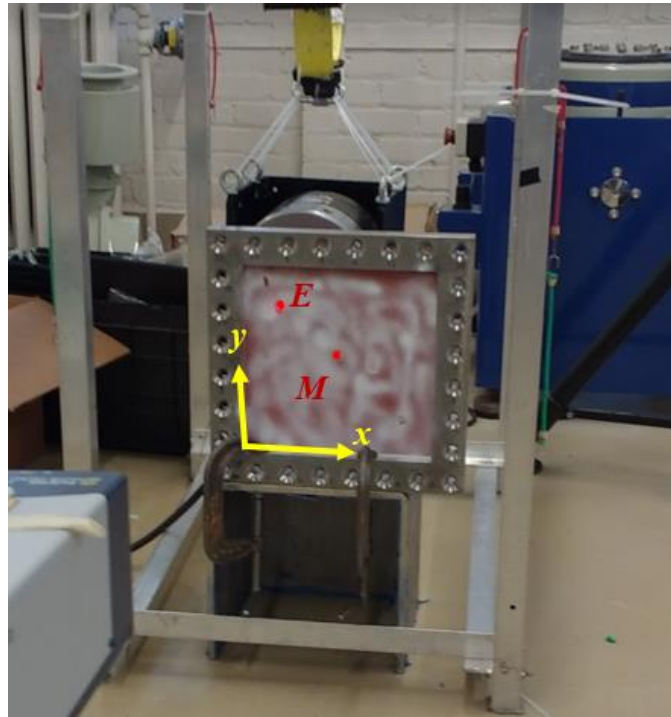
Fig. 4-3: Silicone rubber plate glued to a square metal frame; experimental setup. E: excitation point; M: vibration measurement point. The head of the Polytec scanning laser Doppler vibrometer is in the low left corner and the B&K electrodynamic exciter is suspended behind the plate.
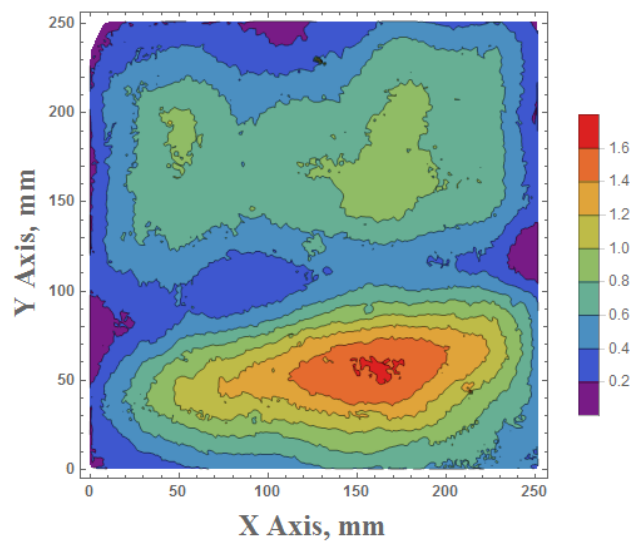
Fig. 4-4: Contour plot showing the deviations from the flat configuration of the silicone rubber plate.

The plate was excited by transverse point force using a stinger connected to a Brüel & Kjær model 4824 electrodynamic exciter. The excitation point was placed close to the top left corner at 50 mm from the vertical edge and 60 mm from the top horizontal edge, with coordinates (x=0.19a, y=0.77b). This point was chosen to minimize the interaction between the electrodynamic exciter and the plate during geometrically nonlinear vibrations. A Brüel & Kjær model 8203 force transducer was glued to the plate and connected to the stinger to measure the excitation force applied. A Polytec PSV 400 automatic scanning laser Doppler vibrometer was utilized to measure the vibration. A linear modal analysis was performed by using the LMS Test.Lab software with the PolyMAX algorithm. The natural frequencies and damping ratios identified from the experiments are reported in Tab. 4-1; here two integers (n, m) give the number n of horizontal and m of vertical half-waves that identify the vibration mode shape. The natural frequency of the fundamental mode (1, 1) of the plate is 17.1 Hz and the corresponding damping ratio is 2.2 % ($\zeta_{1,1}$ =0.022).

The nonlinear vibration experiments were conducted with step-sine excitation at different force levels. The plate was excited by harmonic force at a fixed level, starting at a frequency below the fundamental natural frequency. The excitation frequency was increased in 0.05 Hz steps while keeping the excitation force within ± 0.5% tolerance by using the LMS feedback controller in the step-sine test module. The test was then repeated, this time decreasing the excitation frequency. Therefore, two curves were obtained at any excitation level: one measured increasing the excitation frequency and the other one decreasing it. These two curves are superimposed in case of linear vibration of the plate; during nonlinear tests, these curves present jumps and hysteresis. At any frequency step, 40 periods were discharged to eliminate the transient vibration of the plate. The next 40 periods were recorded; the time signals were measured using the 6400 Hz sampling frequency. The laser was pointed close to the centre of the plate, since the fundamental mode shape has its maximum vibration amplitude at that point. The exact position of the measurement point was 5 mm away from the center in horizontal direction and 5 mm in vertical direction, with coordinates (x=0.52a, y=0.48b). Therefore, the second (1, 2) and third mode (2, 1) significantly contributed to the forced vibration response. The fundamental mode (1, 1) was selected for the nonlinear vibration experiments. Five force levels (0.25, 0.5,

0.75, 1.5 and 2.5 N) were chosen and the nonlinear forced responses of the plate were measured in the time domain at any frequency step to obtain the frequency-response curves.

4.9 COMPARISON OF EXPERIMENTAL AND NUMERICAL RESULTS

In the numerical simulations, a reduced-order model is built with 41 DOFs that represent the terms in the expansion of u, v and w in eq. (4.47). The generalized coordinates utilized are

$$w_{1,1}, w_{1,2}, w_{2,1}, w_{1,3}, w_{3,1}, w_{3,3}, w_{5,1}, w_{5,3}, w_{1,5}, w_{3,5}, w_{5,5}, w_{7,1}, w_{7,3}, w_{1,7}, w_{3,7},$$

$$u_{1,1}, u_{1,3}, u_{3,1}, u_{3,3}, u_{5,1}, u_{5,3}, u_{1,5}, u_{3,5}, u_{5,5}, u_{7,1}, u_{7,3}, u_{1,7}, u_{3,7},$$

$$v_{1,1}, v_{1,3}, v_{3,1}, v_{3,3}, v_{5,1}, v_{5,3}, v_{1,5}, v_{3,5}, v_{5,5}, v_{7,1}, v_{7,3}, v_{1,7}, v_{3,7}.$$

In particular, modes (1,2) and (2,1) are considered only for their transverse contribution since they have a small (linear) influence on the fundamental mode of the plate, which is the one investigated here. They are retained because they represent the second and third natural modes of the plate and they have a little contribution to the forced vibration response in the low frequency range even if, for symmetry reasons, they do not contribute to the first natural mode and its shape modification in case of nonlinear response. The frequency independent part of the stiffness, i.e. the Young's modulus, $E = 51$ MPa and Poisson ratio $v = 0.5$ were used in the numerical simulations. The damping ratio $\zeta_{m,n} = 0.022$ represents the linear dissipation and has been used for all the normal coordinates, including η_1 associated to the fundamental mode (1,1). The nonlinear cubic damping coefficient $\tilde{\beta}_{1,1} = 1.35$ has been used to match the experimental results together with order of the fractional derivative $\alpha = 1$, i.e. in case of classic derivative. This value of α is found to give good results in the present case, while $\alpha < 1$ would be the proper choice for biological materials.

Mode (m,n)	(1,1)	(1,2)	(2,1)	(2,2)	(1,3)	(3,1)	(3,3)
$\dfrac{A_{m,n}}{h}$	0.45	0.07	-0.03	-0.02	0.18	0.07	0.03

Tab. 4-2: Modal expansion of the measured surface imperfections of the silicone rubber plate.
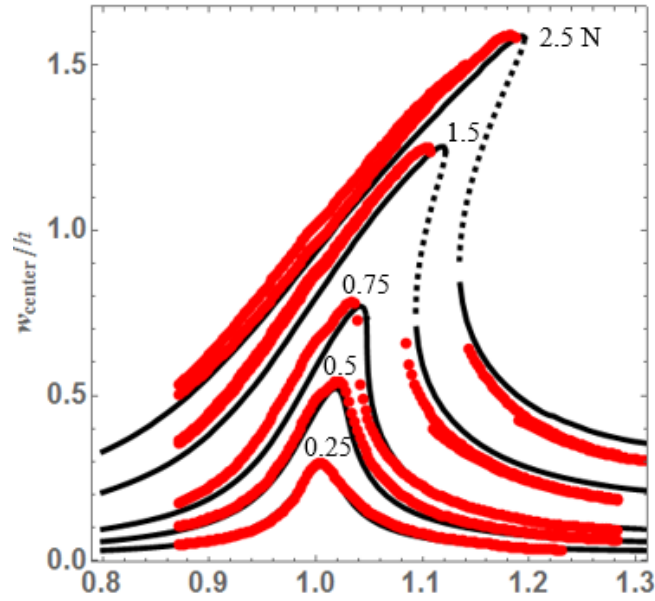
Fig. 4-5: First harmonic of the non-dimensional vibration amplitude versus non-dimensional frequency at the point of coordinates (x=0.52a, y=0.48b) for the silicon rubber plate. Comparison of experimental (red dots) and numerical (black lines; continuous line, stable solution; dotted line, unstable solution) results at five different levels of harmonic excitation: 0.25, 0.5, 0.75, 1.5 and 2.5 N.
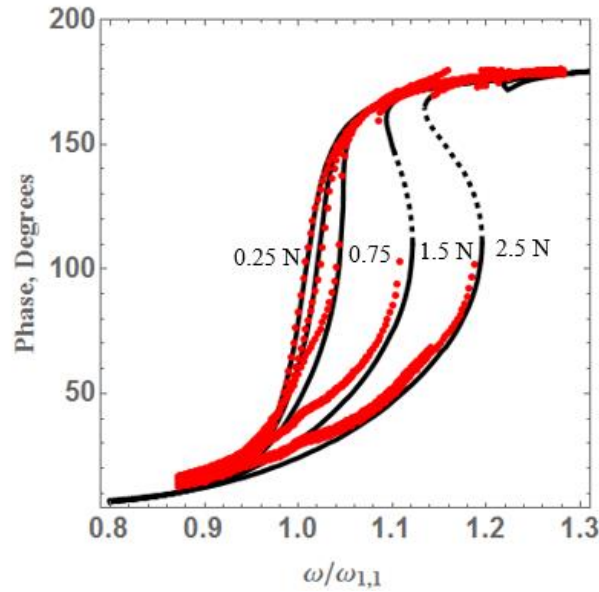
Fig. 4-6: Phase angle versus non-dimensional frequency of the first harmonic of the vibration at the point of coordinates (x=0.52a, y=0.48b) for the silicon rubber plate. Comparison of experimental (red dots) and numerical (black lines; continuous line, stable solution; dotted line, unstable solution) results at five different levels of harmonic excitation: 0.25, 0.5, 0.75, 1.5 and 2.5 N.

The surface of the rubber plate measured by the scanning system is shown in Fig. 4-4 and was expanded using the first seven natural modes of the plate; the respective participation coefficients are listed in Tab. 4-2. The participation coefficient to the global imperfection of the fundamental mode shape (1, 1) is $A_{1,1} = 0.45\ h$, which is much larger than the coefficients of the other mode shapes; the second largest coefficient is $A_{1,3} = 0.18\ h$. For simplicity, the geometric imperfection was inserted in the model of the plate taking in consideration only the fundamental mode shape, i.e. using eq. (4.48) with $\bar{N} = 1$ and $\bar{M} = 1$, with the coefficient $A_{1,1} = 0.62\ h$, slightly larger than the one measured due to the truncation approximation (i.e. higher harmonics of the imperfection are truncated). The computer program AUTO (Doedel et al., [7]) for continuation and bifurcation of ordinary differential equations was applied to obtain the nonlinear vibration of the plate for the five force levels: 0.25, 0.5, 0.75, 1.5 and 2.5 N.

Force, N	ζ
0.1	0.022
0.25	0.022
0.5	0.024
0.75	0.0271
1.5	0.035
2.5	0.042

Tab. 4-3: Equivalent damping ratio in case of linear viscous damping for the silicone rubber plate

The first harmonic of the experimental and numerical vibration amplitudes at the point of coordinates ($x=0.52a$, $y=0.48b$) versus frequency are plotted in Fig. 4-5 for five force levels and the corresponding phase angles are presented in Fig. 4-6. The natural frequency $\omega_{1,1}$ of the fundamental mode is used to non-dimensionalize the excitation frequency ω in both figures. In a similar way, the plate thickness h is utilized to render the vibration amplitude non-dimensional. The lowest force level 0.25 N is almost a linear vibration response and the frequency at the peak is practically coincident with the natural frequency $\omega_{1,1}$. However, from the second force level onwards, the frequency of the peak progressively increases with respect the natural frequency, which is typical of hardening nonlinear systems like a plate. The largest two force levels, which are at 1.5 and 2.5 N, display hysteresis and jumps in Fig. 4-5 and Fig. 4-6. The 2.5 N force level

displays a maximum vibration amplitude equal to about 1.6 times the plate thickness. The frequency increase at the peak with respect to the natural frequency is almost 20 % in this case. The comparison of numerical and experimental results is very good for all the force levels, indicating that the nonlinear damping is capable to reproduce the dissipation at all the levels without adjusting the viscous damping coefficient at any level. In fact, if the cubic damping is removed, then the damping ratio ζ needs to have a different value at any force level in order to match the experiments. The ζ values necessary to match the experimental results are given in Tab. 4-3 and show a damping increase of 1.9 times between the 0.25 N and the 2.5 N levels.

Since Fig. 4-5 presents only the first harmonic of the vibration, the average value of the displacement, which is different from zero due to the quadratic geometrically nonlinear stiffness terms introduced by the geometric imperfection, was removed. This average value makes the vibration inwards and outwards, with respect to the center of curvature of the imperfect plate, to be different in amplitude. The time response obtained at excitation frequency very close to the peak of the response amplitude (maximum vibration amplitude) at the point of coordinates (x=0.52a, y=0.48b) for force level 1.5 N and excitation frequency $\omega/\omega_{1,1} = 1.1028$ is presented in Fig. 4-7 after filtering to leave only the first harmonic (so the average displacement does not appear). An excellent comparison of the numerical and experimental results is observed in this case.
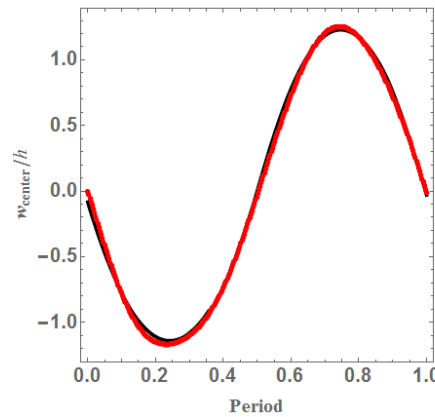
Fig. 4-7: Time response of the first harmonic of the non-dimensional vibration at the point of coordinates (x=0.52a, y=0.48b) for the silicon rubber plate. Comparison of experimental (red dots) and numerical (black line) results at excitation 1.5 N and frequency $\omega/\omega_{1,1} = 1.1028$, very close to the peak of the response.

4.9.1 STORAGE ENERGY, DISSIPATED ENERGY AND LOSS FACTOR

The energy dissipated in a full vibration cycle by a single-degree-of-freedom system subjected to harmonic forced vibrations is given by (Amabili [93])

$$\Delta W_d = \int_{cycle} F \, dx \tag{4.75}$$

where

$$F(t) = \tilde{f} \cos(\omega t) \tag{4.76}$$

For the plate, a similar dissipated energy is built by using the excitation force F, applied at the excitation point ($x_1=0.19a$, $y_1=0.23b$), and the dynamic displacement x at the point ($x=0.52a$, $y=0.48b$) where the plate vibration is measured, filtered in order to keep only the first harmonic. In this way, eq. (4.75) can be used also for the plate, which is a continuous system, even if this does not represent the dissipated energy since the excitation and measured dynamic displacement are in different points and the plate has different displacements at different positions. However, this quantity is related to the energy dissipated in a cycle and for simplicity it is named dissipated energy here. The dissipated energy is made non-dimensional for simplicity dividing the displacement x of the plate at the point ($x=0.52a$, $y=0.48b$) by the thickness h and the excitation force F is made nondimensional with the expression

$$\frac{F \sin(\pi x_1 / a) \sin(\pi y_1 / b)}{\sin(\pi 0.52) \sin(\pi 0.48)} \frac{1}{\omega_{1,1}^2 h \left(\rho h \dfrac{a}{2} \dfrac{b}{2} \right)} \tag{4.77}$$

where the force F has been projected on the point ($x=0.52a$, $y=0.48b$); $\rho h \dfrac{a}{2} \dfrac{b}{2}$ is the modal mass of the plate and $\omega_{1,1}$ the natural frequency of the fundamental mode ($m=1$, $n=1$) of the plate. A plot of the experimental and computed hysteresis loops of the nondimensionalized excitation force versus the nondimensionalized plate displacement is presented in Fig. 4-8 for the case of 1.5 N excitation force and excitation frequencies $\omega / \omega_{1,1} = 0.99$, 1.11, 1.15 (before, at the peak, and after resonance, respectively); the shapes of the loops are close to ellipses and the comparison of experimental and computed results is particularly good. The experimental and

computed loops at the peak of the response for excitation 1.5 N in Fig. 4-8 are obtained at a very slightly different excitation frequency (smaller than 0.01 Hz). The area inside each of these loops represents the dissipated energy obtained from eq. (4.75), nondimensionalized as previously
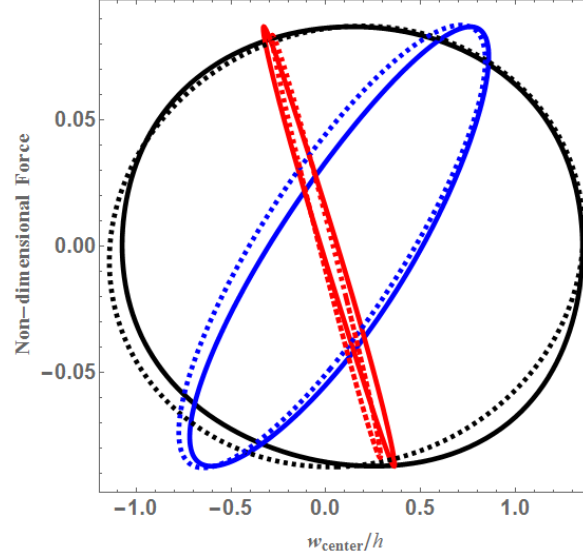
Fig. 4-8: Comparison of experimental (dots) and computed (continuous lines) hysteresis loops in the force-displacement (both made non-dimensional) plane for three different excitation frequencies: $\omega/\omega_{1,1} = 0.99$ (blue), 1.11 (black), 1.15 (red), i.e. before, at the peak, and after resonance; force excitation 1.5 N.
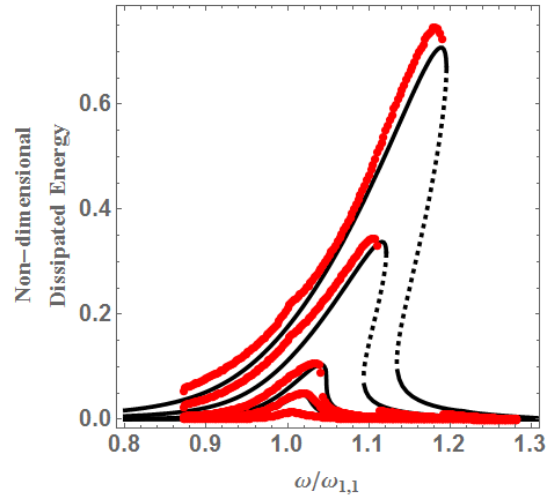
Fig. 4-9: Comparison of numerical and experimental non-dimensional dissipated energy versus non-dimensional excitation frequency for five different levels of harmonic excitation: 0.25, 0.5, 0.75, 1.5 and 2.5 N. Experimental (red dots) and numerical (black lines; continuous line, stable solution; dotted line, unstable solution) results.

explained. The dissipated energy versus excitation frequency for the five excitation levels is shown in Fig. 4-9. The comparison of numerical and experimental results is very satisfactory.

The storage energy of a nonlinear single-degree-of-freedom system with linear stiffness k, quadratic stiffness k_2 and cubic stiffness k_3 can be defined as (Amabili, [93] 2018a)

$$W_s = \frac{\displaystyle\int_0^{x_{\max}} \left(k\,x + k_2 x^2 + k_3 x^3 \right) \mathrm{d}x - \int_{x_{\min}}^{0} \left(k\,x + k_2 x^2 + k_3 x^3 \right) \mathrm{d}x}{2}$$

$$= \frac{(k\,x_{\max}^2 + \frac{1}{3}k_2 x_{\max}^3 + \frac{1}{4}k_3 x_{\max}^4) + (k\,x_{\min}^2 + \frac{1}{3}k_2 x_{\min}^3 + \frac{1}{4}k_3 x_{\min}^4)}{2},$$

(4.78)

where $x_{\max} \geq 0$ and $x_{\min} \leq 0$ are the maximum and minimum displacement registered at the point (x=0.52a, y=0.48b) during a vibration cycle. In case of quadratic nonlinearities, $x_{\max} \neq |x_{\min}|$ due to the presence of an average displacement value different from zero, which is removed if the first harmonic of the vibration is considered. Eq. (4.78) can be extended to the plate by considering the equivalent stiffness, which is the frequency-dependent dynamic stiffness, of the plate at the point (x=0.52a, y=0.48b) where the dynamic displacement is measured. The storage energy is made non-dimensional by

$$W_s = \frac{(k\,x_{\max}^2 + \frac{1}{3}k_2 x_{\max}^3 + \frac{1}{4}k_3 x_{\max}^4) + (k\,x_{\min}^2 + \frac{1}{3}k_2 x_{\min}^3 + \frac{1}{4}k_3 x_{\min}^4)}{2\omega_{1,1}^2 h^2 \left(\rho h \dfrac{a}{2}\dfrac{b}{2} \right)}$$

$$= \frac{1}{2}\left\{ \left[\left(\frac{x_{\max}}{h}\right)^2 + \frac{\tilde{k}_2}{3}\left(\frac{x_{\max}}{h}\right)^3 + \frac{\tilde{k}_3}{4}\left(\frac{x_{\max}}{h}\right)^4 \right] + \left[\left(\frac{x_{\min}}{h}\right)^2 + \frac{\tilde{k}_2}{3}\left(\frac{x_{\min}}{h}\right)^3 + \frac{\tilde{k}_3}{4}\left(\frac{x_{\min}}{h}\right)^4 \right] \right\},$$

(4.79)

where the non-dimensional quadratic and cubic stiffness parameters are given by

$$\tilde{k}_2 = \frac{k_2}{\omega_{1,1}^2 h \left(\rho h \dfrac{a}{2}\dfrac{b}{2} \right)}, \qquad\qquad \tilde{k}_3 = \frac{k_3}{\omega_{1,1}^2 \left(\rho h \dfrac{a}{2}\dfrac{b}{2} \right)}.$$
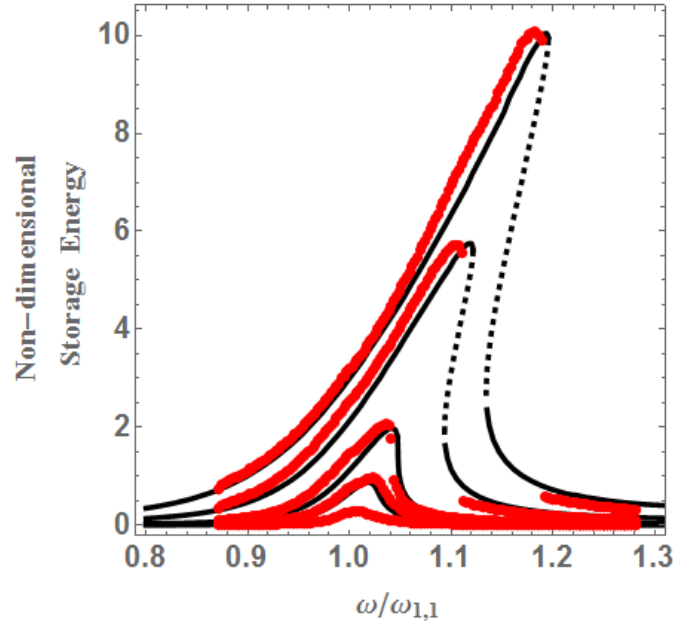
Fig. 4-10: Comparison of numerical and experimental non-dimensional storage energy versus non-dimensional excitation frequency for five different levels of harmonic excitation: 0.25, 0.5, 0.75, 1.5 and 2.5 N. Experimental (red dots) and numerical (black lines; continuous line, stable solution; dotted line, unstable solution) results.
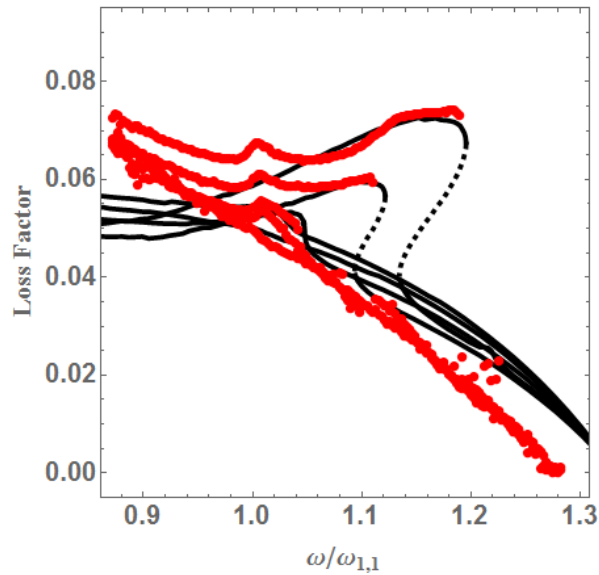
Fig. 4-11: Comparison of numerical and experimental loss factor versus non-dimensional excitation frequency for five different levels of harmonic excitation: 0.25, 0.5, 0.75, 1.5 and 2.5 N. Experimental (red dots) and numerical (black lines; continuous line, stable solution; dotted line, unstable solution) results.

The values of x_{max} and x_{min} are obtained as extremes horizontal points of the loops, as those shown in Fig. 4-8. The values of the non-dimensional quadratic and cubic stiffness parameters are obtained by fitting the experimental or numerical data with the algorithm outlined in (Amabili, Alijani and Delannoy [58]). The storage energy versus excitation frequency for the five excitation levels is shown in Fig. 4-10 for both numerical and experimental results.

It is convenient to introduce the specific damping capacity Ψ as

$$\Psi = \frac{\Delta W_d}{W_s}. \tag{4.80}$$

Then the loss factor is defined as $\Psi / (2\pi)$. The loss factor coincides with the loss tangent in case of linear viscoelasticity. However, the validity of the loss factor goes beyond the linear viscoelasticity. The loss factor versus excitation frequency for the five excitation levels of the plate is shown in Fig. 4-11. The comparison of numerical and experimental results is satisfactory.
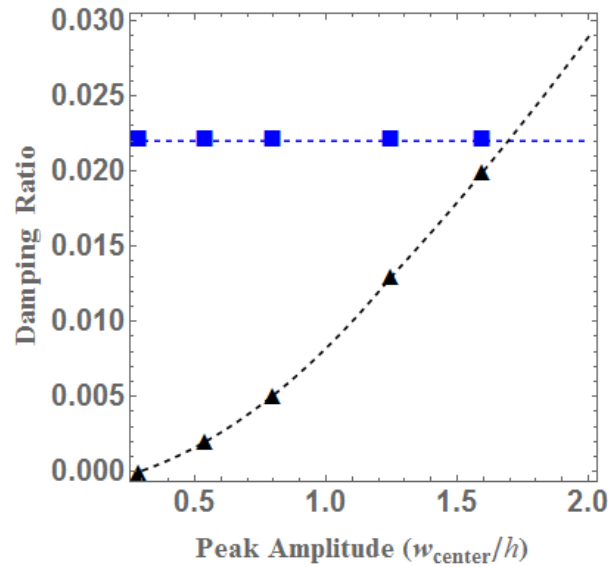
Fig. 4-12: Contribution to the global damping ratio of the linear damping term and of the cubic damping term versus the maximum normalized vibration amplitude (peak amplitude divided by h).

The linear damping coefficient and the cubic damping one to the plate are compared in

Fig. 4-12 as a function of the maximum (i.e. at the peak) normalized vibration amplitude. The frequency-dependent linear damping associated to the main normal coordinate $\eta_1(t)$ for $\alpha = 1$ is given by

$$\frac{2\zeta_{1,1}\omega_{1,1}}{1+\left(2\zeta_{1,1}\dfrac{\omega}{\omega_{1,1}}\right)^2}\dot{\eta}_1(t),\tag{4.81}$$

so that the coefficient plotted in Fig. 4-12 is $\zeta_{1,1}$. The frequency-dependent cubic damping acting on mode (1,1) is represented by

$$\frac{4\zeta_{1,1}\tilde{\beta}_{1,1}\,\omega_{1,1}}{1+\left(2\zeta_{1,1}\dfrac{\omega}{\omega_{1,1}}\right)^2}\left(\frac{\eta_1(t)}{h\,\mu}\right)^2\dot{\eta}_1(t).\tag{4.82}$$

The coefficient in front of $\dot{\eta}_1(t)$ in eq. (4.82) is time-dependent since it depends on $\left(\eta_1(t)\right)^2$. In the case of harmonic vibration, it presents double oscillation frequency with respect to the vibration. Therefore, it is impossible to use the maximum value of $\eta_{1,1}(t)$ in eq. (4.82) in order to evaluate the coefficient $2\tilde{\beta}_{1,1}\left(\dfrac{\eta_1(t)}{h\,\mu}\right)^2$ to insert in Fig. 4-12. Instead, the cubic damping in Fig. 4-12 has been obtained by using the equivalent linear viscous damping necessary to fit the experimental results that are given in Tab. 4-3 and then subtracting $\zeta_{1,1}$ to it. The cubic damping is negligible with respect to the linear damping ratio when the maximum vibration amplitude (at the peak) is smaller than 0.5h. The linear and the cubic terms reach the same value around maximum vibration amplitude 1.7h; for larger amplitudes the cubic term becomes dominant.
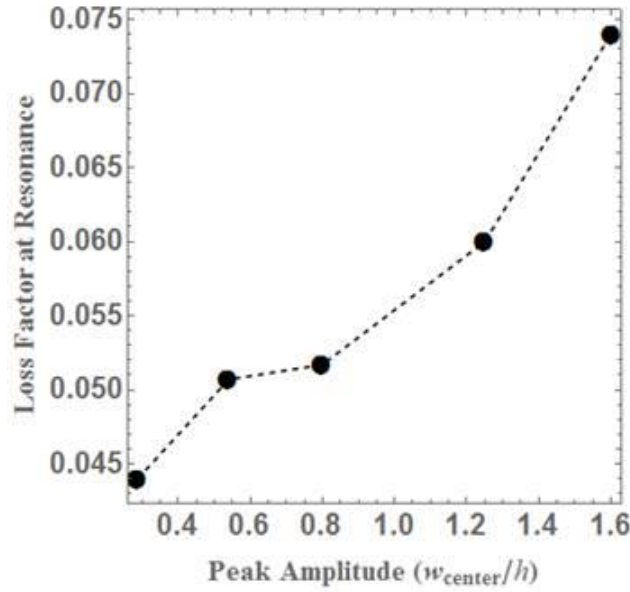
Fig. 4-13: Experimental values of the loss factor at the peak of the vibration amplitude *versus* the maximum normalized vibration amplitude (peak amplitude divided by *h*).

The experimental values of the loss factor at the peak amplitude of the vibration response for each excitation level are shown in Fig. 4-13 versus the maximum normalized vibration amplitude (peak amplitude divided by h). In particular, the loss factors have values close to twice the sum of the linear damping ratio plus the cubic damping given in Fig. 4-12.

4.10 CONCLUSIONS

The derivation of nonlinear damping of plates from viscoelasticity was first addressed by Amabili [108]. However, no frequency-dependent stiffness and damping were considered in that study, as well as no fractional derivative constitutive model of the material. In the present study these limits have been removed in order to address rubber-type and biological materials. In fact, the theory was applied to a rubber square plate with a very satisfactory comparison of numerical and experimental results for the vibration responses in the frequency and time domains at different excitation levels, but also with comparisons of dissipated energy and loss factor. The identification of the energy dissipated by the linear damping terms and the nonlinear damping terms was also carried out. The comparison of Fig. 4-12 with the analogous figure obtained by Amabili [108] for a stainless steel rectangular (almost square) plate shows a reduced importance

of the cubic damping for the rubber plate. The main differences in term of parameters between the two plates are the (i) stiffness and fundamental natural frequency, (ii) linear damping ratio, and (iii) the thickness ratio h/a. In particular, the rubber plate has a linear damping ratio more than ten times larger than the stainless steel plate and a thickness ratio 0.01288 instead of 0.002, which is more than six times larger, while the natural frequency is reduced little more than four times. Therefore, it may be possible to speculate that the increase of the damping and thickness ratio can be the main reasons for a reduced nonlinear damping effect for the rubber plate with respect to the stainless steel plate. However, further experiments are necessary to separate the effects of the material and geometric parameters.

4.11 ACKNOWLEDGEMENTS

4.12 APPENDIX A: FRACTIONAL DERIVATIVE

A periodic vibration response can be expanded in the complex Fourier series

$$x(t) = \sum_{n=-\infty}^{\infty} a_n \, e^{i2n\pi t/T}, \tag{4.83}$$

Where

$$a_n = \frac{1}{T} \int_0^T x(t) \, e^{-i2n\pi t/T} \, \mathrm{d}t, \tag{4.84}$$

i is the imaginary unit and T is the principal period. It is assumed that the zero-order value a_0 of periodic functions has zero fractional derivative. The fractional derivative of order $0 < \alpha \leq 1$, based on the Weyl integro-differential operator, is defined as (West, Bologna & Grigolini, [113]),

$$D_t^\alpha x(t) = \frac{\mathrm{d}^\alpha x(t)}{\mathrm{d}t^\alpha} = \sum_{n=-\infty}^{\infty} (i2n\pi/T)^\alpha \, a_n \, e^{i2n\pi t/T}, \tag{4.85}$$

It is useful to observe in eq. (4.85) that

$$i^{\alpha} = e^{i\alpha\pi/2} = \cos(\alpha\pi/2) + i\sin(\alpha\pi/2). \tag{4.86}$$

Eq. (4.85) is not the only definition available of fractional derivative. The most used definitions of fractional derivative are probably the Riemann-Liouville left and right-hand formulations (West, Bologna & Grigolini,[113]), the Caputo (Di Paola, Pirrotta & Valenza, [115]), and the Grunwald-Letnikov one (Zu, Cai & Spanos, [116]). It is interesting to observe that different definitions of fractional derivative lead out to expressions that are not equivalent. For example, according to the Riemann-Liouville formulation, the fractional derivative of a periodic function is non-periodic, which makes it not convenient in dealing with harmonic functions. However, the definition of the Weyl fractional integral is in complete agreement with the Riemann-Liouville definition of the fractional derivative with the lower bound of the integral being -∞ (West, Bologna & Grigolini, [113]).

For $x(t) = \sin(\omega t)$ or $\cos(\omega t)$, where $\omega = 2\pi/T$, the Weyl fractional derivative of order α gives

$$D_t^{\alpha}\sin(\omega t) = \omega^{\alpha}\left[\cos\left(\alpha\frac{\pi}{2}\right)\sin(\omega t) + \sin\left(\alpha\frac{\pi}{2}\right)\cos(\omega t)\right], \tag{4.87}$$

$$D_t^{\alpha}\cos(\omega t) = \omega^{\alpha}\left[\cos\left(\alpha\frac{\pi}{2}\right)\cos(\omega t) - \sin\left(\alpha\frac{\pi}{2}\right)\sin(\omega t)\right]. \tag{4.88}$$

For $\alpha = 1$, the classical first derivative is obtained, while $\alpha = 0$ gives the original function.

For $x(t) = a e^{i\omega t}$, the Weyl fractional derivative of order α gives

$$\begin{aligned} D_t^{\alpha}\left(a e^{i\omega t}\right) &= a\,\omega^{\alpha}\left[\cos\left(\alpha\frac{\pi}{2}\right)e^{i\omega t} + i\sin\left(\alpha\frac{\pi}{2}\right)e^{i\omega t}\right] \\ &= \omega^{\alpha}\cos\left(\alpha\frac{\pi}{2}\right)x(t) + \omega^{\alpha-1}\sin\left(\alpha\frac{\pi}{2}\right)\dot{x}(t). \end{aligned} \tag{4.89}$$

5 NONLINEAR VIBRATIONS OF NUCLEAR FUEL ROD

After the successful attempt to model the nonlinear stiffness and damping of rectangular rubber plates, slender metallic tubes in various configurations were tested for large amplitude vibrations. In total, six configurations were tested. Slender tubes represent fuel rods inside the nuclear fuel assembly of pressurized water reactors. Understanding their damping variation during large amplitude vibrations will help engineers design more efficient nuclear fuel assemblies against seismic excitations. The damping variation studied here can also be used for similar applications involving slender beams. The experimental data measured during this part of the study are unique as they feature one-to-one internal resonance, jump-ups, jump-downs, and fluid-structure interaction. A parameter identification tool (based on the SDOF model approximation) developed earlier was used to extract the nonlinear stiffness and damping parameters for two of the six configurations. The results of this study are published in the journal Nuclear Engineering and Design and are presented here in this chapter.

Non-linear vibrations of nuclear fuel rods

Giovanni Ferrari [a], **Prabakaran Balasubramanian** [a], Stanislas Le Guisquet [a], Lorenzo Piccagli [b], Kostas Karazis [c], Brian Painter [c], Marco Amabili [a]

[a] McGill University, Dept. of Mechanical Engineering, Macdonald Engineering Bldg.,
817 Sherbrooke St. W, Montreal H3A 0C3, Quebec, Canada
[b] University of Parma, Dept. of Industrial Engineering, Mechanical Engineering Building,
Parco Area delle Scienze, 181/A, 43124 Parma PR, Italy.
[c] Framatome Inc., 3315 Old Forest Rd., Lynchburg, 24501 VA, USA

5.1 ABSTRACT

Single zirconium alloy nuclear fuel rods with clamped-clamped boundary conditions and subjected to harmonic excitation at various force levels were experimentally studied. Different configurations were implemented and the fuel rods were tested in air and submerged in quiescent water. Moreover, the effect of the contained fuel pellets was also reproduced by representative

metallic pellets inside the rods. Non-linear stiffness and damping parameters were extracted from experimental vibration response curves by means of a specifically-developed identification tool. For the cases where the fuel pellets were removed or axially compressed, it was found that the axial-symmetry of the fuel rod resulted in a pronounced one-to-one internal resonance. The internal motion of fuel pellets is source of friction and impacts during vibrations, thus complicating further the linear and non-linear dynamic behavior of the system. A very significant increase of the viscous modal damping with the vibration amplitude was observed during geometrically non-linear vibrations, which is particularly relevant and in advantage of safety.

5.2 INTRODUCTION

Clusters of cylindrical arrays subjected to external flow, with axial and cross flow components, are common in the power generation [117-119] and aerospace component manufacturing [120] industries. In most cases these arrays are designed to minimize the fluid-structure interaction induced by the flowing fluid to avoid large amplitude array instabilities. Nevertheless, flow-induced vibrations of cylindrical arrays remain a significant performance and safety concern in the power generation industry. Past studies [121] have estimated that the cumulative damages for the power industry over a decade, due to fluid-elastic instabilities of cylindrical arrays, are close to one billion US dollars. A recent example of flow-induced vibration failure in the power generation industry is the premature failure of the San Onofre nuclear plant steam generators that ultimately cost approximately three to four billion US dollars at the utility ratepayers' expense.

In nuclear plants, fuel assemblies are used in the reactor core to provide the fuel for the generation of power. In pressurized water reactors (PWR), a fuel assembly is defined by the United States Nuclear Regulatory Commission (US NRC), to be a structured group of fuel rods which are long, slender, zirconium metal tube(s) containing pellets of fissionable material, which provide fuel for nuclear reactors. Spacer grids are utilized to bundle the fuel rods in a square configuration to form a fuel assembly. Fuel assemblies and fuel rods, in classical PWR square, hexagonal or CANDU type cores, are subjected to flowing water and are susceptible to large fluid-structure oscillation amplitudes [118, 122, 123]. In addition, seismic and loss-of-coolant accident conditions generate *external* excitations that could induce undesired complex fuel assembly component oscillations. Thus, flow-induced vibration remains a significant component

failure mechanism for nuclear reactors and is related to plant safety and operating plant costs. In addition, tubes used in steam generators undergo similar types of complex excitations and suffer from similar types of flow induced instabilities [124]. Even though flow induced vibrations have been studied extensively and empirical formulations are available for use in the nuclear industry, questions related to the underlying mechanisms for the onset of rod instability (*e.g.,* flow-induced damping, internal resonances, effect of pellets, and so on) when subjected to complex boundary conditions, flow conditions and external excitations remain unanswered.

Previous studies in the literature have investigated numerically the fluid coupled vibrations of fuel bundles [125, 126] as well as flow induced vibrations of fuel rods and heat exchanger tubes [127-135]. A detailed finite-element analysis of the behavior of fuel rods supported by nuclear fuel grids in quiescent water and a comparison with experiments can be found in [136]. Furthermore, flow-excited vibrations of a single mockup fuel rod were measured by De Pauw *et al.,* [137]. Fuel rod non-linear vibrations are also related to wear due to fretting in correspondence of the spacer grids and may lead to fuel leaks; the impact of fluid-induced vibration and of the gap during operation between rods and grids were investigated numerically [138-140].

Non-linear parameter identification of the coupled systems is difficult but important. A number of approaches to develop numerical tools for the identification of non-linear parameters that play significant role in large amplitude oscillations are described in [141]. Furthermore, the work by Piteau *et al.,* [142] cites a number of challenges for specific identification tools designed to extract experimental fluid-elastic forces. Adhikari and Woodhouse [143, 144] in a two-series study developed theoretical models identifying viscous and non-viscous damping parameters based on experimental results for modes and frequencies of a system. A more recent development to identify the non-linear parameters of large fuel rod vibrations is the work by Alijani *et al.*, [22]; Amabili *et al.*, [58]; and Delannoy *et al.*, [145]. The tools developed in the last three studies help the designer in identifying useful dynamic parameters that describe the large-amplitude vibrations reached by structures, at their resonant frequencies, during experiments and possibly during operation. The work in these recent papers consisted of reference experiments on simple geometries with and without fluid-structure interaction and the development of simplified numerical tools and methods for the identification of non-linear

vibration parameters of vibrating structures. More complex cases involving internal resonances - the non-linear interactions between different vibration modes at one resonant frequency - were also considered (Delannoy *et al.*, [146]).

In the present study, a number of dedicated vibration experiments and subsequent identification of critical system parameters were performed on zirconium alloy nuclear fuel rods provided by Framatome in order to characterize the non-linear behavior of nuclear core elements. Single fuel rods were subjected to clamped-clamped boundary conditions and to linear and geometrically non-linear vibrations in absence and in presence of quiescent surrounding fluid. Flowing fluid conditions, clusters of tubes and spacer grids were excluded by the present investigation but will be featured in upcoming studies.

The large amplitude vibration of single fuel rods under harmonic excitation in a small frequency range around a resonant frequency can be described by a single degree-of-freedom (DOF) modified Duffing oscillator (Amabili [5]). The 1-DOF oscillator can model a wide variety of non-linear vibration phenomena such as non-linear jumps in vibration amplitude, hysteresis cycles and several types of instability leading to chaos. Geometrical non-linearities are taken into account by the modified Duffing equation and the presence of internal resonances can be taken into account by a model with two degrees of freedom. The vibration amplitude for such an oscillator undergoing forced external harmonic excitation is controlled by damping around resonance. The evolution of damping of a fuel assembly in flowing water has been studied in the past (Viallet and Kestens, [147]) indicating a nonlinear relationship between reduced damping coefficient and the first eigenfrequency of the fuel assembly for different oscillatory amplitudes and irradiation conditions. For fuel rods, the weak nonlinearity of the hydrodynamic damping with respect to fluid flow velocity is described in Connors *et al.* [148] and an empirical formulation to describe damping is established. Additional studies (Hassan, [149]) investigated the effect of damping on triggering multi-span tube instabilities using time domain modeling for tube arrays. Finally, experimental and theoretical studies on flow-induced fuel assembly and fuel rod damping highlighted the nonlinear response of the fuel assembly and fuel rod for higher flow conditions and different types of external excitation (Brenneman and Shah, [150]; Collard *et al.*, [151]; Fardeau *et al.*, [152];). Modeling of the damping parameters for flow induced vibrations was investigated by Vandiver [153] who recommended the definition of a dimensionless

damping parameter for cylinders experiencing flow-induced vibration. It is well understood that damping in the nonlinear regime can be described by several models; for instance, an innovative non-linear damping model is discussed in recent papers by Amabili, [111] and Balasubramanian *et al.*, [2]. A traditional modal damping ratio, based on viscous dissipation, was retained in the current study. Its value has to be adjusted according to the vibration amplitude in order to capture the experimental results. This is a clear indication that damping and stiffness are both non-linear. While the presence of geometrically non-linear stiffness is well known, the presence of a strong increase of damping with the vibration amplitude is still not established in the literature on nonlinear dynamics. Since the vibration amplitude in the non-linear regime is not proportional to the excitation amplitude, the current study conducted stepped-sine experiments at several constant force amplitude levels, thus implying the identification of one damping ratio per force amplitude level. In previous studies it had been shown that, for sufficiently large excitation levels, damping increases with the amplitude of the response in plates and panels (Alijani *et al.* [22]; Amabili & Carra, [154]; Amabili *et al.*, [58]) and in water-filled circular cylinders (Delannoy *et al.*, [146]; Amabili *et al.*, [67]). The present research shows that damping increases for fuel rods as well, which constitutes an obvious safety design advantage.

The presence of one-to-one internal resonances in axisymmetric structures significantly complicates the damping behavior as the increasing energy of large amplitude vibrations is not only dissipated through non-linear damping but also transferred from the main vibration mode (*driven mode*) to the non-linearly coupled mode (*companion mode*). Since the distribution of kinetic energy between two modes reduces the maximum amplitude reached by the vibration of each mode, this phenomenon may correspond to a reduction of the severity of the oscillation.

Uranium pellets, normally present inside fuel rods during operation with a spring-operated system to keep the pellets compressed during operation, were included as mechanically equivalent inert metal pellets were inserted inside the rods. A compression system was implemented to reduce the axial play of the pellets. Pellets are supposed to introduce two strongly non-linear mechanisms – dry friction and shocks – while they move with respect to each other and shake against the fuel rod walls. These phenomena were not modeled mathematically in the present work, although their effect on the non-linear vibrations of the system under test was studied experimentally as they manifested themselves during laboratory testing. In general,

modeling the effect of pellets on the stability of the fuel rod system is rather difficult (Park *et al.*, [155]), but it could be approximated by comparing the natural frequencies from modal test results of the rod with pellets against the tube without pellets. Impacts and dry friction constitute ultimately non-linear mechanisms of energy dissipation. Therefore, their effect on vibration is captured by the non-linear dependence of the equivalent modal damping parameter on vibration amplitude. It has to be noted, however, that the motion of the pellets constitutes an additional "internal" (in the sense that it is not visible outside the tube but describe vibrations happening inside it) degree of freedom of the physical system, which is modelled less accurately by the 1-DOF Duffing equation.

5.3 EXPERIMENTAL SETUP

Several hollow zirconium rods were sourced and employed for experiments. These rods are identical to the ones used in fuel assemblies of pressurized water reactors. However, they are made shorter and are not filled with real nuclear fuel pellets. The zirconium rods considered in the tests are 988 mm long and the distance between the two supports is 900 mm (free length); this distance is slightly larger than the common distance between two spacer grids in the fuel assembly. This small difference in length is not expected to alter the dynamic response of the fuel rod system. The external diameter is 9.50 mm and the wall thickness 0.61 mm. The material properties of the zirconium alloy are displayed in Tab. 5-1. One end of the zirconium rods is flared to facilitate the insertion into the spacer grids that group nuclear fuel rod bundles inside nuclear cores. The other end presents a clamping diameter. Fig. 5-1 shows one example of the fuel rod used in the test.

Density $(kg.m^3)$	Young's modulus (GPa)	Poisson's ratio
6450	95	0.37

Tab. 5-1: Material properties of a zirconium-alloy rod

(a)

(b)

(c)

Fig. 5-1: Zirconium fuel rod under test, (a).
Clamping end (b); insertion end (c).

Test rods were provided both empty and filled with cylindrical tungsten carbide pellets, which model uranium fuel pellets in terms of dimension and density. The ratio between the weight of the rod filled with tungsten pellets and the empty rod is 5.80. A radial gap between the pellets and the internal wall of the zirconium rod is present. Being that the sum of the axial length of the pellets is slightly shorter than the axial clearance present inside the zirconium fuel rods, a modest axial gap is also present. In an operating nuclear reactor, axial springs keep fuel pellets tightly packed while allowing thermal expansion. Some of the zirconium rods in the present study were tested without recovering the axial gap, thus leaving the fuel pellets free to move axially and radially. In some other rods a simple threaded device was installed to keep the pellets in a tightly packed configuration axially. It must be noted that such precaution prevents axial play but does not prevent the radial motion of the pellets – although the latter becomes more difficult as the friction between the pellets limits or anyway modifies the radial motion.

During operation, nuclear fuel rods are grouped in bundles through the use of metallic spacer grids with sliding contacts. The experiments described in the following paragraphs feature simplified fixed-fixed boundary conditions. These reference boundary conditions were chosen so that the focus is on the fuel rod structure and its material behavior rather than on the constraints.

A steel frame was designed; the possibility of axial displacement while not being excited was allowed through the use of dedicated bolts, since the dynamics of beams fixed at the two ends is strongly dependent on thermal stresses. The frame is shown and described in Fig. 5-2 and Fig. 5-3. The axis of the rod was kept parallel to the ground as gravity does not play a significant role in the dynamics of the beam, thanks to its light weight.
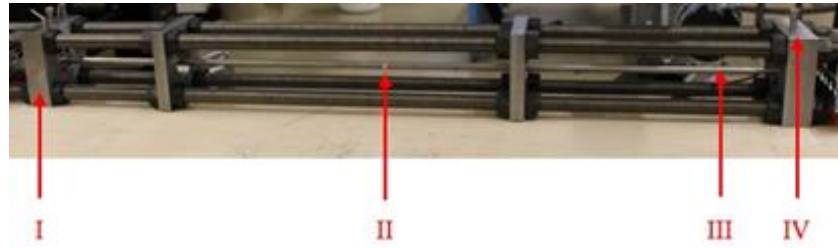
Fig. 5-2: Vibrating system complete with boundary conditions: I) steel frame; II) vibrating zirconium alloy rod; III) forced vibration excitation system; IV) axial pre-stress release bolts.
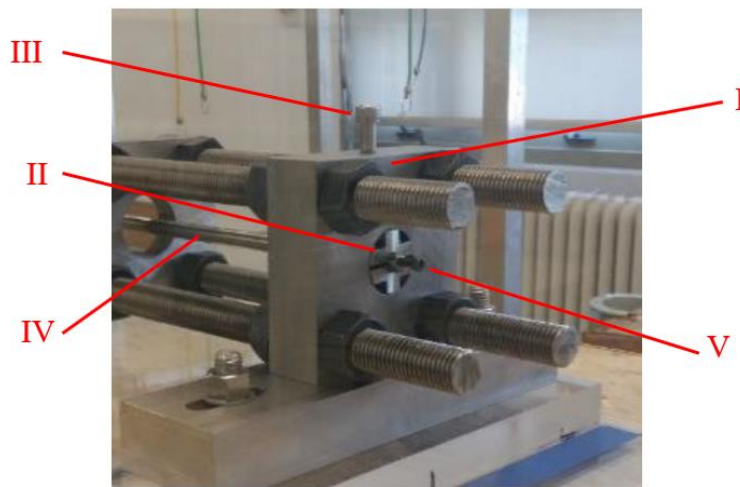
Fig. 5-3: Detail of the practical implementation of fixed boundary conditions: I) heavy-weight bases; II) two-piece sleeve; III) axial pre-stress release bolts; IV) fuel rod; V) set screw for the axial constraint of fuel pellets.

Vibration experiments were conducted in presence of air and in presence of quiescent water surrounding the nuclear fuel rods. In this study the body of still water in the tests has been chosen large enough to approximate an infinitely extended volume around the fuel rod, thus reducing the fluid-structure interaction effect to a virtual added modal mass given by the fluid displaced during vibrations. The water body was implemented by building a transparent acrylic

tank 1524 mm long, 300 mm wide and 300 mm deep. The previously described stainless steel frame can be secured to the base of the tank by means of bolts. The tank does not include a lid so that the water presents a free surface. This is useful to allow access to instrumentation and measurement systems while it was verified that no sloshing waves of any meaningful amplitude happen.

An electrodynamic exciter (Brüel & Kjær model 4810) was used to apply a lateral dynamic force excitation 50 mm away from one end of the rod in horizontal or vertical direction, depending on the practical requirements of the specific tests; this distance was chosen so that low frequency modes of the rod were excited without giving excessive interaction between the exciter and the structure during large amplitude vibrations. A force transducer (Brüel & Kjær model 8203) was interposed so that real time force measurement is obtained during vibration. The forced vibration excitation system is shown in Fig. 5-4.
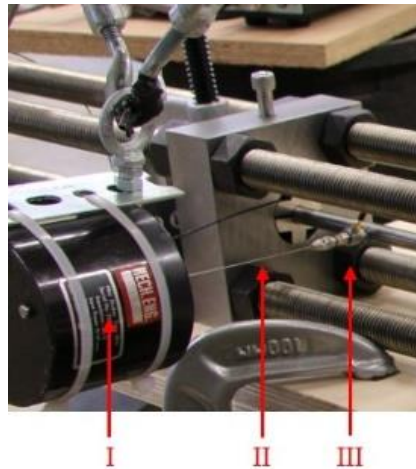
Fig. 5-4: Detail of the forced vibration excitation system: I) electrodynamic exciter Brüel & Kjær 4810; II) harmonic steel wire stinger; III) force transducer Brüel & Kjær 8203. A Brüel & Kjær amplifier model 2718 is needed to power the electrodynamic exciter.

The weight of the vibrating structure is extremely low; therefore, a non-contact measurement system based on laser Doppler vibrometry was employed. Laser Doppler vibrometers are capable of measuring the vibration of structures even in presence of surrounding water. The acrylic walls of the water tank do not constitute a problem since they are transparent. The measurement system is presented in Fig. 5-5.
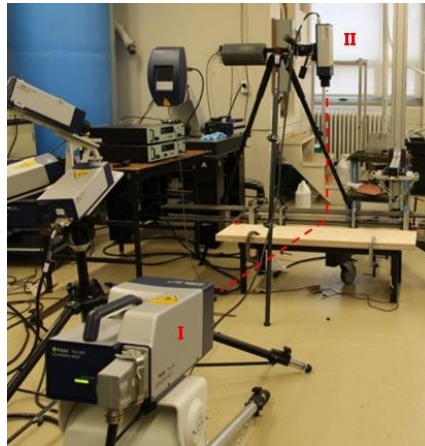
Fig. 5-5: Measurement by laser Doppler vibrometry: I) Polytec PSV 400 scanning head, measuring the horizontal component of vibration; II) Polytec OFV 505 single point head, measuring the vertical component of vibration.

A scanning laser head by Polytec was employed for the measurement of several points along the rod, which allowed for the reconstruction of mode shapes and the application of experimental modal analysis. In particular, broadband pseudo-random excitation signals were used to obtain the Frequency Response Function of the structure. For large-amplitude vibrations, accurate single point laser heads by Polytec were used. Since the transversal section of the rod is axisymmetric, two identical normal modes are expected to appear in orthogonal planes sharing the same natural frequency. The mode directly excited (driven mode) is the one laying in the plane of the dynamic excitation force, while the companion mode appears in the orthogonal plane if the excitation amplitude is sufficient to activate non-linear coupling (Amabili [5]). Consequently, one laser head was oriented horizontally and one vertically for the measurement of the motion of the beam at its mid-length: each laser measures one of the two modes. The mid-length point was chosen as the first (fundamental) mode of the rod has an antinode there. While geometrical imperfections could modify the location of the antinode, it was verified experimentally that no displacement of the antinode was measurable. The stepped-sine excitation technique was used to obtain frequency-amplitude curves at several forcing levels. A sinusoidal signal is employed to apply high energy levels at specific frequencies; the amplitude of the signal is kept accurately constant by means of a feedback control algorithm and the frequency varies slowly and monotonically in a neighborhood of the resonance frequency of interest. Force

feedback is required because the force generated by electrodynamic exciters is not proportional to the driving signal around resonance. The monotonous variation of the frequency is required because hysteresis cycles and instabilities may arise. It has to be noted that the study of the first resonance only can be approximated with a one-degree-of-freedom nonlinear model and vibration measurement in one direction only is required, unless internal resonances appear. The stepped-sine algorithm is managed by a data acquisition and post-processing system produced by LMS TEST LAB® (Siemens). During the experiments the closed-loop control for the force, which is kept constant when the frequency is varied, was set with a tolerance of 0.5 %. The laser Doppler vibrometers are instead extremely precise.

5.4   EXPERIMENTAL RESULTS

A large quantity of experiments was carried out in numerous configurations. In fact, the vibration of the zirconium rods was studied both in absence and in presence of surrounding quiescent water. In both configurations the effect of nuclear fuel pellets was also investigated by considering completely empty rods, rods containing freely moving pellets and rods containing pellets blocked axially by means of a dedicated set screw. Moreover, several configurations showed clearly the appearance of a one-to-one internal resonance, giving rise to a circumferentially traveling wave as a combination of the driven and companion modes. While the two vibration modes happen in two orthogonal planes, their composition appears as a traveling wave around the axis of the rod due to a phase shift. That is, the geometric center of each normal section of the rod appears to follow an elliptical or circular trajectory. This phenomenon is caused by the axial symmetry of the structure. It is likely that during the operation of a nuclear reactor several factors break the symmetry of the configuration of the nuclear fuel rods, thus limiting severely or preventing the appearance of such traveling waves. In one experimental configuration, symmetry breaking was introduced and the resulting vibration was studied. In total, consequently, we have seven experimental configurations that will be described in the sub-sections: 3.1 Empty rod in air; 3.2 Empty rod in air with axial symmetry breaking; 3.3 Rod with freely moving pellets in air; 3.4 Rod with axially constrained pellets in air; 3.5 Empty rod in water; 3.6 Rod with freely moving pellets in water; 3.7 Rod with axially

constrained pellets in water. For each sub-section, the linear experimental modal analysis results are initially presented in a table giving the mode shapes, natural frequencies and damping ratios. The normal mode sequence remains the same for all tests, which simplifies the presentation. Afterwards, for each sub-section, several figures are employed to present non-linear vibration results.

Non-linear vibrations are described by frequency-amplitude curves and frequency-phase curves (amplitude and phase diagrams present several curves measured at different force amplitude levels). These diagrams show together results for increasing and decreasing of the excitation frequency ("UP" and "DOWN" curves, respectively), which differ since the response of non-linear systems depends on the history of the system itself. The non-linearity in the rod is due to geometrical non-linearity in the stiffness (i.e. due to large enough deflection that makes the hypothesis of linear mechanics no more applicable). In particular, a clamped rod presents a stiffness that increases with the deflection; this is referred to as hardening type system.

The non-linear vibration response of clamped rods is typically hardening: the frequency at the peak of the vibration amplitude increases with the value of the harmonic excitation force. This means that the non-linear resonance (i.e. the peak of the vibration response) is obtained progressively at higher frequencies when the excitation is increased. A typical non-linear response is obtained by putting together both the measured "UP" and "DOWN" curves for each excitation level. In fact, the "UP" curve starts at low frequency and follows the stable solution until the peak of the vibration response is reached. Since at this point the solution has a fold and then becomes unstable (Amabili, [93]), the "UP" curve jumps down to the stable solution after the second folding point. On the other hand, the "DOWN" curve starts at higher frequency and then decreases the excitation frequency following the stable solution until the second folding point is reached. Here the "DOWN" curve jumps up to the upper stable solution, and then it follows it. The "UP" and "DOWN" curves coincide before the first jump and after the second jump; observed differences in these regions are due to measurement inaccuracy. Due to the multiple solutions and the jumps, UP curves reach larger vibration amplitudes than DOWN curves for hardening non-linear systems. The different behaviour of "UP" and "DOWN" curves create a hysteresis.

Another very important nonlinear feature of the rod is the following: it presents double

eigenvalues with two mode shapes that are in magnitude the same but orthogonal in space. In linear vibrations, if one excites the beam with a force of constant direction, it is expected to see the vibration happening in the plane of the excitation force. However, in non-linear vibration, the fact that two natural modes have exactly the same natural frequency allows to transfer energy for the mode directly excited (driven mode) to the orthogonal one (companion mode). This phenomenon is called one-to-one (1:1) internal resonance (Amabili, [5]). The non-linear vibration of the rod does not happen in one plane only; the plane of the excitation force contains the driven mode, while the companion mode appears in the orthogonal plane. When a phase difference of about 90 degrees is observed between the driven and companion modes and their vibration amplitude is about the same, the combination of the two standing (i.e. with fixed nodes in space) mode shapes give rise a vibration mode shape with nodes that travel around the rod: in this case the rod vibration describes a circle. This phenomenon is a particular feature of non-linear vibrations and of the one-to-one internal resonance that appears for axisymmetric systems. It is also very interesting to observe that the one-to-one internal resonance is active just in a narrow frequency range, when the excitation frequency matches the resonance frequency of this double eigenvalue. When this internal resonance is activated, the companion mode is abruptly activated and, when this happens, the driven mode reduces its vibration amplitude: this gives an energy sharing between the two modes.

Nonlinear curves are presented for both driven and companion mode. Where necessary, some further comparisons between driven and companion modes have been included to show the nonlinear interaction between the two.

The typical measurement error can be estimated evaluating the difference between the "UP" and "DOWN" curves before and after the jump zone, where they should coincide.

5.4.1 EMPTY ROD IN AIR

The modal analysis of the empty rod in air gives a series of normal modes of vibration that corresponds perfectly to what can be predicted numerically by means of reduced order models or finite element models for a fixed-fixed rod of isotropic zirconium alloy. Each one of the first four vibration modes presents a number of longitudinal flexural half-waves equal to the order of the mode, as shown in Fig. 5-6; the corresponding sum of the Frequency Response Functions (FRFs)

is shown in Fig. 5-7. The same mode order was observed in all the experimental cases under study. The modal damping values are extremely low, as displayed in Tab. 5-2. It was verified that the first four vibration modes and the external excitation share the same plane.
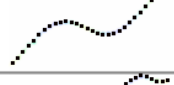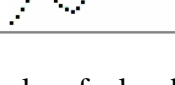
MODE	LONGITUDINAL WAVES	MODE SHAPE
I	1	
II	2	
III	3	
IV	4	

Fig. 5-6: Normal modes of vibration of a fixed-fixed nuclear fuel rod, experimentally determined.
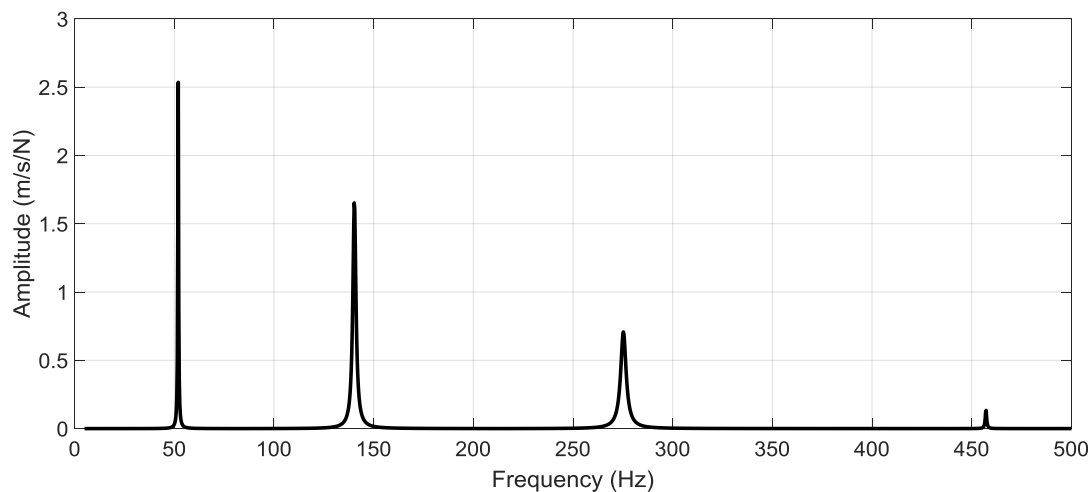
Fig. 5-7: Sum of the FRFs for the empty rod in air configuration.

No. half waves	Mode number	Frequency (Hz)	Damping (%)	Viscous damping coefficient (N s/m)
1	I	51.94	0.41	0.094
2	II	140.33	0.67	0.462
3	III	257.27	0.60	0.755
4	IV	457.14	0.09	0.201

Tab. 5-2: Modal parameters of the empty rod in air

If excited by sinusoidal forces of constant amplitude around the first natural frequency, the rod presents vibrations as large as 2 mm for a force of only 0.1 N in the direction of the excitation. This represents a vibration amplitude approximately 3.3 times larger than the thickness of the rod, but five times smaller than the diameter. The non-linear character of the vibration is evident by the examination of the frequency-amplitude curves of the driven mode (vibration in the same plane of the excitation) for increasing excitation frequency in Fig. 5-8. In fact, non-linear jumps are present at the maximum vibration amplitude of each curve. These jumps are present even for the lowest force amplitude experimentally tested with the stepped-sine algorithm. The trend of the response is clearly hardening, since the peak vibration frequency shifts towards higher values for larger forces. Fig. 5-9 shows the non-linear amplitude curves for the companion mode and finally Fig. 5-10 presents together the driven and companion modes. The companion mode is always activated and a traveling wave in circumferential direction is present since the companion and driven modes share a portion of frequency-amplitude curves.
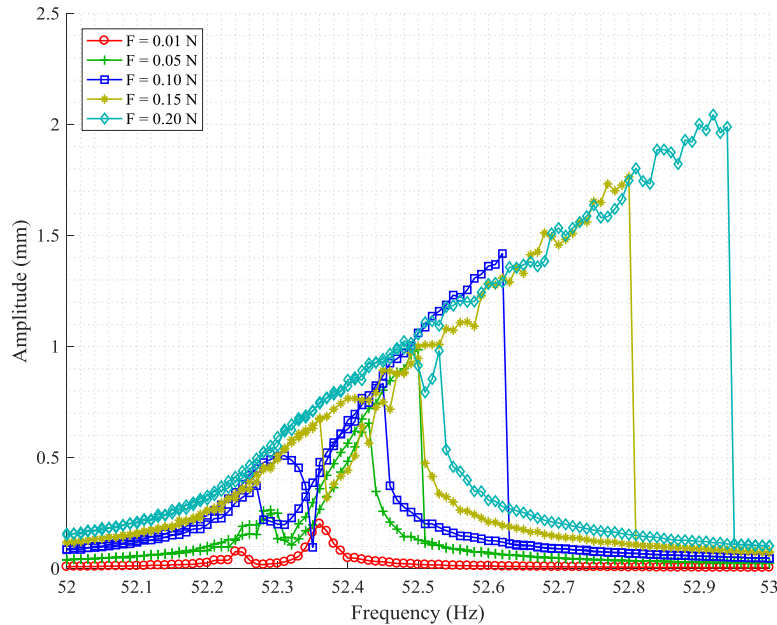
Fig. 5-8: Frequency – Amplitude curves for the driven mode of the empty rod in air.
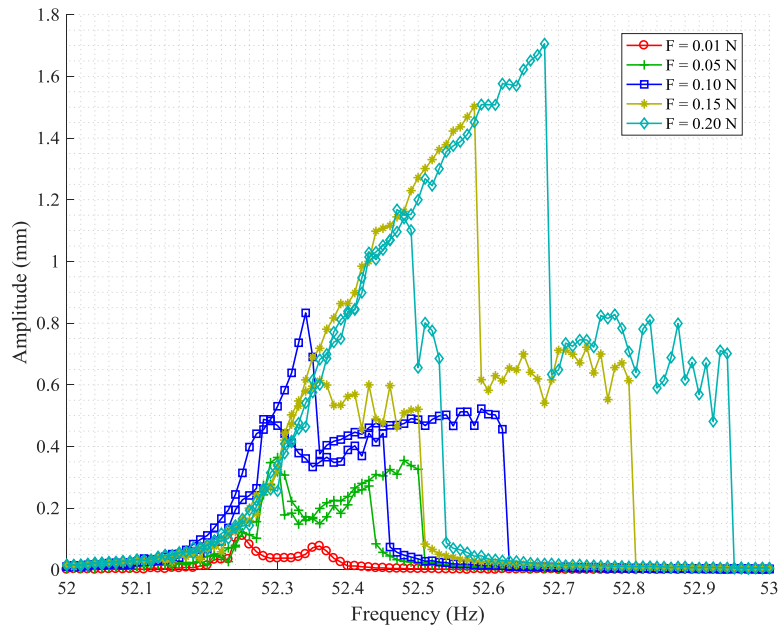
Fig. 5-9: Frequency – Amplitude curves for the companion mode of the empty rod in air.
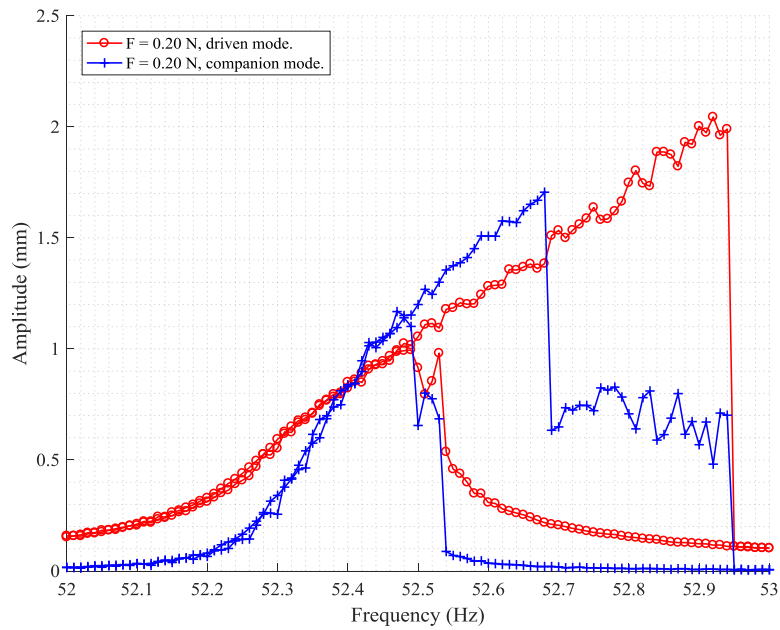
Fig. 5-10: Driven and companion mode, empty rod in air.

5.4.2 EMPTY ROD IN AIR WITH AXIAL SYMMETRY BREAKING

In this case it was attempted to break in the symmetry of the vibrating rod in air, so that no one-to-one internal resonance was activated. One-to-one internal resonances in rods appear because such systems are perfectly symmetric with respect to the longitudinal axis. Therefore, there are two identical normal modes of bending character at each natural frequency. The angle between the two planes of these modes is 90 degrees. However, the angular orientation of these two planes with respect to an absolute reference system is not defined. In general, if an external force excitation is present, one normal mode will lie on the plane of the excitation and it will be named driven mode. Systems of imperfect axial symmetry may still present two identical bending modes at 90 degrees. However, a frequency split will appear between the two natural frequencies. If the frequency split is sufficiently large, the two modes do not interact in the non-linear regime and one mode may fall completely outside the frequency neighborhood of the resonance of the other mode.

In this case, a protruding 50 g steel mass was glued at one half of the length of the rod, location of the maximum vibration amplitude for the first normal mode of the structure. The protruding mass was positioned in the plane of the companion mode. In correspondence of linear motions of the geometric center of the rod, the inertia of the mass applies identically to both driven and companion mode; however, the rotary inertia given by the mass increases the moment of inertia around the neutral axis of the bending given by the companion mode to a greater extent. As a result, the frequencies of both modes decrease, but the natural frequency of the companion mode decreases further and falls outside the frequency range of the driven mode. The identification of the non-linear parameters of this system is particularly relevant and will be discussed in a following section. The experimental frequency-amplitude curves in case of frequency split reveal, in Fig. 5-11, a standard hardening behavior with non-linear jumps and hysteresis from 0.1 N excitation onwards.
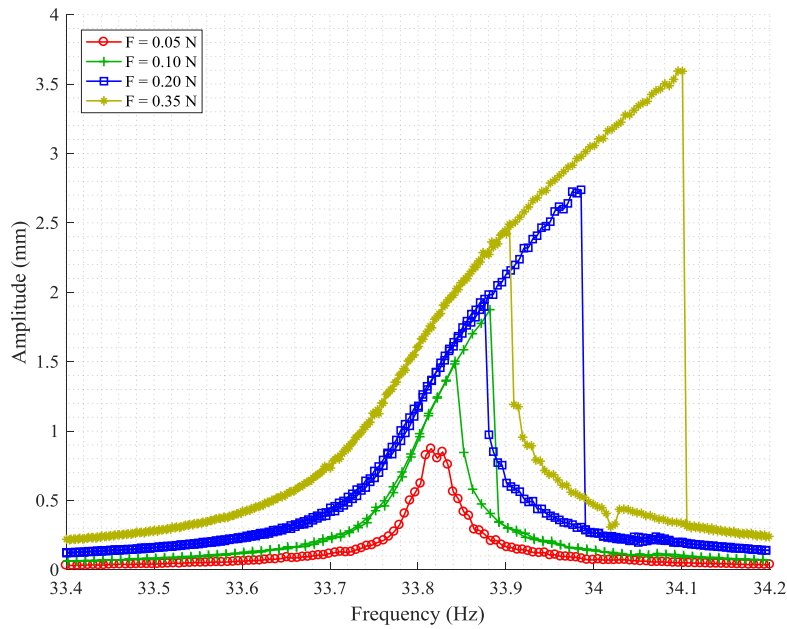
Fig. 5-11: Frequency – Amplitude curves for the empty rod in air with added central mass.

5.4.3   ROD WITH FREELY MOVING PELLETS IN AIR

The presence of the added mass of pellets reduces the natural frequencies of the system, as shown in Tab. 5-3 (no added steel mass in these experiments). Since the pellets are free to move inside the rod, they do not change the stiffness of the rod. Damping is larger than in the case without pellets and larger forces are required to excite large amplitude vibrations. Mode IV was not detected at all. A mixed behavior, initially softening and then hardening, is shown by the driven and the companion modes in Fig. 5-12 and Fig. 5-15. Nonlinear jumps are presents beyond a force level of 2 N. Only beyond 7 N the driven mode is disturbed by the appearance of the companion mode. Hysteresis cycles of modest amplitude are detected.

   The companion mode, shown in Fig. 5-13, does not appear for forces lower than 5 N, approximately. It shows the same mixed softening-hardening behavior of the driven mode. Beyond 9 N of excitation level, the companion mode shows a quite unique behavior as it begins to decrease with force amplitude. This result seems due to the presence of the pellets. With the increase of the force level, some energy is likely to be not only transferred from the driven mode to the companion mode, but also to be dissipated by the motion of the pellets. Examining the

relative amplitude of driven and companion mode in Fig. 5-14, it can be noted that a perfect traveling wave is not developed. The amplitude of the companion mode remains lower than the amplitude of the driven mode.

A comparison of the phase curves of driven and companion mode at a fully nonlinear regime (Fig. 5-15) shows that the phase difference between the two modes while the imperfect traveling wave is present is approximately 90 degrees as expected. Although the phase angle is shown for the full frequency range (from 20 to 23 Hz), the meaningful part for the companion mode is only between 21.8 and 22.7 approximately, since outside this range the amplitude of the companion mode is practically zero. Driven and companion mode are not only perpendicular in space but also in phase quadrature. Therefore, while one reaches the maximum vibration amplitude, the other presents zero vibration amplitude. The result is that the composition of the sinusoidal motions of the transversal sections of the beam along two perpendicular axes appears as following a circular trajectory, characteristic of the traveling wave phenomenon. If the amplitude of driven and companion mode is not identical, the trajectory is not circular but elliptical.

No. half waves	Mode number	Frequency (Hz)	Damping (%)
1	I	21.65	0.53
2	II	56.27	4.10
3	III	108.31	7.27
4	IV	-	-

Tab. 5-3: Modal parameters of the rod with freely moving pellets in air
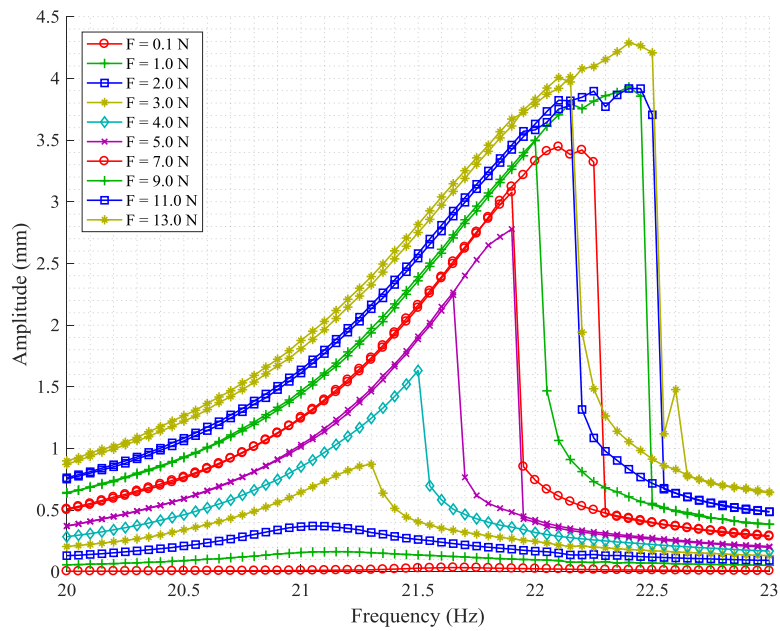
Fig. 5-12: Frequency – Amplitude curves for the driven mode of the rod with freely moving pellets in air.

Fig. 5-13: Frequency – Amplitude curves for the companion mode of the rod with freely moving pellets in air.
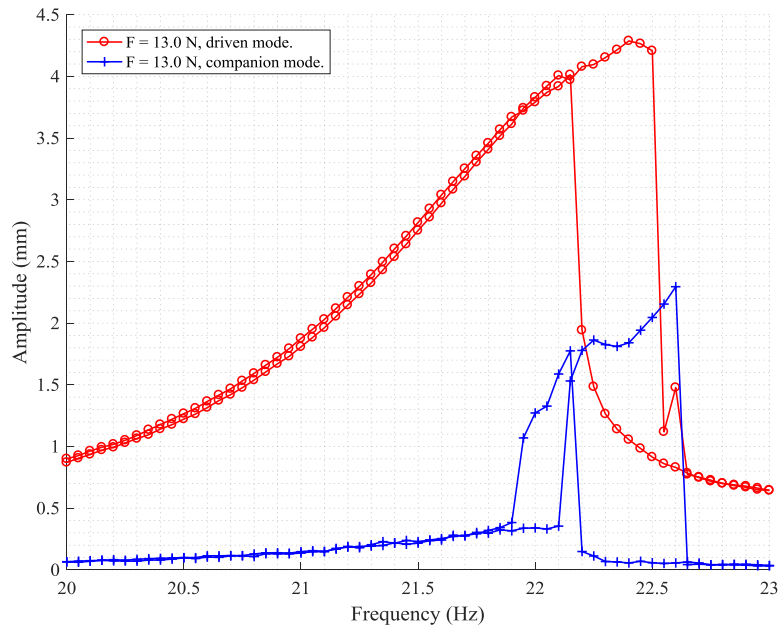
Fig. 5-14: Driven and companion mode, freely moving pellets in air.
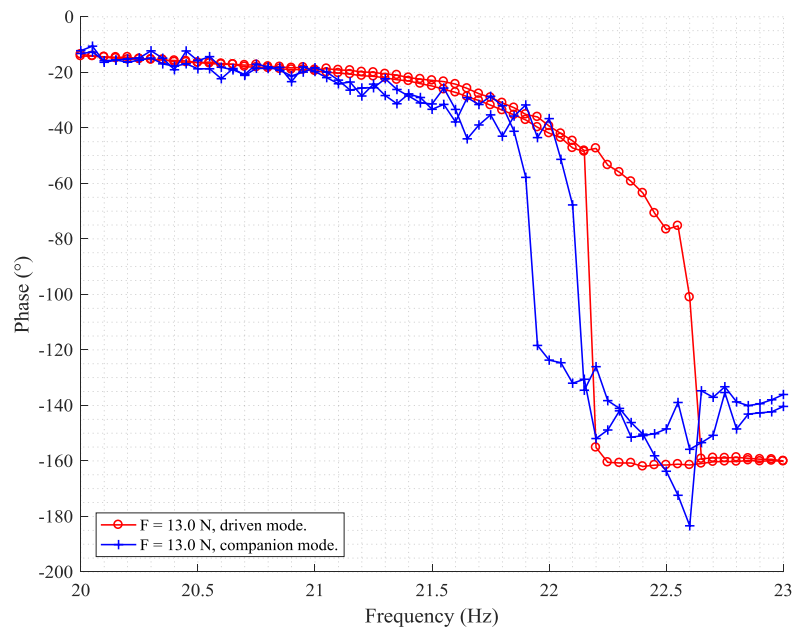
Fig. 5-15: Phase curves for the driven and the companion mode, freely moving pellets in air.

5.4.4 ROD WITH AXIALLY CONSTRAINED PELLETS IN AIR

With respect to the previous case, the mass of the vibrating system does not change. However, the stiffness is likely to increase since the pellets are compressed axially and are not free to move independently. The preload on the pellet stack, moreover, is transferred onto the beam walls, which are thus put into tension. Accordingly, the natural frequencies of the system increase. As it can be expected as well, the damping values are lower because the motion of the pellets and, correspondingly, their friction and impacts are reduced. The modal parameters are given in Tab. 5-4.

No. half waves	Mode number	Frequency (Hz)	Damping (%)
1	I	27.35	0.27
2	II	73.95	0.28
3	III	144.08	0.46
4	IV	236.91	0.31

Tab. 5-4: Modal parameters of the rod with axially constrained pellets in air.

The system requires higher forces to enter the non-linear regime than the empty rod but lower forces than the rod with free pellets. Observing the driven mode (Fig. 5-16) it is possible to notice that the behavior is slightly softening until a level of 3 N is reached. Afterwards, the behavior becomes hardening and non-linear jumps appear. All curves are disturbed by the resonance of the companion mode, which happens at lower frequencies than the resonance of the driven mode. DOWN and UP curves are identical up to 3 N, afterwards they differ and hysteresis cycles appear, although modest in amplitude.
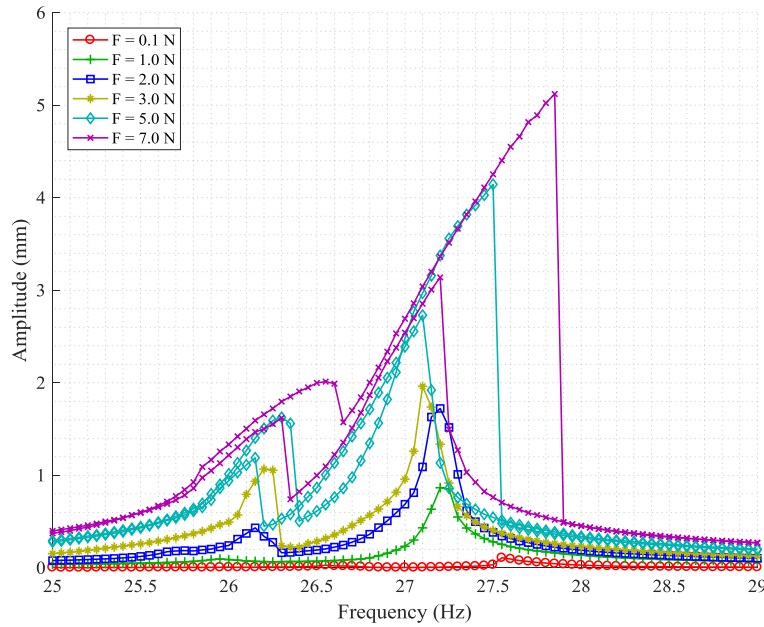
Fig. 5-16: Frequency – Amplitude curves for the driven mode of the rod with axially constrained pellets in air.

The companion mode (Fig. 5-17) is clearly coupled to the driven mode. The frequency-amplitude curve of the companion mode shows two peaks, similar to what is observed for the driven mode. However, the relative amplitude of these two peaks is exchanged, being the first peak larger for the companion mode for any force larger than 2 N. For excitation forces higher than 2 N, the first peak of the companion mode becomes higher and is followed by non-linear jumps. For a certain range of forces, the first peak of the companion mode is higher than the corresponding amplitude of the driven mode, as clearly shown in Fig. 5-18. The reverse is obtained at the second peak. Therefore, no pure traveling wave develops since the amplitude of the driven mode is not equal to the amplitude of the companion mode. The fact that the companion mode appears at frequencies different from the ones of the driven mode (for example, at lower frequencies in this experimental case) shows that the perfect symmetry of the system was broken. The main causes of unwanted symmetry break during experiments were found to be i) the action of gravity and ii) the fixed boundary conditions realized by means of the two-piece sleeve represented in Fig. 5-3. Gravity and eccentricity in the compression of the sleeve may in fact impart an initial curvature to the axis of the fuel rod, which deviates therefore from a
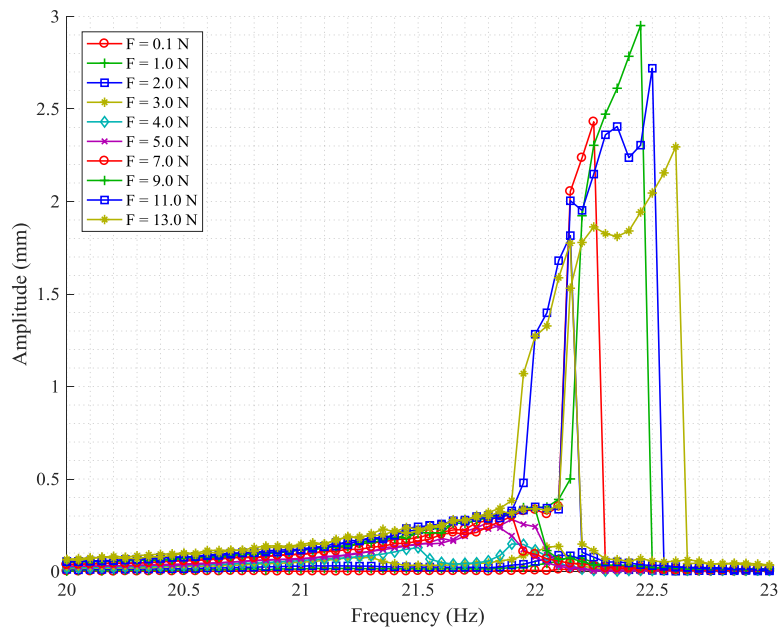
perfectly symmetrical configuration.
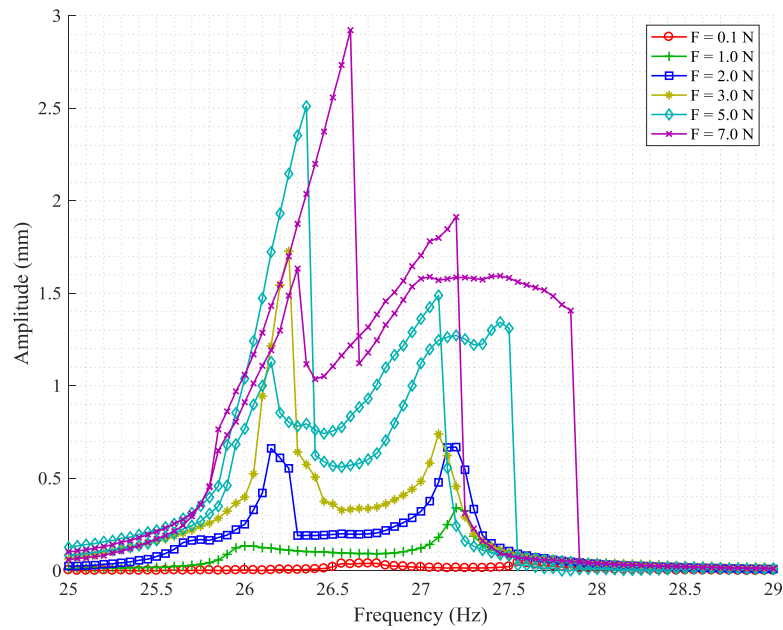
Fig. 5-17: Frequency – Amplitude curves for the companion mode of the rod with axially constrained pellets in air
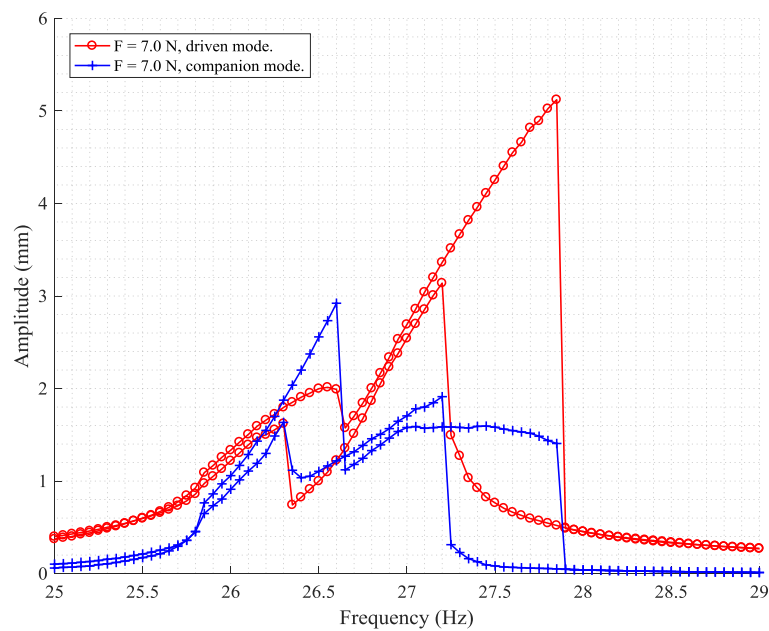
Fig. 5-18: Driven and companion mode, axially constrained pellets in air.

5.4.5 EMPTY ROD IN WATER

The natural frequencies in presence of water are lower than with the similar configuration in air, as presented by Tab. 5-5. When comparing Tab. 5-2 and Tab. 5-5, it appears that the viscous damping coefficients are increasing for the rod vibrating in water with respect to air: this is particularly evident for the first and 4th mode. The frequency change is also relevant, being of 20 % on average, which is also relevant in dissipation. The experimental ratio between the modal mass of the rod vibrating in water and the modal mass of the same rod vibrating in air is also given in Tab. 5-5 and varies between 1.39 and 1.63 for the four modes analyzed. The damping ratios are not so different in water and in air. The fact that still unconfined water does not affect damping ratio significantly in linear regime has been previously observed (Askari *et al.*, [156]). It must be noted that the dimensional form of viscous damping in still water is amplitude and frequency dependent (Sarpkaya, [157]).

No. half waves	Mode number	Frequency (Hz)	Damping (%)	Viscous damping coefficient (N s/m)	Modal mass in water/modal mass in air
1	I	41.12	0.78	0.227	1.59
2	II	112.66	0.42	0.361	1.55
3	III	218.65	0.50	0.740	1.39
4	IV	358.32	0.46	1.31	1.63

Tab. 5-5: Modal parameters of the empty rod in water.

However, frequency-amplitude curves in the non-linear regime show that, in presence of water, larger forces are required to achieve specific levels of vibration amplitude. The behavior remains linear up to a force of 1 N, as shown by Fig. 5-19. For forces below 1 N, the frequency at the amplitude peak of the driven mode is lower than the natural frequency in Tab. 5-5; such discrepancies are frequent in these experiments and are due to slight changes in the laboratory ambient temperature which are responsible for generating axial compression forces on the rod decreasing its natural frequency. As usual, the level of vibration amplitude remains below the dimension of the diameter of the rod, nevertheless several non-linear phenomena appear. After

1 N of excitation, the behavior is hardening but jumps appear only beyond 5 N, giving rise to hysteretic cycles of modest amplitude. For levels higher than 3 N, the curves of the driven mode are disturbed by the appearance of the companion mode.
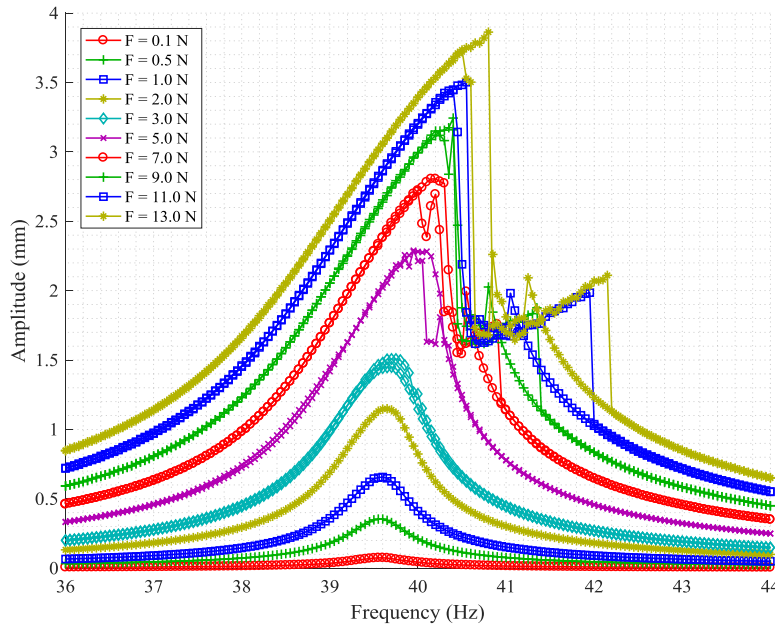
Fig. 5-19: Frequency – Amplitude curves for the driven mode of the empty rod in water.

The companion mode is presented in Fig. 5-20. As previously observed, it appears only for forces higher than 3 N and grows monotonically thereafter, showing jumps and hysteresis after 5 N. The companion mode appears in a small frequency range of about 2 Hz close to the peak of the driven mode. Its appearance "cuts" the peak of the driven mode, as clearly shown in Fig. 5-21. From the comparison of driven and companion mode in Fig. 5-21 it is possible to notice that a pure traveling wave is developed, since in the frequency range between 40.8 and 42.2 Hz the amplitude of the two modes is roughly equal. Observing the frequency-amplitude curves it could be argued that the growth of the driven mode in the direction of increasing frequency is impaired by the appearance of the companion mode with the resulting energy subtraction. Such complex behavior is typical of one-to-one internal resonances. The corresponding time-history curves, presented in Fig. 5-22, taken at 41.5 Hz show that the two vibration responses are in quadrature, not only spatially but also approximately in time (*i.e.* 90

degrees of phase), and have almost the same amplitude. This generates a pure travelling wave in angular direction, which means that the vibration mode is not fixed in space but rotates around the rod. This is also evident in phase curves (Fig. 5-23).
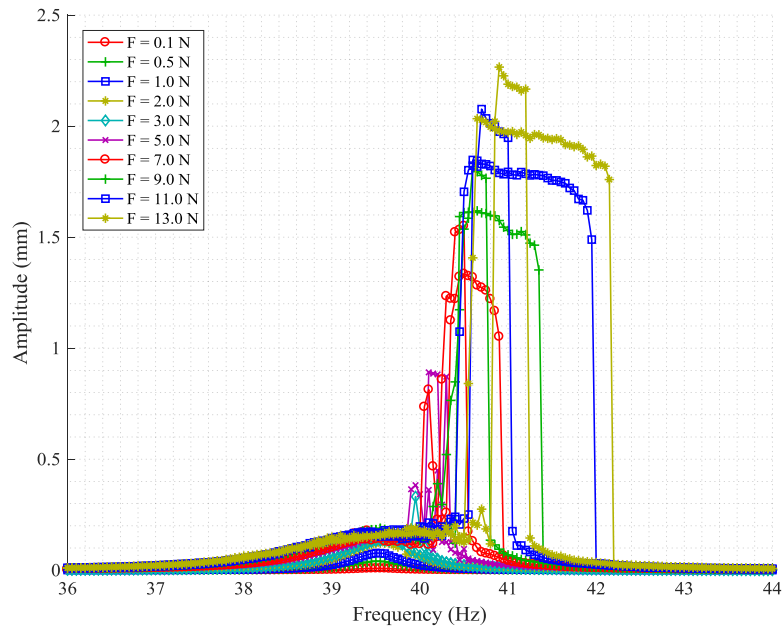
Fig. 5-20: Frequency – Amplitude curves for the companion mode of the empty rod in water.
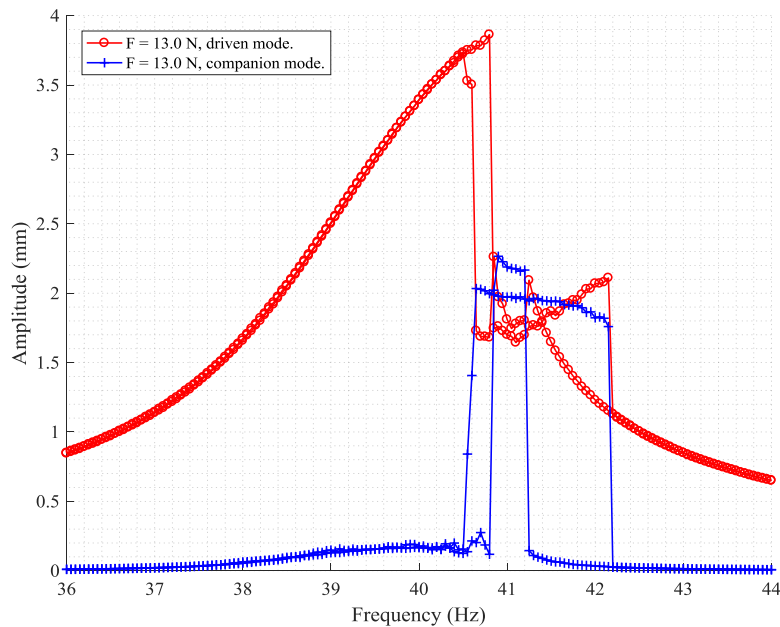
Fig. 5-21: *Driven and companion mode, empty rod in water.*
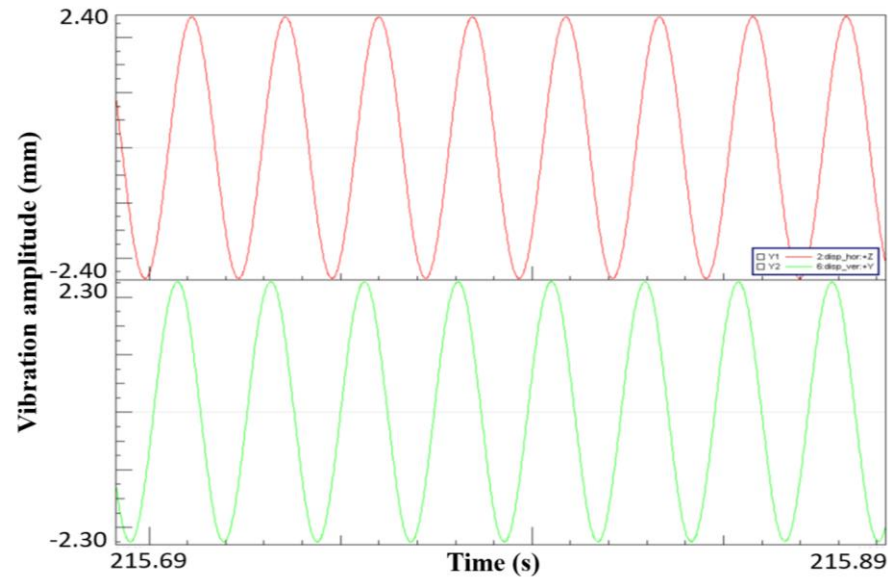
Fig. 5-22: Travelling wave phenomena, driven and companion mode, empty rod in water, 13N force (UP) at 41.5 Hz. Red: time response of the companion mode, top quadrant; green: time response of the driven mode, bottom quadrant.
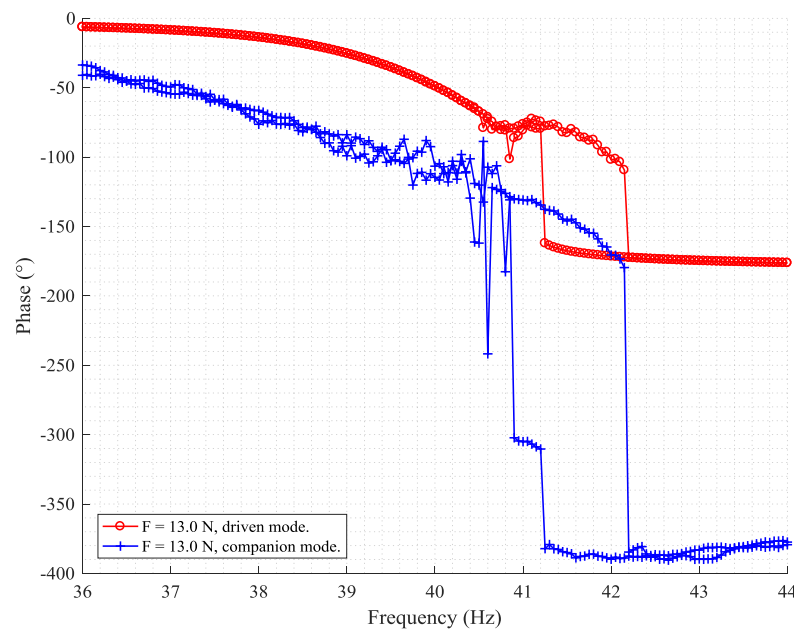
Fig. 5-23: Phase curves of the driven and companion mode, empty rod in water.

5.4.6 ROD WITH FREELY MOVING PELLETS IN WATER

With respect to the configuration with freely moving pellets in air, the modal analysis presented in Tab. 5-6 gives a reduction of 10 % of the natural frequency of the fundamental mode, which can be attributed to the added virtual mass constituted by water, while the second and third mode have very small frequency changes. The fourth mode was detected in this case. Damping for the fundamental mode is slightly reduced. However, a huge damping reduction was obtained for the second and third mode. A reason for this behavior is that, in the linear regime, lower amplitudes were reached in this case and, consequently, the motion of pellets was insignificant, so that less energy was dissipated in impacts and friction. In fact, damping ratios in Tab. 5-6 are very similar for all the first four modes. On the other hand, damping of the second and third mode was one order of magnitude larger for the rod with freely moving pellets in air, when pellets oscillation was important. Damping was so prevalent on the fourth mode that it was impossible to identify it experimentally. In the present case, this is not happening.

No. half waves	Mode number	Frequency (Hz)	Damping (%)
1	I	19.50	0.30
2	II	55.32	0.25
3	III	109.36	0.21
4	IV	181.13	0.24

Tab. 5-6: Modal parameters of the rod with freely moving pellets in water.

Non-linear frequency-amplitude curves show that, with respect to the same case in air, similar amplitudes are reached for a given excitation amplitude. For example, Fig. 5-24 shows a peak vibration amplitude around 5 mm for excitation of 13 N. For the same case in air, it was concluded that an effective amplitude of 4.8 mm, combination of driven and companion mode, was obtained for the same excitation force. The observed non-linear forced vibration response is initially softening and turns hardening at 5 N. Non-linear hardening jumps and hysteresis cycles are present from 7 N onwards only. The UP and DOWN curves remain very similar and hysteresis cycles remain modest.
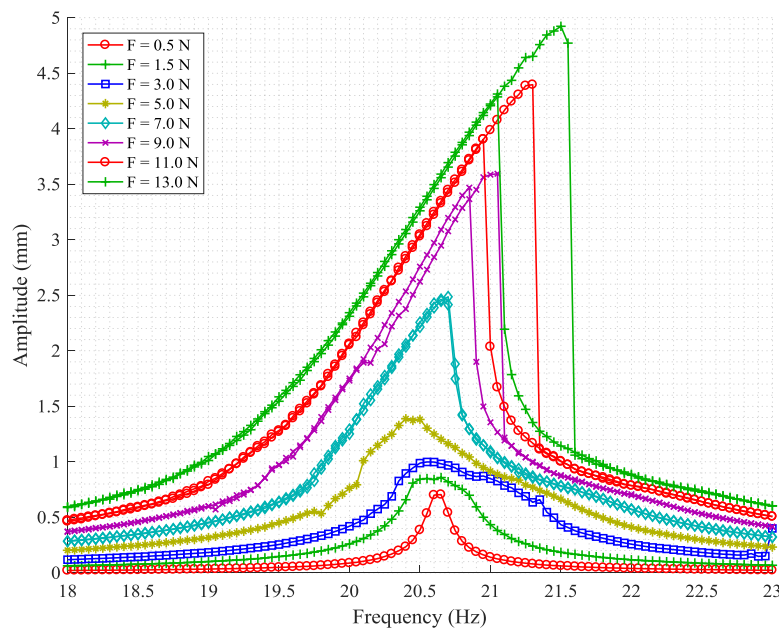
Fig. 5-24: Frequency – Amplitude curves for the driven mode of the rod with freely moving pellets in water.

The behavior of the companion mode, see Fig. 5-25 to Fig. 5-27, is interesting since it remains much smaller, and practically negligible, with respect to the driven mode even for high levels of force amplitude. It is likely that the energy transfer between driven and companion mode is disturbed by the energy absorbed by the motion of the pellets. The participation of the companion mode is so small that it is practically indistinguishable from the noise produced by the driven mode vibration at the node. It is safe to conclude that the companion mode is not activated in this case.

Fig. 5-25: Frequency – Amplitude curves for the companion mode of the rod with freely moving pellets in water.
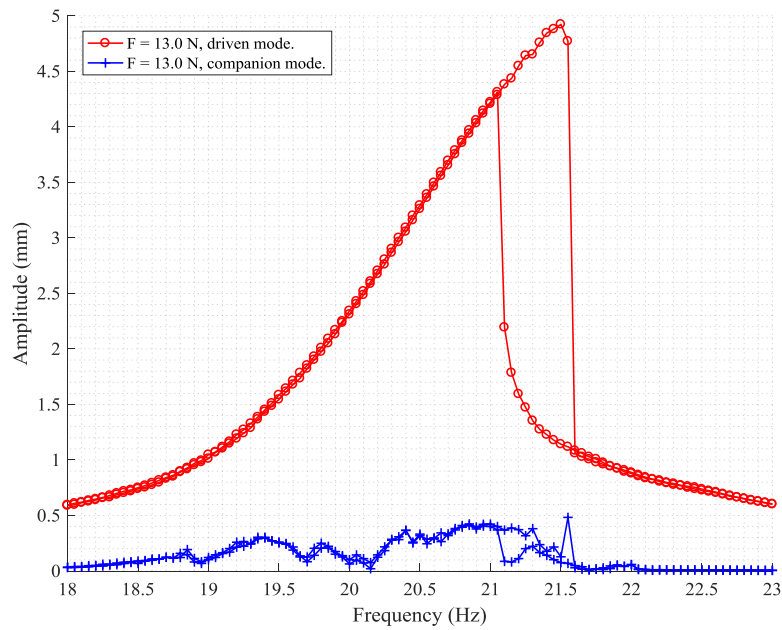
Fig. 5-26: Driven and companion mode, freely moving pellets in water.
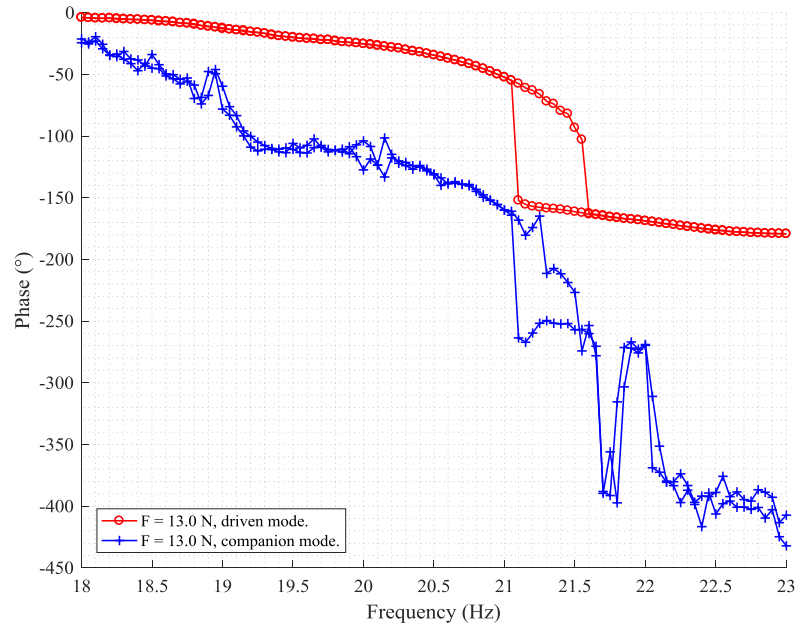
Fig. 5-27: Phase curves of the driven and companion mode, freely moving pellets in water.

5.4.7 ROD WITH AXIALLY CONSTRAINED PELLETS IN WATER

With respect to the rod with blocked pellets in air, the rod with axially blocked pellets in water presents lower natural frequencies, specifically reduced between 5 and 7% for all the four modes considered, and lower damping values except for the fourth mode, as shown in Tab. 5-7. The damping change is not as prevalent as in the case of freely moving pellets. This configuration requires larger forces to develop non-linear vibrations with respect to the other cases in this investigation. By observing the frequency-amplitude curves in Fig. 5-28, it is possible to notice that the highest vibration amplitude is not reached in correspondence of the highest level of excitation amplitude. This rare phenomenon could be justified by the fact that beyond 7 N the energy drawn by the companion mode is sufficient to reduce the peak vibration of the driven mode and, in fact, to split the peak of the driven mode into two lower peaks. A softening behavior is noticed under 1 N (i.e. only for the lowest three excitation levels), while thereafter an almost linear (very slightly hardening) behavior appears. No jumps and hysteresis are observed in this case. This indicates that damping values are sufficiently high during non-linear vibrations

to fully eliminate the unstable branch of the vibration response, which is the source of the jumps.

No. half waves	Mode number	Frequency (Hz)	Damping (%)
1	I	25.33	0.15
2	II	70.02	0.25
3	III	135.19	0.34
4	IV	219.69	0.54

Tab. 5-7: Modal parameters of the rod with axially constrained pellets in water.
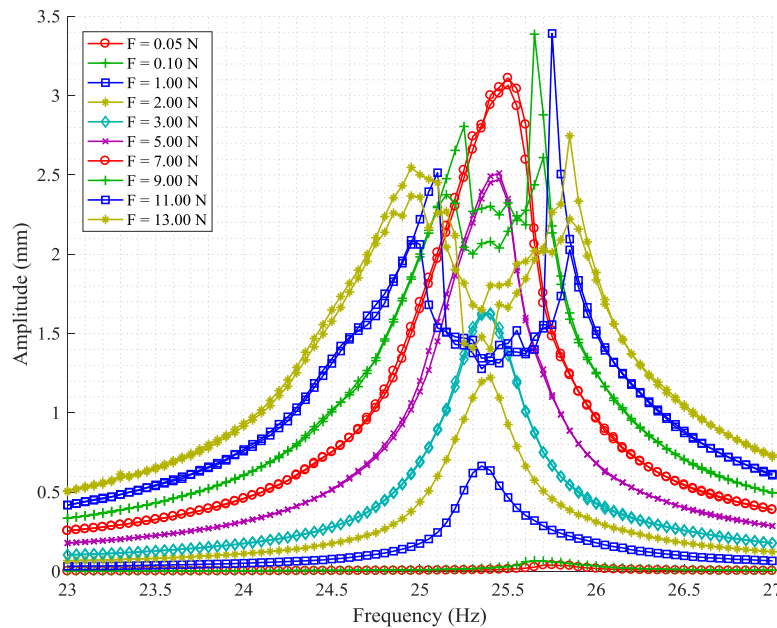
Fig. 5-28: Frequency – Amplitude curves for the driven mode of the rod with axially constrained pellets in water.

Non-linear hysteresis is modest and appears only after a force amplitude level of 7 N. UP and DOWN curves share a similar path. However, the peak amplitudes may differ. DOWN curves reach higher peak vibration amplitudes. The companion mode, presented in Fig. 5-29 , appears for forces larger than 1 N. Unlike the driven mode, the companion mode grows monotonically in peak amplitude with the forcing level. The companion mode remains lower than the driven mode below 7 N, afterwards the companion mode reaches and even goes beyond the amplitude of the driven mode. Frequency ranges of pure traveling wave are detected in Fig. 5-30 and Fig. 5-31. For excitation force equal to 13 N, a 2 Hz frequency range (between 24 and 26 Hz) of strong

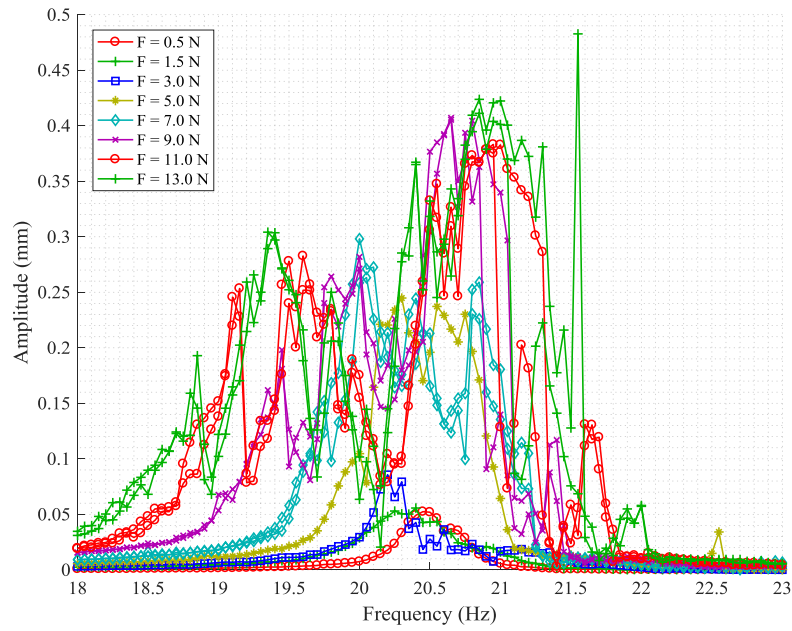interaction between driven and companion mode is detected.
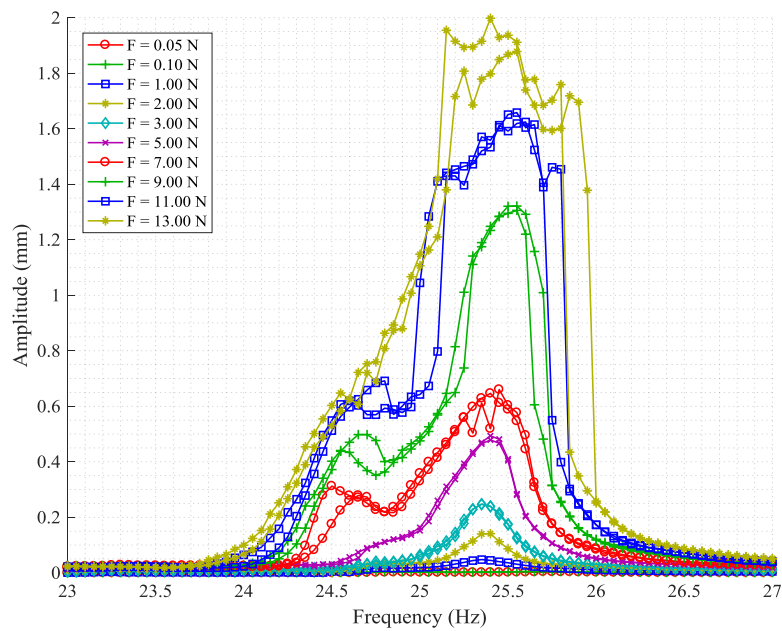
Fig. 5-29: Frequency – Amplitude curves for the companion mode of the rod with axially constrained pellets in water
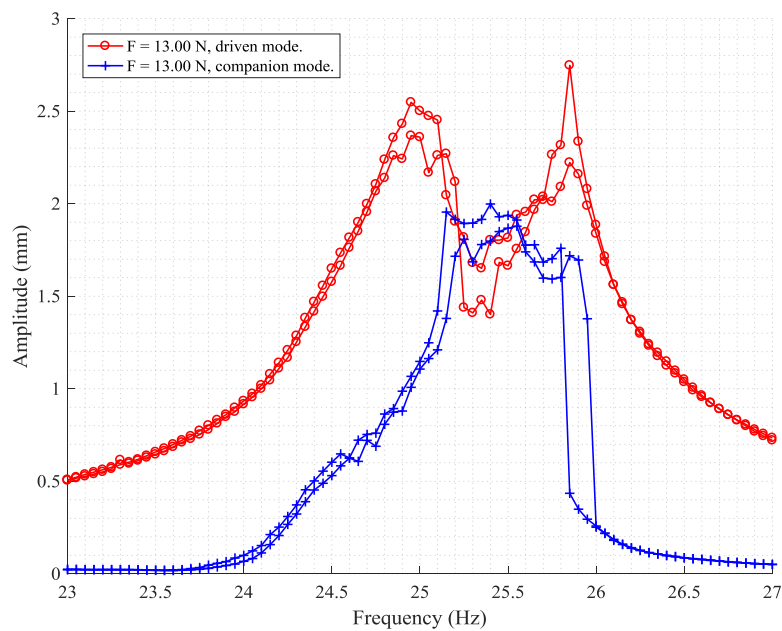
Fig. 5-30: Driven and companion mode, axially constrained pellets in water.
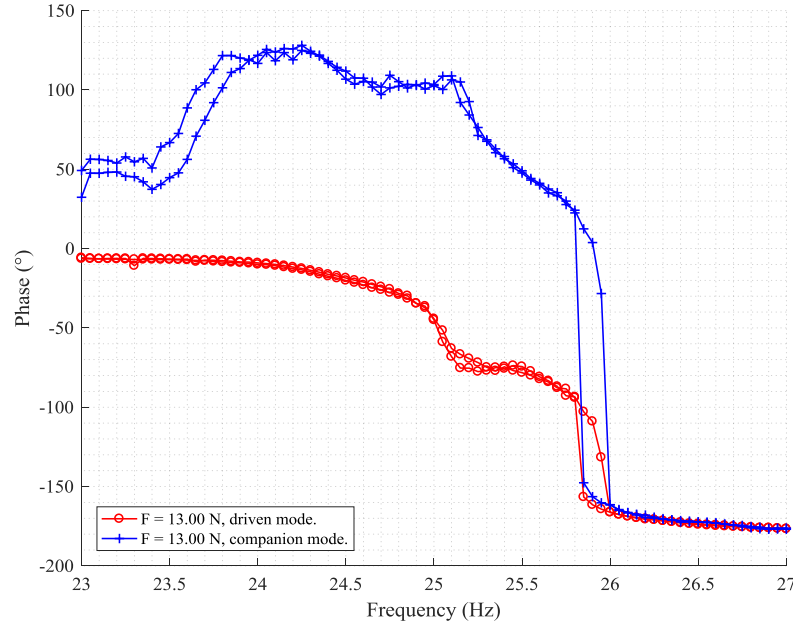
Fig. 5-31: Phase curves for the companion mode of the rod with axially constrained pellets in water.

5.5   IDENTIFICATION OF NONLINEAR PARAMETERS

5.5.1   IDENTIFICATION PROCESS

In order to model the non-linear vibration behaviors for design purposes, an identification of model parameters is needed. It has been achieved here for two cases. The first one is the single empty fuel rod with symmetry breaking achieved with a localized added mass. This rod does not present any one-to-one internal resonance and its behavior around the fundamental natural frequency can be described by using a single-degree-of-freedom nonlinear resonator which is a modified Duffing equation with quadratic and cubic non-linear stiffness. The second case is a single empty fuel rod in quiescent water presenting one-to-one internal resonance but no significant split of natural frequency between the excited (driven) mode and the coupled orthogonal (companion) mode. Therefore, this second case can be described by a two-degrees-of-freedom nonlinear resonator.

The single-degree-of-freedom model, in non-dimensional form, is given by

$$r^2 \ddot{x} + 2\zeta r \dot{x} + x + \eta_2 x^2 + \eta_3 x^3 = \lambda \, c_\lambda \, cos(t) \tag{4.90}$$

while the two-degree-of-freedom model is

$$\begin{cases} r^2\ddot{x} + 2\zeta r\dot{x} + x + \eta_2 x^2 + \eta_3 x^3 + \eta_3^{(c)} x x^{(c)2} = \lambda\, c_\lambda\, \cos(t) \\ \left(\dfrac{r}{\alpha}\right)^2 \ddot{x}^{(c)} + 2\zeta^{(c)}\dfrac{r}{\alpha}\dot{x}^{(c)} + x^{(c)} + \eta_2 x^{(c)2} + \eta_3 x^{(c)3} + \eta_3^{(c)} x^{(c)} x^2 = 0 \end{cases}$$

(4.91)

where x and $x^{(c)}$ are the dimensionless displacements of the rod at the central point: x is measured in the excitation plane (driven mode) and $x^{(c)}$ in the plane orthogonal to the excitation one and passing through the rod axis (companion mode); both of them are non-dimensionalized by dividing the vibration amplitude by the wall thickness of the rod (0.61 mm); r is the dimensionless frequency obtained by dividing by the natural frequency, α is the ratio between the companion and driven modes natural frequencies, λ is the dimensionless excitation force applied, c_λ is the ratio of the excitation force by the linear one, ζ and $\zeta^{(c)}$ are the damping ratios of the driven and companion modes, respectively, and η_2, η_3 and $\eta_3^{(c)}$ are the quadratic, cubic and coupling stiffness parameters, respectively. The solution of eq. (5.1) and eq. (5.2) is obtained by third-order harmonic balance. In the harmonic balance method, the displacements x and $x^{(c)}$ are replaced by a single-harmonic expansion of the experimental data, thus giving a system of algebraic equations from which damping ratios and stiffness parameters can be obtained. The dimensionless excitation force, along with the linear damping ratio, was previously identified by the linear system response obtained at low excitation force. The identification of the response is then processed over all frequencies and all excitation levels applying a least-squares method to the system of equations. In order to have a non-zero mean displacement and quadratic stiffness, since the experimental displacement data are obtained from velocity measurements, a more complicated minimization process is run, reconstructing the zero-order displacement. The identification tools used here are explained in detail in (Ferrari *et al.*, [158]) for the single-degree-of-freedom identification and in (Delannoy *et al.*, [146]) for the two-degrees-of-freedom identification. In particular, two different damping ratios have been identified for the two-degrees-of-freedom case for the driven mode, one (ζ_1) over the frequency range when the companion mode is not activated and a second one (ζ_2) in case of companion mode participation. For the companion mode, the single damping ratio $\zeta^{(c)}$ is used. Once the parameters are identified, the equations of motion are numerically integrated via the ODE45 routine of

MATLAB using an explicit Runge-Kutta (4th, 5th order) scheme over a time span sufficient to reach the steady-state. The steady-state time response obtained at each excitation frequency enables to obtain the numerical frequency-amplitude curves, which are compared to the experimental data.

5.5.2 RESULTS: EMPTY FUEL ROD WITH SYMMETRY BREAKING

The identification of the empty fuel rod with symmetry breaking has been run with no reconstruction of the mean displacement, thus assuming zero quadratic stiffness, since it displays a hardening behavior. The identified parameters are presented in Tab. 5-8.

Applied force (N)	ζ	λ	η_2	η_3
0.05	4.37 x 10-4			
0.10	4.42 x 10-4			
0.15	5.77 x 10-4	8.296 x 10-4	0	0.0017
0.20	6.03 x 10-4			
0.25	6.64 x 10-4			
0.30	7.20 x 10-4			

Tab. 5-8: Identified parameters of the single empty fuel rod with added mass

The numerical frequency-amplitude curves are plotted versus the experimental data in Fig. 5-32. Only some curves are displayed for clarity purposes.
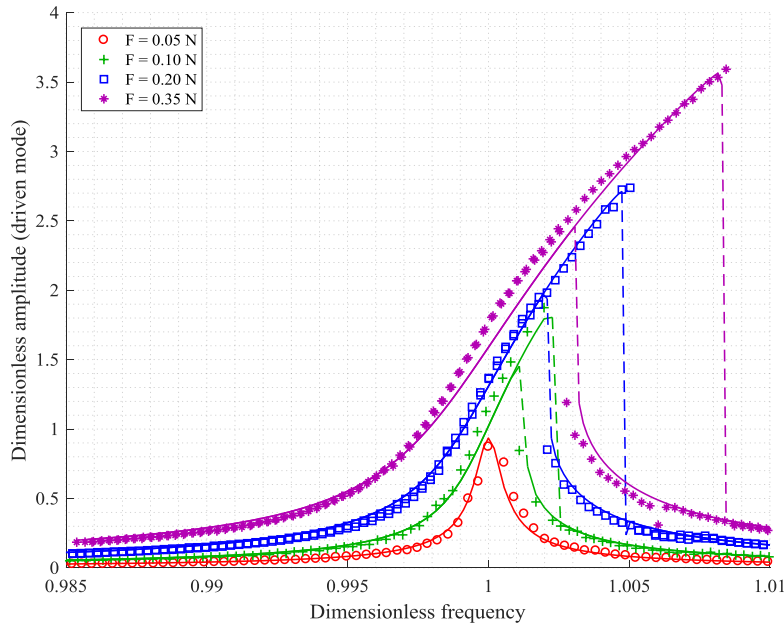
Fig. 5-32: Frequency response curves of the dimensionless amplitude of the first harmonic for the empty fuel rod with added mass. Experimental data are represented by markers while identified data are represented by continuous line.

It can be noticed that the model fits well the experimental data, without quadratic stiffness. Moreover, as shown by Fig. 5-33, the damping ratio increases with the applied excitation force up to 183% of the linear damping ratio for force excitation 0.35 N. This is a result of great relevance since it displays a very large damping increase in case of large-amplitude vibrations, which can be achieved by fuel rods only in exceptional conditions (*e.g.* large earthquakes). A large damping increase is clearly beneficial for safety.
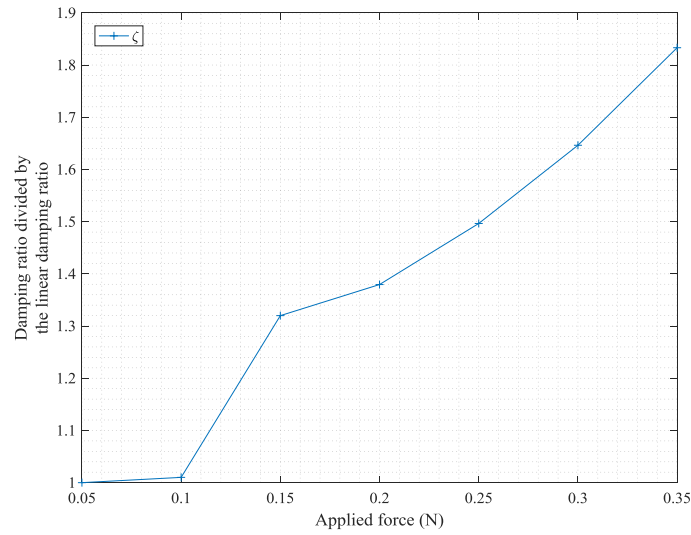
Fig. 5-33: Evolution of the damping ratio divided by the linear one versus the applied excitation force for the empty fuel rod with added mass.

5.5.3 RESULTS: EMPTY FUEL ROD IN QUIESCENT WATER

The identification of the empty fuel rod in quiescent water has been studied by the two-degrees-of-freedom version of the identification tool since it displays a one-to-one internal resonance. The identified parameters are presented in Tab. 5-9 and Tab. 5-10.

λ	η_2	η_3	$\eta_3(c)$
1.223×10^{-4}	0.7061	1.0429	3.4295

Tab. 5-9: Identified dimensionless force and stiffness parameters of the single empty fuel rod in quiescent water.

Applied force (N)	ζ_1	ζ_2	$\zeta(c)$
0.1	7.73×10^{-4}	-	-
0.5	7.99×10^{-4}	-	-
1	8.42×10^{-4}	-	-
2	9.29×10^{-4}	-	-
3	1.03×10^{-3}	1.08×10^{-3}	6.99×10^{-4}
5	1.15×10^{-3}	1.33×10^{-3}	1.13×10^{-3}
7	1.21×10^{-3}	1.56×10^{-3}	1.24×10^{-3}
9	1.30×10^{-3}	1.90×10^{-3}	1.20×10^{-3}
11	1.41×10^{-3}	2.22×10^{-3}	1.16×10^{-3}
13	1.51×10^{-3}	2.44×10^{-3}	1.26×10^{-3}

Tab. 5-10: Identified damping ratios of the single empty fuel rod in quiescent water.

The numerical frequency-amplitude curves, presenting the first harmonic of the vibration response, obtained by solving the equations of motion are plotted versus the experimental data for the driven mode in Fig. 5-34 and for the companion mode in Fig. 5-35. Only some curves are displayed for clarity purposes.
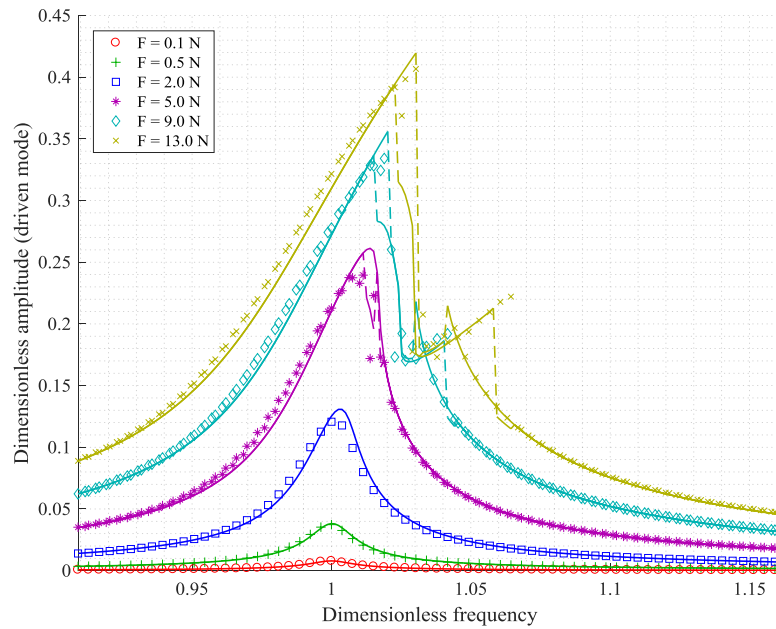
Fig. 5-34: Frequency response curves of the dimensionless amplitude of the first harmonic of the driven mode for the empty fuel rod in quiescent water. Experimental data are represented by

markers while identified data are represented by continuous line.
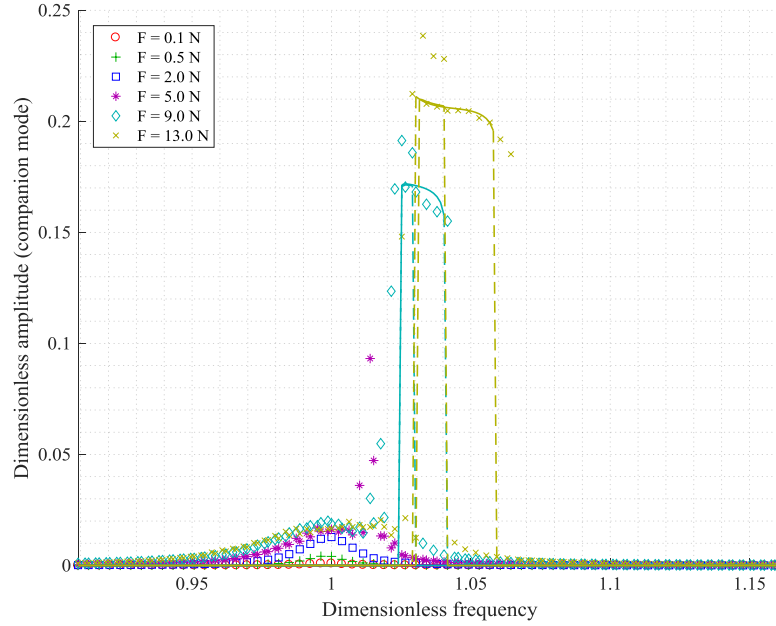
Fig. 5-35: Frequency response curves of the dimensionless amplitude of the first harmonic of the companion mode for the empty fuel rod in quiescent water. Experimental data are represented by markers while identified data are represented by continuous line.

It can be noticed that the model fits well the experimental data. Fig. 5-36 shows that the damping ratios increase with the applied excitation force. Indeed, the damping ratio of the driven mode increases regularly with the force when the companion mode is not activated, up to almost double for $F = 13N$. The damping of the driven mode when the companion mode is activated increases regularly with the applied excitation force up to triple its initial value for $F = 13$ N. The damping of the companion mode increases up to $F = 5$ N with the force, before stabilizing around an average of one and half times its original value. The companion mode has been considered activated only starting from $F = 3N$.
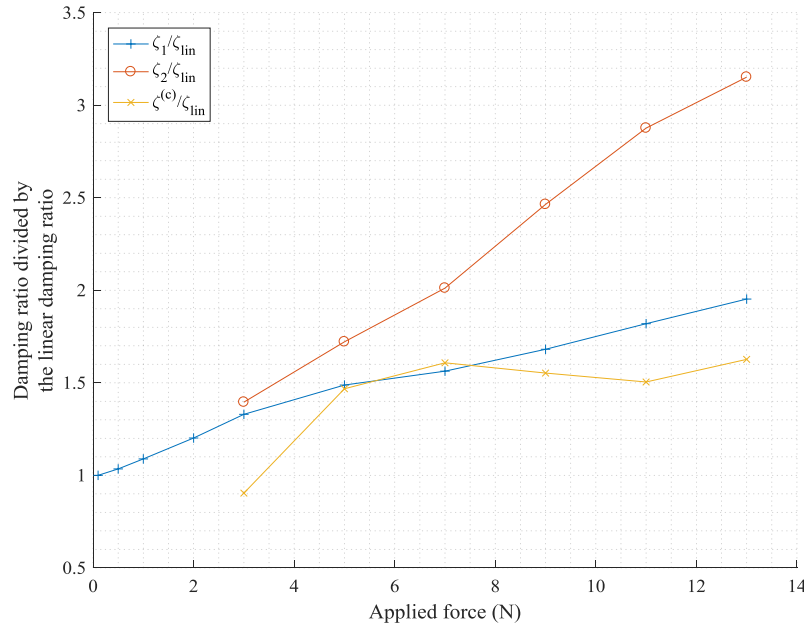
Fig. 5-36: Evolution of the damping ratios, for the driven mode when the companion mode is activated (O) or not (+) and for the companion mode (X), divided by the linear one versus the applied excitation force for the empty fuel rod in quiescent water.

It can be noticed that the driven mode damping is significantly higher in case of companion mode activation. Therefore, a larger energy dissipation is activated in case of one-to-one internal resonance. It appears that a constant damping ratio is not suitable to model such behavior. A reliable non-linear damping model seems very relevant in the design of nuclear fuel assemblies. The present study shows that a very relevant damping increase is observed for the simple case of a clamped fuel rod. Cluster of rods supported by spacer grids should be the next step to unveil the complex behavior of a fuel assembly.

5.6   CONCLUSIONS

The characterization of the forced vibration response of a nuclear fuel assembly in case of seismic excitation is a complex procedure as many factors contribute to the non-linear dynamic response of the system. This a preliminary study on the vibration response of a single clamped empty fuel rod in air and immersed in almost unconfined water. It investigates different

configurations in order to identify single effects, *e.g.* the presence of pellets and fluid-structure interaction, in the fuel rod response.

The experimental results presented were not previously available in the literature according to the authors. The experimental setup developed in this occasion has proven perfectly suitable for the measurement of the linear and non-linear dynamics of the rods immersed in water and it will be hopefully adapted successfully to even more complex dynamic experiments on nuclear fuel bundles. The presence of quiescent and almost unconfined water in turn has proven to be not particularly effective in modifying the dynamics of the fuel rods; the effect of the liquid is mostly that of an added virtual mass that reduces the natural frequencies of vibration. The vibration of empty rods is in general dominated by the one-to-one internal resonance due to the axial symmetry of the rod and by the appearance of traveling waves; non-linear features such as jumps between multiple stable solutions are appearing and damping values are modest. It is interesting to note that fuel rods often present a mixed softening-hardening behavior, probably caused by initial geometric imperfections (small initial curvature of the rod or axial force due to thermal expansion). Moreover, in all the cases under study, the trend of damping with excitation amplitude is non-linearly increasing, thus confirming previous findings for plates and shells (Alijani *et al.*, [22]). The increase of damping with excitation amplitude confirms the inadequacy of modal viscous damping to describe dissipation during large amplitude vibrations. The increase of damping acts in the direction of safety for nuclear applications.

The presence of pellets modifies substantially the linear and non-linear behavior of the system, in particular in relation to damping. Pellets constitute a separated vibrating system that is not described by the underlying single (or double in case of internal resonance) DOF model used for non-linear vibrations around a resonance. Therefore, their effect cannot be interpreted by the current simple model, which does not take dry friction and impacts into consideration. In any case, important non-linear vibration effects were noticed, such as the possible presence of thresholds levels for the energy dissipation of pellets and of saturation levels for vibration. The presence of pellets also seems to act in the direction of added safety, since their motions dissipates the kinetic energy. The presence of pellets also interacts with the energy transfer between driven and companion modes. The energy interaction between driven and companion mode, once again, reduces the maximum vibration amplitude along one direction thus increasing

apparent damping and safety.

Future developments of this investigation are expected to improve damping identification in case of one-to-one internal resonance. The inclusion of the pellets as an additional degree of freedom is also desirable in this context. More importantly, the experimental setup presented here will be adapted to the study of more representative fuel bundle models. In particular, the following complicating effects are planned to be considered: (i) zirconium spacer grids as boundary constraints for fuel rods; (ii) flowing water at high speed along the axis of the rods; (iii) fuel bundles constituted by a cluster of parallel fuel rods with a guide tube. This will improve the understanding of non-linear vibrations and dissipation in PWR cores.

5.7 ACKNOWLEDGEMENT

6   CONCLUSION

This thesis primarily concerns with modelling the nonlinear damping characteristics of viscoelastic plates and slender beams under large amplitude vibrations. Understanding the damping variation in large amplitude vibrations of these structures can help develop efficient and safe structures.

Large amplitude vibrations were experimentally measured around the fundamental mode of rubber plates and slender beams. These experiments helped capture these structures' nonlinearity and hysteresis characteristics providing insight into the nonlinear response. It was observed that in general the damping increases during large amplitude vibrations of rubber plates and slender tubes. Nonlinear damping models are necessary to correctly model them.

For rubber plates manufactured from silicone and neoprene, the damping value increases to about 60% of the value observed for small amplitude (linear) vibrations at the maximum vibration amplitude of 3 times the thickness. These results are coherent with the results observed for large amplitude vibration studies conducted for elastic plates described in [22, 58]. Subsequently, the following three nonlinear damping models were developed to evaluate its suitability to capture the observed nonlinear behavior in rubber plates.

   a) Kelvin-Voigt (KV) based nonlinear damping model
   b) Standard Linear Solid (SLS) based nonlinear damping model
   c) Loss factor based on dissipated and stored energies model

These numerical models were validated by comparing the nonlinear stiffness between the model and experiments.

The Kelvin-Voigt material model which includes the effect of geometric nonlinearity could not model the damping variation observed experimentally. The SLS material model which included the geometrical nonlinear springs could model the observed frequency dependent stiffness and damping variation of viscoelastic materials. The SLS model essentially introduces an additional nonlinear damping term $x^2\dot{x}$ along with the linear viscous damping term $\dot{x}$. The SLS model

proved to be more accurate in capturing the damping variation than the other two models. The SLS model also confirms the phenomenological nonlinear damping term introduced by other scholars to capture the nonlinear damping variation in MEMS and NEMS [59, 60]. In addition to effectively capturing the observed nonlinear characteristics of the viscoelastic plates and slender beams [111], the SLS model was also found to accurately capture the same behavior in other elastic structures also [111]. It can be concluded that a reliable nonlinear damping model is developed and validated for modelling the dissipation present in thin walled structures of different materials and different boundary conditions. This advancement in modelling the dissipation would help us take advantage of new materials and push the conventional limits for designing better structures.

The loss factor based on energies model calculates the damping estimate independent of frequency. This model provides a unique understanding of the variation of damping with frequency and vibration amplitude. This model helps to understand the observed behavior that dissipated energy is higher as the structure undergoes nonlinear vibrations.

In addition to the above three models, a time domain-based parameter identification tool was also developed to identify the stiffness and damping parameters. This method deals with time domain information rather than frequency domain information resulting in avoiding any re-construction of the mean displacement required for characterizing softening type of systems typical of shells and panels. This model serves to quickly characterize the structure from experimental data. The results from this simplified model closely approximates the results of the SLS based reduced-order model.

For the experiments on slender beams, large amplitude vibration measurements were obtained on three zirconium beams with three different configurations: empty tube, tube with freely moving pellets (modeling nuclear fuel pellets) and tube with fixed pellets. These three tubes were also tested in air and water. In total, six different configurations of the slender beams were tested. These six configurations were chosen to understand and study the impact of characteristics like: stiffness, damping, one-to-one internal resonance, and fluid-structure interaction. These slender

tubes were meant to closely represent the nuclear fuel rods in Pressurized Water Reactors (PWR). The measured large amplitude vibrations will help understand the nonlinear damping expected from fuel assemblies during a large amplitude excitation like a seismic excitation. Thereby an accurate estimate of safety margin present in the nuclear fuel assemblies can be found out in case of critical scenarios.

A large volume of experimental data was collected as a part of this thesis. This data can be used to validate numerical models developed by other researchers. The nonlinear damping model developed and validated here would help engineers and researchers across many disciplines to model the damping expected out of thin structures experiencing large amplitude vibrations accurately. This would eliminate the current practice of using linear damping models and thereby lead to efficient, safe and economical structures.

6.1 SUGGESTIONS FOR FUTURE WORK

In this thesis, models were developed to characterize the nonlinear damping behavior for thin-walled viscoelastic plates and slender beams. It is the author's hypothesis that these models could describe the nonlinear damping behavior of other thin walled viscoelastic structures like panels and shells despite these structures exhibiting a softening type response. It could be an interesting exercise to verify this hypothesis.

In the current study, the slender tubes evaluated were subjected to large amplitude vibrations under fixed-fixed boundary condition at the ends. It would be interesting to test these tubes under more realistic boundary conditions. Further, a cluster of slender beams can be studied for their large amplitude vibrations both in air, in water and in water flow conditions. The results of these future studies combined with the present study help nuclear fuel engineers to better understand the complex mechanism of damping present in the nuclear fuel assembly.

Only two of the six configurations tested were used to extract nonlinear parameters and damping. Other four configurations can be used to identify the parameters. And possibly to understand the influence of the different configuration on stiffness and damping.

REFERENCES

[1] P. Balasubramanian, G. Ferrari, M. Amabili, and Z. J. G. N. del Prado, "Experimental and theoretical study on large amplitude vibrations of clamped rubber plates," *International Journal of Non-Linear Mechanics,* vol. 94, pp. 36-45, 2017.

[2] P. Balasubramanian, G. Ferrari, and M. Amabili, "Identification of the viscoelastic response and nonlinear damping of a rubber plate in nonlinear vibration regime," *Mechanical Systems and Signal Processing,* vol. 111, pp. 376-398, 2018.

[3] M. Amabili, P. Balasubramanian, and G. Ferrari, "Nonlinear Fractional Damping and Frequency-Depending Storage Modulus in Nonlinear Vibrations of Viscoelastic Rectangular Plates," *submitted to an International Journal,* 2019.

[4] G. Ferrari *et al.*, "Non-linear vibrations of nuclear fuel rods," *Nuclear Engineering and Design,* vol. 338, pp. 269-283, 2018.

[5] M. Amabili, *Nonlinear Vibrations and Stability of Shells and Plates*. Cambridge University Press, 2008.

[6] "2 Concepts, definitions and methods," in *Fluid-Structure Interactions*, vol. Volume 1, P. P. Michael, Ed.: Academic Press, 1998, pp. 6-58.

[7] E. J. Doedel, A. R. Champneys, T. F. Fairgrieve, Y. A. Kuznetsov, B. Sandstede, and X. Wang, "Continuation and bifurcation software for ordinary differential equations (with HomCont)," *AUTO97, Concordia University, Canada,* 1997.

[8] S. S. Rao and F. F. Yap, *Mechanical vibrations*. Prentice hall Upper Saddle River, 2011.

[9] A. W. Leissa, "The free vibration of rectangular plates," *Journal of Sound and Vibration,* vol. 31, no. 3, pp. 257-293, 1973/12 1973.

[10] T. Von Kármán, *Festigkeitsprobleme im maschinenbau*. Teubner, 1910.

[11] M. Sathyamoorthy, "Nonlinear vibrations of plates. a review," 1983.

[12] C.-Y. Chia, "Geometrically Nonlinear Behavior of Composite Plates: A Review," *Applied Mechanics Reviews,* vol. 41, no. 12, pp. 439-451, 1988.

[13] H. G. Chu HN, "Influence of large amplitude on free flexural vibrations of rectangular elastic plates," *Journal of Applied Mechanics,* no. 23, pp. 532–540, 1956.

[14] V. T. Ganapathi M, Sarma BS, "Nonlinear flexural vibrations of laminated rectangular plates," no. 36, pp. 685-688, 1991.

[15] S. Rao, A. Sheikh, and M. Mukhopadhyay, "Large-amplitude finite element flexural vibration of plates/stiffened plates," *The Journal of the Acoustical Society of America,* vol. 93, no. 6, pp. 3250-3257, 1993.

[16] M. Amabili, "Nonlinear vibrations of rectangular plates with different boundary conditions: Theory and experiments," *Computers and Structures,* vol. 82, no. 31-32, pp. 2587-2605, 2004.

[17] M. Amabili, "Theory and experiments for large-amplitude vibrations of rectangular plates with geometric imperfections," *Journal of Sound and Vibration,* vol. 291, no. 3-5, pp. 539-565, 2006.

[18] A. K. Noor, C. M. Andersen, and J. M. Peters, "Reduced basis technique for nonlinear vibration analysis of composite panels," *Computer Methods in Applied Mechanics and Engineering,* vol. 103, no. 1-2, pp. 175-186, 1993.

[19] B. Harras, R. Benamar, and R. G. White, "Geometrically non-linear free vibration of

fully clamped symmetrically laminated rectangular composite plates," *Journal of Sound and Vibration,* vol. 251, no. 4, pp. 579-619, 2002.

[20]   F. Alijani and M. Amabili, "Nonlinear vibrations of laminated and sandwich rectangular plates with free edges. Part 1: Theory and numerical simulations," *Composite Structures,* vol. 105, pp. 422-436, 2013.

[21]   F. Alijani, M. Amabili, G. Ferrari, and V. D'Alessandro, "Nonlinear vibrations of laminated and sandwich rectangular plates with free edges. Part 2: Experiments & comparisons," *Composite Structures,* vol. 105, pp. 437-445, 2013.

[22]   F. Alijani, M. Amabili, P. Balasubramanian, S. Carra, G. Ferrari, and R. Garziera, "Damping for large-amplitude vibrations of plates and curved panels, Part 1: Modeling and experiments," *International Journal of Non-Linear Mechanics,* vol. 85, pp. 23-40, 2016.

[23]   D. Hui, "Effects of geometric imperfections on large-amplitude vibrations of rectangular plates with hysteresis damping," *Journal of applied mechanics,* vol. 51, no. 1, pp. 216-220, 1984.

[24]   W. Flügge, *Viscoelasticity*. Springer Science & Business Media, 2013.

[25]   S. P. Marques and G. J. Creus, *Computational viscoelasticity*. Springer Science & Business Media, 2012.

[26]   S. N. Mahmoodi, N. Jalili, and S. E. Khadem, "An experimental investigation of nonlinear vibration and frequency response analysis of cantilever viscoelastic beams," *Journal of Sound and vibration,* vol. 311, no. 3, pp. 1409-1419, 2008.

[27]   M. H. Ghayesh, "Nonlinear dynamic response of a simply-supported Kelvin–Voigt viscoelastic beam, additionally supported by a nonlinear spring," *Nonlinear Analysis: Real World Applications,* vol. 13, no. 3, pp. 1319-1333, 2012.

[28]   E. Esmailzadeh and M. Jalali, "Nonlinear oscillations of viscoelastic rectangular plates," *Nonlinear Dynamics,* vol. 18, no. 4, pp. 311-319, 1999.

[29]   Y. Sun and S. Zhang, "Chaotic dynamic analysis of viscoelastic plates," *International Journal of Mechanical Sciences,* vol. 43, no. 5, pp. 1195-1208, 2001.

[30]   D. Balkan and Z. Mecitoğlu, "Nonlinear dynamic behavior of viscoelastic sandwich composite plates under non-uniform blast load: theory and experiment," *International Journal of Impact Engineering,* vol. 72, pp. 85-104, 2014.

[31]   M. Amabili, "Nonlinear vibrations of viscoelastic rectangular plates," *Journal of Sound and Vibration,* vol. 362, pp. 142-156, 2016.

[32]   Q. Han and H. Hu, "Bifurcation analysis of a nonlinear viscoelastic panel," *European Journal of Mechanics-A/Solids,* vol. 20, no. 5, pp. 827-839, 2001.

[33]   B. K. Eshmatov, "Nonlinear vibrations and dynamic stability of viscoelastic orthotropic rectangular plates," *Journal of Sound and Vibration,* vol. 300, no. 3, pp. 709-726, 2007.

[34]   M. Salehi and A. Safi-Djahanshahi, "Non-Linear analysis of viscoelastic rectangular plates subjected to in-plane compression," ed: MRA, 2010.

[35]   T.-W. Kim and J.-H. Kim, "Nonlinear vibration of viscoelastic laminated composite plates," *International Journal of Solids and Structures,* vol. 39, no. 10, pp. 2857-2870, 2002.

[36]   T. Ramesh and N. Ganesan, "Vibration and damping analysis of cylindrical shells with a constrained damping layer," *Computers & structures,* vol. 46, no. 4, pp. 751-758, 1993.

[37]   F. Badalov, K. Éshmatov, and B. Anzhiev, "Investigation of physically and geometrically

nonlinear osciliations of viscoelastic plates and shells by the averaging method," *International Applied Mechanics,* vol. 21, no. 3, pp. 263-269, 1985.

[38] B. K. Eshmatov, "Nonlinear vibrations of viscoelastic cylindrical shells taking into account shear deformation and rotatory inertia," *Nonlinear Dynamics,* vol. 50, no. 1-2, pp. 353-361, 2007.

[39] M. Paidoussis, "Dynamics of cylindrical structures subjected to axial flow," *Journal of sound and vibration,* vol. 29, no. 3, pp. 365-385, 1973.

[40] M. Lighthill, "Note on the swimming of slender fish," *Journal of fluid Mechanics,* vol. 9, no. 02, pp. 305-317, 1960.

[41] "Fluid-Structure Interactions A2 - Paidoussis, Michael P," in *Fluid-Structure Interactions (Second Edition)*Oxford: Academic Press, 2014, p. i.

[42] S.-s. Chen and M. W. Wambsganss, "Parallel-flow-induced vibration of fuel rods," *Nuclear Engineering and Design,* vol. 18, no. 2, pp. 253-278, 1972.

[43] G. Taylor, "Analysis of the swimming of long and narrow animals," in *Proceedings of the Royal Society of London A: Mathematical, Physical and Engineering Sciences*, 1952, vol. 214, no. 1117, pp. 158-183: The Royal Society.

[44] D. Mateescu, M. Paıdoussis, and F. Bélanger, "A time-integration method using artificial compressibility for unsteady viscous flows," *Journal of Sound and Vibration,* vol. 177, no. 2, pp. 197-205, 1994.

[45] H. Liu, X. Luo, and Z. Cai, "Stability and energy budget of pressure-driven collapsible channel flows," *Journal of Fluid Mechanics,* vol. 705, pp. 348-370, 2012.

[46] A. Jamal, M. P. Païdoussis, and L. G. Mongeau, "Linear and Nonlinear Dynamics of Cantilevered Cylinders in Axial Flow," in *ASME 2014 Pressure Vessels and Piping Conference*, 2014, pp. V004T04A027-V004T04A027: American Society of Mechanical Engineers.

[47] Q. Ni, M. Li, M. Tang, Y. Wang, Y. Luo, and L. Wang, "In-plane and out-of-plane free vibration and stability of a curved rod in flow," *Journal of Fluids and Structures,* vol. 49, pp. 667-686, 2014.

[48] C. Semler, W. Gentleman, and M. Paï̈, "Numerical solutions of second order implicit non-linear ordinary differential equations," *Journal of Sound and Vibration,* vol. 195, no. 4, pp. 553-574, 1996.

[49] J.-L. Lopes, M. Païdoussis, and C. Semler, "Linear and nonlinear dynamics of cantilevered cylinders in axial flow. Part 2: The equations of motion," *Journal of Fluids and Structures,* vol. 16, no. 6, pp. 715-737, 2002.

[50] M. Païdoussis and P. Besançon, "Dynamics of arrays of cylinders with internal and external axial flow," *Journal of Sound and Vibration,* vol. 76, no. 3, pp. 361-379, 1981.

[51] Y. Modarres-Sadeghi, M. Païdoussis, C. Semler, and E. Grinevich, "Experiments on vertical slender flexible cylinders clamped at both ends and subjected to axial flow," *Philosophical Transactions of the Royal Society of London A: Mathematical, Physical and Engineering Sciences,* vol. 366, no. 1868, pp. 1275-1296, 2008.

[52] Y. Modarres-Sadeghi, M. Païdoussis, and C. Semler, "A nonlinear model for an extensible slender flexible cylinder subjected to axial flow," *Journal of Fluids and Structures,* vol. 21, no. 5, pp. 609-627, 2005.

[53] Y. Modarres-Sadeghi, C. Semler, M. Wadham-Gagnon, and M. Païdoussis, "Dynamics of cantilevered pipes conveying fluid. Part 3: Three-dimensional dynamics in the presence

of an end-mass," *Journal of Fluids and Structures,* vol. 23, no. 4, pp. 589-603, 2007.

[54]   P. Moretti and R. Lowery, "Hydrodynamic inertia coefficients for a tube surrounded by rigid tubes," *Journal of Pressure Vessel Technology,* vol. 98, no. 3, pp. 190-193, 1976.

[55]   S. Chen and J. Jendrzejczyk, "Experiments on fluidelastic vibration of cantilevered tube bundles," *Journal of Mechanical Design,* vol. 100, no. 3, pp. 540-548, 1978.

[56]   S.-S. Chen, "Dynamic responses of two parallel circular cylinders in a liquid," *Journal of Pressure Vessel Technology,* vol. 97, no. 2, pp. 78-83, 1975.

[57]   S.-S. Chen, "Vibrations of a Row of Circular Cylinders in a Liquid," *Journal of Engineering for Industry,* vol. 97, no. 4, pp. 1212-1218, 1975.

[58]   M. Amabili, F. Alijani, and J. Delannoy, "Damping for large-amplitude vibrations of plates and curved panels, part 2: Identification and comparisons," *International Journal of Non-Linear Mechanics,* vol. 85, pp. 226-240, 2016.

[59]   S. Zaitsev, O. Shtempluck, E. Buks, and O. Gottlieb, "Nonlinear damping in a micromechanical oscillator," *Nonlinear Dynamics,* vol. 67, no. 1, pp. 859-883, 2012.

[60]   A. Eichler, J. Moser, J. Chaste, M. Zdrojek, I. Wilson-Rae, and A. Bachtold, "Nonlinear damping in mechanical resonators made from carbon nanotubes and graphene," *Nature nanotechnology,* vol. 6, no. 6, pp. 339-342, 2011.

[61]   D. O. Fearnow, "Investigation of the Structural Damping of a Full-scale Airplane Wing," 1951.

[62]   A. Fellowes, T. Wilson, G. Kemble, C. Havill, and J. Wright, "Wing box nonlinear structural damping," in *Proc. 15th Int. Forum on Aeroelasticity and Structural Dynamics (IFASD 2011), Paris, France*, 2011, vol. 26, p. 30.

[63]   W. Klippel, "Nonlinear damping in micro-speakers," in *Proc. AIA-DAGA 2013 Conf. on Acoustics, Merano, Italy*, 2013, vol. 18, p. 21.

[64]   S. Elliott, M. G. Tehrani, and R. Langley, "Nonlinear damping and quasi-linear modelling," *Phil. Trans. R. Soc. A,* vol. 373, no. 2051, p. 20140402, 2015.

[65]   M. Amabili, K. Karazis, and K. Khorshidi, "Nonlinear vibrations of rectangular laminated composite plates with different boundary conditions," *International Journal of Structural Stability and Dynamics,* vol. 11, no. 4, pp. 673-695, 2011.

[66]   M. Amabili, "Theory and experiments for large-amplitude vibrations of circular cylindrical panels with geometric imperfections," *Journal of Sound and Vibration,* vol. 298, no. 1-2, pp. 43-72, 2006.

[67]   M. Amabili, P. Balasubramanian, and G. Ferrari, "Travelling wave and non-stationary response in nonlinear vibrations of water-filled circular cylindrical shells: Experiments and simulations," *Journal of Sound and Vibration,* vol. 381, pp. 220-245, 2016.

[68]   G. Ferrari, "Experimental Investigation of Vibration Damping in Linear and Nonlinear Vibration," McGill University Libraries, 2017.

[69]   D. Davidovikj, F. Alijani, S. J. Cartamil-Bueno, H. S. van der Zant, M. Amabili, and P. G. Steeneken, "Young's modulus of 2D materials extracted from their nonlinear dynamic response," *arXiv preprint arXiv:1704.05433,* 2017.

[70]   S. Wolfram, *The mathematica book*. Wolfram Media, Incorporated, 1996.

[71]   E. Doedel, A. Champneys, T. Fairgrieve, Y. A. Kuznetsov, B. Sandstede, and X. Wang, "Auto97, continuation and bifurcation software for ordinary differential equations (with homcont). 1997," *Available by anonymous ftp from ftp. cs. concordia. ca, directory pub/doedel/auto*.

[72]   M. R. Sayag and E. H. Dowell, "Linear Versus Nonlinear Response of a Cantilevered Beam Under Harmonic Base Excitation: Theory and Experiment," *Journal of Applied Mechanics,* vol. 83, no. 10, p. 101002, 2016.

[73]   M. Amabili, "Reduced-order models for nonlinear vibrations, based on natural modes: the case of the circular cylindrical shell," *Phil. Trans. R. Soc. A,* vol. 371, no. 1993, p. 20120474, 2013.

[74]   M. D. Rao, "Recent applications of viscoelastic damping for noise control in automobiles and commercial airplanes," *Journal of Sound and Vibration,* vol. 262, no. 3, pp. 457-474, 2003.

[75]   E. E. Ungar and E. M. Kerwin Jr, "Loss factors of viscoelastic systems in terms of energy concepts," *The Journal of the acoustical Society of America,* vol. 34, no. 7, pp. 954-957, 1962.

[76]   H. T. Banks and D. Inman, "On damping mechanisms in beams," *Journal of applied mechanics,* vol. 58, no. 3, pp. 716-723, 1991.

[77]   E. E. Ungar and J. A. Zapfe, "Structural damping," *Noise and Vibration Control Engineering: Principles and Applications, Second Edition,* pp. 579-609, 2007.

[78]   G. Lee and B. Hartmann, "Specific damping capacity for arbitrary loss angle," *Journal of sound and vibration,* vol. 211, no. 2, pp. 265-272, 1998.

[79]   J.-M. Berthelot, M. Assarar, Y. Sefrani, and A. El Mahi, "Damping analysis of composite materials and structures," *Composite Structures,* vol. 85, no. 3, pp. 189-204, 2008.

[80]   W. Liu and M. S. Ewing, "Experimental and analytical estimation of loss factors by the power input method," *AIAA journal,* vol. 45, no. 2, p. 477, 2007.

[81]   R. Lin and S. Ling, "Identification of damping characteristics of viscoelastically damped structures using vibration test results," *Proceedings of the Institution of Mechanical Engineers, Part C: Journal of Mechanical Engineering Science,* vol. 210, no. 2, pp. 111-121, 1996.

[82]   O. Gottlieb and G. Habib, "Non-linear model-based estimation of quadratic and cubic damping mechanisms governing the dynamics of a chaotic spherical pendulum," *Journal of Vibration and Control,* vol. 18, no. 4, pp. 536-547, 2012.

[83]   M. Amabili, "(In Press) Nonlinear damping in large-amplitude vibrations: modelling and experiments," *Nonlinear Dynamics,* 2017.

[84]   B. Peeters, H. Van der Auweraer, P. Guillaume, and J. Leuridan, "The PolyMAX frequency-domain method: a new standard for modal parameter estimation?," *Shock and Vibration,* vol. 11, no. 3-4, pp. 395-409, 2004.

[85]   S. Wolfram, *The mathematica book.* Wolfram Media, 2000.

[86]   D. G, "Erzwungene Schwingung bei veranderlicher Eigenfrequenz und ihre technische Bedeutung," Vieweg ed. Braunschweig, 1918.

[87]   G. Kerschen, K. Worden, A. F. Vakakis, and J. C. Golinval, "Past, present and future of nonlinear system identification in structural dynamics," *Mechanical Systems and Signal Processing,* vol. 20, no. 3, pp. 505-592, 2006.

[88]   R. S. Lakes, *Viscoelastic materials.* Cambridge University Press, 2009.

[89]   C.-Y. Chia, *Nonlinear Analysis of Plates.* New York: McGraw-Hill, 1980.

[90]   M. Sathyamoorthy, "Nonlinear Vibration Analysis of Plates: A Review and Survey of Current Developments," *Applied Mechanics Reviews,* vol. 40, no. 11, pp. 1553-1561, 1987.

[91]   P. Ribeiro and M. Petyt, "Geometrical non-linear, steady state, forced, periodic vibration of plates, part I: model and convergence studies," *Journal of Sound and Vibration,* vol. 226, no. 5, pp. 955-983, 1999.

[92]   F. Alijani and M. Amabili, "Non-linear static bending and forced vibrations of rectangular plates retaining non-linearities in rotations and thickness deformation," *International Journal of Non-linear Mechanics,* vol. 67, pp. 394-404, 2014.

[93]   M. Amabili, *Nonlinear Mechanics of Shells and Plates in Composite, Soft and Biological Materials*. Cambridge University Press, 2018.

[94]   Z. Xia and S. Łukasiewicz, "Non-linear, free, damped vibrations of sandwich plates," *Journal of sound and vibration,* vol. 175, no. 2, pp. 219-232, 1994.

[95]   Z. Xia and S. Łukasiewicz, "Nonlinear damped vibrations of simply-supported rectangular sandwich plates," *Nonlinear Dynamics,* vol. 8, no. 4, pp. 417-433, 1995.

[96]   Y. A. Rossikhin and M. Shitikova, "Analysis of free non-linear vibrations of a viscoelastic plate under the conditions of different internal resonances," *International Journal of Non-Linear Mechanics,* vol. 41, no. 2, pp. 313-325, 2006.

[97]   E. H. Boutyour and M. Potier-Ferry, "A harmonic balance method for the non-linear vibration of viscoelastic shells," *Comptes Rendus Mécanique,* vol. 334, no. 1, pp. 68-73, 2006.

[98]   M. Bilasse, L. Azrar, and E. Daya, "Complex modes based numerical analysis of viscoelastic sandwich plates vibrations," *Computers & Structures,* vol. 89, no. 7-8, pp. 539-555, 2011.

[99]   S. Mahmoudkhani and H. Haddadpour, "Nonlinear vibration of viscoelastic sandwich plates under narrow-band random excitations," *Nonlinear Dynamics,* vol. 74, no. 1-2, pp. 165-188, 2013.

[100]   S. Mahmoudkhani, H. Haddadpour, and H. Navazi, "The effects of nonlinearities on the vibration of viscoelastic sandwich plates," *International Journal of Non-Linear Mechanics,* vol. 62, pp. 41-57, 2014.

[101]   Y. A. Rossikhin, M. V. Shitikova, and J. C. Ngenzi, "A new approach for studying nonlinear dynamic response of a thin plate with internal resonance in a fractional viscoelastic medium," *Shock and Vibration,* vol. 2015, 2015.

[102]   P. Litewka and R. Lewandowski, "Nonlinear harmonically excited vibrations of plates with Zener material," *Nonlinear Dynamics,* vol. 89, no. 1, pp. 691-712, 2017.

[103]   P. Litewka and R. Lewandowski, "Steady-state non-linear vibrations of plates using Zener material model with fractional derivative," *Computational Mechanics,* vol. 60, no. 2, pp. 333-354, 2017.

[104]   M. Permoon, H. Haddadpour, and M. Javadi, "Nonlinear vibration of fractional viscoelastic plate: Primary, subharmonic, and superharmonic response," *International Journal of Non-Linear Mechanics,* vol. 99, pp. 154-164, 2018.

[105]   J. L. Trueba, J. Rams, and M. A. Sanjuán, "Analytical estimates of the effect of nonlinear damping in some nonlinear oscillators," *International Journal of Bifurcation and Chaos,* vol. 10, no. 09, pp. 2257-2267, 2000.

[106]   B. Jeong, H. Cho, M.-F. Yu, A. F. Vakakis, D. M. McFarland, and L. A. Bergman, "Modeling and measurement of geometrically nonlinear damping in a microcantilever–nanotube system," *ACS nano,* vol. 7, no. 10, pp. 8547-8553, 2013.

[107]   S. J. Elliott, L. Benassi, M. J. Brennan, P. Gardonio, and X. Huang, "Mobility analysis of

active isolation systems," *Journal of Sound and Vibration,* vol. 271, no. 1-2, pp. 297-321, // 2004.

[108] M. Amabili, "Nonlinear damping in nonlinear vibrations of rectangular plates: Derivation from viscoelasticity and experimental validation," *Journal of the Mechanics and Physics of Solids,* vol. 118, pp. 275-292, 2018/09/01/ 2018.

[109] M. Amabili, "Derivation of nonlinear damping from viscoelasticity in case of nonlinear vibrations," *Nonlinear Dynamics,* pp. 1-13, 2018.

[110] R. Koeller, "Applications of fractional calculus to the theory of viscoelasticity," *Journal of Applied Mechanics,* vol. 51, no. 2, pp. 299-307, 1984.

[111] M. Amabili, "Nonlinear damping in large-amplitude vibrations: modelling and experiments," *Nonlinear Dynamics,* pp. 1-14, 2018.

[112] Y. Fung, "Foundation of Solid Mechanics, Prentice-Hall, Englewood Cliffs, NJ, 1968."

[113] B. West, M. Bologna, and P. Grigolini, *Physics of fractal operators*. Springer Science & Business Media, 2012.

[114] M. Amabili, "Nonlinear Damping in Nonlinear Vibrations of Rectangular Plates: Derivation from Viscoelasticity and Experimental Validation," *Journal of the Mechanics and Physics of Solids,* 2018.

[115] M. Di Paola, A. Pirrotta, and A. Valenza, "Visco-elastic behavior through fractional calculus: an easier method for best fitting experimental results," *Mechanics of Materials,* vol. 43, no. 12, pp. 799-806, 2011.

[116] S. Zhu, C. Cai, and P. D. Spanos, "A nonlinear and fractional derivative viscoelastic model for rail pads in the dynamic analysis of coupled vehicle–slab track systems," *Journal of Sound and Vibration,* vol. 335, pp. 304-320, 2015.

[117] S.-S. Chen, "Flow-induced vibration of circular cylindrical structures," Argonne National Lab.1985.

[118] M. P. Païdoussis, "Real-life experiences with flow-induced vibration," *Journal of Fluids and Structures,* vol. 22, no. 6, pp. 741-755, 2006/08/01/ 2006.

[119] D. S. Weaver, S. Ziada, M. K. Au-Yang, S. S. Chen, M. P. Païdoussis, and M. J. Pettigrew, "Flow-Induced Vibrations in Power and Process Plant Components—Progress and Prospects," *Journal of Pressure Vessel Technology,* vol. 122, no. 3, pp. 339-348, 2000.

[120] F. A. Lepore, "Flow induced vibrations in the SSME injector heads," 1991.

[121] M. P. Païdoussis, S. J. Price, and E. De Langre, *Fluid-structure interactions: cross-flow-induced instabilities*. Cambridge University Press, 2010.

[122] A. Bhattacharya, *Investigations on Flow and Flow-induced Vibration of CANDU Fuel Bundles*. 2014.

[123] Y. G. Dragunov, V. Solonin, V. Perevezentsev, and I. Petrov, "Vibrations of fuel-element bundles in VVER fuel assemblies excited by turbulent coolant flow," *Atomic Energy,* vol. 113, no. 3, pp. 153-162, 2013.

[124] H. Yuan, J. Solberg, E. Merzari, A. Kraus, and I. Grindeanu, "Flow-induced vibration analysis of a helical coil steam generator experiment using large eddy simulation," *Nuclear Engineering and Design,* vol. 322, pp. 547-562, 2017.

[125] S.-S. Chen, "Vibration of nuclear fuel bundles," *Nuclear Engineering and Design,* vol. 35, no. 3, pp. 399-422, 1975.

[126] M. Paidoussis and L. R. Curling, "An analytical model for vibration of clusters of flexible

cylinders in turbulent axial flow," *Journal of Sound and Vibration,* vol. 98, no. 4, pp. 493-517, 1985.

[127] M. Au-Yang and J. Burgess, "Critical velocity of a nonlinearly supported multispan tube bundle," *Journal of pressure vessel technology,* vol. 129, no. 3, pp. 535-540, 2007.

[128] D. De Santis and A. Shams, "Numerical modeling of flow induced vibration of nuclear fuel rods," *Nuclear Engineering and Design,* vol. 320, pp. 44-56, 2017.

[129] E. Ter Hofstede, S. Kottapalli, and A. Shams, "Numerical prediction of flow induced vibrations in nuclear reactor applications," *Nuclear Engineering and Design,* vol. 319, pp. 81-90, 2017.

[130] S. KN, H. Kim, Y. KH, and J. YH, "Verification test and model updating for a nuclear fuel rod with its supporting structure," *Nuclear Engineering and Technology,* vol. 33, no. 1, pp. 73-82, 2001.

[131] H. K. Kim and M. S. Kim, "Vibration analysis of PWR fuel rod," *Journal of sound and vibration,* vol. 282, no. 1-2, pp. 553-572, 2005.

[132] C. Liu, Y. Ferng, and C. Shih, "CFD evaluation of turbulence models for flow simulation of the fuel rod bundle with a spacer assembly," *Applied Thermal Engineering,* vol. 40, pp. 389-396, 2012.

[133] H. Liu, D. Chen, L. Hu, D. Yuan, and H. Gao, "Numerical investigations on flow-induced vibration of fuel rods with spacer grids subjected to turbulent flow," *Nuclear Engineering and Design,* vol. 325, pp. 68-77, 2017.

[134] S. Sandström, "Vibration analysis of a heat exchanger tube row with ADINA," *Computers & Structures,* vol. 26, no. 1-2, pp. 297-305, 1987.

[135] J.-p. Simoneau, T. Sageaux, N. Moussallam, and O. Bernard, "Fluid structure interaction between rods and a cross flow–Numerical approach," *Nuclear Engineering and Design,* vol. 241, no. 11, pp. 4515-4522, 2011.

[136] M. H. Choi, H. S. Kang, K. H. Yoon, and K. N. Song, "Vibration analysis of a dummy fuel rod continuously supported by spacer grids," *Nuclear Engineering and Design,* vol. 232, no. 2, pp. 185-196, 2004/08/01/ 2004.

[137] B. De Pauw, W. Weijtjens, S. Vanlanduit, K. Van Tichelen, and F. Berghmans, "Operational modal analysis of flow-induced vibration of nuclear fuel rods in a turbulent axial flow," *Nuclear Engineering and Design,* vol. 284, pp. 19-26, 2015.

[138] J. Bakosi, M. A. Christon, R. B. Lowrie, L. Pritchett-Sheats, and R. Nourgaliev, "Large-eddy simulations of turbulent flow for grid-to-rod fretting in nuclear reactors," *Nuclear Engineering and Design,* vol. 262, pp. 544-561, 2013.

[139] Z. Hu, M. D. Thouless, and W. Lu, "Effects of gap size and excitation frequency on the vibrational behavior and wear rate of fuel rods," *Nuclear Engineering and Design,* vol. 308, pp. 261-268, 2016.

[140] K.-T. Kim, "The effect of fuel rod supporting conditions on fuel rod vibration characteristics and grid-to-rod fretting wear," *Nuclear Engineering and Design,* vol. 240, no. 6, pp. 1386-1391, 2010/06/01/ 2010.

[141] D. E. Adams and A. J. Allemang, "Survey of Nonlinear Detection and Identification Techniques for Experimental Vibrations," in *in Proceedings of the International Conference on Noise and Vibration Engineering*, 1998: Citeseer.

[142] P. Piteau, X. Delaune, L. Borsoi, and J. Antunes, "Experimental identification of the fluid-elastic coupling forces on a flexible tube within a rigid square bundle subjected to

single-phase cross-flow," *Journal of Fluids and Structures,* vol. 86, pp. 156-169, 2019.

[143]   S. Adhikari and J. Woodhouse, "Identification of damping: part 1, viscous damping," *Journal of Sound and Vibration,* vol. 243, no. 1, pp. 43-61, 2001.

[144]   S. Adhikari and J. Woodhouse, "Identification of damping: part 2, non-viscous damping," *Journal of Sound and Vibration,* vol. 243, no. 1, pp. 63-88, 2001.

[145]   J. Delannoy, M. Amabili, B. Matthews, B. Painter, and K. Karazis, "Non-linear damping identification in nuclear systems under external excitation," in *ASME 2015 International Mechanical Engineering Congress and Exposition*, 2015, pp. V04AT04A051-V04AT04A051: American Society of Mechanical Engineers.

[146]   J. Delannoy, M. Amabili, B. Matthews, B. Painter, and K. Karazis, "Identification of non-linear damping of nuclear reactor components in case of one-to-one internal resonance," in *ASME 2016 International Mechanical Engineering Congress and Exposition*, 2016, pp. V04AT05A039-V04AT05A039: American Society of Mechanical Engineers.

[147]   E. Viallet and T. Kestens, "Prediction of flow induced damping of a PWR fuel assembly in case of seismic and LOCA load case," *In: Transactions of the 17th International Conference on Striuctural Mechanics in Reactor Technology (SMiRT 17),* August 17-22, 2003 2003.

[148]   H. Connors, S. Savorelli, and F. Kramer, "Hydrodynamic damping of rod bundles in axial flow," *Am. Soc. Mech. Eng., Pressure Vessels Piping Div.,(Tech. Rep.) PVP;(United States),* vol. 63, no. CONF-820601-, 1982.

[149]   M. A. Hassan, R. J. Rogers, and A. G. Gerber, "Damping-controlled fluidelastic instability forces in multi-span tubes with loose supports," *Nuclear Engineering and Design,* vol. 241, no. 8, pp. 2666-2673, 2011.

[150]   B. Brenneman and S. Shah, "Damping in Fuel Assemblies for Axial Flow," *ASME-PUBLICATIONS-PVP,* vol. 414, no. 1, pp. 167-170, 2000.

[151]   B. Collard, "Flow induced damping of a PWR fuel assembly," 2005.

[152]   P. Fardeau, D. Barbier, E. DeLangre, and J. Rigaudeau, "Damping from axial coolant flow in the response of PWR fuel assemblies to horizontal seismic loads," in *Transactions of the 14th International Conference on Structural Mechanics in Reactor Technology (SMiRT14), Lyon, France*, 1997.

[153]   J. K. Vandiver, "Damping Parameters for flow-induced vibration," *Journal of Fluids and Structures,* vol. 35, pp. 105-119, 2012/11/01/ 2012.

[154]   M. Amabili and S. Carra, "Experiments and simulations for large-amplitude vibrations of rectangular plates carrying concentrated masses," *Journal of Sound and Vibration,* vol. 331, no. 1, pp. 155-166, 2012.

[155]   N.-G. Park, H. Rhee, J.-K. Park, S.-Y. Jeon, and H.-K. Kim, "Indirect estimation method of the turbulence induced fluid force spectrum acting on a fuel rod," *Nuclear Engineering and Design,* vol. 239, no. 7, pp. 1237-1245, 2009.

[156]   E. Askari, K.-H. Jeong, and M. Amabili, "Hydroelastic vibration of circular plates immersed in a liquid-filled container with free surface," *Journal of sound and vibration,* vol. 332, no. 12, pp. 3064-3085, 2013.

[157]   T. Sarpkaya, "On the parameter β= Re/KC= D2/νT," *Journal of fluids and structures,* vol. 21, no. 4, pp. 435-440, 2005.

[158]   G. Ferrari, S. Le Guisquet, P. Balasubramanian, M. Amabili, B. Painter, and K. Karazis, "Identification of Non-Linear Parameters of a Nuclear Fuel Rod," in *ASME 2017*

International Mechanical Engineering Congress and Exposition, 2017, pp. V04AT05A041-V04AT05A041: American Society of Mechanical Engineers.